DOE/NV/11508-41

[redacted]

Water Resources Center

EVALUATION OF GROUNDWATER FLOW AND TRANSPORT AT THE FAULTLESS UNDERGROUND NUCLEAR TEST, CENTRAL NEVADA TEST AREA

prepared by

Karl Pohlmann, Jenny Chapman, Ahmed Hassan, and Charalambos Papelis

submitted to

Nevada Operations Office
U.S. Department of Energy

SEPTEMBER 1999

Publication No. 45165

CNT

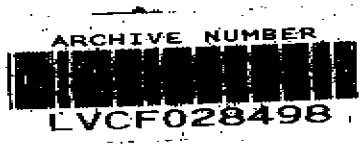

DOE/NV/11508-41

EVALUATION OF GROUNDWATER FLOW AND TRANSPORT AT THE FAULTLESS UNDERGROUND NUCLEAR TEST, CENTRAL NEVADA TEST AREA

prepared by

Karl Pohlmann, Jenny Chapman, Ahmed Hassan, and Charalambos Papelis
Water Resources Center
Desert Research Institute
University and Community College System of Nevada

Publication No. 45165

submitted to

Nevada Operations Office
U.S. Department of Energy
Las Vegas, Nevada

September 1999

The work upon which this report is based was supported by the U.S. Department of Energy under Contract #DE-AC08-95NV11508. Approved for public release, further dissemination unlimited.

EXECUTIVE SUMMARY

Groundwater flow and contaminant transport processes at the Faultless underground nuclear test are examined using numerical modeling. Faultless was the only test conducted at the Central Nevada Test Area (CNTA), located in Hot Creek Valley, between Tonopah and Ely, Nevada. The test occurred on January 19, 1968 at a depth of 975 m below ground surface and had an announced yield of between 200 and 1,000 kilotons (U.S. DOE, 1994). Extensive site characterization activities were conducted in Hot Creek Valley and adjacent regions as part of locating the CNTA. These activities included the drilling and testing of many wells and these data are the foundation for the modeling analysis.

Hot Creek Valley contains hundreds of meters of alluvium derived from adjacent volcanic mountain ranges with minor carbonate contributions. Below the alluvium is a thick volcanic sequence comprised of tuffaceous sediments, nonwelded and welded tuffs and rhyolite lavas. Three hydrogeologic categories are defined based on lithology, electrical resistivity, and hydraulic conductivity (K): Quaternary alluvium (geometric mean K of 2.4×10^{-3} m/d), Tertiary volcanics having low hydraulic conductivity (geometric mean K of 1.2×10^{-4} m/d), and Tertiary volcanics having high hydraulic conductivity (geometric mean K of 1.4×10^{-1} m/d). Tuffaceous sediments and nonwelded tuffs generally fall in the category of low-K volcanic rocks and rhyolites and welded tuffs generally fall in the category of high-K volcanic rocks. Most of the volcanic section at Faultless is comprised of low-K tuffaceous sediments; no rhyolites and only a single 24-m-thick interval of densely welded tuff (at a single well) have been identified.

The CNTA model was developed using stochastic methods that described the natural subsurface heterogeneity in two phases. In the first phase, the geometry of the hydrogeologic categories was described using the sequential indicator simulation (SIS) algorithm. Drilling, aeromagnetic, and seismic data are used to define the boundary between the alluvium and volcanics. Geophysical log signatures, specifically electrical resistivity logs, are used to map the three-dimensional occurrence of the volcanic units. The SIS simulations were conditioned using lithologic and electrical resistivity logs from wells at the site. In the second phase, the distribution of hydraulic conductivity within each hydrogeologic category was described using the sequential Gaussian simulation (SGS) algorithm. The SGS simulations were conditioned using hydraulic conductivity data from the packer tests.

The scale of the model is intermediate between the scale of the near-test environment and the scale of regional groundwater flow. The domain extends from the UC-1 land withdrawal area south to include the UC-3 land withdrawal area, a distance of 8 km. It extends 6.5 km east to west. The thickness is 1,350 m, beginning 290 m above sea level, within the saturated alluvial section. The domain is discretized into a grid of 130 x 160 x 27 cubic cells of 50 m length. The model simulates the complex hydraulic head relationships indicated by regional data. This includes southward flow through the alluvium, while flow in the deeper volcanic section is directed northward to northeastward. Strong vertically downward hydraulic gradients are present in the north part of the domain, while strong vertical gradients upward from the volcanics to the alluvium are present to the

south, consistent with discrete hydraulic head measurements. Groundwater recharge was not directly simulated in the model. Rather, the top of the model is a no-flow boundary, as are the east and west faces. The north, south and bottom faces are specified-head boundaries and are based on the head relationships observed in CNTA wells in Hot Creek Valley.

The immediate area of the Faultless test is characterized in the model as a zone of very low flow, directed downward and slightly to the north. Thus, flow that passes through the cavity region moves down through the low-*K* tuffaceous sediments before reaching hypothesized high-*K* pathways in the welded tuffs. Vertical flow rates in the source volume range from 3.2×10^{-9} to 5.8×10^{-6} m/d, so that the time of transport from the source to the welded tuffs is very long. This representation of low hydraulic conductivities and long groundwater residences times is consistent with the hydraulic properties of the chimney calculated based on water-level recovery rates, and with isotopic data from groundwater samples that indicate residence times on the order of many tens of thousands of years.

Contaminants from the Faultless test are assumed to reside within the cavity and begin migration at the conclusion of the 30-year recovery to pre-test hydraulic head levels. The cavity is simulated as a cube with edge lengths of 200 m. Radionuclides are apportioned between surface deposits and volume deposits in nuclear melt glass, based on their volatility and previous observations. Surface-deposited radionuclides are released hydraulically after equilibration of the cavity with the surrounding flow system. Release from the nuclear melt glass is patterned after dissolution of volcanic glass and assuming a specific surface area of 0.05 m^2/g. The radionuclides were grouped into six unique combinations of geochemical release fraction and retardation. The very long travel times simulated by the model render the release function an insensitive parameter, with the peaks of the breakthrough curves for the six solute classes passing the control plane in order of increasing retardation coefficient.

Equilibrium sorption experiments were conducted using the three aquifer rock types. Distribution coefficients were scaled by a ratio between surface areas measured on the ground experimental material and surface areas measured using a particle size analysis. This resulted in a reduction in the distribution coefficient by up to two orders of magnitude. The retardation coefficients calculated using this scaled value still indicate significant decreases in contaminant velocities. The retardation coefficients vary from 1 (no retardation) to 8,000 for strongly sorbing cations.

Transport of radionuclides from the cavity to the control plane at the site land withdrawal boundary was calculated using particle tracking methods on the same grid discretization and domain size as the groundwater flow model. Two fundamentally different conceptualizations of transport were evaluated: first, treating all three hydrogeologic categories as a porous medium having a homogeneous porosity of 0.18 (consistent with core data from the site), and second, treating the welded tuffs (Category 3) as a fractured unit having a homogeneous flow porosity of 0.005 accompanied by diffusion into a porous matrix. Both model formulations also included the release function, retardation, radioactive decay, and ingrowth of daughter products. Prompt injection was

considered in a sensitivity analysis, but colloidal transport was not included. Unit mass values were used to avoid classified data security issues and the results can be scaled.

The fracture flow/matrix diffusion approach simulates significant retardation and mass distribution over long time periods, and thus is less conservative (simulates less mass breakthrough) than the porous medium approach for most radionuclides. Despite the more conservative formulation, the porous medium approach showed that essentially no breakthrough of contaminants occurred at the UC-1 land withdrawal boundary during the 1,000-year period of interest. Quantifying the breakthrough that is projected to occur after 1,000 years is hampered by the classified nature of the initial source masses. Unclassified estimates, based on gross relationships with test yield, were made for ^{3}H, ^{90}Sr and ^{137}Cs; however, with their relatively short half lives, none of these radionuclides "survived" to the breakthrough plane. Normalized mass fluxes of the remaining radionuclides in the source term are generally also very low, with many of the shorter-lived species also not surviving to the breakthrough plane. The peak mean breakthroughs of the surviving radionuclides occur between 2,000 years for short-lived species with no retardation, up to 75 million years for long-lived radionuclides with significant retardation. The actual mass fluxes of these species can only be determined by scaling the results using the true classified masses. Estimates of groundwater age in excess of 20,000 years, based on carbon-14, support long residence times and thus low groundwater velocities in the volcanic rocks in the Faultless area.

For two very short-lived nuclides with no sorption properties, ^{3}H and ^{85}Kr, the fracture flow formulation is more conservative, as rapid migration in the fractures occurred with little retardation, followed by rapid radioactive decay of the remaining mass. Using the unclassified estimate of initial tritium mass to scale the tritium breakthrough gives an estimated peak mean concentration of almost 1 pCi/L, and a mean plus one standard deviation of 10 pCi/L, occurring at 153 years after the Faultless test. This rapid transport is facilitated by densely welded tuffs stochastically simulated below the Faultless test based on sparse regional data; densely welded tuffs were not encountered at the UC-1 drillhole or instrument holes.

Sensitivity analyses focused on model parameters that are most likely to reduce the long travel times simulated by the model. The sensitivity cases studied included increasing the vertical correlation length of hydraulic conductivity, increasing the mean hydraulic conductivity of the alluvium, simulating prompt injection of tritium into the upper portions of the chimney, and increasing the local dispersion. None of these individual cases significantly altered the base-case transport results during the 1,000-year period of interest; however, combining the prompt injection scenario with the higher hydraulic conductivity in the alluvium created a scenario having significant ^{3}H breakthrough at the southern land withdrawal boundary.

The characteristics of very low hydraulic conductivity and downward-directed gradients at the source control the transport behavior of radionuclides from the Faultless test. For sorbing radionuclides, strong sorption characteristics of the aquifer matrix are also important. The major uncertainties identified by the numerical model are the magnitude and direction of hydraulic gradients and the existence of densely welded tuffs below the nuclear test horizon.

ACKNOWLEDGEMENTS

The authors gratefully acknowledge the many people and organizations whose contributions made possible the work reported here. We specifically note the following: the support and guidance of the Department of Energy, Nevada Operation Office, specifically Peter Sanders, Robert Bangerter, and Monica Sanchez; the insightful reviews and discussions of the Modeling Subcommittee of the Underground Test Area Technical Working Group, comprised of Andrew Tompson, Andrew Wolfsberg, David Prudic, and Sirous Djafari; David Smith, of Lawrence Livermore National Laboratory for his assistance in source term issues; Brad Lyles and Todd Mihevc, DRI, for invaluable field data collection; Craig Shirley, DRI, for assistance in interpreting the geophysical logs; Greg Pohll, David Benson, Todd Mihevc, and Marjory Jones, DRI, for providing internal reviews; and Debi Noack and Heather Nelson, DRI, for their outstanding electronic publishing support.

CONTENTS

5. Anion and Cation Sorption on Aquifer Materials from the Central Nevada Test Area
6. Mass Flux and Concentration Data

LIST OF FIGURES

LIST OF TABLES

LIST OF ACRONYMS

BET	Bruanuer, Emmett and Teller model
CADD	Corrective Action Decision Document
CAIP	Corrective Action Investigation Plan(s)
CFR	*Code of Federal Regulations*
CNTA	Central Nevada Test Area
DOE	U.S. Department of Energy
DOE/NV	U.S. Department of Energy, Nevada Operations Office
DRI	Desert Research Institute
EDX	energy dispersive x-rays
FFACO	*Federal Facility Agreement and Consent Order*
MPC	maximum permissible concentration
MSL	mean sea level
MWL	meteoric water line
NA	not analyzed
NTS	Nevada Test Site
PCG	preconditional conjugate-gradient
PDF	probability density function
ptrw	Particle Tracking Random Walk
SEM	scanning electron microscopy
SGS	sequential Gaussian simulation
SIS	sequential indicator simulation
SMOW	standard mean ocean water
XRD	X-ray diffraction

1.0 Introduction

Since 1962, all United States nuclear tests have been conducted underground. A consequence of this testing has been the deposition of large amounts of radioactive materials in the subsurface, sometimes in direct contact with groundwater. The majority of this testing occurred on the Nevada Test Site (NTS), but a limited number of experiments were conducted in other locations. One of these is the subject of this report, the Central Nevada Test Area (CNTA), located about 95 km northeast of Tonopah and 175 km southwest of Ely, Nevada (Figure 1.1). The only underground nuclear test conducted at CNTA was Faultless. The Faultless test consisted of a 200 to 1,000 kt yield nuclear detonation (U.S. DOE, 1994), which occurred on January 19, 1968. Faultless was designed to study the behavior of seismic waves generated by a nuclear test in Hot Creek Valley and evaluate the usefulness of the site for higher-yield tests.

Characterization of groundwater contamination at CNTA is being conducted by the U.S. Department of Energy (DOE) under the Federal Facility Agreement and Consent Order (FFACO) with the State of Nevada Division of Environmental Protection and the U.S. Department of Defense (DoD). This order prescribes a Corrective Action Strategy (FFACO, Appendix VI), which, as applied to underground nuclear tests, involves preparing a Corrective Action Investigation Plan (CAIP), Corrective Action Decision Document (CADD), Corrective Action Plan, and Closure Report.

The CAIP for CNTA is currently under negotiation between the DOE and the state of Nevada. The scope of the CAIP is flow and transport modeling to establish contaminant boundaries that are protective of human health and the environment. This report describes the current status of the flow and transport modeling for CNTA.

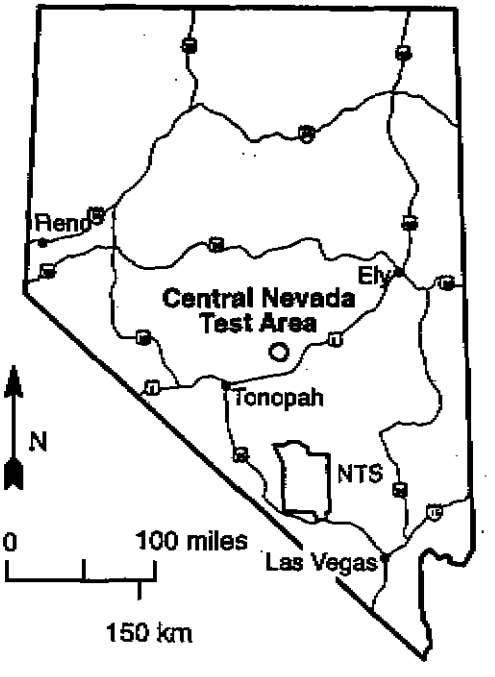

Figure 1.1. Location map of the Central Nevada Test Area in the state of Nevada.

1.1 Purpose

The purpose of this work is to characterize groundwater flow and contaminant transport at CNTA through numerical modeling, which utilizes site-specific hydrologic data. This requires a scope including development of a conceptual model of the groundwater flow environment at CNTA based on geologic, hydrologic, and chemical information, development of a numerical flow model, development of a conceptual model of contaminant release and transport properties from the nuclear test cavity, development of the numerical model of transport, and performance of associated sensitivity and uncertainty analyses. The focus of contaminant transport is on tritium, as specified in Section 5.2 of the FFACO, Appendix VI, though other parts of the radionuclide source term are also considered.

1.2 Previous Work

Investigations of the geology and hydrogeology of CNTA began in the late 1960s and continue to the present. Work began in the region as part of a search for a supplemental test site to support higher-yield underground nuclear tests that were not possible at the NTS due to ground motion issues in Las Vegas. As such, regional geologic and hydrogeologic work was carried out, extending beyond the limits of Hot Creek Valley itself. This work included geologic mapping, geophysical logging, water chemistry analyses, and hydraulic testing. After the Faultless test, studies were initiated to monitor the response of the hydrologic system to the test and monitor for the migration of contaminants. The most pertinent of these previous works are listed in Table 1.1.

Table 1.1. Investigations and Associated Scope for Faultless-Related Projects.

Investigation	Scope
Anderson *et al.*, 1967; Ekren *et al.*, 1968; Ekren *et al.*, 1973a; Ekren *et al.*, 1973b; Quinlivan and Rogers, 1974	Geologic maps
Barnes and Hoover, 1968; Corchary, 1967; Dixon and Snyder, 1967; Hoover, 1968a; Hoover, 1968b; Snyder, 1967	Site-specific lithology based on drillhole data
McKeown *et al.*, 1968	Geologic structure phenomena resulting from Faultless
Dinwiddie and West, 1970	Hydrologic phenomena resulting from Faultless
Rush and Everett, 1966	Regional groundwater hydrology
Dinwiddie and Schroder, 1971	Summary of hydraulic testing in many wells and data interpretation regarding flow directions and velocities
Dinwiddie 1968; 1969a; 1969b; 1970a; 1970b; 1970c; 1970d	Hydrologic testing in individual wells
Fiero *et al.*, 1974	Regional hydrochemical analysis
Fiero and Illian, 1969; Fiero *et al.*, no date	Regional groundwater flow descriptions
Thordarson, 1985 and 1987	Monitoring the hydrologic response to Faultless
Chapman *et al.*, 1994; Mihevc *et al.*, 1996	Water sampling and hydrologic logging
Pohlmann *et al.*, 1995	Exposure assessment performed to support the Environmental Impact Assessment

2.0 Hydrogeologic Setting

2.1 General Description of Study Area

The CNTA is in south-central Nevada in the Hot Creek Valley (Figure 2.1). The Faultless test was conducted in emplacement boring UC-1, located at north 1,414,340 ft and east 629,000 ft, Nevada State Coordinates, central zone. UC-1 penetrated alluvium and volcanic sediments to a depth of 998 m. The test was conducted within a 0.66-m-diameter casing string, at a depth of 975 m, on January 19, 1968.

Hot Creek Valley extends approximately 110 km between north-south-oriented ranges in the Basin and Range physiographic province, and varies from 8 to 30 km wide. To the west of Faultless, the Hot Creek Range rises to an elevation of 3,111 m at Morey Peak (Figure 2.2). The valley floor elevation varies from 1,580 to 1,830 m (National Geodetic Vertical Datum, 1929). The Faultless site itself is on the western alluvial fan at an elevation of approximately 1,859 m. Hot Creek Valley drains southeastward to Railroad Valley in the vicinity of Twin Springs Ranch, though there is little streamflow on the valley floor except during periods of large runoff from mountain streams.

The climate in Hot Creek Valley is semi-arid. Annual precipitation averages 19.4 cm/yr at the Blue Jay weather station, on U.S. Highway 6, south of Faultless. The average snowfall is 13 cm/yr. Large diurnal and seasonal temperature changes occur. January is the coldest month, with an average maximum temperature of 7.2°C and an average minimum temperature of -10.6°C. July is the warmest month, with an average maximum temperature of 34.4°C and an average minimum temperature of 10.2°C. The valley floor of Hot Creek Valley is dominated by sagebrush, while the higher elevations support pinyon pine and juniper.

2.2 Geology

Hot Creek Valley is a long graben containing a thick sequence of Quaternary- and Tertiary-age fill (up to 1,200 m) underlain by a thick section of Tertiary-age volcanic rocks. The bounding ranges on either side of the valley are comprised of Tertiary-age volcanics (principally tuffs and rhyolite lavas) that generally overlie Paleozoic-age carbonates. The contact between the valley and ranges is defined by north-south-trending high-angle faults. In addition to Great Basin fault block terrain, other large-scale structural features are calderas. The Faultless site occurs within the Morey Peak-Hot Creek Caldera complex, while the Pancake Range Calderas occur to the south (Ekren *et al.*, 1973b). The Paleozoic rocks exposed in the Hot Creek Range are from Cambrian to Permian in age and are complexly folded and faulted. The volcanic rocks are heavily faulted, containing normal, thrust, and strike-slip faults. Older alluvium in the area is late Tertiary to Quaternary in age and occurs on alluvial fans and pediments. It is formed by debris washed from the mountains and is poorly sorted and unconsolidated (Rush and Everett, 1966), including fragments of tuff, welded tuff, and rare Paleozoic rocks. The younger alluvium consists of playa and stream deposits at the bottom of the valley. Volcanism was active during the early deposition of the alluvium, seen by interbedding with undisturbed tuffs and tuffaceous sediments with the deep alluvium (Hoover, 1968a).

Figure 2.1. Location of the DOE UC–1, UC–3, and UC–4 land withdrawal areas of the Central Nevada Test Area. The area within the dashed box is shown in detail in Figure 5.1

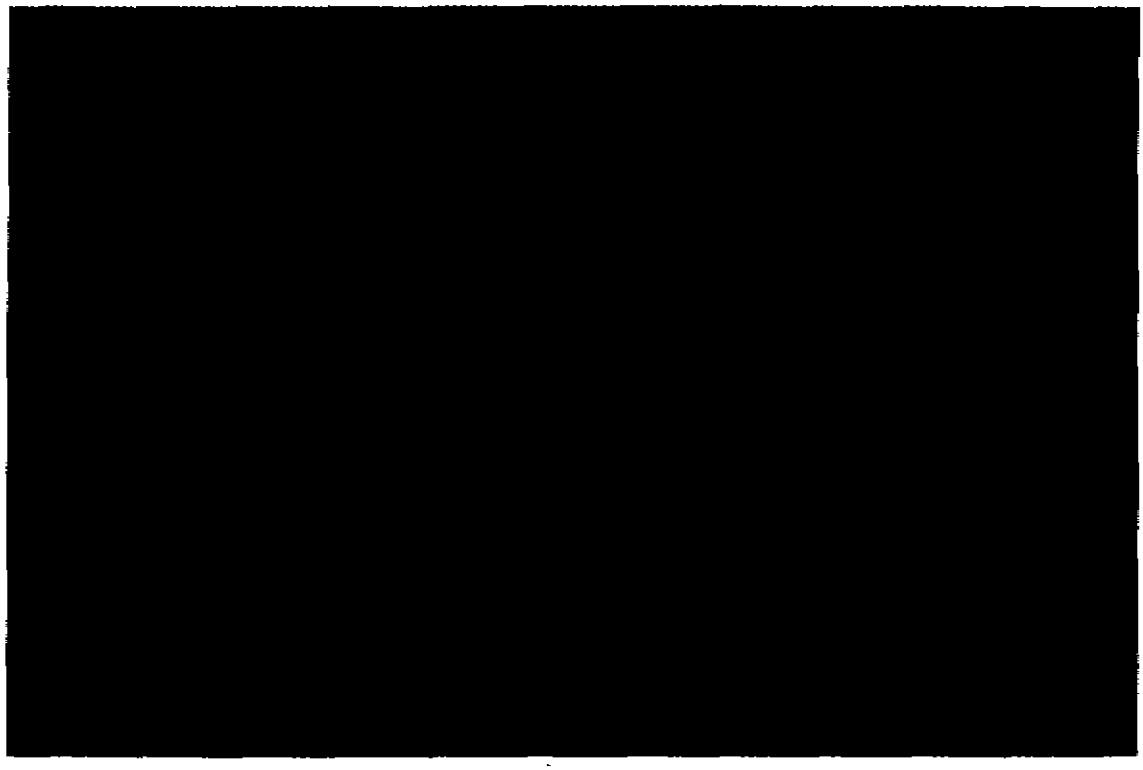

Figure 2.2. Photo of CNTA, looking west toward Morey Peak in the Hot Creek Range. The surface casing for the emplacement hole, UC-1, is in the foreground. Photograph taken April 2, 1998.

At the Faultless emplacement hole, UC-1, the valley-fill alluvium is 732 m thick, with tuffaceous sediments and zeolitized tuff below that to the 998 m total depth of the hole (Table 2.1), (Hoover, 1968a). No welded tuffs were noted in the volcanic section at UC-1 or in any of the UC-1 instrument holes or postshot holes. The only well that identified welded tuff in the vicinity of UC-1 was HTH-1, which showed a single 24-m-thick interval of densely welded tuff separating the overlying alluvium from underlying tuffaceous sediments. Boreholes in the UC-3 and UC-4 land withdrawal areas encountered varying thicknesses of densely welded tuff and rhyolite within the volcanic section.

The alluvium contains pebble- to boulder-size fragments of welded tuff and rare Paleozoic rocks, enclosed in a clay-cemented matrix of sand-sized crystal grains, particles of welded tuff, and some Paleozoic chert, siltstone, and carbonate fragments and is derived from nearby volcanic rocks and Paleozoic sediments. The upper 150 to 300 m are generally unconsolidated, with induration increasing with depth.

The Tertiary tuffaceous sediments include consolidated clastics, which, like the overlying alluvium, were derived from surrounding volcanic rocks and Paleozoic sediments (Hoover, 1968b). The tuffaceous sediments are similar in texture, fragment sizes (though lacking the larger fragments) and general appearance to the alluvium, but differ in several important ways (Hoover, 1968b). The tuffaceous sediments are more indurated, as a result of zeolitization of volcanic glass and larger amounts of clay matrix materials. The tuffaceous sediments also contain thin intervals of nonwelded

zeolitized tuff, densely welded tuff, reworked ash-fall tuff, and tuffaceous sandstones and siltstones. Finally, the tuffaceous sediments display evidence of only minor reworking, very short transportation, and possible active volcanism during deposition.

Table 2.1. Lithologic Log of the UC-1, UC-1-I-1, and UC-1-I-2 Boreholes at the Faultless Site and a Description of the Densely Welded Tuff at HTH-1 (from Hoover, 1968b).

Lithology (percentages are approximate)	Thickness (m)	Depth to base of unit (m)
Alluvium; contains subrounded to rounded pebbles to cobbles of welded tuff (10-15) percent and medium-to dark-gray Paleozoic calcareous siltstone, chert, and claystone (1-5 percent in upper 549 m and <1 percent below 549 m) in a matrix (50-90 percent) of sand-size grains of quartz, feldspar, rare biotite, and rock fragments, bound by clay. Welded tuff fragments are light- to dark-gray, brown and pale-pink in upper 88 m, mostly greenish-gray and gray with some buff to white between 401 and 549 m, and mostly buff to white with some greenish-gray and gray fragments between 549 and 733 m. White welded-tuff fragments with large biotite phenocrysts are abundant below 582 m. No samples between 88 and 401 m because of lost circulation. Contact cored at 733 m.	733	733
Tuffaceous sediments; consisting of very pale-orange to grayish-orange-pink to light-brownish-gray conglomerates and conglomeratic sandstones (90 percent) similar in texture, fragment size, and appearance to the alluvium but containing varying quantities of altered volcanic glass; white to light-yellowish-gray reworked ash-fall tuffs, tuffaceous sandstones and siltstones (<10 percent) relatively free of large fragments; and yellowish-gray zeolitized nonwelded ash-flow tuffs (<1 percent); conglomerate and conglomeratic sandstones contain pebbles to boulders (10-75 percent) of gray, reddish-brown and purplish-gray welded tuff and gray to black Paleozoic chert, siltstone, and calcareous siltstone (1-10 percent above 914 m and <1 percent below 914 m); beds with larger and more abundant fragments have more clay in matrix than conglomeratic sandstones that are partly zeolitized; zeolitization and euhedral biotite plates in matrix indicate nearby source of volcanic glass--probably ash-fall tuffs; matrix consists of sand-size quartz, feldspar, biotite, and rock fragments bound by clay derived by erosion, and clay (?) and zeolites derived by alteration of volcanic glass; core from 1,064 to 1,067 m is a conglomerate containing subangular to subrounded pebbles to cobbles of dark-greenish-gray welded tuff (25-70 percent) containing coarse quartz (5-10 percent), plagioclase (?) altered to bright green clay (15-25 percent), glassy sanidine (5-10 percent), mostly coarse black biotite (2-5 percent), and rare lapilli pumice or lithic fragments altered to green clay, in a matrix that also contains coarse biotite; reworked ash-fall tuffs, tuffaceous sandstones and siltstones consist mostly of volcanic glass altered to clay and zeolites; quartz, feldspar and biotite grains (5-20 percent) and sand- to pebble-size welded-tuff fragments (<5 percent); zeolitized nonwelded ash-flow tuffs cored at 947 m and 973 to 976 m contain fine to coarse quartz and feldspar (<5 percent), rare black tine biotite, and lapilli pumice (5 percent).	334	1,067
The following is a description of the densely welded tuff logged at HTH-1: Tuff, ash-flow, light-brownish-gray to light-gray, devitrified, densely welded; contains quartz, feldspar, biotite (1-2 percent) and rare hornblende.	24	752

Note: Terms denoting grain sizes in alluvium and tuffaceous sediments are as follows: silt and clay, <1/16 mm; sand, 1/16-4 mm; pebbles, 4-64 mm; cobbles, 64-256 mm; boulders >256 mm. In volcanic rocks, fragment and phenocryst sizes are as follows: fine, <1 mm; coarse, 1-4 mm; lapilli, 4-32 mm. Contacts are corrected to geophysical logs.

The Tertiary volcanics consist of tuffs, tuffaceous sediments, sandstones, basalts, and rhyolite lavas ranging in age from Oligocene to Pliocene (Ekren *et al.*, 1973b). The tuffs are generally fine-grained and tightly welded and contain numerous fractures and normal, thrust, and strike-slip faults.

2.3 Groundwater Flow

Groundwater flow in the carbonate rock province of the eastern Great Basin is conceptualized as having two components: a local component comprising flow from mountain ranges to adjacent valleys, and a regional component, where groundwater is transmitted through carbonate rocks beneath mountain ranges and valleys to discharge areas at distant springs or terminal sinks (Prudic *et al.*, 1993). Hot Creek Valley is located within the Railroad Valley region, defined by regional discharge at the terminal sink in Railroad Valley (Figure 2.3).

Groundwater in Hot Creek Valley occurs in alluvium, volcanic sediments, and volcanic rocks. No wells penetrate Paleozoic carbonates, though they are believed to underlie the valley at great depth. Previous workers have divided the groundwater flow system in the valley into two sections. The shallow flow component in the valley was represented by Dinwiddie and Schroder (1971) by hydraulic head measurements in the upper 300 m below ground surface. Depending on location within the valley, this upper system occurs in alluvium and the top part of the volcanic section. The general direction of flow for the shallow component of the system is toward the south and southeast, generally following that of the surface topography. Recharge is believed to occur principally in the higher mountain ranges to the west (Hot Creek Range and Kawich Range), with groundwater flowing down the valley axis toward an area of evapotranspiration near where State Route 375 crosses the southern end of the Pancake Range (Figure 2.4 and Appendix 1).

The deeper flow component in Hot Creek Valley was defined by Dinwiddie and Schroder (1971) using hydraulic head data collected between 1524 and 2134 m below land surface. All of these data are from the volcanic section. The direction of groundwater flow in this deeper component is markedly different from that in the shallow component; flow in the deep volcanic aquifers moves generally northeastward and eastward toward Railroad Valley. Comparison of the potentiometric surface maps for the deep and shallow systems reveals a line of intersection (Figure 2.5) (Dinwiddie and Schroder, 1971). North and east of the line, hydraulic head decreases with depth, defining an area of groundwater recharge where groundwater has the potential to move downward through the system. South and west of the line, heads increase with depth and indicate that groundwater has the potential to move upward. The potential for downward flow in the northern part of Hot Creek Valley and upward flow in the southern valley was also demonstrated by vertically distributed head measurements in individual wells tested as part of CNTA site characterization. Dinwiddie and Schroder (1971) conclude that if vertical groundwater movement occurs, it must be very slow relative to lateral flow, due to significant anisotropy in hydraulic properties.

Plots of the vertical distribution of hydraulic head prior to the Faultless test for the seven CNTA wells in Hot Creek Valley (Figure 2.6) show the inferred directions of the ambient vertical gradients between the flow systems outlined by Dinwiddie and Schroder (1971). To the north of Faultless, the

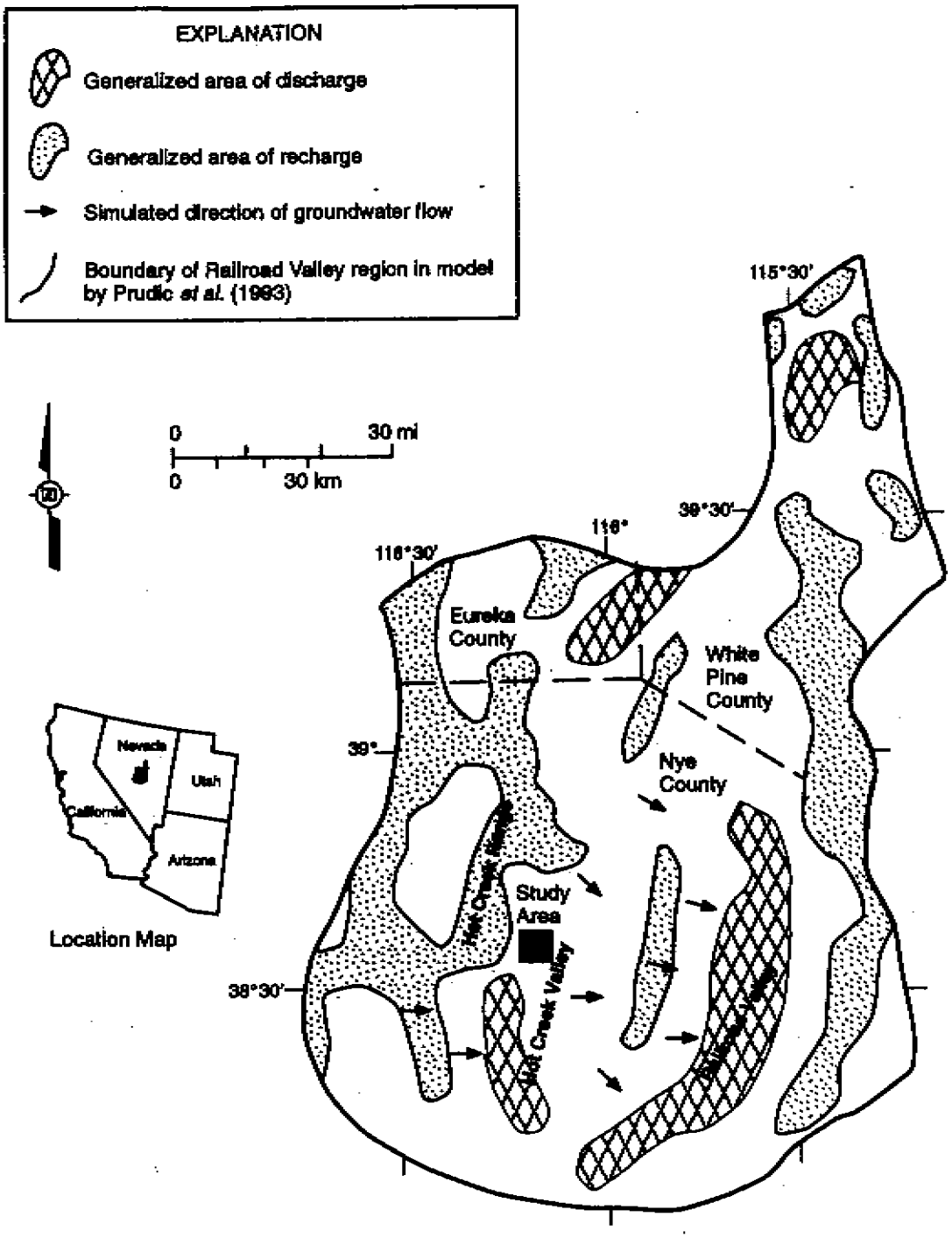

Figure 2.3. Simplified view of the Railroad Valley region, including Hot Creek Valley, from the regional groundwater flow model developed by Prudic *et al.* (1993), showing general areas of recharge and discharge. Only flow directions pertinent to Hot Creek Valley are shown and these encompass flow in the upper and lower model layers of Prudic *et al.* The dark box shows the approximate area of interest for the CNTA work.

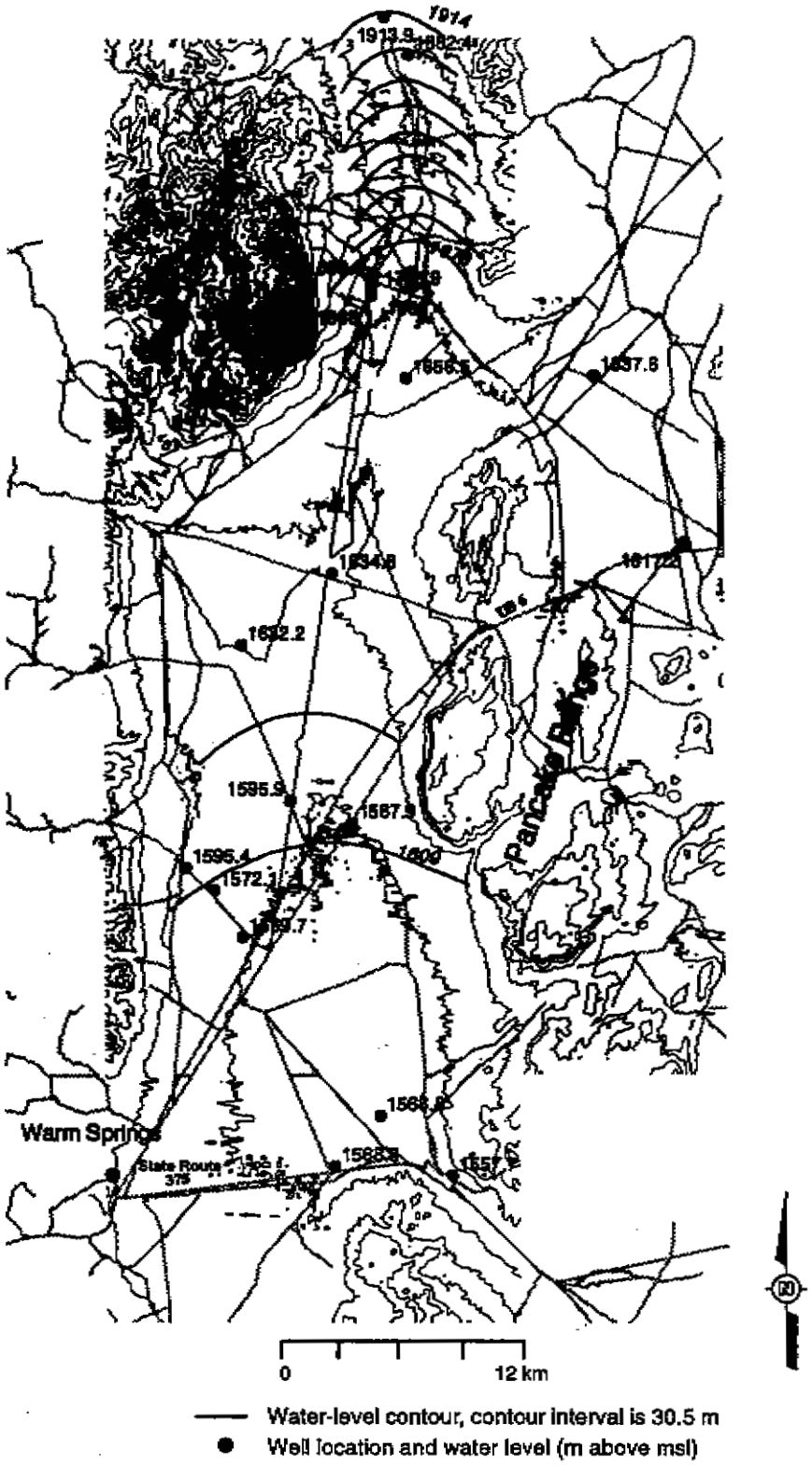

Figure 2.4. Water level contour map of Hot Creek Valley, based on head values measured in August 1997. The letter-report upon which this is based is in Appendix 1.

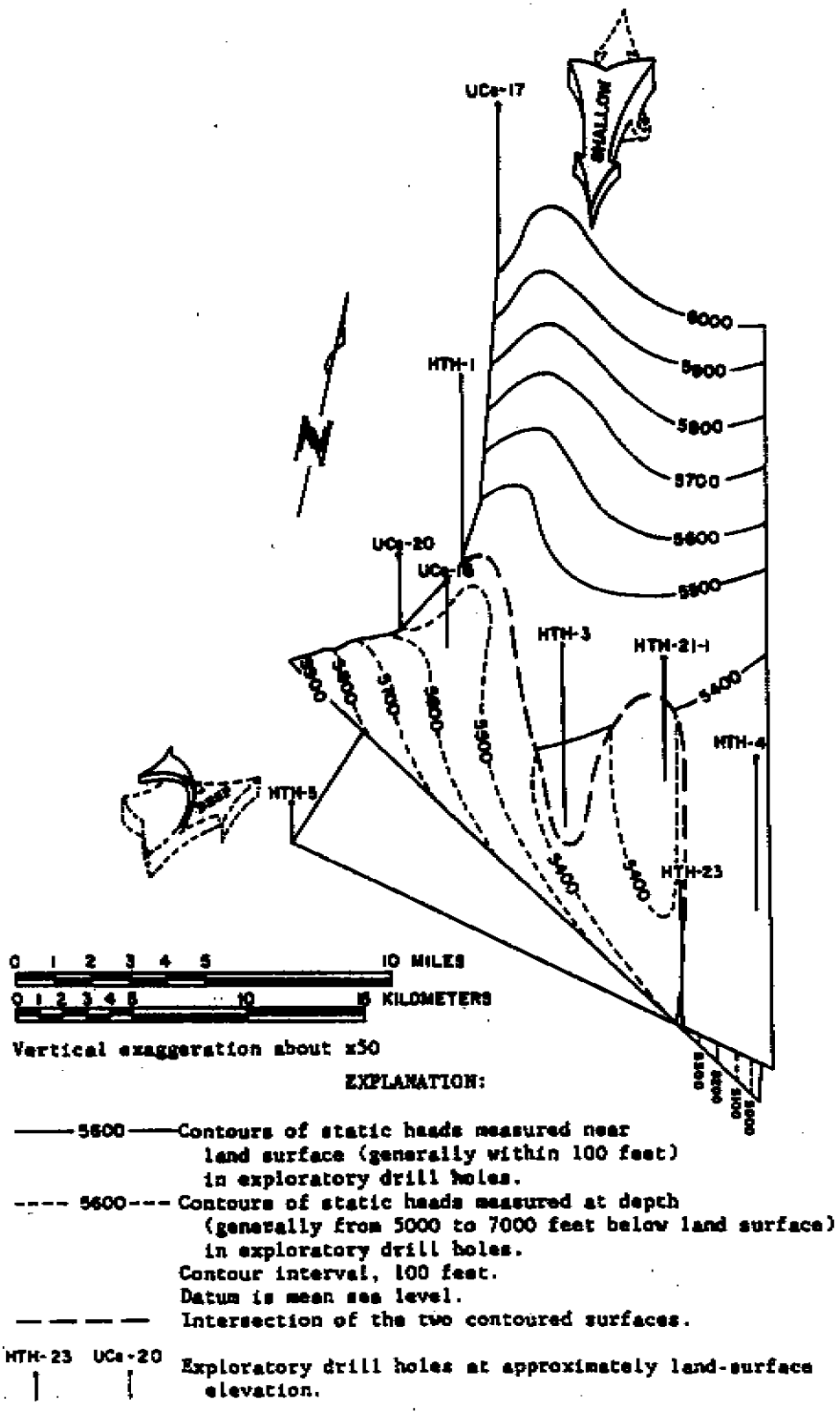

Figure 2.5. Diagrammatic view of generalized flow system in Hot Creek and Little Smoky valleys, central Nevada (Dinwiddie and Schroder, 1971). Feet may be converted to meters by multiplying by 0.3048.

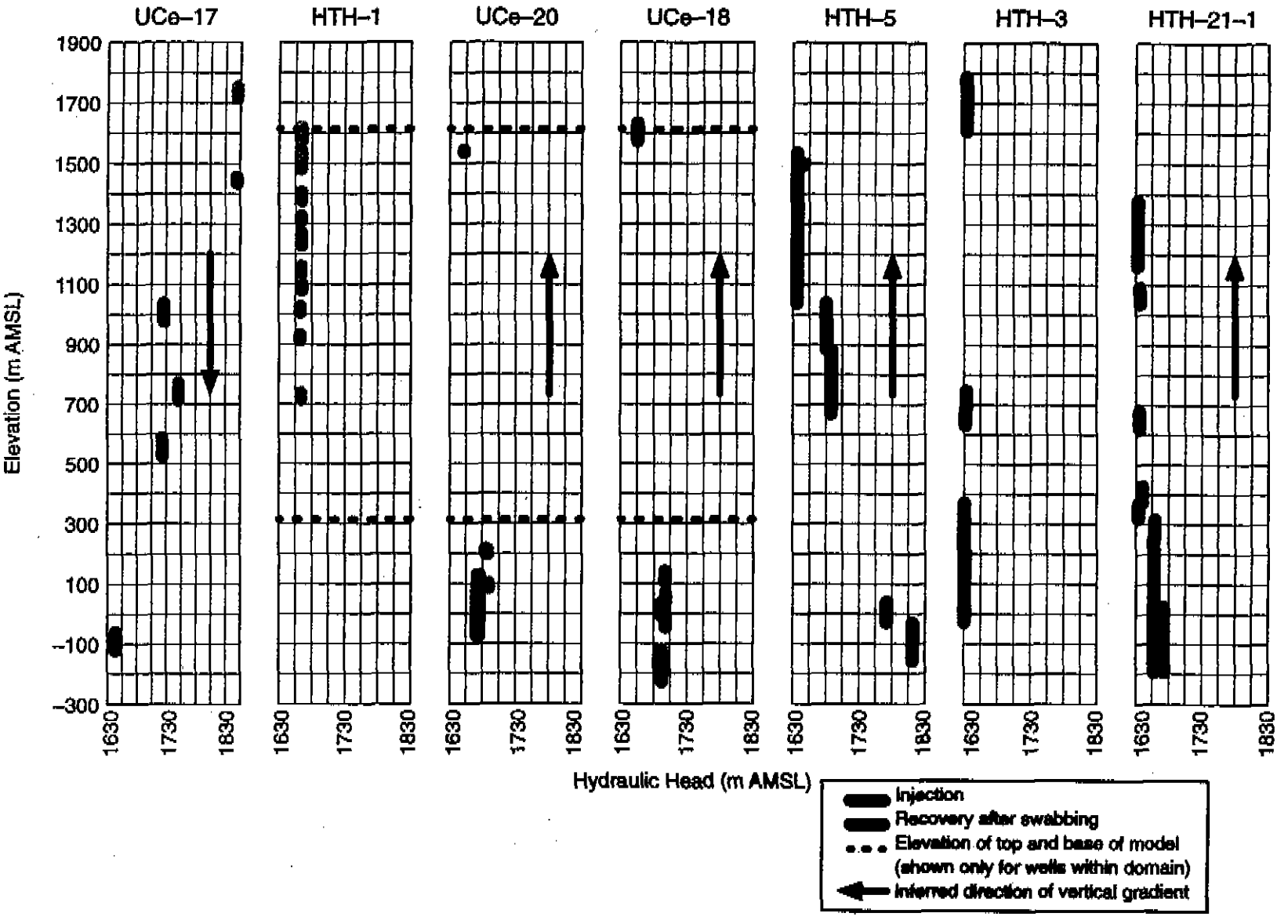

Figure 2.6. Plots of the vertical distribution of hydraulic head measured using straddle packers in CNTA exploratory wells in Hot Creek Valley. The length of the bars represents the length of the isolated interval.

gradient measured at UCe-17 had a magnitude of approximately 0.1 and heads declined with increasing depth. A tracer test conducted in the open borehole under non-pumping (static) conditions measured downward flow at rates as high as 150 m^3/d, confirming the head distribution and suggesting that the borehole intersected important conductive zones. The flow rates declined with increasing depth in the borehole, reaching zero at about 1445 m depth (38 m elevation). To the south of UC-1, the gradients measured at UCe-18 and UCe-20 had magnitudes of approximately 0.02 and heads increased with increasing depth. Static tracer tests conducted in these boreholes showed no measurable flow over most of their open intervals, although downward flow at a rate of 33 m^3/d was measured at the bottom of UCe-18. Dinwiddie and Schroder (1971) suggest that the lack of borehole flow in UCe-20 indicates very little hydrostatic head difference in the vertical section, insufficient hydraulic conductivity, or both. This statement is difficult to reconcile with the data, since heads are quite variable at the base of UCe-20, and several hydraulic conductivity values estimated from the packer tests are at the high end of the range of values. It can only be assumed that this statement refers only to the open interval at the base and not the entire borehole, which overall shows a large vertical gradient implied by the difference in head from the base of the borehole to the top.

In the Faultless area, ambient heads at HTH-1 suggest very low vertical gradients. The head measured in the densely welded tuffs in the interval of 1,082.2 to 1,100.6 m elevation of HTH-1 was slightly higher than heads measured above and below, suggesting potential flow from this unit upward and downward into the adjacent units. A static tracer test confirmed the head distribution, showing upward flow from this interval at a rate of more than 15 m^3/d and downward flow at a rate of more than 20 m^3/d (Dinwiddie and Schroder, 1971). More recent thermal flowmeter measurements in HTH-1 found lower flow rates, directed upward at less than 5 m^3/d (Mihevc *et al.*, 1996).

2.4 Hydrochemistry

Groundwater in the Faultless area can be divided into two distinct hydrochemical facies (Table 2.2 and Figure 2.7), supported by isotopic distinctions as well (Figure 2.8) (Chapman *et al.*, 1994). Groundwater sampled from the alluvium in well HTH-2 is of the calcium-bicarbonate facies, with a low salinity (total dissolved solids concentrations near 290 mg/L). The stable isotopic composition varies around values of $\delta^{18}O$ of -14‰ and δD of -107‰. The groundwater collected from HTH-2 has no detectable tritium, but is relatively young with an uncorrected ^{14}C age of approximately 2,000 years before present (Davisson *et al.*, 1994).

Groundwater originating in volcanic aquifers sampled at well HTH-1 is of the sodium-bicarbonate facies (Chapman *et al.*, 1994), typical of groundwater in contact with volcanic rocks. Though HTH-1 is screened across both alluvium and volcanic units, flow logs have demonstrated that all water in the well originates in the lower volcanics, moving upward to discharge from the uppermost screen; thus all samples (which were collected with discrete bailers under static conditions) represent water from volcanic aquifers. The salinity is higher than that of groundwater in the alluvium, with total dissolved solids contents between 480 and 530 mg/L. The stable isotopic

Table 2.2. Chemical and Isotopic Analyses of Groundwater Samples from the Faultless Site. All units are mg/L unless noted otherwise. From Chapman *et al.* (1994) and Mihevc and Lyles (1998).

Well	Depth (m)	Date	T (°C)	pH* (S.U.)	EC* (µS/cm)	SiO_2	Ca	Mg	Na	K	Cl	SO_4	HCO_3*	CO_3	NO_3	F	^{13}C† (‰)	^{14}C† (pmc)	^{14}C age† (yr)	$\delta^{18}O$ (‰)	δD (‰)	^{3}H (pCi/L)
HTH-1	183	14-Nov-93																				<10
HTH-1	236	28-Jul-92	23	8.23/8.40	536/545	55.4	3.28	0.10	126	1.52	16.7	33.5	189/238	4.1	<.04	9.4	-2.4	1.7	32,730	-15.4	-117	214±7
HTH-1	236	14-Nov-93																				<10
HTH-1	236	27-Oct-97																				<10
HTH-1	274	14-Nov-93																				<10
HTH-1	320	28-Jul-92	26	8.35/8.31	519/539	56.0	3.10	0.07	125	1.39	16.8	33.4	217/243	0.6	<.04	10.4				-15.4	-117	33±1
HTH-1	320	14-Nov-93																				<10
HTH-1	442	28-Jul-92	26	8.38/8.30	542/542	56.5	3.53	0.07	125	1.37	16.8	33.5	211/244	0.4	<.04	10.4				-15.4	-117	
HTH-1	501	14-Nov-93																				<10
HTH-1	515	28-Jul-92	26	8.27/8.43	516/546	57.5	4.51	0.09	125	1.37	16.8	33.4	220/238	4.7	<.04	10.5				-15.4	-117	
HTH-1	578	28-Jul-92	25	8.34/8.32	524/540	56.8	3.22	0.07	127	1.37	16.8	33.1	211/242	0.9	<.04	10.5				-15.4	-118	
HTH-1	686	28-Jul-92	24	8.44/8.40	516/543	57.1	3.06	0.05	125	1.42	17.0	33.5	226/237	3.6	<.04	10.5				-15.5	-118	
HTH-1	741	29-Jul-92	24.5	8.25/8.27	509/548	64.3	2.95	0.06	128	1.55	18.2	33.4	199/247		<.04	9.4				-15.4	-118	<10
HTH-1	741	27-Oct-97	20.1	8.32/8.40	546/547		2.77	<0.1	124	1.41	17.2	34.6	/240	3	<.04							<5
HTH-1	815	29-Jul-92	26.5	8.15/8.24	508/561	66.2	2.93	0.07	129	1.55	19.1	34.5	205/249		<.04	10.4	-2.4	1.4	35,110	-15.5	-118	
HTH-1	853	20-May-93		8.17	588	68.4	3.0	0.1	134	2.16	21.4	38.9	261		<.04							
HTH-1	853	27-Oct-97	18.4	8.36/8.29	603/593	69.9	2.9	<0.1	136	1.54	20.5	36.2	260	1.1	<.01							<5
HTH-2	174	22-May-93		8.01	287	28.3	36.9	5.24	19.1	1.44	4.1	0.66	177		3.19					-14.1	-107	<10
HTH-2	174	27-Oct-97	16.9	8.24/8.20	255/286	28.8	36.0	5.17	17.9	1.50	4.5	5.93	174		3.63							<5
HTH-2	198	6-Aug-92		8.27	304	28.9	40.7	5.48	19.0	1.47	2.7	4.11	194		2.13					-14.3	-108	<10
HTH-2	229	29-Jul-92	19.5	7.84/8.10	303/300	29.2	40.8	5.52	19.0	1.47	2.6	4.08	177/196		2.22	0.08	-7.3	75.5	2,320	-14.2	-107	
HTH-2	229	22-May-93																		-14.3	-106	
HTH-2	274	22-May-93																		-13.9	-105	
HTH-2	297	29-Jul-92	20.5	7.94/8.13	299/293	29.5	40.8	5.49	18.4	1.44	2.6	4.08	161/197		2.22	0.06				-14.2	-107	
HTH-2	297	27-Oct-97	18.6	8.10	272																	<5

*First number is a measurement in the field at the time of sample collection. Second number is a laboratory measurement. If there is only one number, it is a laboratory measurement.
†Carbon isotopic data from Lawrence Livermore National Laboratory (Davisson et al., 1994)

Table 2.2. Chemical and Isotopic Analyses of Groundwater Samples from the Faultless Site. All units are mg/L unless noted otherwise. From Chapman *et al.* (1994) and Mihevc and Lyles (1998) (Continued).

Well	Depth (m)	Date	T (°C)	pH* (S.U.)	EC* (µS/cm)	SiO_2	Ca	Mg	Na	K	Cl	SO_4	HCO_3*	CO_3	NO_3	F	^{13}C† (‰)	^{14}C† (pmc)	^{14}C age† (yr)	$\delta^{18}O$ (‰)	δD (‰)	^{3}H (pCi/L)
UC-1-P-1S	91	23-May-93		8.27	217	25.5	23.5	1.78	23.1	1.38	2.6	0.62	134		1.33					-14.1	-104	<10
UC-1-P-1S	150	27-Oct-97	19.8	7.96/8.33	196/213	22.3	22.5	1.59	22.2	1.40	2.8	5.24	128		1.33							<5
UC-1-P-1S	229	23-May-93		8.16	217	24.5	23.1	1.70	23.0	1.36	2.9	0.64	134		1.37					-14.1	-105	<10
UC-1-P-1S	229	27-Oct-97	20.2	7.87/8.24	205/217	24.9	24.4	1.65	22.0	1.43	2.4	5.01	134		1.02							<5
UC-1-P-2SR	208	26-Oct-95																				4870±242
UC-1-P-2SR	238	July-92															-6.5	30.4	9,340			6760±234
UC-1-P-2SR	238	24-May-93		9.86	277	6.0	1.40	0.22	59.9	1.32	7.6	16.6	58.0	38.9	<.04					-15.1	-114	8680±407
UC-1-P-2SR	238	15-Nov-93																				6760±234
UC-1-P-2SR	320	26-Oct-95																				4520±241
UC-1-P-2SR	471	29-Jul-92																		-15.1	-115	
UC-1-P-2SR	485	29-Jul-92															-8.6	32.3	9,340	-15.1	-115	
UC-1-P-2SR	485	24-May-93		9.86	282	15.4	1.80	0.22	61.6	1.15	5.0	21.1	53.6	41.1	<.04					-15.1	-114	5210±329
UC-1-P-2SR	485	15-Nov-93																				4510±285
UC-1-P-2SR	485	26-Oct-95																				4510±225
UC-1-P-2SR	485	23-Oct-97	19.2	9.74/9.72	253/281	17.6	1.69	<0.1	59.8	1.06	4.5	22.1	63.4	35.1	0.09							4020±1180
UC-1-P-2SR	561	26-Oct-95																				4340±244
UC-1-P-2SR	575	23-Oct-97	17.3	9.93/9.70	244/281	17.5	1.57	<0.1	60.7	1.09	4.5	22.1	63.2	34.9	0.04					-15.1	-116	4020±1190
UC-1-P-2SR	668	29-Jul-92																		-15.1	-116	
UC-1-P-2SR	668	24-May-93		9.10	343	30.6	2.69	<.1	78.1	0.80	6.1	30.7	124	19.8	<.04					-15.4	-115	220,000±1840
UC-1-P-2SR	668	15-Nov-93																				6600±245
UC-1-P-2SR	668	26-Oct-95																				143,000±1100
UC-1-P-2SR	786	24-May-93																		-13.1	-117/-116	

*First number is a measurement in the field at the time of sample collection. Second number is a laboratory measurement. If there is only one number, it is a laboratory measurement.
†Carbon isotopic data from Lawrence Livermore National Laboratory (Davisson et al., 1994)

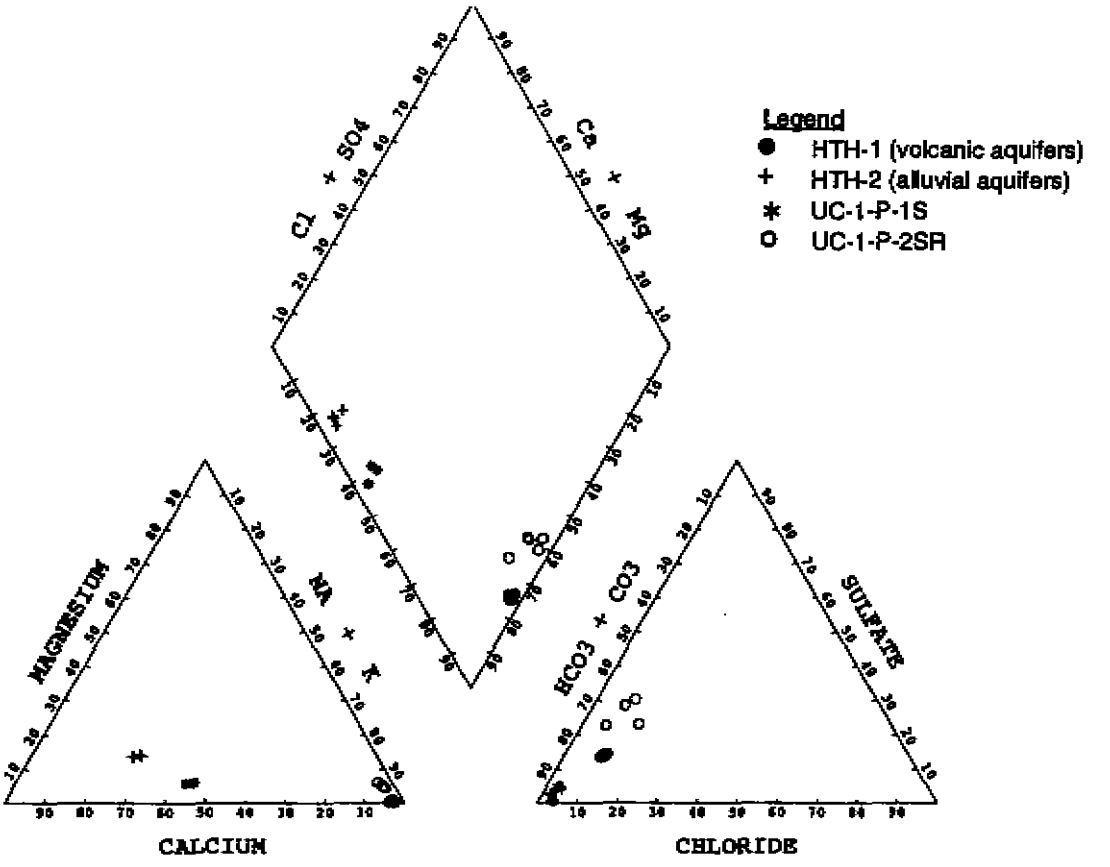

Figure 2.7. Trilinear diagram of water analyses from the Faultless site. The Na-HCO_3 water found in HTH-1 and UC-1-P-2SR is typical for groundwater in contact with volcanic rocks. It is distinct from the higher calcium water found in HTH-2 and UC-1-P-1S, which may reflect carbonate material in the alluvium.

composition is significantly more depleted in the heavy isotopes, with $\delta^{18}O$ values near -15.5‰ and δD values near -118‰. This depletion in heavy isotopes, as compared to area runoff (Figure 2.8), suggests recharge during cooler pluvial climate conditions. Uncorrected ^{14}C ages for water sampled from HTH-1 are on the order of 30,000 to 50,000 years before present (Davisson *et al.*, 1994).

The chemical and isotopic distinctions between groundwater found in the alluvium and groundwater originating in the volcanic units in the Faultless area suggest the presence of distinct flow systems that experience little interaction (*i.e.*, limited vertical flow between groundwater in the alluvium and the volcanic units). The chemical data indicate that groundwater in the alluvium is less evolved than that in the underlying volcanics, consistent with young ^{14}C-derived ages. The stable isotopic composition of the alluvial water is similar to that of a grab sample of runoff from Morey Peak (Figure 2.8), consistent with recharge under current climate conditions. The nearest isotopic precipitation records are from the NTS. These data are enriched in the heavy isotopes, as compared to the alluvial groundwater in Hot Creek Valley, indicating that recharge in Hot Creek occurs primarily under cooler temperatures and at higher elevations than present at the NTS. The NTS area also receives more summer precipitation from the south ("monsoonal" storms) than probably reach

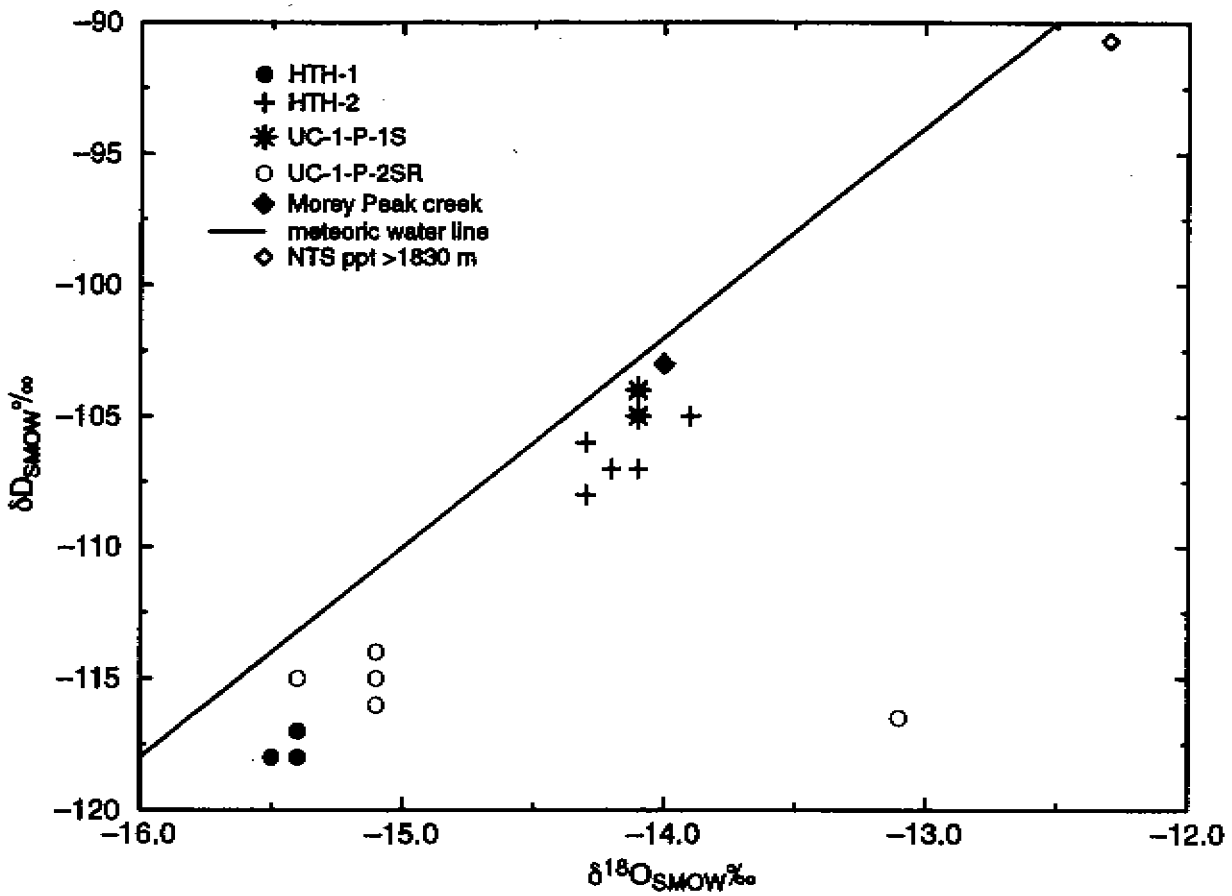

Figure 2.8. Stable isotopic composition of groundwater in the Faultless area, reported relative to Standard Mean Ocean Water (SMOW) and compared to the global meteoric water line, a grab sample of runoff from a creek on Morey Peak (the nearby recharge area) and the mean value of five years of precipitation data collected at eight locations on the NTS, ranging in elevation from 1830 to 2230 m. The NTS data are from Ingraham *et al.* (1991). The alignment of the data along the meteoric water line indicates little evaporation has occurred; the one outlier (at $\delta^{18}O$=-13‰) is a deep sample from the Faultless postshot well and reflects isotopic enrichment caused by the test (possibly by vaporization of carbonates).

Hot Creek Valley. The shallow groundwater could chemically evolve into that found in the volcanic units, with cation exchange of sodium for calcium and additional mineral dissolution. The isotopic distinctions, however, suggest that very little alluvial-signature groundwater migrates into the volcanic units and/or that such migration takes a very long time. Conversely, the groundwater found in the alluvial units near Faultless cannot be derived from the groundwater found in the volcanics without significant mixing with a more dilute source.

2.4.1 Description of Straddle-Packer Tests and Pumping Test Data

Extensive hydraulic testing was conducted in nine of the exploratory boreholes during the CNTA investigations in the 1960s (Dinwiddie and Schroder, 1971). The tests were conducted in open-hole intervals or through perforated casing using inflatable straddle packers and were designed

to characterize vertical variations in hydraulic head, transmissivity, hydraulic gradient, relative specific capacity, storage coefficient, groundwater velocity, and hydrochemistry. The packer test data form the basis for characterization of the spatial distribution of K in the present CNTA groundwater flow model and are summarized in Appendix 2. The packer intervals ranged from 6 to 204 m in length, with an average length of 53 m. Dinwiddie and Schroder (1971) used the type-curve method of Cooper *et al.* (1967) to calculate transmissivity values from the time-drawdown and time-recovery data from the packer tests. Their analysis produced 58 values of hydraulic conductivity (K) using the transmissivity values and the thicknesses of the tested intervals. The distribution of $\log_{10}$-transformed K data is notable both for its wide range of variability and for its overall relatively low values (Figure 2.9). Most of the CNTA K values are between 1×10^{-4} and 1.0 m/d, a range that falls at the lower end of the range of K values reported for both unconsolidated deposits and fractured rocks by Freeze and Cherry (1979), and both alluvium and volcanic rocks at the NTS by Rehfeldt *et al.* (1996). The low K of the alluvium is likely related to the poor sorting and clay-cemented matrix noted on the lithologic logs (Hoover, 1968b). Increased induration, zeolitization of volcanic glass, and a larger proportion of clay matrix (Hoover, 1968b) contribute to further reduction of K in the tuffaceous sediments.

A pumping test utilizing wells HTH-1 and HTH-2 was also conducted at the Faultless site prior to the nuclear test. This test involved isolation of the two highest perforated zones in HTH-1 from the rest of the borehole, and pumping HTH-1 while measuring drawdown and recovery in HTH-1 and HTH-2. The pumped zones in HTH-1 and the open-hole interval in HTH-2 were both open only to the alluvium. HTH-1 was pumped for 10,008 minutes (6.95 days) at an average rate of 665 m^3/d.

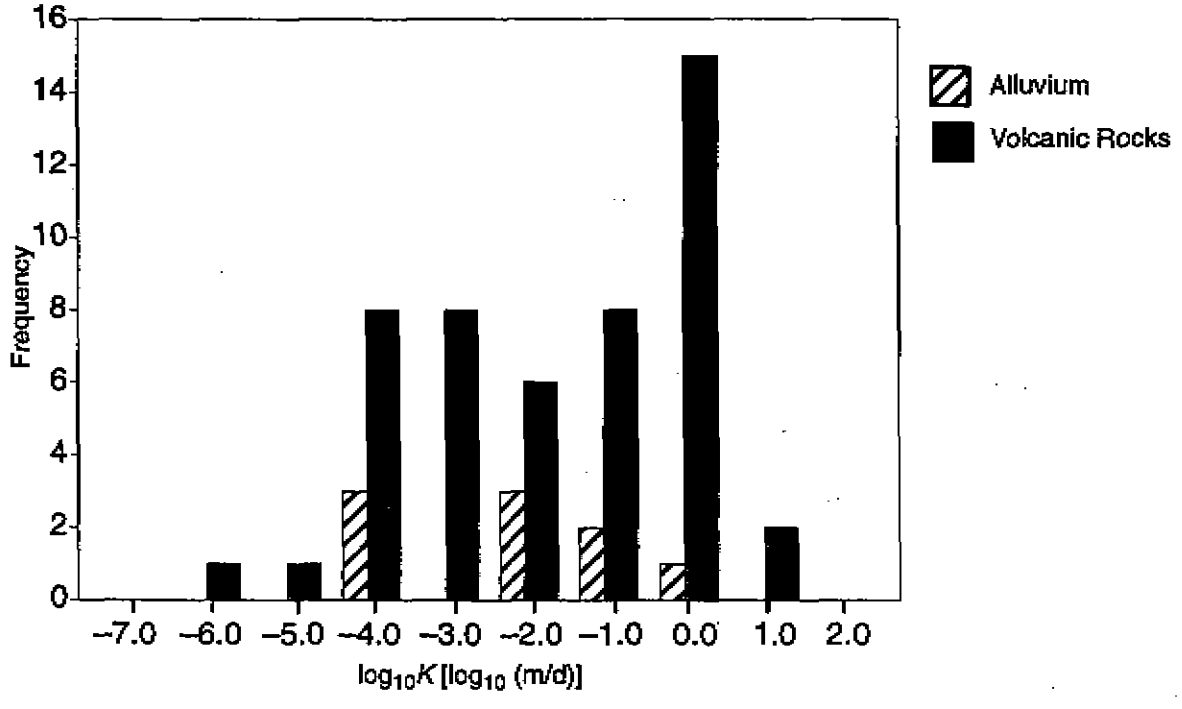

Figure 2.9. Histogram of hydraulic conductivity values estimated from straddle-packer tests in CNTA exploratory wells.

Dinwiddie and Schroder (1971) estimated the hydraulic conductivity to range between 0.56 and 0.96 m/d, depending on whether the aquifer thickness was assumed to include the entire thickness from the water table to the base of the perforated zone (182 m) or the combined thickness of the most permeable beds (107 m), respectively. Dinwiddie and Schroder (1971) noted that these values were higher than the mean of the values obtained from the packer tests in the same intervals, attributing the difference to the different scales of the tests and the possible presence of drilling mud during the packer tests. The difference in K estimated from the pumping test and straddle packer tests is in fact small when compared to the overall range of variability of K in the alluvium (Figure 2.10). This figure also shows that the pumping test and the packer tests in the uppermost intervals resulted in the highest estimates of K in the alluvium. Below this depth the tests indicate a trend of declining K with increasing depth, possibly related to increasing induration of the alluvial sediments noted in the lithologic descriptions of the UC-1 emplacement and instrument holes (Hoover, 1968b).

After the Faultless test, three injection tests were conducted in postshot hole UC-1-P-2SR, constructed in the chimney and cavity region. The borehole was open to the formation below an elevation of 1,504.08 m, presumably to alluvium and tuffaceous sediments (based on the lithology

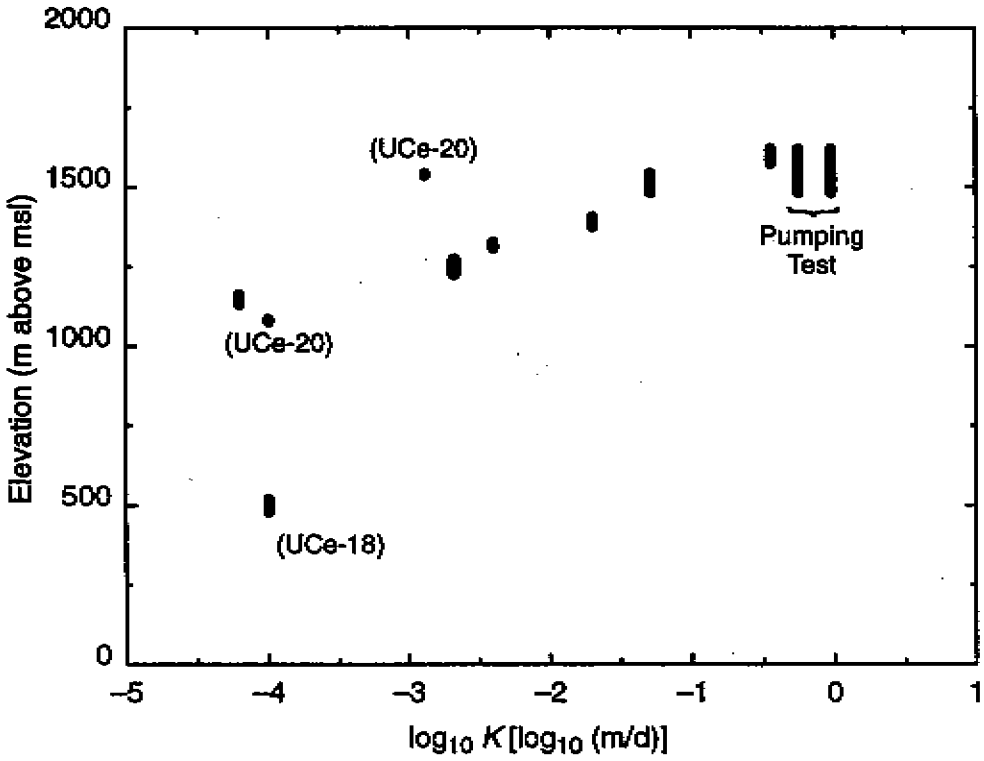

Figure 2.10. Plot showing the trend of declining K with decreasing elevation in the alluvium. All values are from straddle-packer tests in HTH-1 except those noted otherwise. The vertical lengths of the bars correspond to the vertical intervals tested. Note that the values estimated from the pumping test are at the upper end of the range of K and elevation.

observed at UC-1), to an obstruction at 1,052.4 m elevation. Thordarson (1987) estimated hydraulic conductivity from the third injection test, reporting a value of 7.9×10^{-4} m/d. This value falls within the range of values Dinwiddie and Schroder (1971) estimated from packer tests in the alluvium at the corresponding elevation in HTH-1, but is approximately two orders of magnitude lower than the value reported for tuffaceous sediments at HTH-1.

2.5 Description of Nuclear Test and Hydrologic Impacts

The Faultless test was detonated at a depth of 975 m within the tuffaceous sediment section (Figure 2.11). Details of the test remain classified, including the specific yield of the test and the size of the resultant cavity. The announced yield range for Faultless is 200 to 1,000 kt (U.S. DOE, 1994). Using the rough, generic relationships between yield and cavity size, and yield and depth of burial, and cancelling out yield (Glasstone and Dolan, 1977), leads to an estimated cavity radius of 100 m for the depth of the Faultless test. These relationships are based on testing history at the NTS and depths of burial required to assure containment of radionuclides below land surface. Though Faultless was fully contained, its collapse was atypical of NTS experience. This leads to additional uncertainty in the cavity radius estimate, which can be relieved by using classified data if required. The cavity size is used to define the source geometry in the model and also to generate an unclassified tritium estimate for discussion purposes. As such, it is not a sensitive element of the modeling.

2.5.1 Collapse Block

The Faultless test created a collapse feature much different from the concentric crater usually formed by underground explosions. Instead, a large quasi-sink area formed, bounded by structurally controlled fractures and faults (McKeown *et al.*, 1968). The sink is considered to be a graben, bounded on the northwest, southeast, and south by fractures (Figure 2.12). The northeast margin appears to be a hinge line, with the greatest displacement along the fracture at the south margin. Most fractures occurred along existing lineaments (McKeown and Dickey, 1969). Vertical displacements are as much as 4.5 m, and horizontal displacements are as much as a meter. The volume of the sink cannot be related to that of the underlying cavity because high-speed photography revealed large vertical displacements along the fractures too soon after the explosion to be caused as a result of cavity collapse (McKeown *et al.*, 1968). Rather, a significant fraction of the total sink volume is the result of faulting, believed to be the surface evidence of a small earthquake induced by the explosion. Indeed, the expected subsidence volume for the Faultless test was somewhat larger than the volume calculated by excluding the volumetric effects of the faults (McKeown *et al.*, 1968), so that the chimney conditions remain uncertain (*i.e.*, it is likely that the Faultless chimney does not extend to land surface, despite the large subsidence block). Chimneys are typically four to six times the cavity radius (Glasstone and Dolan, 1977). The Faultless test may have induced increased earthquake activity that extended through an area up to 40 km from the site of the test (Boucher *et al.*, 1969).

2.5.2 Near-Field Hydrology

Significant hydrologic effects accompanied the geologic impacts of the Faultless test, and these have been monitored through the years (Dinwiddie and West, 1970; Dinwiddie, 1972; Thordarson,

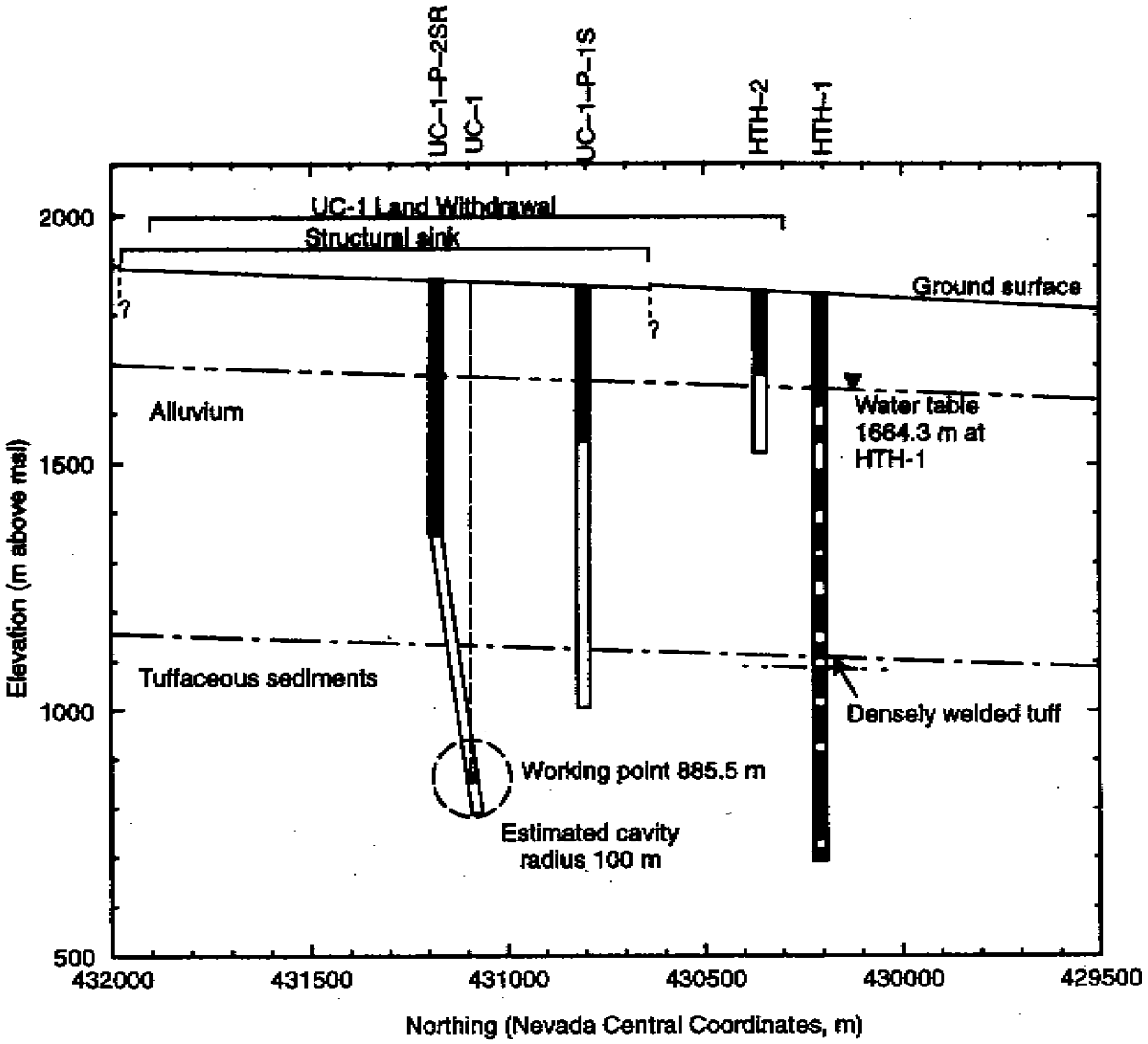

Figure 2.11. Illustration of the hydrogeologic section at Faultless. The cross section is oriented N-S and passes through UC-1, showing the position of the cavity within the tuffaceous sediments. Also shown are exploratory holes and post-test holes used in this study for characterizing the near-field hydrogeology. The deviation of UC-1-P-1S toward the cavity is not shown because deviation survey data are unavailable. The boreholes are projected to the cross section from their actual locations (refer to Figure 2.12). The dark-shaded intervals shown on these holes were cased and the unshaded intervals were perforated casing or uncased at the time of construction. UC-1-P-1S is actually deviated strongly toward the cavity but deviation data are unavailable.

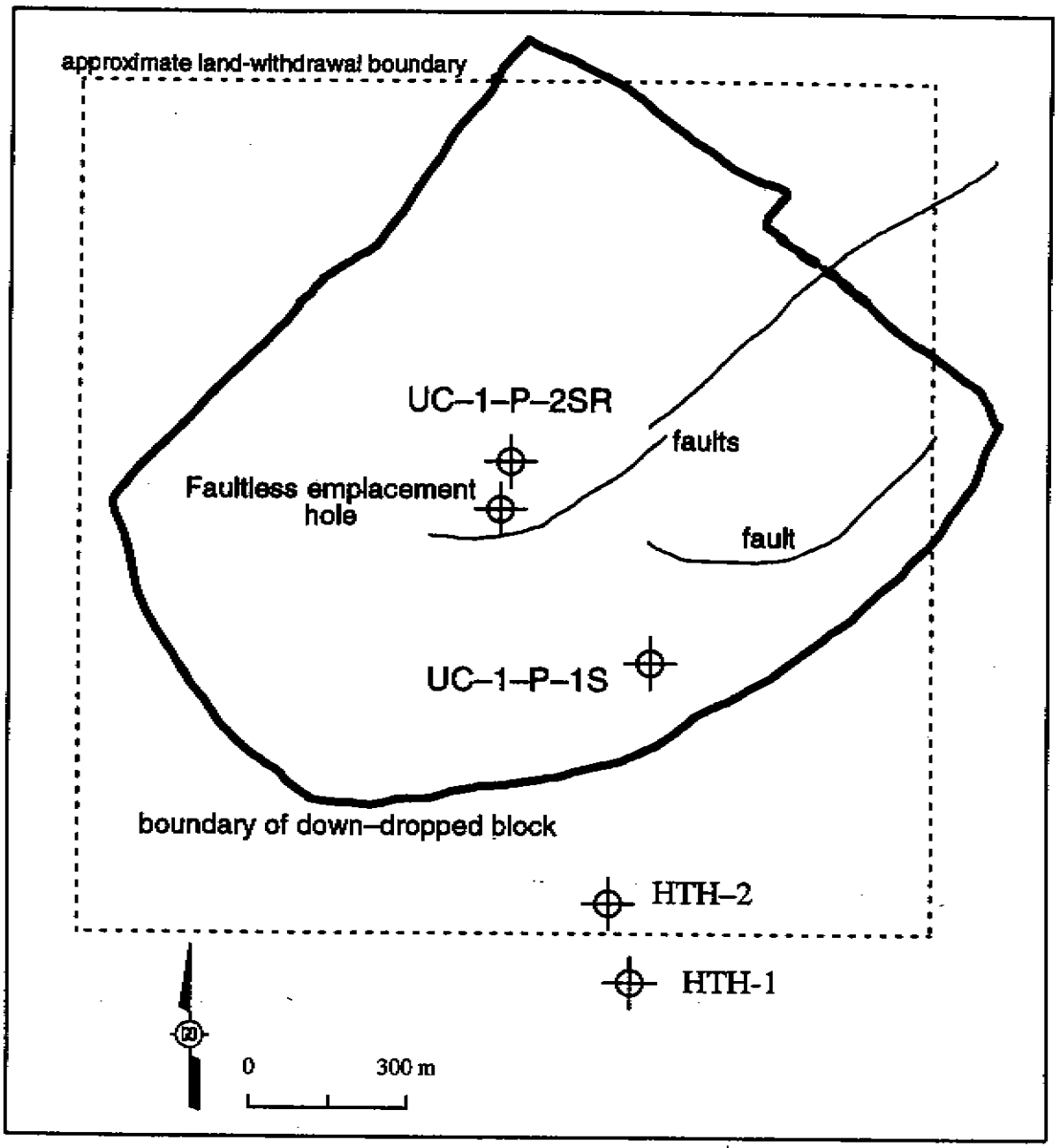

Figure 2.12. The large structurally controlled sink created by the Faultless test is shown by the heavy dark line. The northeast margin is considered a hinge line, with the greatest displacements along the fracture at the south margin. Several interior faults are shown, and many others are evident on the original map by McKeown *et al.* (1968).

1985; Thordarson, 1987; Chapman *et al.*, 1994; Mihevc *et al.*, 1996). Water levels in both HTH-1 and HTH-2 responded immediately to the explosion with a short-term head increase of 65 m at HTH-1 and more than 400 m at HTH-2 (Dinwiddie and West, 1970). The water level measurement was still 39 m above the pre-test level at HTH-2 one day after the explosion (Figure 2.13), while the maximum head at HTH-1 did not occur until three days after the test. The pressure at UCe-18 rose more than 30 m, but an instrument failure prevented measuring the maximum. The water levels in HTH-1 and HTH-2 have not returned to pre-test conditions, remaining elevated 6 m in HTH-1 and 3.7 m in HTH-2 (Figure 2.13). Two hypotheses have been suggested to account for this long-term change in water levels (Mihevc *et al.*, 1996): the "pre-test" water level reported for HTH-1 may be representative of head in the alluvial aquifer, whereas the current level is representative of natural, higher head, conditions in the volcanic aquifers and has created a mound in the water table that is affecting HTH-2 as well; or a long-term change has occurred in hydraulic conditions (*e.g.*, hydraulic conductivity), caused by the nuclear test.

The two postshot holes reflect near-field conditions of the nuclear test. A typical water-level response entails a large, short-lived, hydraulic mound (the dashed line noted as "shortly after detonation" on Figure 2.14), followed by a large depression in the water table centered on the cavity. At this time, there is a ring of high heads surrounding the low encompassing the cavity, with this ring also higher than head in the outlying area (the hachured line indicated as "post-collapse" on Figure 2.14). The ring eventually subsides, with a general depressed water level around the test, recovering as adjacent groundwater flows toward the low (noted as "post-shot approaching pre-shot conditions" on Figure 2.14).

Of the two postshot wells, well UC-1-P-1S was drilled first and is strongly deviated from vertical toward the Faultless cavity. Hole conditions caused it to be abandoned, and though there remains access in the well to a measured depth (not corrected for deviation) of approximately 260 m, the degree of communication with the underlying hole that originally extended to 833 m is unknown. Artesian conditions were encountered during drilling UC-1-P-1S, soon after the Faultless test, and after a rapid decline from the artesian conditions, the water level has remained reasonably constant, though very elevated, in the well (at a hydraulic head of approximately 1,772 m) (Figure 2.13). The sustained, elevated water level may represent the hydraulic mound created by the test that has been preserved between hydraulic barriers created by surrounding faults.

The second postshot hole, UC-1-P-2SR, was drilled to a depth of 822.9 m, then three sidetrack holes were drilled from that point. The sidetrack that was cased, 2SR, was drilled to a depth of 1,097.2 m. The water level in this well is depressed relative to estimated pre-test conditions, but it has been steadily rising (Figure 2.13). Hydraulic head in the well was at 1660.7 m as of October 1997, as compared to the pre-shot estimate of 1,687 m presented by Thordarson (1987). The depressed water level is the result of thermal and compressional forces generated by the nuclear test and the resultant bulking produced by the collapse of the rubble chimney into the cavity void (Mihevc *et al.*, 1996). The subsequent water level increase is due to recovery of the cavity and chimney by inflow from surrounding saturated rocks. An analysis of the water level recovery (Appendix 3) predicts total recovery to the pre-test estimate by the year 2001.

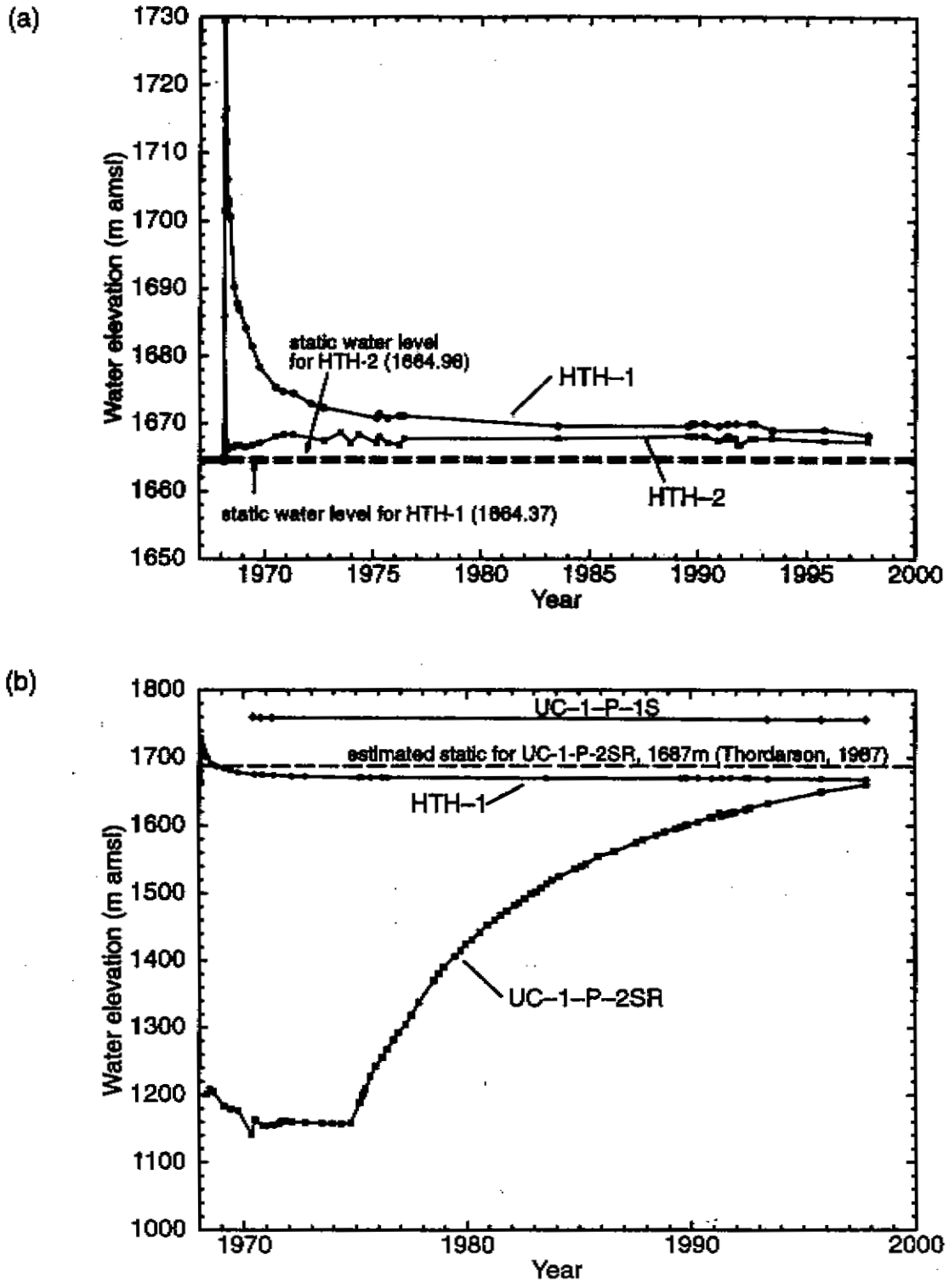

Figure 2.13. (a) Water elevations in HTH-1 and HTH-2 from 1968 to 1997. The sharp increase in early time reflects the impact of the Faultless test on January 19, 1968. (b) Water elevations in UC-1-P-1S and UC-1-P-2SR from 1968 to 1997. The early-time delay in water-level recovery in UC-1-P-2SR was interpreted by Thordarson (1987) as representing a perched water level.

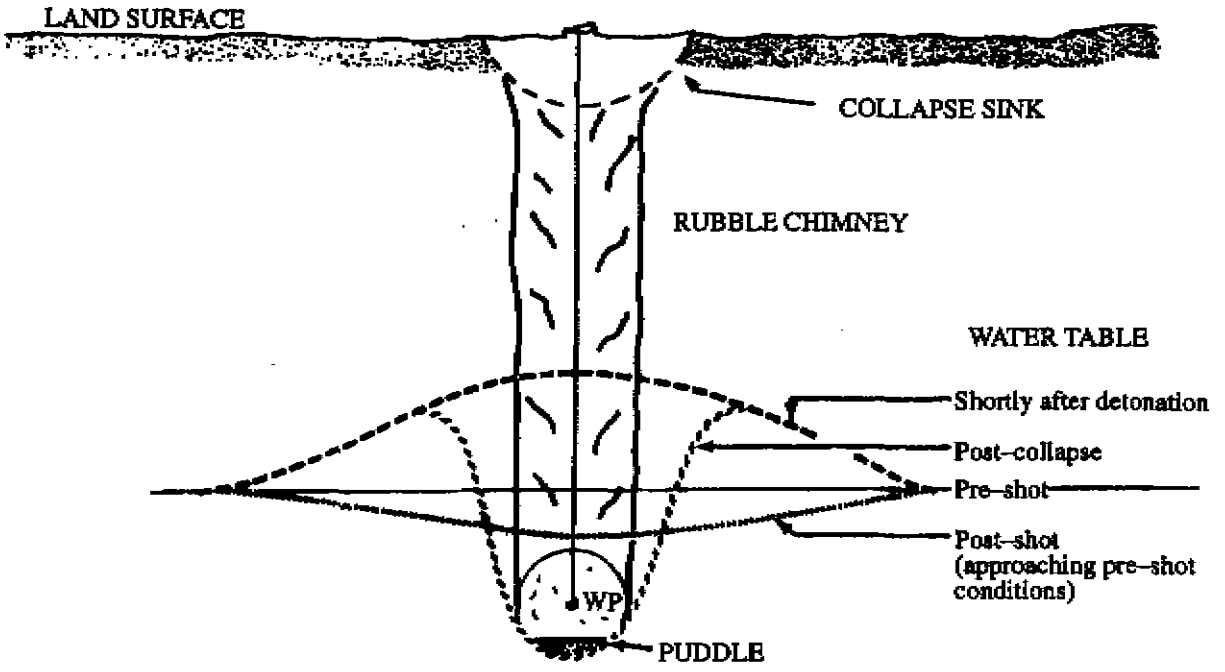

Figure 2.14. Typical water-table response to a detonation in the saturated zone at Yucca Flat, Nevada Test Site, modified from Gonzalez (1977). These same general features have been recorded by wells near the Faultless test: the elevation of the water table shortly after the detonation can be seen in the hydrographs of wells HTH-1 and HTH-2 (Figure 2.13), and appears to be permanently reflected in the head at UC-1-P-1S presumably due to hydraulic isolation caused by bounding faults created by the test. The post-collapse depression in the water table and subsequent increase approaching pre-test conditions is recorded by water levels in UC-1-P-2SR (Figure 2.13).

The chemical signature of the water sampled from UC-1-P-1S is consistent with that of groundwater sampled from the alluvial units in HTH-2 (Table 2.2, Figure 2.7). It is a low-salinity, Ca-HCO_3 groundwater, whereas the groundwater sampled from UC-1-P-2SR is a Na-HCO_3 type characteristic of water in the volcanic units in HTH-1. The stable isotopic compositions support these associations, with the UC-1-P-2SR groundwater depleted in the heavier isotopes, relative to water from the alluvium.

2.5.3 Hydraulic Analysis of Cavity Filling

The long-term water level recovery observed in UC-1-P-2SR following the Faultless test was analyzed to obtain a first-order estimate of hydraulic conductivity in and around the chimney. The rising water levels observed in UC-1-P-2SR represent refilling of the cavity and chimney by inflow from surrounding saturated rocks. This process is roughly analogous to the recovery of water levels in a borehole subsequent to a slug test although hydrogeologic conditions near the Faultless cavity may be more complex. The Hvorslev (1951) analytical method for interpretation of slug test data uses the equation

$$K = \frac{r^2 \ln(\frac{L}{r})}{2LT_0} \tag{2.1}$$

where r is the radius of the uncased borehole, L is the length of the uncased hole, and T_0 is the "basic time lag" determined from a plot of the recovery data.

Groundwater was assumed to be incompressible and of uniform temperature in this analysis; although temperatures in the cavity remain above those predicted by the geothermal gradient. The thermal impact is most pronounced in the immediate vicinity of the cavity and diminishes upward through the chimney as discussed in Section 2.5.4. The cavity and chimney were treated as an open borehole of diameter 84 m, the diameter equivalent to a chimney of diameter 200 m and porosity 0.18 (refer to Section 5.4.4 for a discussion of CNTA porosity values). The open interval was assumed to be 500 m, using the midpoint of the range of four to six times the estimated cavity radius (100 m, Section 2.5). A plot of the head ratio h/h_0 versus time t after the test is presented in Figure 2.15, where h is the head at time t and h_0 is the head at the time that recovery began, t_0. Field test conditions are thought to be a reasonable approximation of the assumption of the Hvorslev method since the data after 6.7 years fall on the straight line on the semilog plot, as predicted by the Hvorslev

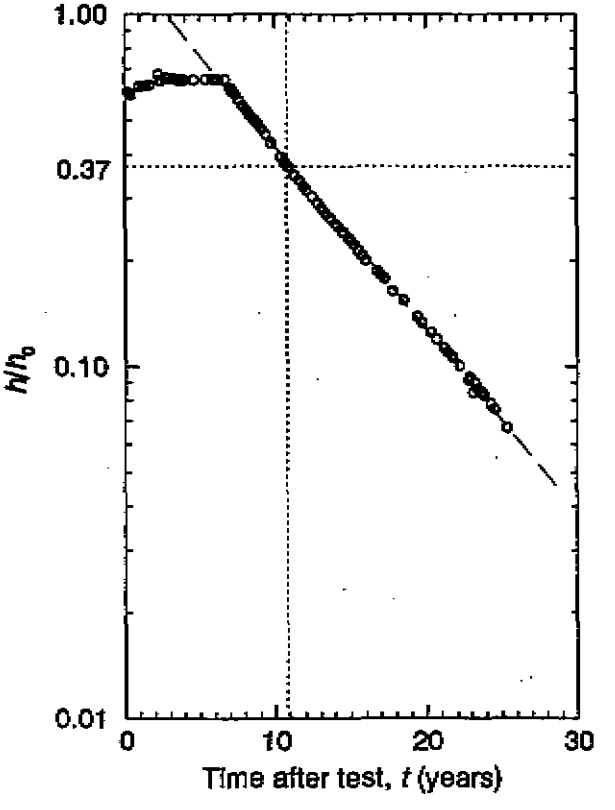

Figure 2.15. Plot of head ratio versus time for water level recovery in UC-1-P-2SR, a postshot hole constructed in the Faultless chimney.

method. Using the T_0 value of 10.8 years that is obtained from the plot for the h/h_0 value of 0.37 (see Hvorslev, 1951) and Equation (2.1) results in a K estimate of 1.1×10^{-3} m/d.

The value estimated here is in close agreement with the value of 7.9×10^{-4} m/d estimated by Thordarson (1987) from the injection test in the same well, and the K values reported by Dinwiddie and Schroder (1971) from packer tests in the base of the alluvium at HTH-1. However, the value is considerably lower than the values reported by Dinwiddie and Schroder (1971) from packer tests in the tuffaceous sediments at HTH-1, and the discrepancy may result from several factors. First, the value calculated here assumes uniform flow into the entire chimney, and therefore represents a composite K of the rocks penetrated by the chimney. Second, there may have been a slight reduction in K in the tuffaceous sediments associated with subsidence of the collapse block. Finally, the packer tests were generally designed to test the most conductive intervals, so their results may be biased toward higher values. In any case, the general agreement of these results using independent datasets and analyses clearly indicates that the rocks in the vicinity of the Faultless test are of relatively low hydraulic conductivity.

2.5.4 Thermal Effects

The energy released by a nuclear detonation is partly consumed through ground motion, and vaporizing and melting rock, but also results in a large increase in temperature in the cavity. This thermal pulse dissipates with time by conduction through the geologic material and convection through groundwater. While temperatures in the cavity region remain above ambient, they affect the groundwater flow system and alter geochemical reaction rates that are temperature dependent. All of these affects are relatively short-term and were not included in the modeling effort presented here because it focuses on long-term transport away from the test area.

Logging in the several years following Faultless identified a sharp increase in the temperature gradient in the post-shot hole below a depth of 756 m (Thordarson, 1987). The deepest measurement was at 801 m and was 75°C in 1971, with a temperature of 100°C projected for a depth of 825 m. Logging in subsequent years has documented the slow cooling in the chimney (Chapman *et al.*, 1994; Mihevc and Lyles, 1998). The temperature in the postshot well at a depth of 680 m in 1997 is approximately the temperature predicted by the geothermal gradient. The bottom hole temperature in 1997 (at 795 m as the bottom of the accessible borehole) was 53°C, 0.7°C cooler than in 1993, but approximately 14°C warmer than predicted based on the geothermal gradient. The relatively slow rate of cooling in the cavity supports the conclusion of low hydraulic conductivity in the vicinity of the test indicated by the hydraulic recovery data.

In their analysis of underground nuclear tests in the South Pacific, the International Atomic Energy Agency (IAEA, 1998) evaluated the thermal impact of the tests. It found that the temperature difference with ambient temperature decays to zero over a period of about 500 years. The hydrologic impact was to create a vertically upward flowpath above the cavity-chimney, driven by thermal buoyancy. Preliminary analysis performed by Desert Research Institute of thermal effects of a nuclear test in a region of downward groundwater flow in the Aleutian islands indicates that the thermal input from the test is not significant enough to overcome the natural gradient in the

downward direction. It is notable that this test had a larger yield than Faultless, and thus greater heat production, but both cooled and recovered hydraulically much more rapidly than Faultless (Claassen, 1978), indicating the significant control of not only infill, but also cooling, by the hydraulic conductivity of surrounding aquifers.

Vertical flow has been noted in the Faultless post-shot well, both upward and downward in the wellbore, presumably as a result of thermal effects (Chapman *et al.*, 1994; Mihevc *et al.*, 1996). However, strong stratification in the well bore is evidenced by distinct zones of temperature and chemical composition that have persisted for decades (Thordarson, 1987; Mihevc and Lyles, 1998). The effect of distributing tritium vertically upward, whether through prompt injection or by thermally driven mixing, is considered in a sensitivity analysis later in the report.

2.5.5 Summary of Near-Field Hydrology

The Faultless underground test had a significant impact on the local geology and hydrology. Dramatic differences between the hydraulic head in several nearby wells suggest that faults generated by the test may behave as low-permeability hydraulic barriers. Recovery of the depressed potentiometric surface at the cavity, typical of an underground nuclear test, has been very slow, indicating that rocks near the test are of relatively low hydraulic conductivity. The slow rate of cooling of the cavity also supports low hydraulic conductivity as inhibiting convective cooling. Ground motion from the Faultless test may have altered the hydraulic conductivity farther afield (outside the fault block), though the apparent changes in hydraulic head that suggest this may actually be due to the manner in which the wells are completed.

2.6 Monitoring Results and Estimates of Radionuclide Transport

Test-related radionuclides have only been identified in groundwater sampled from postshot well UC-1-P-2SR, drilled into the Faultless chimney and cavity. A strong degree of stratification of radionuclides and temperature has been recorded in the well as infilling proceeds (Thordarson, 1987) and continues to this day. Though some variation occurs, presumably as the result of borehole mixing caused by bailer movement through the casing, high tritium concentrations are confined to the deepest part of the well, just above the impassable bridge at 795 m depth. The highest tritium concentration ever measured in UC-1-P-2SR is 9.2×10^{8} pCi/L, for a sample collected in September 1976 (Thordarson, 1985). The most recent deep sample from the well yielded a tritium value of 1.57×10^{7} pCi/L in October 1997 (Mihevc and Lyles, 1998). Concentrations decrease rapidly with decreased depth, so that 200 m higher in the borehole, tritium is below drinking water limits. Davisson *et al.* (1994) reported concentrations of up to 27,093 pCi/L of ^{85}Kr, 434 pCi/L of ^{39}Ar, and above background $^{36}Cl/Cl$ ratios of up to 1×10^{-8} in water samples from UC-1-P-2SR, but ^{99}Tc was not detected nor was gamma activity above background for ^{60}Co, ^{125}Sb, and ^{137}Cs. Gamma scans performed on the samples collected at 795 m in October 1997 detected ^{137}Cs, and ^{239}Pu and ^{240}Pu were detected on the filter used to filter water from that depth (Mihevc and Lyles, 1998). No radionuclide concentrations above background have been found in the other wells, UC-1-P-1S, HTH-1, and HTH-2.

The first estimate of radionuclide transport from the Faultless test was briefly presented by the U.S. Atomic Energy Commission (1973, Appendix 2). It estimated a time of infilling for the Faultless chimney of 80 to 100 years, and subsequent groundwater migration at a rate of 0.12 m/yr in a general south-southeast direction. It concluded that radionuclides in groundwater will be at background concentrations well before reaching the boundary of the land-withdrawal area.

Pohlmann *et al.* (1995) modeled potential migration of tritium away from the Faultless cavity as part of the Environmental Impact Statement for DOE activities in Nevada. They evaluated the possible risk to an individual consuming groundwater at two locations: at the land-withdrawal boundary, and at the first existing downgradient supply well (located 14 km away), for a lifetime centered around the peak tritium concentration. Their work focused on transport in alluvium and tuffaceous sediments using analytical methods to calculate the downgradient breakthrough of tritium. They used a groundwater velocity of 42 m/yr, based on hydrologic data and consistent with the range estimated by Dinwiddie and Schroder (1971) of 40 to 70 m/yr, but they note much uncertainty in the flow and transport parameter values. At the first existing supply well, the range in excess risk was within the U.S. Environmental Protection Agency (EPA) goal (10^{-6}), even for sensitivity cases incorporating high spatial variability and/or high uncertainty in the mean groundwater velocity. At the land-withdrawal boundary, the range in excess risk exceeded the EPA goal, regardless of the values for spatial variability and uncertainty.

3.0 Conceptual Model

3.1 Conceptual Flow Model

Although a substantial amount of hydrogeologic data has been collected at the Faultless site and in the surrounding region, there remain uncertainties about certain details of the flow system. The flow model represents a synthesis of as much site data as possible to provide a realistic description of groundwater flow for the transport calculations. The flow model was based on hydrogeologic conditions prior to the Faultless test, under the assumption that transport over the long term would be controlled by these factors rather than the relatively short-term effects of the test. Furthermore, flow was considered to be at steady state owing to the large size of the Hot Creek Valley hydrologic system and the absence of excessive groundwater withdrawals (1,890 acre-feet per year were committed out of a perennial yield of 5,500, as of 1988; State of Nevada, 1988) such that significant temporal fluctuations in regional water levels are not expected under current climatic conditions. Local structural features such as faults were not explicitly included owing to the lack of information regarding their subsurface locations and hydraulic characteristics. If the subsidence faults related to the Faultless test are hydraulic barriers, as suggested by water-level data near the site (see Section 2.5.2), then our predictions of horizontal flow and transport in the alluvium are overestimates. The impact on deeper flow and transport depends on the depth to which these faults extend, information that is not currently available.

The area considered for modeling is at a scale intermediate between the scale of the near-cavity environment and the scale of regional groundwater flow, focusing on the UC-1 land-withdrawal area. The principal hydrogeologic units are divided into the three general categories of Quaternary

alluvium; Tertiary tuffaceous sediments, bedded tuffs, and partially welded tuffs; and Tertiary rhyolites and densely welded tuffs. The rhyolites and densely welded tuffs are highly fractured and faulted and where present are considered the primary pathways for groundwater flow and transport.

Importantly, hydrogeologic investigation at the Faultless site identified no rhyolites and only a single 24-m-thick interval of densely welded tuff (at HTH-1), although lithologic evidence suggests that densely welded tuffs may be present at depths below the extent of drilling at the site. The absence of densely welded tuffs at UC-1 is unusual for the volcanic section in the vicinity of Hot Creek Valley where the volcanic intervals of many CNTA exploratory boreholes are comprised primarily of moderately to densely welded tuff. For example, thick sections of densely welded tuffs were logged below the elevation of the Faultless test at UCe-17 to the north and UCe-20 to the south of UC-1 (Appendix 4). Barnes and Hoover (1968) and Banister and Johnson (1969) suggest high-angle faults have displaced the volcanic section in Hot Creek Valley, and in the vicinity of UC-1 placed the densely welded tuffs at depths below the Faultless test horizon. In any case, the stochastic approach used here accounts for the uncertainty in lithology at depth, some realizations include densely welded tuffs and some realizations do not. The great majority of the volcanic section at Faultless consists of tuffaceous sediments and nonwelded tuffs that tend to be poorly sorted, well indurated, commonly zeolitized, and supported by a clay-cemented matrix. Although matrix porosity of these rocks may be moderately high, most pores are unconnected. In addition, the clay and zeolite matrices tend to reduce interstitial hydraulic conductivity to very low values. Finally, the nonwelded tuffs observed at UC-1 and UC-3 contain few fractures (Hoover, 1968a; Dixon and Snyder, 1967; Barnes and Hoover, 1968). The combination of these factors causes the tuffaceous sediments and nonwelded tuffs to have low hydraulic conductivity relative to the densely welded tuffs.

Like many flow systems in the Basin and Range province, groundwater flow in Hot Creek Valley is a complicated system of overlapping and interacting components. To conduct flow modeling in such a setting, the ambient flow system was simplified to its principal horizontal and vertical components. Hydraulic head measurements in wells in Hot Creek Valley indicate that groundwater flow in the alluvium is directed toward the south, generally following the slope of the valley surface. Head relationships in the deeper volcanic system, including surrounding valleys, indicate flow toward the northeast and east toward regional discharge points further south in Hot Creek Valley and east in southern Railroad Valley. Strong vertically downward hydraulic gradients are present to the north (near UC-1) where land surface elevations are higher and recharge from precipitation is likely to be taking place. To the south (near UC-3), strong vertical hydraulic gradients from the volcanic section upward to the alluvium are present, and may be related to the regional discharge. The head distributions representing these components of the flow system were developed using head measurements made in the packer intervals in the CNTA exploration boreholes, as reported by Dinwiddie and Schroder (1971). These measurements were all conducted prior to the detonation of the Faultless test and thus represent ambient conditions at the site. An idealized cross section through a portion of Hot Creek Valley showing our conceptualization of the ambient flow system is shown in Figure 3.1.

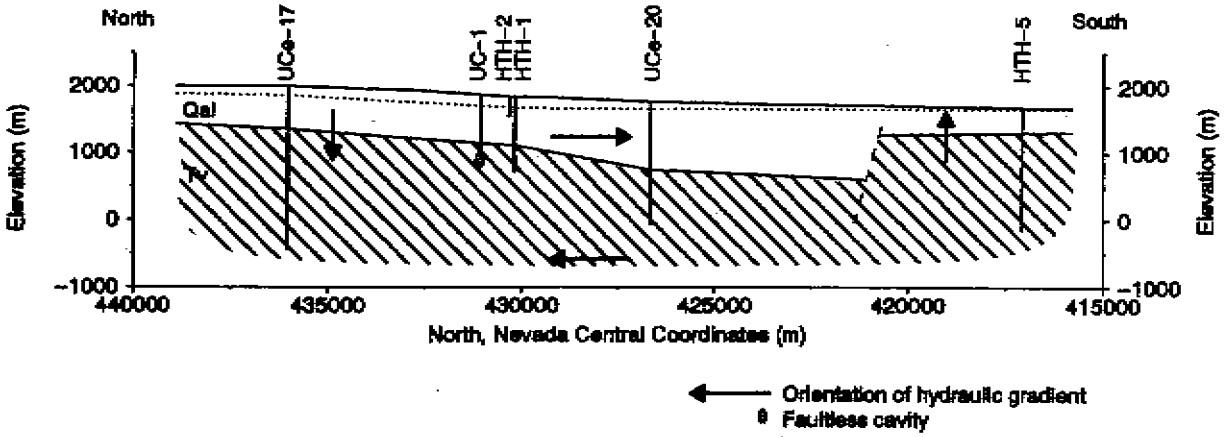

Figure 3.1. Diagrammatic vertical cross section showing major components of conceptual flow model in Hot Creek Valley.

Although groundwater recharge may occur in localized areas of Hot Creek Valley, the absence of site-specific data prevents adequate characterization of its quantity and distribution. Groundwater recharge that occurs in the higher elevations of the Hot Creek Range was included in the numerical flow model by implication of the strong vertically downward hydraulic gradients in the portion of the model underlying the highest land surface elevations. However, recharge was not applied areally to the top boundary of the model. Previous investigation of groundwater recharge in central Nevada has suggested that recharge at the elevation of UC-1 is minimal. Rush and Everett (1966) used the Maxey-Eakin method (Eakin *et al.*, 1951) to provide preliminary basin-scale estimates of the average annual precipitation and groundwater recharge in Hot Creek Valley. The Maxey-Eakin method, which has been widely applied in Nevada, assumes that recharge originates primarily from precipitation in the mountains, and bases the estimates of the percentage of precipitation that recharges the groundwater reservoir on elevation. Although the method has significant limitations, it does provide reasonable estimates of recharge at the basin scale (Avon and Durbin, 1992). Rush and Everett (1966) used precipitation zones of 2,743 m (original value reported as 9,000 ft) and above, 2,438 to 2,743 m (8,000 to 9,000 ft), 2,134 to 2,438 m (7,000 to 8,000 ft), and 2,134 m (7,000 ft) and below. Most of the land surface included in the model domain lies below 2,134 m, with about five percent (on the western edge), at elevations between 2,134 and 2,438 m. Rush and Everett (1966) estimated that no recharge from precipitation occurred below elevations of 2,134 m, and that recharge was equivalent to about three percent of precipitation between the elevations of 2,134 m and 2,438 m, which corresponded to about 0.68 cm of recharge per year.

3.2 Conceptual Transport Model

The migration of contaminants from the Faultless underground nuclear test involves a complex system of physical and chemical processes. Some of these processes are poorly understood and are the subject of ongoing research conducted by DOE. For this analysis, many assumptions were made based on currently available data. A diagrammatic representation of the transport model source and processes considered is shown in Figure 3.2.

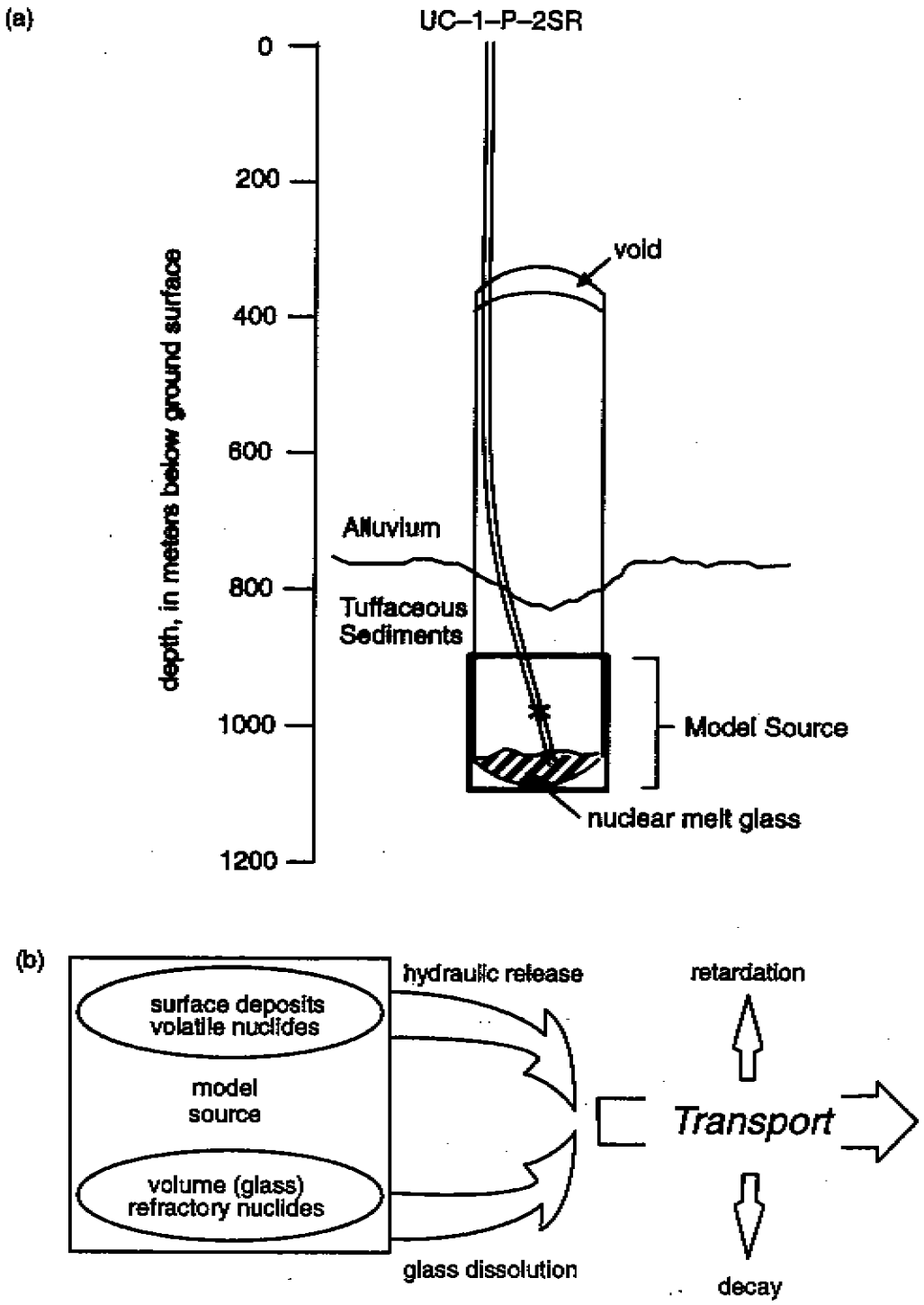

Figure 3.2. Part (a) is a representation of the Faultless rubble chimney, as presented by Thordarson (1987). Details of the test are classified, but the diagram shows a void at the top of the chimney, a depression in the alluvium-tuffaceous sediment caused by collapse, and the position of melt glass at the base of the cavity. The source used in the transport model is a cube, 200 m on a side, centered on ground zero. Part (b) is a flow chart of the apportioning of source nuclides and transport processes considered.

The contaminants considered consist of the radionuclides produced by the Faultless test and the daughters that are created by radioactive decay. The nuclides are assumed to all be initially located within the cavity. Distribution upward through the chimney region was neglected in the base case, though considered in sensitivity calculations.

Radionuclides are distributed according to their volatility among surface deposits and volume deposits in nuclear melt glass. Volatile and surface-deposited nuclides are assumed to migrate once hydraulic equilibrium conditions are reached (see below). Nuclides within the glass are released according to glass dissolution rates calculated based on volcanic glass dissolution behavior and radionuclide melt glass characteristics.

It is assumed that no migration of radionuclides occurs until the cavity has infilled with groundwater, following the dewatering caused by the thermal and compressional forces of the nuclear test. Calculations (see Appendix 3) indicate that the flow of low-contaminant-concentration groundwater toward the hydraulic sink is much larger than the movement of contaminants away from the sink driven by concentration gradients (molecular diffusion) until the last several months prior to the conclusion of infill. Early-time cavity conditions and near-field properties affected by the nuclear test were not considered in the analysis. Data within the collapse region around the test, discussed in a previous section, reveal a complex and poorly understood near-field environment characterized by faults, fractures, and elevated temperatures. The assumption made here is that these hydraulic and thermal changes are local and short-term, and that long-term transport (over hundreds to thousands of years) can be approximated using our understanding of the pre-test hydrologic conditions.

The treatment of mass in the glass was different than the mass outside the glass, which was released via hydraulic release. Particles representing the mass released hydraulically were tracked in the space-time domain at the infill time. Particles representing the radionuclide mass trapped in the glass were released according to an exponential release function. At each time step, a certain number of particles was released from the glass mass in such a way that the total glass mass was released very slowly over time.

Once released, some nuclides are subjected to a retardation factor to account for reactions with the aquifer matrix. Retardation factors were calculated from distribution coefficients derived from batch experiments. Nuclides were grouped according to assumed general sorptive behavior and assigned the same retardation factor because radionuclide-specific data were not available for many of the contaminants in the CNTA environment. Daughter products were assigned the same retardation factor as the parent nuclide as a result of the computational method. The effect of colloidal particles on transport behavior was not modeled due to the lack of data to support such calculations.

The retardation process of matrix diffusion was included for the scenario of transport by fracture flow through the welded tuff units. Two fundamentally different approaches to transport in the welded tuff are considered: migration through an equivalent porous medium, consistent with porosity values measured on cores; and, migration through fractures running through matrix blocks

having porosity consistent with the core data. Matrix diffusion is not considered for the porous medium case, but is an important retardation process included in the fracture scenario. Matrix diffusion is accounted for in a post-processing mode. A non-decayed breakthrough curve is obtained by the random walk particle tracking method and then convoluted with a retention function that accounts for matrix diffusion (e.g., Cvetkovic and Dagan, 1994; Cvetkovic *et al.*, 1999). This approach treats the fractured system as a stochastic continuum. The retention function, however, is derived for discrete fractures. There is, therefore, some inconsistency in this analysis as the discrete and continuum approaches are mixed. However, this is not unreasonable and it has been used in many European studies dealing with safety analysis and risk assessment (e.g., NAGRA, 1994; Cvetkovic, 1999 Personal Communications). For simplicity in the analysis, this mixed approach is used as a tool to compare the results based on a porous medium setting with large porosity and a fractured system with very low flow porosity, but with mass diffusing into the rock matrix.

The transport calculations were performed using a particle tracking method. An initial mass was released and its movement tracked through the model domain. The peak passage at the control plane was noted (after accounting for radioactive decay) and that time was used to sum the particles and convert mass to concentration. Mass breakthrough curves and concentration breakthrough curves through time are presented for the land-withdrawal boundary surrounding the Faultless test. Transport was performed using units of moles to allow for decay to daughter products. The effect of radioactive decay and matrix diffusion was calculated in a post-processing mode.

All of the contaminant masses used in the transport modeling were assigned a value of one mole. The results can then be scaled by the classified masses available in Goishi *et al.* (1995) because all of the processes modeled (*e.g.*, retardation) are linear. If rate-limited processes are included, scaling would no longer be possible as a way to transfer the model results into classified data. At the present time, the state of knowledge about reactive transport parameters at CNTA does not justify the complexity and added uncertainty of modeling kinetic, non-equilibrium processes. Unclassified estimates of the tritium, ^{90}Sr, and ^{137}Cs were made and used to scale the results for presentation in this report.

4.0 Methodology

The hydrogeologic heterogeneity of natural formations is usually manifested as complex spatial variability, while the information available to describe the variability is often extremely limited. It is therefore virtually impossible to construct a detailed deterministic description of the hydrogeologic heterogeneity for use in models of groundwater flow and transport. An alternative is to use stochastic methods to generate a set of equiprobable subsurface K maps conditioned on the available hard data (Delhomme, 1979; Dagan, 1986; Gelhar, 1986). Contaminant migration is then simulated for each map and the resulting set of responses (*e.g.*, contaminant breakthrough curves, contaminant plumes) is obtained as a distribution of equiprobable outcomes.

Characterizing and accurately predicting contaminant migration in the subsurface is highly dependent on detailed delineation of groundwater flowpaths. Of particular importance is the determination of the continuity of zones of high hydraulic conductivity. In a heterogeneous

formation with K values ranging over several orders of magnitude, flow occurs primarily through connected zones of high K (*e.g.*, fractures in a fractured rock). These connected high-K zones may be the primary mechanism for contaminant migration, though they may represent only a very small proportion of the total rock mass. Under these conditions, the bulk of the rock mass and randomly disconnected small fractures may in fact contribute very little to the total flow. A multiple covariance approach is used to provide independent descriptions of the spatial distribution of hydrogeologic categories, and in particular, high and low values of K.

The CNTA groundwater flow and radionuclide transport model was developed using stochastic methods and incorporates descriptions of the heterogeneity of hydrogeologic units and hydraulic conductivity, representations of the groundwater flow field, and simulations of radionuclide transport. The numerical methods utilized in these aspects of the study are described in the following sections. More detailed treatment of the approach used to characterize the heterogeneity can be found in Andricevic *et al.* (1995), Pohlmann *et al.* (1996), and Shirley *et al.* (1996).

4.1 Description of Hydrogeologic Heterogeneity

The natural subsurface hydrogeologic heterogeneity at CNTA was described in two phases. In the first phase, the geometry of the hydrogeologic units most important to groundwater flow and contaminant transport was described using the sequential indicator simulation (SIS) algorithm (Alabert, 1987). SIS allows the entire range of variability of a random field (*e.g.*, lithology, K) to be divided into categories. Each category is assigned a unique spatial correlation structure based on analysis of the field data. In this way, the spatial continuity of each category can be distinguished from the others, and the unique descriptions of all categories are incorporated in the simulated three-dimensional maps of hydrogeologic units. The SIS simulations were conditioned using lithologic and electrical resistivity logs, in conjunction with packer-test data, from wells at the site. In the second phase, the distribution of K within each hydrogeologic category was described using the sequential Gaussian simulation (SGS) algorithm (Deutsch and Journel, 1998). The SGS simulations were conditioned using K values estimated from the packer tests. An important advantage of using this two-phase process is that the hydraulic data from the packer tests, of which there are a fairly limited number, could be augmented by the much more extensive coverage of the geophysical data.

Electrical resistivity logs, lithologic logs, and packer test data were used to identify important hydrogeologic categories. First, the packer test data and the lithologic logs were used to divide the saturated hydrogeologic section into three categories: Quaternary alluvium, volcanic rocks having low K, and volcanic rocks having high K. Then, the relationship between electrical resistivity and hydraulic conductivity in the volcanic rocks was described. Finally, the resistivity logs were used to identify the three categories at locations where packer-test data were absent. The result of this process was a categorical dataset used for describing the spatial correlation structure of the hydrogeologic categories and for conditioning the SIS simulations. Further details of the simulation process as it was applied at the CNTA site are described in the Flow Model section of this report.

The spatial correlation structures of the categorical and hydraulic conductivity datasets were described using variograms, $\gamma(r)$, expressed as:

$$\gamma(r) = \frac{1}{2}E[(Z(x)-Z(x+r))^2] \tag{4.1}$$

where r is the lag distance between sample locations x and $x + r$ of random variable Z. Using Equation (4.1), experimental variograms were computed for each category of the categorical dataset and each category of K. Theoretical variogram models were then developed using mathematical expressions to approximate the experimental variograms of the categorical and K datasets. The two expressions used were the exponential model and the nugget-effect model. The exponential model is expressed as

$$\gamma(r) = \sigma^2_{\log K}(1-\exp(-\frac{3r}{\lambda})) \tag{4.2}$$

where the correlation length λ (effective range a of Deutsch and Journel, 1998) represents the distance at which correlation between data points ceases. The exponential model is often employed to describe the correlation structure of K because it has been found to correspond to log K data and is straightforward to apply (Hoeksema and Kitanidis, 1985). The exponential variogram increases from zero as r increases and reaches a plateau value of the variogram (sill) asymptotically.

The isotropic nugget-effect model is expressed as

$$\gamma(r) = C_0(1-\delta(r)) = \begin{cases} C_0, & \text{for } r > 0 \\ 0, & \text{for } r = 0 \end{cases} \tag{4.3}$$

where C_0 is the nugget variance and $\delta(r)$ is the Kronecker delta that is 1 if $r = 0$, and 0 for all other cases. The nugget variance represents small-scale variability (scale smaller than the sampling interval) as well as uncertainty in the measurements, and is distinct from the variability attributed to spatial separation.

The categorical dataset was also used to determine the conditional probabilities of each category, essential information required for the SIS simulation. The probability that an attribute is in a particular category is determined by its indicator value. The indicator is set to 1 if the location x belongs to category s_k, where k is the number of categories, and to zero otherwise. Thus, instead of working with a continuous range of a random variable $Z(x)$, as in classic geostatistics, the nonparametric indicator approach considers only the indicator values $I(x)$. The average value of $I(x)$ over the entire domain represents the cumulative probability distribution function (CPDF) of $Z(x)$ in s; that is, the proportion of $Z(x)$ in each category s, *i.e.*

$$E\{I(x; s_k)\} = P\{I(x; s_k) = 1\} = p_{s_k} \tag{4.4}$$

The expected value of the product $I(x;s_k)$ and $I(x';s_k)$ is the noncentered covariance and represents the bivariate distribution of $Z(x)$ for locations x and x' for category s_k:

$$E\{I(x; s_k)I(x'; s_k)\} = P\{I(x) = 1; I(x') = 1\} \quad (4.5)$$

The above equation is a measure of the two-point spatial continuity of a particular category of the attribute. The higher the covariance, the greater the probability of having two values $I(x)$ and $I(x')$, which jointly are not in the same category (Journal and Alabert, 1990). Thus, the indicator covariance accounts for the spatial connectivity patterns of the individual categories. When this connectivity pattern indicates layers and lenses of high K, potential groundwater flowpaths are identified.

The SIS algorithm estimates a value of a subsurface attribute at an unsampled location such that the new value is consistent with the inferred spatial correlation structure of that variable (Alabert, 1987). The simulation begins by defining a random path through all of the model cells. At each cell, the conditioning data present within a given search neighborhood are identified and the closest points are retained for kriging. For each category, a kriging system using the appropriate variogram model is constructed and solved. The new value is added to the existing dataset (conditioning data) and the process is repeated until all of the cells have been simulated. The original conditioning data include only the known data, but as the SIS simulation proceeds, the conditioning dataset grows with the addition of each newly simulated point. Thus, the final simulated map honors the known data at their locations as well as the spatial correlation structure inferred from the known conditioning dataset.

Each SIS simulation represents a single realization of the subsurface heterogeneity. Multiple equiprobable realizations are required to simulate the full range of variability at the site. The SIS simulations in this study were generated using the FORTRAN program SISIM (Deutsch and Journel, 1998) used in the formulation for categorical variables.

The three-dimensional maps of the hydrogeologic categories simulated using SIS are used as the basis for the maps of K, which are produced using the SGS algorithm (Deutsch and Journel, 1998). The SGS algorithm generates three-dimensional realizations of a Gaussian process using a given variogram model. Variogram models of the spatial structure of K are developed for each hydrogeologic category based on the hydraulic information available for each class. In SGS, a random path through the simulation grid is defined such that every cell is visited once. As each cell is visited, a predefined neighborhood is searched for conditioning data, including both known conditioning data and previously simulated values. Simple kriging is used to estimate the value at the current cell based on the pre-defined Gaussian distribution of the simulation variable. This value is then added to the conditioning dataset and the simulation proceeds to the next cell. After completion, the values of the simulation variable $Z(x)$, which are normally distributed, are transformed to a log-normal distribution of hydraulic conductivity, $K(x)$ using the expression

$$K(x) = 10^{\mu_{\log K} + \sigma_{\log K} Z(x)} \quad (4.6)$$

One K field is produced for each category of every SIS realization. The final K map associated with each SIS realization is generated by assigning the K value appropriate for each cell, based on the category in which each cell belongs.

4.2 Simulation of Groundwater Flow

Steady-state three-dimensional flow was simulated in the heterogeneous porous medium represented by each K realization. The groundwater flow code MODFLOW-88 (McDonald and Harbaugh, 1988) was used to solve for the hydraulic head field $h(x)$ using a finite difference approximation of the general flow equation:

$$\nabla \cdot [K(x)\nabla h(x)] = 0 \tag{4.7}$$

where $K(x)$ is the hydraulic conductivity field.

Cell-to-cell Darcy fluxes were calculated from the MODFLOW-simulated head fields using

$$q(x) = -K(x)\nabla h(x) \tag{4.8}$$

where $q(x)$ is the Darcy flux field. The Darcy fluxes are converted to groundwater velocities within the solution of the transport equation.

The MODFLOW code was selected for the flow simulations after consideration of the capabilities of several codes as they related to the hydrogeological conditions of the CNTA site, including:

- Fully three-dimensional
- Flexible boundary conditions
- Hydrologic sources and sinks
- Heterogeneous and anisotropic properties
- Steady-state or transient conditions

Computational considerations related to running large three-dimensional models included:

- Capability for multiple realizations
- Pre- and post-processing of data
- Compatibility with existing hardware and software
- Efficient data handling
- Efficient numerical solvers

Finally, access to the source code was considered essential to allow modifications of input and output data structure, make changes as dictated by site-specific conditions, and compile on a variety of computational platforms. Therefore, public-domain, "open-source" codes were preferred. Although several groundwater flow codes meet the criteria outlined above, MODFLOW provides the additional benefits of a long history of successful application to a wide variety of problems, widespread acceptance in the hydrogeology community, and the ability to easily scale the code to the complexity of the modeling problem through the code's modular design.

Three modules were used for the application of MODFLOW to the CNTA site. The Basic (BAS) module specifies the other modules that are to be used, the geometry of the model domain,

the boundary conditions, and the time steps. The Block-Centered Flow (BCF) module handles the grid discretization, aquifer type, and hydraulic parameters required to solve the finite difference equations. The Preconditioned Conjugate-Gradient (PCG) module uses modified incomplete Cholesky preconditioning to efficiently solve the matrix of finite difference equations (Hill, 1990). Modifications to the original code included enhancements to read the three-dimensional K maps and calculate the cell-to-cell Darcy fluxes using Equation (4.8). The modified code was verified by testing against the Darcy equation using a homogeneous K field.

4.3 Simulation of Contaminant Transport

Transport of a nonreactive solute in saturated porous media of constant porosity is described by:

$$\frac{\partial c(x,t)}{\partial t} + \nabla \cdot [c(x,t)v(x)] - \nabla \cdot [\mathbf{D}(x)\ \nabla c(x,t)] = 0 \qquad (4.9)$$

where $c(x,t)$ represents concentration and $\mathbf{D}(x)$ represents the diagonal of the local hydrodynamic dispersion tensor. The components of $\mathbf{D}(x)$ are:

$$\mathbf{D}(x) = a_T\,|v(x)|\,I + (a_L - a_T)\,\frac{v(x)v(x)}{|v(x)|}\,I + D^*\,I \qquad (4.10)$$

where a_L and a_T are the longitudinal and transverse local dispersivities, $|v(x)|$ is the magnitude of velocity, I is the three-dimensional identity matrix, and D^* is the effective coefficient of molecular diffusion.

Several numerical approaches can be used to solve the transport equation; for example, finite differences, finite elements, method of characteristics, and random walk particle-tracking methods. The Peclet number P_e associated with the traditional finite difference and finite element solutions to the advection-dispersion equation can be approximated by the ratio $(V\Delta x) / (a_L V) = (\Delta x) / (a_L)$. To obtain a stable solution when using an implicit finite difference or finite element scheme, the Peclet number should be kept less than unity and thus a very fine grid is needed for small values of longitudinal dispersivity a_L. This becomes prohibitive in three-dimensional simulations of field-scale problems in terms of storage and CPU time. The random walk method provides a suitable alternative that does not suffer from the above restriction. In addition, numerical dispersion that is common in the solution of the transport equation by finite differences or finite elements can be minimized by the random walk method. Moltyaner *et al.* (1993) have shown that the random walk method completely eliminates numerical dispersion as compared to finite differences and finite elements solutions. For this reason and following a major body of literature, the random walk method is used to simulate the transport and evolution of radionuclides in the generated random velocity fields. The injected mass is replaced with a large number of particles NP of equal mass m that are tracked in the space-time domain. The initial concentration C_0, considered to be constant, is given by $C_0 = \mathrm{NP}\, m / \theta\, \Omega$, where θ is the domain porosity and Ω is the volume of the initial source or the cavity. Ahlstrom *et al.* (1977) suggest that 10^3 to 10^4 particles may be sufficient for a

one-component model. We use 20,000 particles in all the transport simulations presented in this study.

The positions of the particles are updated at each time step according to the random walk equation (Kinzelbach, 1988; Tompson and Gelhar, 1990)

$$x_{t+\Delta t} = x_t + [v(x_t, t) + \nabla \cdot \mathbf{D}(v(x_t, t))]\Delta t + [2\mathbf{D}(v(x_t, t))\Delta t]^{1/2} \cdot z \qquad (4.11)$$

where $x_{t+\Delta t}$ is the updated position of the particle that was at x_t in the previous time step, $v(x_t,t)$ is the velocity vector at the old position at time t, $\mathbf{D}$ is the local-scale dispersion tensor, Δt is the time step, and z is a vector of normally distributed random numbers of zero mean and unit variance. The particle velocities needed in the above equation are obtained by using an inverse distance interpolation scheme using the fluxes at the eight corners (in three dimensions) surrounding the particle and then dividing by the porosity of the cell where the particle resides. Other interpolation schemes (linear, bilinear) could be used to obtain the velocity at the particle's location. Based on a previous experience (Hassan *et al.*, 1999), the difference between the bilinear interpolation scheme and the inverse distance scheme used in this study is not significant, and as such either of the two schemes will suffice. The first term on the right-hand side of Equation (4.11) represents the advective step and the second term adds the effect of the gradients of the dispersion tensor on the particle movement. This latter term is important if sharp fronts exist and whenever the gradient of $\mathbf{D}$ is significant. The last term represents the contribution of local-scale dispersion and Brownian diffusion to the movement of the particles. The choice of Δt is an important decision in the random walk method since the computational expense of this method is proportional to the number of time steps employed. In practice Δt is chosen such that the fraction of the cell's length traversed by a particle in a single time is less than unity. If excessively large time steps are used, overshoot problems may occur during the solution of the transport equation via the random walk method (Tompson and Gelhar, 1990). On the other hand, a very short time step may cause an enormous increase in the computational time, which may be prohibitive. To avoid these problems, an upper limit of Δt is chosen such that the cell Courant number C_c, which is the ratio between the average advective step and the grid size, is less than unity:

$$C_c = \frac{\overline{v(x)} \cdot \Delta t}{\Delta x} \qquad (4.12)$$

where $\overline{v(x)}$ is chosen in our simulations to be the mean velocity experienced by the particles from the source to the control plane. To account for the high variance of $\overline{v(x)}$ in this model, we chose a Δt that was eight to ten times lower than the value estimated from Equation (4.12).

Since the radionuclides are divided among surface deposits that can be released via hydraulic release and volume deposits, which are trapped in a puddle glass (see Section 6.2 for definitions), the treatment of particles representing both categories is different. Assume that p is the percentage of mass released hydraulically, and thus 1-p represents the mass in the glass. If the total number of particles is NP, then a number of particles equal to p x NP is released instantaneously into the flow

field and is subject to all the processes involved (advection, local dispersion, retardation, etc.). Particles in the glass, (1-p) NP, are released in patches according to the glass dissolution rate, k = 1.17 x 10^{-6} $days^{-1}$ as will be discussed in Section 6.2.3. Therefore, the number of particles released at any time, $t > 0$, can be obtained from the expression

$$NP_G^t = [(1 - p)NP] * [(1 - e^{-kt}) - (1 - e^{-k(t-\Delta t)})] \quad (4.13)$$

where NP_G^t is the number of particles released from the puddle glass at time $t > 0$. At time $t = 0$, no particles are released from glass and only those released via hydraulic equilibrium are allowed to move with the flow field. Figure 4.1 depicts the number of particles released at every time step for a scenario of 95/5 glass/hydraulic release and a total number of particles of 20,000. The top plot of Figure 4.1 shows that the number of particles released at $t = 0$ (denoted by the square symbol) is 1,000, which represents the hydraulic release (0.05 x 20,000). No particles are released from the puddle glass at this time. After one time step (40,000 days), an initial patch of particles is released from the glass and is equivalent to about 860 particles. This number decreases exponentially until all the mass is released. As the time progresses, the glass dissolution decreases and thus the number of particles released to the flow field becomes smaller. The lower plot in Figure 4.1 shows the cumulative sum of the particles released at any time. After about 200 time steps (21,900 years), almost all the particles representing the glass were released.

Using the particle distribution at every time step, three types of information are obtained. First, the total mass-flux breakthrough is obtained for the control plane, which is taken to be the UC-1 land-withdrawal boundary. The total mass crossing the boundary is computed at every time step and then normalized by the initial injected mass, M_0, to yield the total relative mass flux as a function of time.

The second type of information represents the relative peak-concentration breakthrough curve. The concentration distribution within the control plane is computed at any time step and the peak value is identified and recorded. The concentration is simply obtained by counting the number of particles within each cell at the control plane, computing their total mass, and then dividing by the fraction of the cell's volume occupied by water. The peak concentration is then normalized relative to the initial concentration, C_0, except when prompt injection is considered. For the two breakthrough curves (relative mass-flux and relative peak-concentration), the individual breakthrough curves are averaged over the ensemble of realizations and statistically analyzed to obtain the first two moments, $\langle Q \rangle / M_0$, $\langle C_{max} \rangle / C_0$, σ_Q^2 / M_0^2, $\sigma_{C_{max}}^2 / C_0^2$. However, the results are presented in terms of the mean (first moment) and the standard deviation (square root of the second moment). These undecayed moments will be the same for all nuclides in a given solute class that represents a particular combination of hydraulic/geochemical release ratios and retardation factors. The moments are subsequently decayed for individual nuclides based on their half lives using the formula

$$(\mu_d(t))_i = (\mu(t)) \exp\left(-\frac{\ln 2t}{\omega_i}\right) \tag{4.14}$$

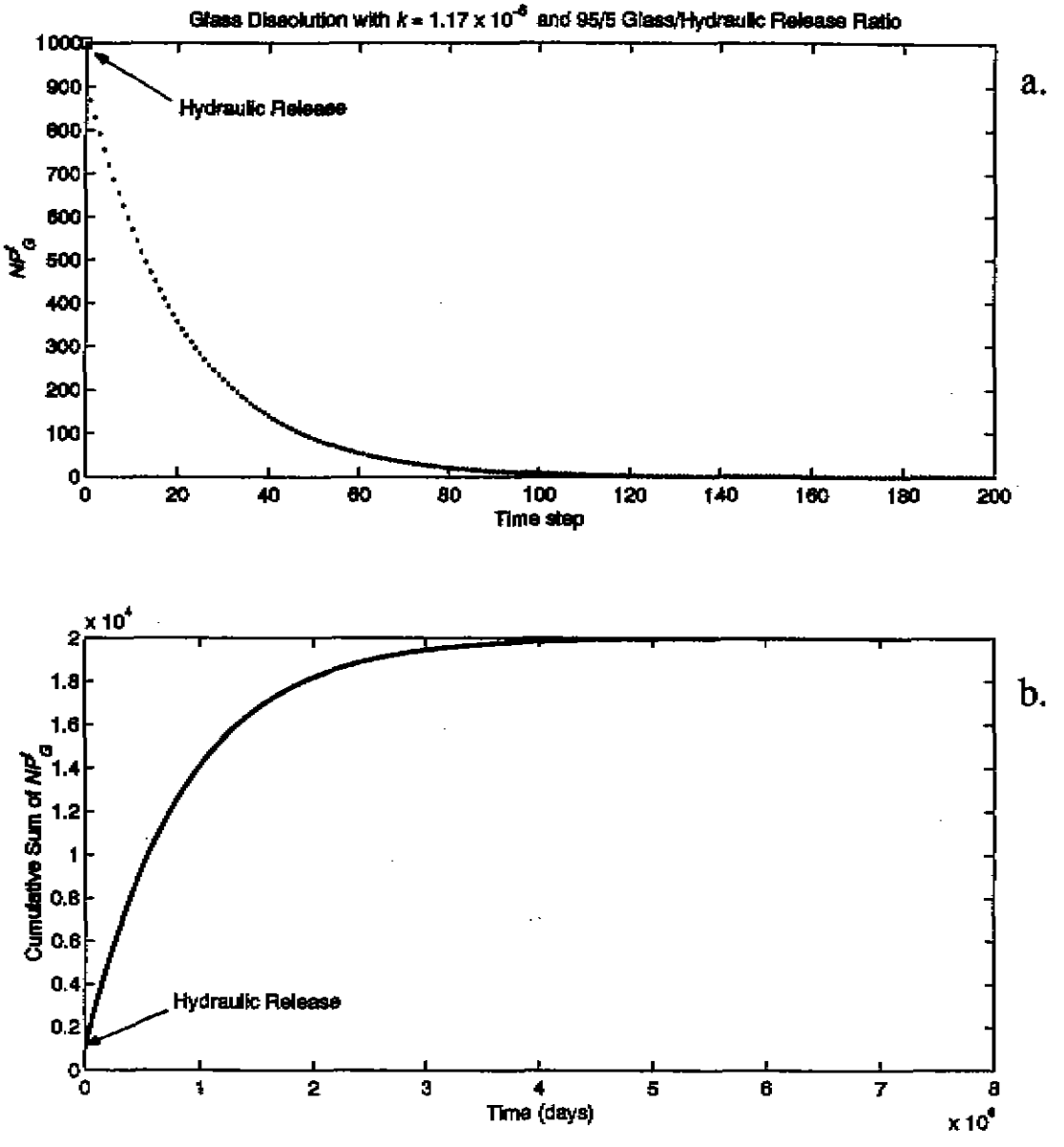

Figure 4.1 Release of particles into the flow field for particle tracking. Radionuclides are apportioned into volatile and surface deposits whose release is controlled by flow through the cavity (hydraulic release), and volume deposits released by a glass dissolution function (slow release). The figures are an example for a radionuclide with 5 percent released hydraulically and 95 percent by glass dissolution. Part "a" depicts the number of particles released at each time step, with the square at time zero indicating 1,000 particles (out of 20,000 total) released hydraulically. The subsequent time-steps show subsequent, declining, volume-released particles. Part "b" is the cumulative sum of particles released for the same situation.

where $(\mu_d(t))_i$ is the decayed moment (mean or standard deviation) for nuclide i at time t, $(\mu(t))$ is the undecayed moment for a certain scenario, ω_i is the half life of nuclide i in days, and t is the time at which moment is computed in days. As will be seen later in the results section, some nuclides with short half lives completely decay before reaching the control plane due to the very low velocities in the areas around the source.

For the general case of the decay of a parent isotope (N_1) to a radioactive daughter (N_2), which decays to a second daughter (N_3) through the final daughter (N_n):

$$N_1 \rightarrow N_2 \rightarrow N_3 \ldots N_n \tag{4.15}$$

the solution, giving the number of atoms of any member of the decay series as a function of time, for the condition that the initial mass of the daughters is zero ($N_2^0 = N_3^0 = \ldots N_n^0 = 0$) has the form (Faure, 1977):

$$N_n = C_1 e^{-\lambda_1 t} + C_2 e^{-\lambda_2 t} \ldots + C_n e^{-\lambda_n t} \tag{4.16}$$

where the coefficients (C_n) are defined as:

$$C_1 = \frac{\lambda_1 \lambda_2 \ldots \lambda_{n-1} N_1^0}{(\lambda_2 - \lambda_1)(\lambda_3 - \lambda_1)\ldots(\lambda_n - \lambda_1)}$$
$$C_2 = \frac{\lambda_1 \lambda_2 \ldots \lambda_{n-1} N_1^0}{(\lambda_1 - \lambda_2)(\lambda_3 - \lambda_2)\ldots(\lambda_n - \lambda_2)} \tag{4.17}$$

and λ_n is the decay rate for radionuclide N_n.

The cases where the initial mass of the daughter radionuclides was not zero were handled separately.

The third type of output from the transport simulations is the contaminant-boundary maps, which delineate the areas of the modeled domain having concentrations of a certain nuclide above the permissible values for drinking water. Unlike the first two outputs, the contaminant boundary computations require the actual value (classified or unclassified) of the initial mass and the inclusion of the decay computations in the transport model. The decayed concentration distribution is obtained at every time step and then the domain cells are binary-coded based on the concentration value as compared to the permissible limit (one if concentration exceeds limit and zero otherwise). The extent of the contaminant boundary is presented for the horizontal plane and the vertical projection of the modeled zone for the entire simulation time.

The above description applies for the porous medium approach. For the analysis of transport in a fractured system, the same non-decayed moments (mass flux and peak concentration mean and variance or standard deviation) are obtained. However, before applying the decay analysis to these moments, matrix diffusion is accounted for using the solute flux analytical solution presented by

Cvetkovic and Dagan (1994) and Cvetkovic *et al.* (1999). The breakthrough curves for total mass flux and for peak concentration after accounting for matrix diffusion can be obtained from

$$Q_{md}(t) = \int_0^\infty \gamma(t,\tau) Q(\tau) d\tau \tag{4.18}$$

where $Q(\tau)$ is the non-decayed mass flux or concentration peak at the control plane at time τ, $Q_{md}(t)$ is the mass flux or concentration peak after accounting for matrix diffusion, and $\gamma(t, \tau)$ is the retention function that incorporate the effect of mass transfer between the fracture and the rock matrix. This retention function is given as (Cvetkovic and Dagan, 1994)

$$\gamma(t,\tau) = H(t-\tau)\frac{\kappa\tau}{2\sqrt{\pi}(t-\tau)^{3/2}}\exp[-\frac{(\kappa\tau)^2}{4(t-\tau)}] \tag{4.19}$$

where H is the dimensionless Heaviside function, τ is the particle travel time (days), t is the time at which the flux is obtained after accounting for matrix diffusion, and κ is the matrix diffusion parameter (days$^{-1/2}$) defined as $\kappa = \frac{\theta_m\sqrt{D_m^* R_m}}{b}$. Here θ_m is the matrix porosity, b is the effective half aperture (m), D_m^* is the effective diffusion coefficient in the rock matrix (m^2/day) and R_m is the dimensionless retardation coefficient in the rock matrix. The main assumptions underlying the derivation of the above analytical retention function are a constant aperture along the streamtube, diffusion only perpendicular to the fracture plane, well-mixed conditions over the cross-sectional area of the fracture, and homogeneous rock matrix with no advection. The radioactive decay can also be incorporated in the retention function. To do so, an additional term exp(-t ln2/ω) should be multiplied by the RHS of the γ expression, with ω being the half-life.

5.0 Flow Model

5.1 Model Grid

The model was designed to simulate flow and transport at a scale intermediate between the scale of the near-field environment and the scale of regional groundwater flow. In addition, the domain was chosen to incorporate as much local data as possible, while allowing simulation of flow and transport beyond the land-withdrawal boundaries, if necessary.

The origin (southwest, lower corner) of the domain is located at 425,000 m North, 188,500 m East (Nevada Central Coordinates), and 290 m above mean sea level. Laterally, the domain encompasses the UC-1 and UC-3 land-withdrawal areas (Figure 5.1) and measures 8 km north to south and 6.5 km east to west. The longer axis is aligned north-south to best accommodate the inferred groundwater flow directions at the site (as discussed below in Section 5.4.2) and the additional data available at the UC-3 land-withdrawal area. The top of the domain is positioned at the ambient water table in the Quaternary alluvium at a depth of 220 m below land surface at UC-1. The domain is 1350 m thick, with the 290-m elevation of the base chosen to cover the vertical flow

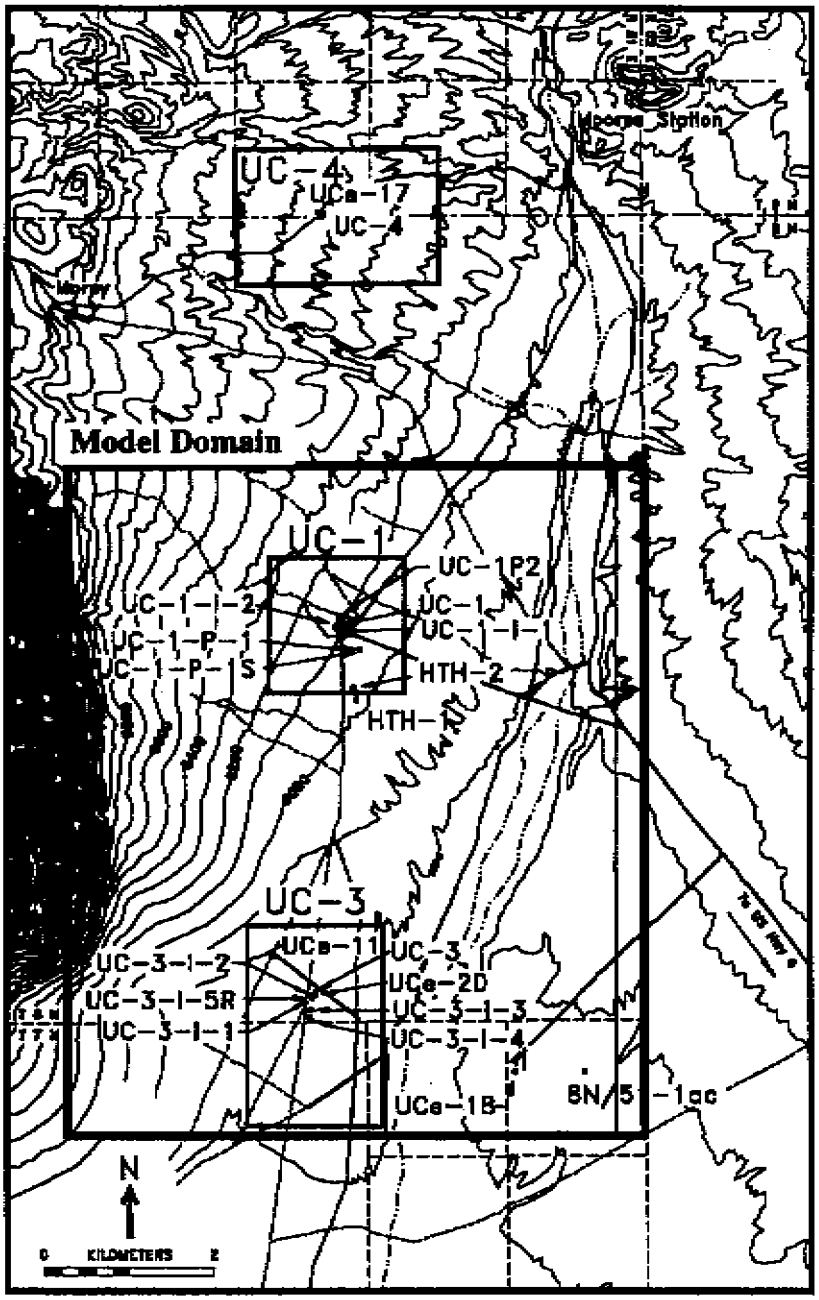

Figure 5.1. Map showing the area of the model domain with respect to the UC-1, UC-3, and UC-4 land-withdrawal boundaries at CNTA. Feet may be converted to meters by multiplying by 0.3048.

components suggested by hydraulic head data. The domain is discretized into a grid of 130 x 160 x 27 (5.616×10^5) cubic cells of length 50 m. The cell size of 50 m was chosen to be consistent with the CNTA hydraulic data, which were collected with straddle packers using a mean test interval of 50 m.

5.2 Representation of Hydrogeologic Categories

The saturated hydrogeologic section was divided among three hydrogeologic categories that were defined based upon lithology, electrical resistivity, and hydraulic conductivity. The categories are Quaternary alluvium, Tertiary volcanics having low hydraulic conductivity, and Tertiary volcanics having high hydraulic conductivity. The geometry of the Quaternary alluvium category was delineated using thicknesses of the alluvium in northern Hot Creek Valley estimated by Healey (1968). The geometries of the Tertiary volcanic categories were delineated, and the two categories distinguished from each other, using borehole lithologic, electrical resistivity, and hydraulic conductivity data. The hydraulic conductivity data are tabulated in Appendix 2, and the lithologic and electrical resistivity logs are presented in Appendix 4.

5.2.1 Quaternary Alluvium

The Quaternary alluvium (Category 1) is found only above the volcanic rocks, therefore, the geometry of the alluvium within the domain is defined by the geometry of the boundary with the underlying Tertiary volcanic rocks. The configuration of this boundary was developed from estimates of the alluvium thickness in northern Hot Creek Valley reported by Healey (1968) using drilling, aeromagnetic, and seismic data. The upper surface of the volcanic rocks for the present study was constructed from elevations of the top of the volcanic section at selected points along Healey's cross sections, from selected other points within the model domain, and from applicable well logs. To conform to the model grid, the surface defined by these scattered points was sampled at 50-m horizontal spacing using a linear interpolation algorithm. The resulting surface is in the configuration of a trough with the deepest portion trending roughly north-south and dipping to the south (Figure 5.2). The depths to the axis of this trough are the most accurately defined, as they are based primarily on well logs. It is important to note that the deepest portion of the overlying alluvium does not directly underlie the axis of Hot Creek Valley, but instead lies to the west almost directly below the UC-1 area. This configuration explains why groundwater flow in this portion of Hot Creek Valley appears to be directed toward the south (along the axis of the "buried valley"), rather than off the Hot Creek Range toward the southeast and the axis of Hot Creek Valley. It should also be noted that the surface of the volcanic rocks extends above the top of the model domain on the western edge and northeastern corner. When extended to land surface, this represents volcanic outcrops at the edges of the Hot Creek Range on the west and the Squaw Hills on the east.

The uncertainty in the estimate of the elevation of the alluvium/volcanic boundary at locations distant from well data points was incorporated as follows: first, the original estimated boundary surface was displaced vertically upward 75 m. This distance was considered to be the maximum uncertainty in either vertical direction from the original estimated boundary (total uncertainty of 150 m). All model cells above the higher boundary surface were considered known to be alluvium and

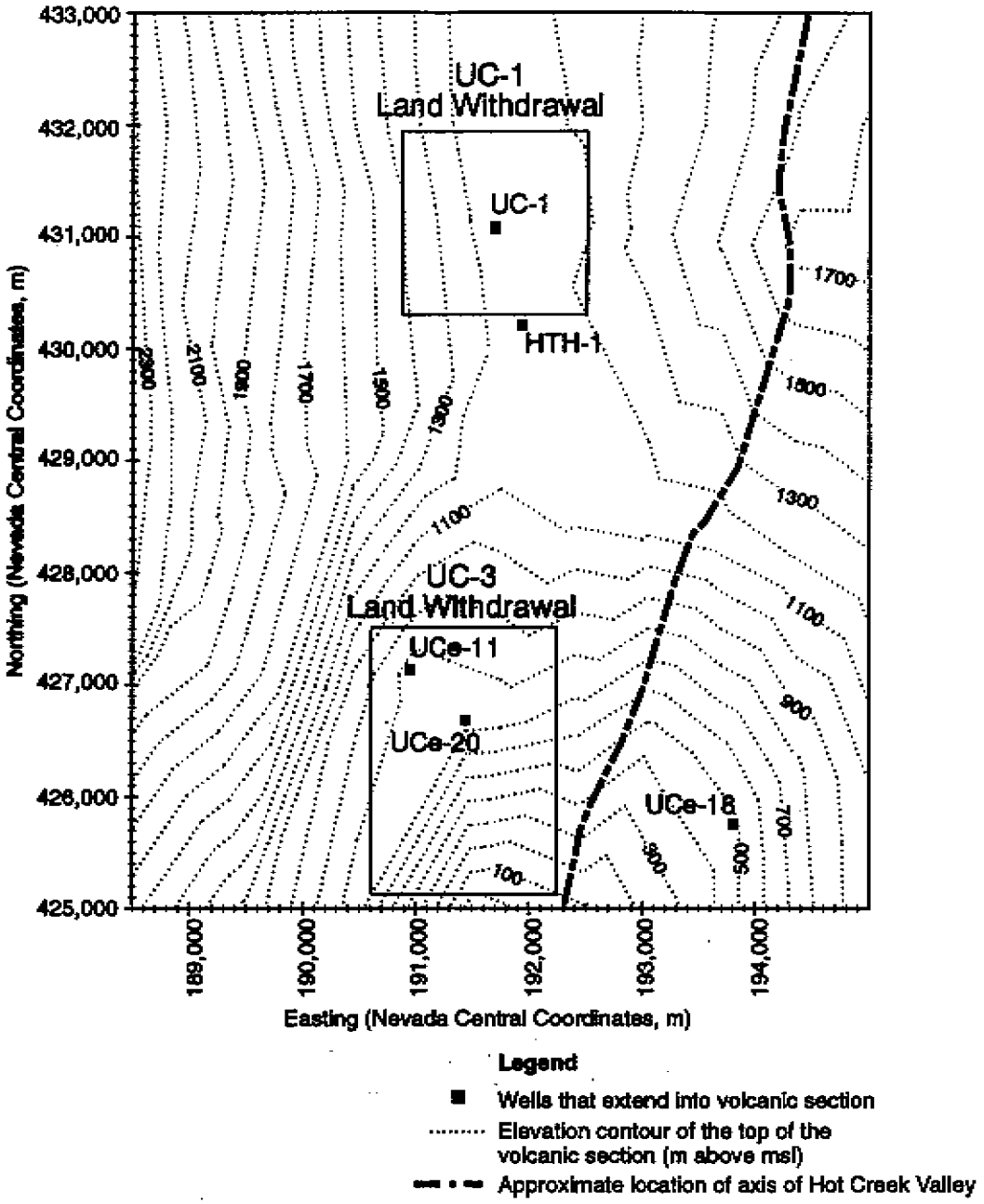

Figure 5.2. Contour map showing the top surface of the Tertiary volcanic section estimated from drilling, aeromagnetic, and seismic data reported by Healey (1968). The trough-shaped surface slopes toward the south and its axis is located to the west of the axis of Hot Creek Valley.

were used as conditioning data for the alluvium category in the SIS simulations. Then, an isotropic spatial correlation model having a correlation length of 150 m was used to simulate alluvium in the 150-m-thick zone of uncertainty centered about the estimated alluvium/volcanic boundary. The lower uncertainty in the elevation of the boundary near well data points was included by assigning cells above the boundary elevation noted on lithologic logs to the alluvium category.

5.2.2 Tertiary Volcanics

The characteristics of ash-flow tuffs that impact their ability to conduct groundwater flow are summarized below from the work of Winograd and Thordarson (1975) at the NTS. Volcanic ash-flow tuffs are deposited as a hot, turbulent mixture of ash, pumice, and gas that is highly fluid and capable of traveling large downslope distances propelled by gravitational forces. As the mixture cools, it comes to rest and is emplaced as a flat sheet, or cooling unit. The well-insulated interior remains hot after emplacement, allowing compaction and welding of mineral grains to increase density and reduce interstitial porosity. Columnar joints also form in the interior due to tensional forces during cooling.

Three distinct zones are found in a complete cooling unit after cooling (Smith, 1960; Ross and Smith, 1961). The nonwelded zone at the upper and lower margins of the cooling unit has the highest interstitial porosity, lowest density, and few fractures. The densely welded zone in the interior has the highest density, lowest interstitial porosity, and many fractures. A partially welded zone lies intermediate between the nonwelded and densely welded zones. Variations in the characteristics of the volcanic eruption and depositional environment may cause large variations in the morphology of ash-flow tuffs, such that the densely welded tuff zone may be absent, or may comprise an entire cooling unit. Although the relation between degree of welding and interstitial porosity is inverse, the relation between degree of welding and hydraulic conductivity is direct (Blankennagel and Weir, 1973; Winograd and Thordarson, 1975). The many joints and fractures in densely welded tuffs lead to high hydraulic conductivity relative to nonwelded tuffs, which have high, but poorly-connected interstitial porosity.

Electrical resistivity logs have been used at the NTS to distinguish rhyolites and densely welded tuffs having high K from nonwelded tuffs having low K (Blankennagel and Weir, 1973; Drellack, 1994; Shirley, 1995). The electrical resistivity tool measures the apparent resistance of a volume of rock to the flow of an electrical current. Most rocks are not good conductors of electricity, so resistivity is a function primarily of the resistance of the pore water (chemical composition) and the volume of water contained in interconnected pores (effective porosity) (Keys, 1990). Pore water is unlikely to have a large impact on differences in apparent resistance of the volcanic rocks at CNTA since the resistance of the volcanic groundwaters is fairly uniform and relatively high due to its low dissolved solids content. The presence of alteration or weathering products such as clays can also be an important influence on apparent resistivity, as well as temperature and pore geometry and morphology (Drellack, 1994). The later two factors have more subtle impacts on apparent resistivity and were not considered in the present study; porosity and clay mineral content were the factors considered most important to the apparent resistivity of volcanic tuffs at CNTA.

Volcanic tuffs having high interstitial porosity, such as air-fall and nonwelded ash-flow tuffs, exhibit low resistivities (Drellack, 1994). Furthermore, the matrices of tuffs altered through zeolitization or argillation are more electrically conductive as a result of the presence of clay minerals and the corresponding cation exchange phenomenon (Carrol, 1990), and therefore also exhibit low resistivity. However, as the degree of welding of a tuff increases, interstitial porosity is

reduced and grain density increases, resulting in a large increase in apparent resistivity. Likewise in rhyolites, very low interstitial porosity and high grain density result in high apparent resistivity. The large difference in the magnitude of the resistivity signal was used in this work to distinguish rhyolites and densely welded tuffs from nonwelded tuffs (including tuffaceous sediments) (Figure 5.3).

The Tertiary volcanic rocks (Categories 2 and 3) include tuffaceous sediments, rhyolites, and nonwelded to densely welded tuffs having various degrees of alteration (argillation, zeolitization). Rocks included in Category 2 are assumed to have lower K than rocks included in Category 3, with the threshold in K that differentiates the categories based on the distribution of K shown in the packer-test data reported by Dinwiddie and Schroder (1971). The $\log_{10} K$ data for the volcanic rocks demonstrate a bimodal distribution with a natural break at a value of about -2.5 (Figure 2.9). Although the number of K measurements produced from the packer tests is sufficient for characterizing the variability of K within each volcanic category, it is not sufficient to describe the variation of K in space. For this we used the correlation between electric and hydrogeologic

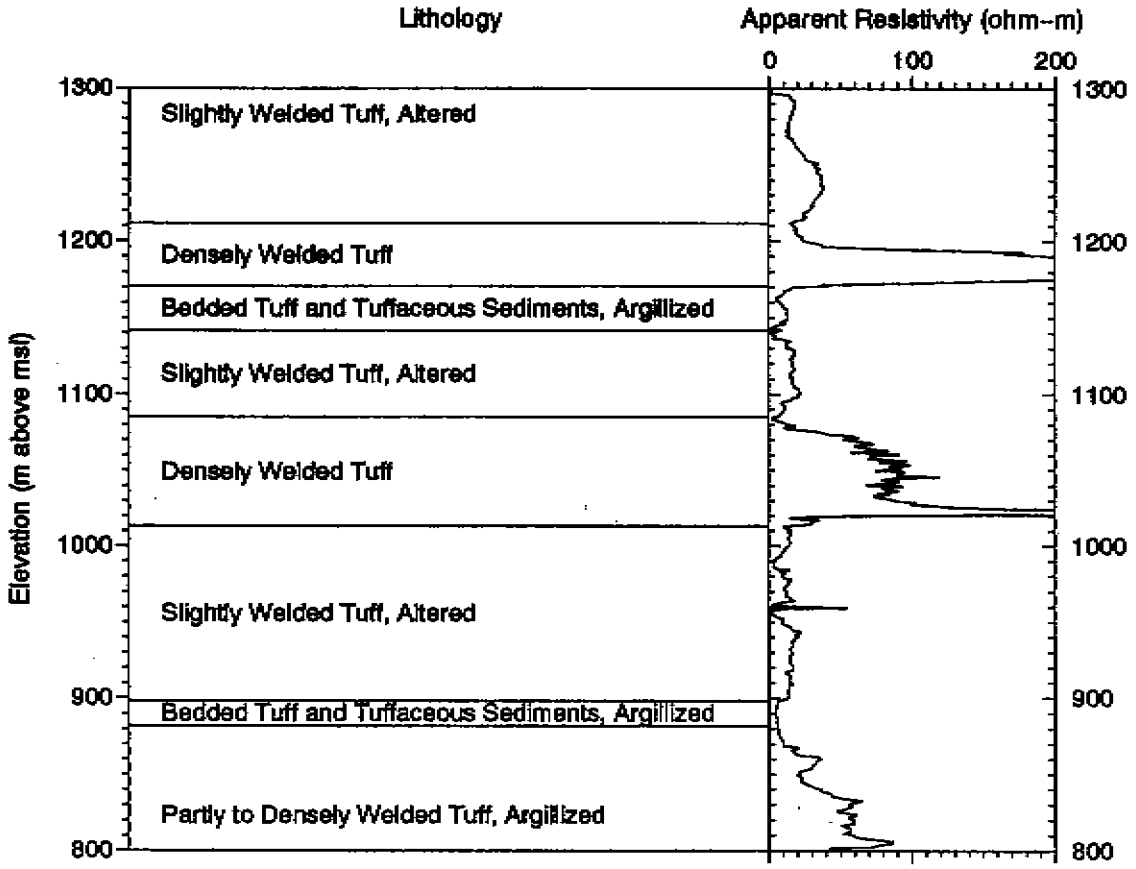

Figure 5.3. Plot of a section of UCe-17 showing the relationship between apparent resistivity and volcanic lithology.

properties of volcanic tuffs at the site to allow the use of electrical resistivity to augment the K data for the purpose of describing the spatial variation of the two categories of hydraulic conductivity.

The lateral log data (Appendix 4), reported on the original logs as apparent resistivity ϱ_a in ohm-m, were averaged over the borehole intervals corresponding to the principal volcanic lithologic units noted at CNTA. Sorting the lithologies as a function of average apparent electrical conductivity shows that the apparent electrical resistivity increases with increasing degree of welding (Figure 5.4).

This relationship demonstrates that hydraulically conductive intervals in the volcanic section at CNTA can be identified in the subsurface by their low electrical conduction (high electrical resistivity), and hydraulically resistant intervals can be identified by their high electrical conduction (low electrical resistivity). Thus, rhyolites and partly to densely welded tuffs are likely to have the highest K values, and tuffaceous sediments, bedded tuffs, and other nonwelded tuffs are most likely to have the lowest K values. This relationship provides a means for using electrical resistivity measurements to differentiate between hydrogeologic Categories 2 and 3 in the volcanic section. The electrical resistivity value of 30 ohm-m represents the threshold dividing the hydraulically conductive densely welded tuffs (Category 3) from the low-K nonwelded tuffs and tuffaceous sediments (Category 2) on borehole logs in the volcanic section. Resistivity values cited in the

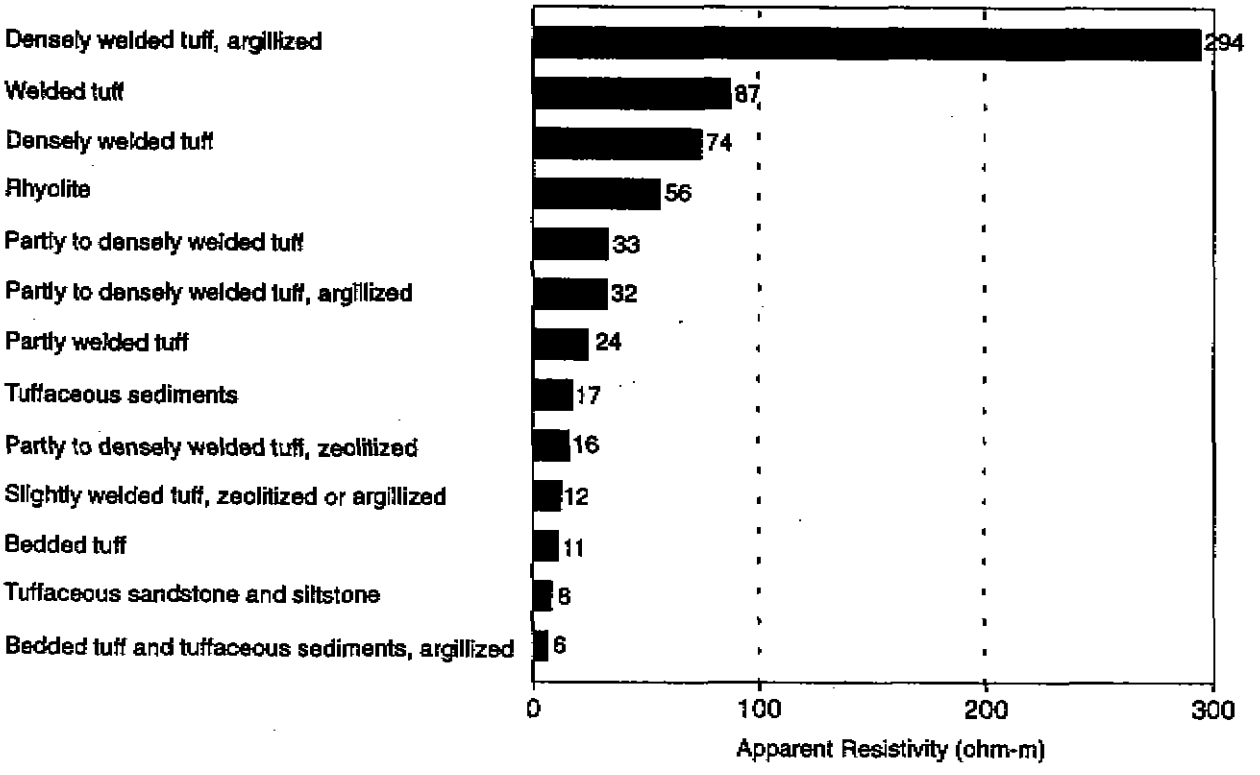

Figure 5.4. Plot of the mean apparent resistivities of selected volcanic lithologic units at CNTA. Densely welded tuffs and rhyolites are more electrically resistive than altered tuffs, bedded tuffs, and tuffaceous sediments. An apparent resistivity threshold of 30 ohm-m separates the two categories.

literature for differentiating between nonwelded tuffs and densely welded tuffs on the NTS include 225 ohm-m (Blankennagel and Weir, 1973), 200 ohm-m (Drellack, 1994), and 300 ohm-m (Shirley, 1995). The lower value used for the present study may result from differences in tool calibration at CNTA and the lower maximum resistivities apparent in the CNTA dataset.

5.2.3 Spatial Analysis

The geometry of Category 1 is predefined by the estimated alluvium/volcanic boundary, as the alluvium is assumed to extend from this surface to the top of the domain. As mentioned above, the uncertainty in the location of this boundary is described by an isotropic spatial correlation model having a correlation length of 150 m.

A description of the spatial correlation structure of Categories 2 and 3 was developed through spatial analysis of the categorical resistivity data in the volcanic section. Theoretical semivariograms were calculated in the vertical direction using the entire CNTA dataset and a resistivity threshold of 30 ohm-m between the volcanic categories, using the GSLIB geostatistical software library, second edition (Deutsch and Journel, 1998). A nested semivariogram incorporating exponential and nugget-effect models was selected to represent the experimental semivariogram (Figure 5.5). Unfortunately, the very large horizontal spacing of wells prevented calculation of horizontal semivariograms from the CNTA data, so the horizontal correlation length for the volcanic-rock category was estimated using a 10:1 horizontal to vertical anisotropy ratio. The value of 3325 m maximizes the horizontal continuity of the welded tuff category, the assumed primary pathway for

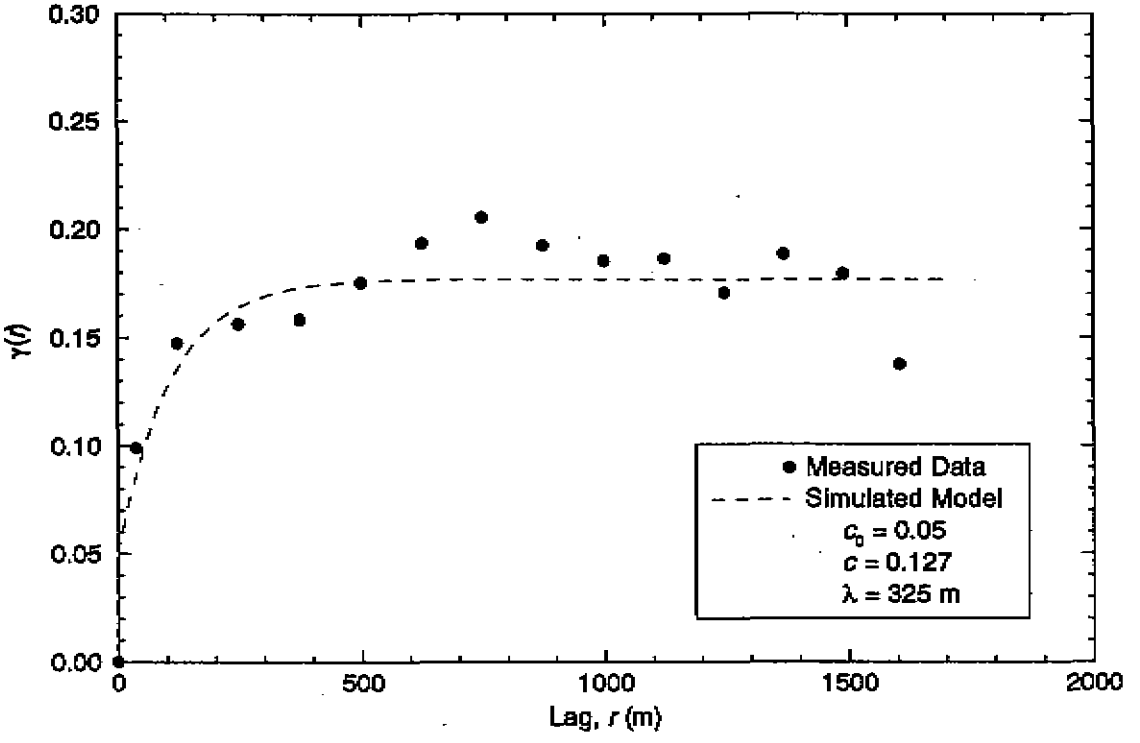

Figure 5.5. Plot of the vertical semivariograms of the categorical resistivity data for Categories 2 and 3.

groundwater flow and transport, while remaining within the constraints imposed by the size of the model domain.

Little evidence concerning the structural attitude of the volcanic categories was available, other than electric log correlations between UCe-11 and UCe-20 that suggest a very gentle southeasterly component of dip in the tuffaceous sediments (Barnes and Hoover, 1968). The categorical semivariograms were aligned with the coordinate directions because the full orientation of this structure could not be determined from only two wells, and data from other local wells do not suggest strong dip in the volcanic section.

5.2.4 Simulation of Maps

Multiple realizations of three-dimensional maps describing the configuration and distribution of the three hydrogeologic categories in the model domain were generated using the SISIM code (GSLIB Version 2; Deutsch and Journel, 1998). The values of the parameters used for these simulations are listed in Table 5.1.

Table 5.1. Values of Parameters used to Generate Maps of Hydrogeologic Categories.

Parameter	Category 1 Quaternary Alluvium	Category 2 Tertiary Volcanics, Low-*K*	Category 3 Tertiary Volcanics, High-*K*
Category Scheme			
Threshold, z_c (ohm-m)	--	30	30
Simulation PDF, p_{zc}	0.31	0.42	0.27
Category Semivariograms			
Type	Exponential	Exponential, Nugget-Effect	Exponential, Nugget-Effect
Nugget, C_o	0.0	0.05	0.05
Sill, c	0.01	0.127	0.127
Correlation length, λ_{xy} (m)	150	3325	3325
Correlation length, λ_z (m)	150	325	325

The SIS simulations were conditioned using the estimated alluvium/volcanic boundary, and categorical resistivity data and lithologic data. The Category 1 conditioning dataset was developed in a way that would produce SIS simulations that incorporate both the known borehole data and the uncertainty in the elevation of the boundary away from the known data points. The Category 1 conditioning dataset includes the entire volume of alluvium 75 m above the estimated alluvium/volcanic boundary, and the cells coincident with intervals of alluvium known from borehole lithologic data. The latter data included only those cells in the 75-m interval from the elevation of the estimated boundary to the elevation of the known boundary. Cells that lie outside the Category 1 conditioning set, but above the estimated alluvium/volcanic boundary, were simulated according to the spatial correlation models of all three categories. However, these cells were predominantly simulated as Category 1 due to their proximity to the Class 1 conditioning data.

Categorical resistivity data, augmented by lithologic data in some locations, were used to condition the SIS simulations in the volcanic section (Figure 5.6). The boreholes in and adjacent to the UC-1 land-withdrawal area (UC-1, UC-1-P-1S, HTH-1, UC-1-I-1) extend no more than 180 m below the working point, so much of the model below the source is unconditioned. Boreholes in and near the UC-3 land-withdrawal area (UCe-11, UCe-18, UCe-20, UC-3-I-1) extend close to or below the bottom of the domain. As described above, intervals of the resistivity logs having values below the 30-ohm-m threshold were assumed to indicate Category 2, while intervals having values above 30 ohm-m were assumed to indicate Category 3. The 1-m vertical resolution of the logs was upscaled to the 50-m resolution of the model by assigning the entire model cell to Category 2 if 50 percent or more of the corresponding 50-m interval of the log fell below the 30-ohm-m threshold. Both lithologic and resistivity data indicate that the majority of the volcanic section in the domain is comprised of tuffaceous sediments and nonwelded tuffs, and is therefore simulated as Category 2.

Values of the probability distribution functions (PDFs) for input to the SIS were selected to produce realizations having the appropriate relative proportions of the three categories. However, the values of the input PDFs were adjusted from the values of the desired simulation PDFs to account for the fact that virtually all of Category 1 consists of conditioning data. The desired volume of Category 1 was 31 percent of the domain volume, based on the percentage of alluvium corresponding to the estimated alluvium/volcanic boundary. The value of the input PDF for

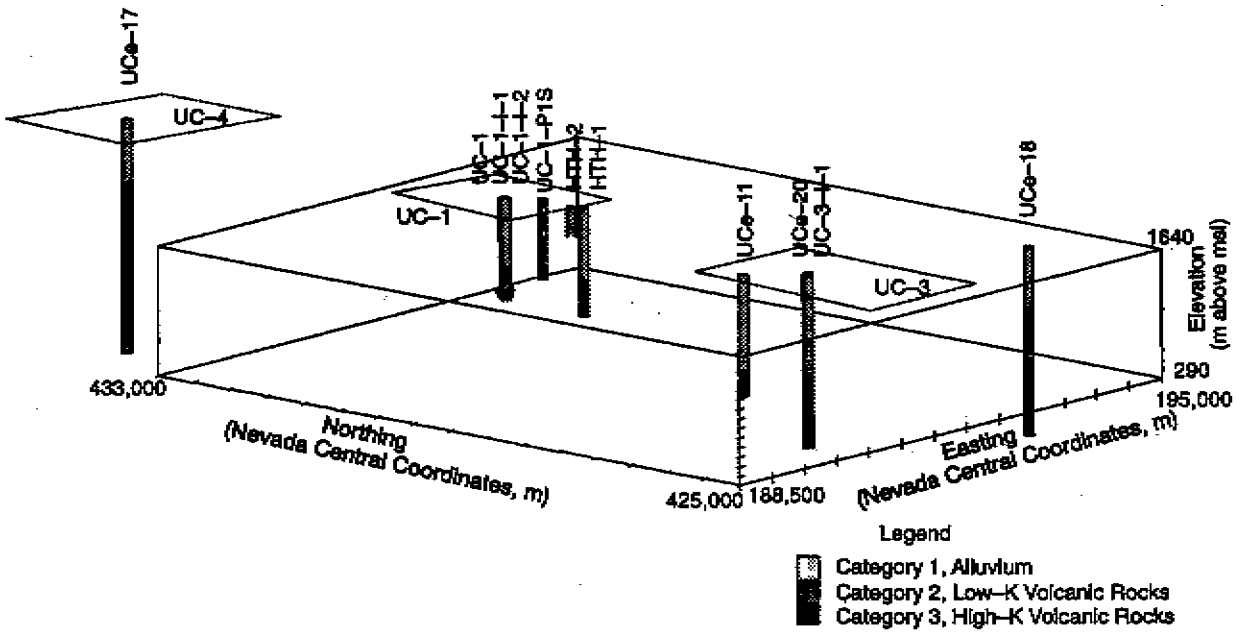

Figure 5.6. Diagram showing the hydrogeologic categories determined using lithologic, electrical resistivity, and hydraulic conductivity data from CNTA boreholes in northern Hot Creek Valley. The data suggest that the majority of the volcanic section within the model domain belongs to Category 2. Although the full extents of the boreholes are shown, only the portions within the model domain are used for conditioning the SIS simulations.

Category 1 was chosen to be just large enough to allow simulation of Category 1 in the uncertain boundary zone, while being small enough to prevent simulation of Category 1 within the volcanic section, a geologically unrealistic outcome.

The target values of the simulation PDFs for Categories 2 and 3 (61 and 39 percent, respectively) are the relative volume percentages of each category in the volcanic section, as indicated by the resistivity logs, and represent a compromise between the values determined from the entire CNTA dataset and the values determined from wells in and near the UC-1, UC-3, and UC-4 land-withdrawal areas. In the entire dataset, the volcanic rocks are evenly divided between Category 2 and Category 3, while the local dataset is dominated by rocks comprising Category 2 (73 percent of the volcanic section penetrated by boreholes). Well UCe-17 represents an approximate mean case between these end points: 59 percent of the penetrated volcanic section is Category 2. Unfortunately, drilling at UC-1 did not extend far below the depth of the working point so the lithology at greater depths is largely unknown. We assumed that the pattern of interbedded welded and nonwelded tuffs observed in the entire CNTA dataset and at UCe-17 is also present to some extent in the volcanic section below the depth of the working point at UC-1. The presence of welded tuff below this depth was also suggested by Banister and Johnson (p. A-13, 1969).

The maps of hydrogeologic categories generated using SIS represent the geometry of the hydrogeologic units most important to groundwater flow and contaminant transport at CNTA. A three-dimensional perspective of a single realization that is representative of the ensemble of generated maps is shown in Figure 5.7. The white circle marks the approximate location and size of the test cavity; it should be noted that cells in the vicinity of the cavity were not conditioned nor

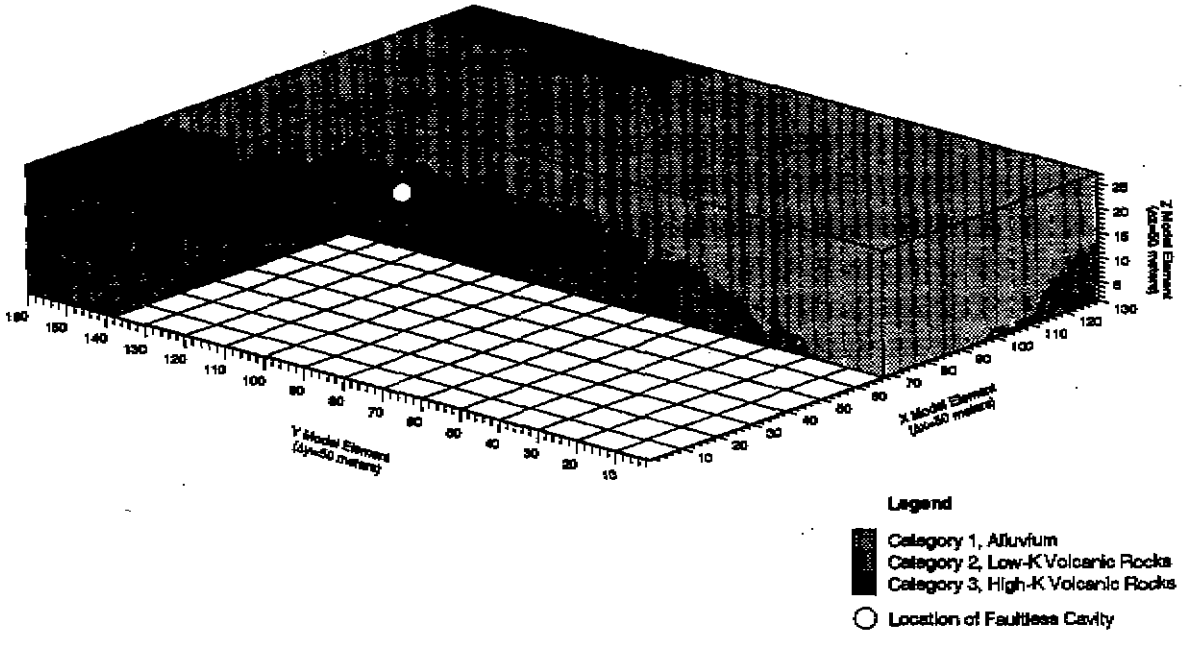

Figure 5.7. Diagram showing a single realization of the three hydrogeologic categories. A section of the volume closest to the viewer is removed to show the distribution of categories simulated near the Faultless cavity.

simulated to account for blast-induced changes to the host rocks. Cells having the lightest shade represent the alluvium of Category 1, while cells having the darker shades represent volcanic rocks of Categories 2 and 3.

The map shows the general configuration of the alluvium/volcanic boundary that slopes to the east and south away from the working point. Also evident is the absence of continuous zones of high-K volcanic rocks simulated laterally adjacent to and directly below the working point, which reflects the general absence of densely welded tuffs observed in boreholes in the vicinity of UC-1. An implication of the simulation of predominantly low-K volcanic rocks (Category 2) around the working point is that simulated groundwater velocities at the source will be very low.

5.3 Representation of Hydraulic Conductivity

5.3.1 Hydraulic Conductivity Field Data

Hydraulic conductivities were simulated within each hydrogeologic category in accordance with the statistics of K in that category as determined from the straddle packer test results reported by Dinwiddie and Schroder (1971) and tabulated in Appendix 2. Not incorporated in the statistical analysis were the K values estimated from the injection tests in UC-1-P-2SR and the infilling of the cavity and chimney. The analyses of these tests required substantial assumptions about the geometry of the well and surrounding environment, therefore including a great deal of uncertainty. These tests also represent flow at a much larger scale than that represented by the packer tests and the discretization of the model. In any case, simulation of K near the source is conditioned by data from HTH-1 and with one exception, these all exceed the K estimates from UC-1-P-2SR. The K values estimated from the pumping test in HTH-1 were also not incorporated. Though consistent with the range of data from the packer tests, the pumping test data were obtained from two well intervals used for packer testing and were considered redundant for the purposes of the statistical and spatial analyses. There was also a need to be consistent in utilizing the entire packer test dataset, rather than only portions of it.

Of the 58 total K values, 18 were denoted by Dinwiddie and Schroder as being "estimated." Though the authors do not discuss the specific conditions leading to these estimates, they appear to have resulted from various difficulties in interpreting the results, particularly during tests with very long recovery times. For completeness, the estimated values were included in the present study. Including the estimated values with the measured values increased the variances of the K distribution for Categories 1 and 2, slightly increased the mean K for Category 3, and slightly reduced the mean K for Categories 1 and 2 (Appendix 2). With the exception of the two slightly reduced means, inclusion of the estimated values resulted in K distributions that incorporate greater variability and thus will produce a greater dispersive effect in the simulations of contaminant transport.

The statistics of the K data were based on nine measurements in Category 1, 23 measurements in Category 2, and 26 measurements in Category 3. All measurements within the alluvium were made near Faultless; six were obtained from HTH-1 and three from UCe-18 and UCe-20, and thus have direct bearing on the description of K for transport modeling from Faultless. As shown in

Section 2.4.1, these data indicate declining values with increasing depth, possibly related to the increasing induration with increasing depth noted in the lithologic descriptions of the UC-1 emplacement and instrument holes (Hoover, 1968b). This trend was preserved in the vicinity of wells having *K* straddle-packer tests by virtue of their use as conditioning data for simulation of the *K* fields, a trend of reduced *K* with increasing depth was not separately superimposed throughout the domain. Twenty three of the 49 *K* values in the volcanic section were obtained from wells in Hot Creek Valley, and three of those are from HTH-1. Values of *K* in the volcanic section do not exhibit a strong trend with respect to depth. Figure 5.8 shows the statistical distribution of *K* values for the three hydrogeologic categories as simulated by SGS, and can be compared to Figure 2.9, which shows the distribution of the measured *K* values. As discussed previously, *K* in the tuffaceous sediments is relatively low, corresponding with induration, alteration (primarily zeolitization), high percentages of clay matrices, and interbedded, reworked and non-welded ash-flow tuffs.

5.3.2 Spatial Analysis

The spatial correlation structure of *K* within each hydrogeologic category was described where possible using a spatial analysis of the full *K* dataset. Unfortunately, issues of data spacing prevented a full description of the correlation structure using site data, and most values of correlation length had to be estimated using accepted practices and literature sources. The GSLIB geostatistical

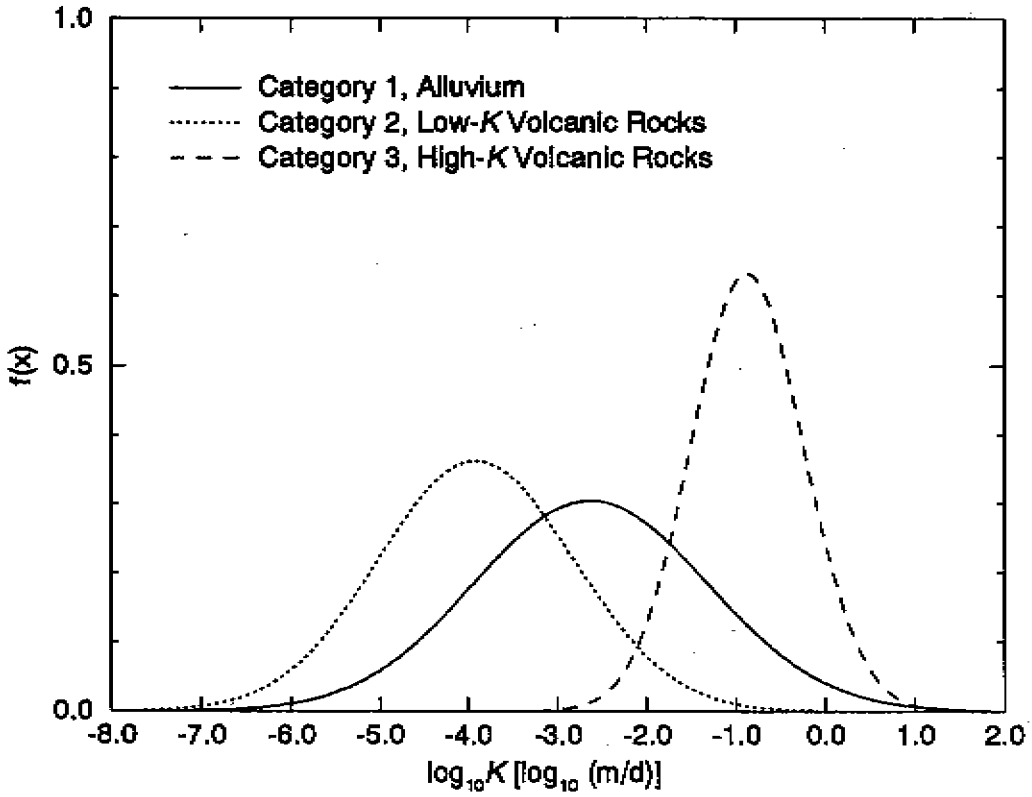

Figure 5.8. Theoretical distribution of hydraulic conductivity for the three hydrogeologic categories as simulated by SGS.

software library, second edition (Deutsch and Journel, 1998) was used for the analysis. The statistics of the K data and the spatial correlation models used in the SGS simulations are listed in Table 5.2.

Table 5.2. Values of Parameters used to Generate Maps of Hydraulic Conductivity.

Parameter	Category 1 Quaternary Alluvium	Category 2 Tertiary Volcanics, Low-K	Category 3 Tertiary Volcanics, High-K
Category Statistics			
Mean, $\mu \log_{10} K$ ($\log_{10}$ [m/d])	-2.6	-3.9	-0.87
Variance, $\sigma^2 \log_{10} K$	1.7	1.2	0.40
Category Semivariograms			
Type	Exponential	Exponential, Nugget	Exponential
Nugget, C_0	0.0	0.6	0.0
Sill, c	1.7	1.2	0.40
Correlation length, λ_{xy}, (m)	800	800	1000
Correlation length, λ_z (m)	50	50	50

The sparsity of data in Category 1 prevented estimation of correlation scales in any coordinate direction. Instead, the correlation length of 800 m in the horizontal direction, λ_{xy}, was based on values from similar alluvial-fan aquifers. Estimated horizontal correlation lengths ranging from 767 to 1,023 m were reported by Hoeksema and Kitanidis (1985) using data from Eagle Valley, Nevada (approximately 300 km west of CNTA) (data reported by Arteaga, 1980). Johnson and Dreiss (1989) estimated maximum horizontal correlation lengths ranging from 620 m along the dip direction to 1800 m along the strike direction for an alluvial-fan aquifer in Santa Clara Valley, California.

The correlation length in the vertical direction, λ_z in Category 1, was chosen to be the smallest fraction of the 800-m-value assumed for λ_{xy} possible given the cell size of 50 m. λ_z was initially chosen to be 150 m, or three times the cell size, to simulate vertical correlation of K above the 50-m scale of the model cells. However, during calibration of the flow model, λ_z was reduced to 50 m, which caused the vertical spatial distribution of K to be random above the 50-m scale. This anisotropic model of spatial correlation has a horizontal-to-vertical anisotropy ratio of 16:1. Horizontal-to-vertical anisotropy ratios reported in the literature for unconsolidated aquifers range from 7:1 to 14:1 (Hess *et al.*, 1992), 23:1 (Sudicky, 1986), and 88:1 to 257:1 (Johnson and Dreiss, 1989).

As with Category 1, the horizontal sparsity of K data in Categories 2 and 3 prevented direct estimation of λ_{xy} from the site data. The λ_{xy} value of 800 m used for Category 1 was also used for Category 2 because depositional and textural characteristics of the tuffaceous sediments included in Category 2 are similar to the characteristics of the alluvium of Category 1. The λ_{xy} value of 1,000 m used for Category 3 is consistent with the observations of Barnes and Hoover (1968) and Hoover (1968a) who noted that electric and lithologic log correlations are present in the volcanic section

between wells located at distances of up to 915 m, but not present between wells located at distances greater than 2500 m.

The vertical correlation lengths for Categories 2 and 3 were based on spatial analysis of the K data from the CNTA packer tests, using the centers of the packed intervals as the locations of the measurements. Vertical semivariogram models using correlation lengths between 50 and 150 m best fit field data (Figure 5.9). Calibration of the flow model was improved with the 50-m correlation length, so this was used to simulate the base-case K maps and resulted in a horizontal-to-vertical anisotropy ratio of 16:1 for Category 2 and 20:1 for Category 3.

The choice of 50 m for λ_z causes the variability in the simulated K fields to be vertically uncorrelated, since there can be no correlation at a scale less than the model cell size. If vertical correlation exists below this scale at the site, it was not captured in the straddle packer tests, which had a mean packer interval of 50 m. Recent research by Purvance (1999) suggests that borehole resistivity logs may be useful for estimating the vertical correlation of K at scales much less than 50 m. Applying these techniques at CNTA might allow better resolution of the vertical correlation structure of K. However, if λ_z is found to be less than 50 m, the model grid will need to be reduced to a much finer resolution to accurately simulate the vertical variability at this scale. This may also require reducing the horizontal size of the model to prevent a much larger number of nodes and to maintain computational efficiency. Higher vertical correlation increases the length of vertically connected high-K zones, thereby increasing flow and transport in the vertical direction. The effect of a higher vertical correlation of K on radionuclide migration was tested as a sensitivity case in the current model.

5.3.3 Simulation of Maps

Multiple realizations of three-dimensional maps describing the configuration and distribution of hydraulic conductivity in the model domain were generated using the SGSIM code (GSLIB Version 2; Deutsch and Journel, 1998). The normally distributed values of the simulation variable $Z(x)$ generated by SGSIM were then transformed to a $\log_{10}$-normal distribution $K(x)$ using Equation (4.6). The values of the parameters used for the simulations are listed in Table 5.2. The simulations were conditioned using the available K data from packer tests at HTH-1, UCe-18, and UCe-20.

A three-dimensional perspective of a single realization that is representative of the ensemble of generated maps is shown in Figure 5.10. The white circle marks the approximate location and size of the test cavity, and it should be noted that cells in the vicinity of the cavity were not conditioned nor simulated to account for blast-induced changes to values or distribution of hydraulic conductivity. The realization of $K(x)$ shown in Figure 5.10 was generated using the realization of hydrogeologic categories shown in Figure 5.7, and the correspondence between $K(x)$ and category is clear. For example, zones of high K simulated near the base of the domain correspond to zones of Category 3 simulated at that location.

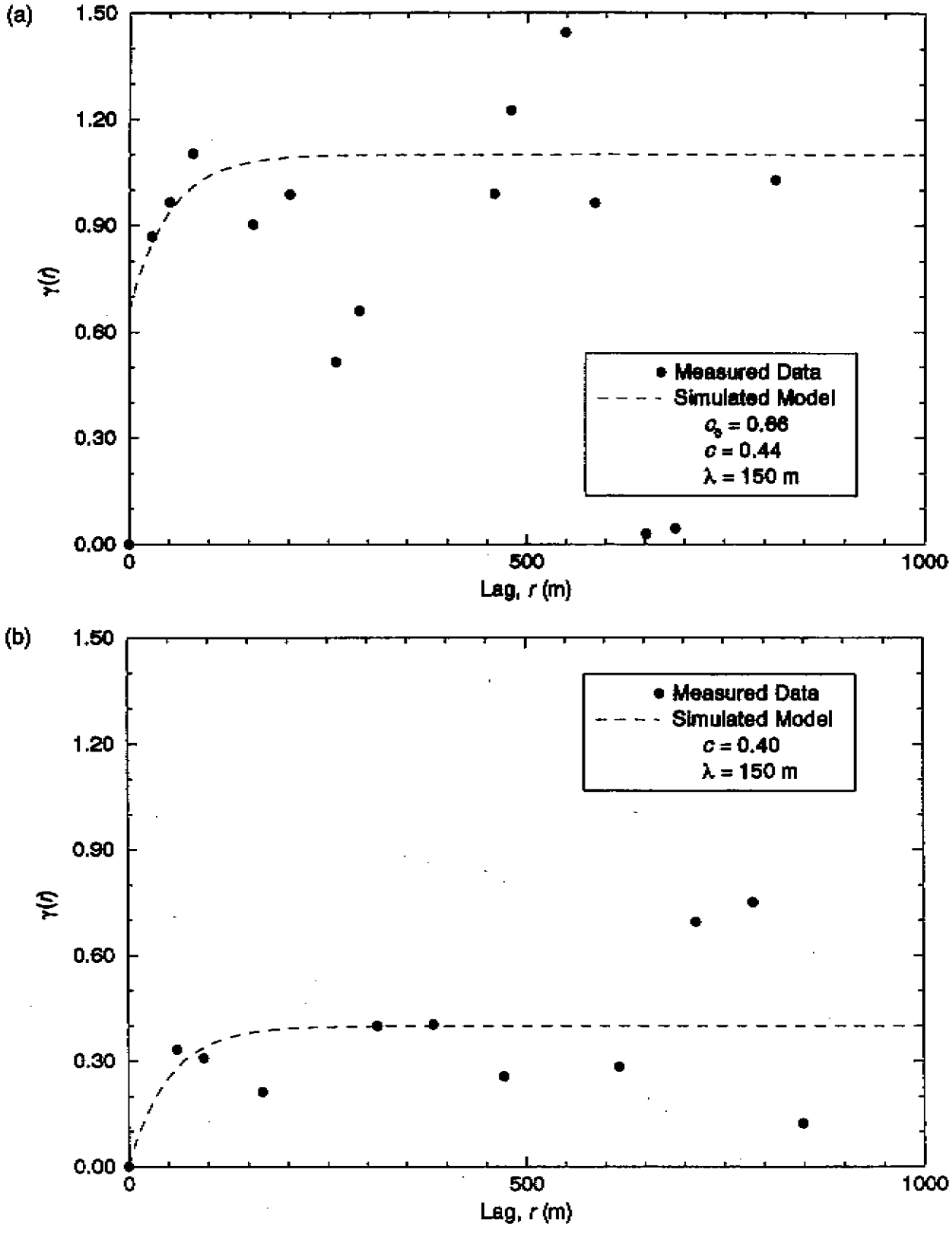

Figure 5.9. Plots of the vertical semivariograms of the hydraulic conductivity data for (a) Category 2, and (b) Category 3.

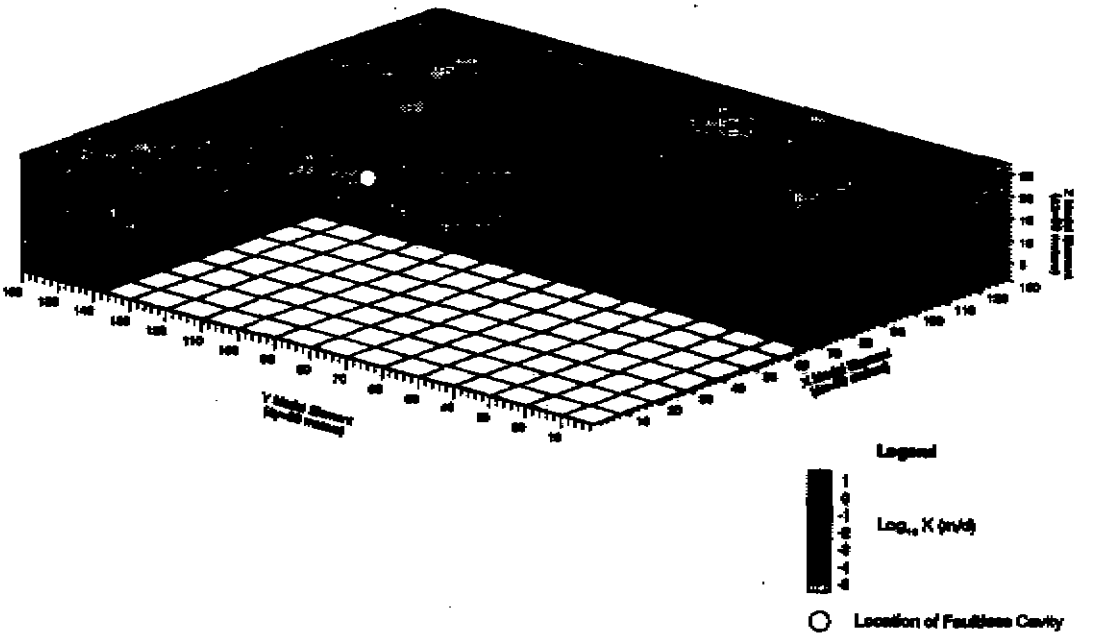

Figure 5.10. Diagram showing a single realization of the distribution of hydraulic conductivity, based on the realization of hydrogeologic categories shown in Figure 5.7. A section of the volume closest to the viewer is removed to show the distribution of *K* simulated near the Faultless cavity.

5.4 Representation of Flow Field

5.4.1 Head Distribution

As shown in the head profiles presented earlier in Figure 2.6, measurements of head were generally located at or near the elevation of the top boundary of the model, and these values were used to represent the heads at this elevation. Measurements of head at greater depths were often at lower elevations than the base of the model domain, so the values at the base elevation were interpolated using linear trends in head from the top to an average of the measurements near the base. These estimates introduce a degree of uncertainty to the assumed head distribution within the model.

The horizontal gradients of hydraulic head at the top and base of the domain were estimated by solving the "three-point" problem using the head values from HTH-1, UCe-18, and UCe-20. These are the three wells nearest to UC-1, and thus best exemplify the head distribution driving advective transport in the vicinity of Faultless. The other wells in northern Hot Creek Valley are at much greater distances from Faultless and are located in different hydrogeologic settings. This analysis produced a gradient of 4.4×10^{-3} oriented 221° from north at the top, and a gradient of 4.8×10^{-3} oriented 321° from north at the base. These estimates were then compared to gradients estimated by kriging the values of the estimated heads at all seven wells in northern Hot Creek Valley to confirm that the local gradients were consistent with the head distributions in the larger area (Figures 5.11 and 5.12). First, it should be noted that the distributions of head in the alluvium and volcanics produced by kriging compare favorably with the distributions of head shown on maps developed by Dinwiddie and Schroder (1971) in the same geologic units (see Figure 2.5). The maps

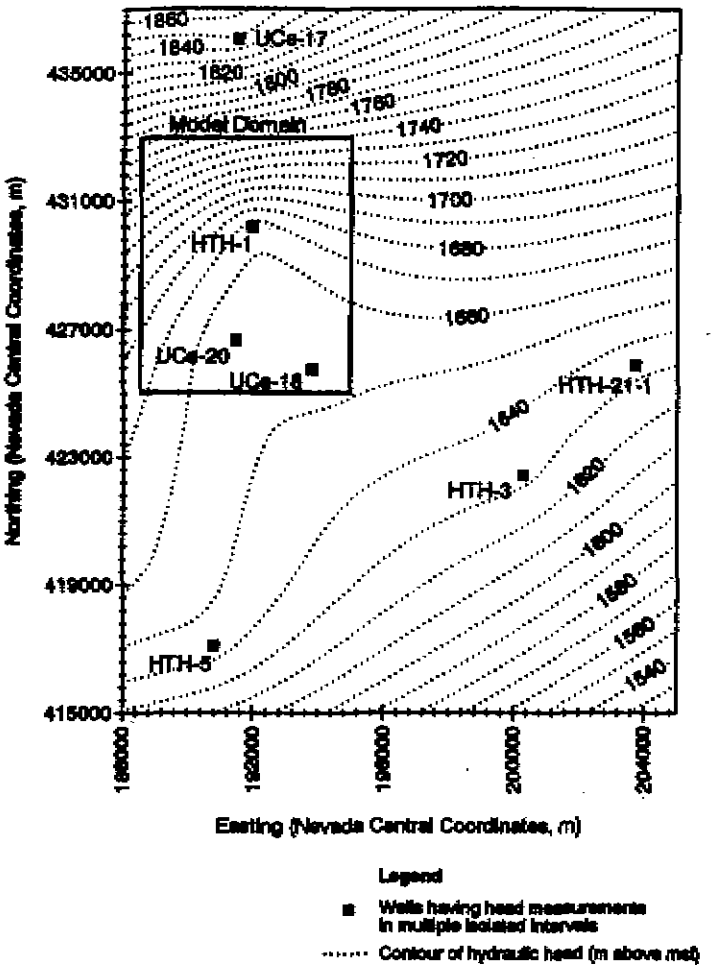

Figure 5.11. Contour map showing results of kriging hydraulic heads estimated at the elevation of the top of the model domain using the wells shown. A southward direction of groundwater flow is suggested near HTH-1. Contour interval is 10 m.

produced in both the earlier study and the present study indicate that near UC-1, a horizontal gradient of flow is directed toward the south at the top of the model domain, which is, as discussed previously, consistent with the geometry of the alluvium in northern Hot Creek Valley. At the base of the domain, the data suggest a horizontal gradient directed toward the northeast, with a component directed toward the north in the vicinity of UC-1. Northeastward-directed flow in the volcanic section toward Railroad Valley is suggested by Dinwiddie and Schroder (1971), while Prudic *et al.* (1993) indicate a more eastward direction of flow from Hot Creek Valley toward Railroad Valley, though they included flow in the deeper volcanic units and underlying carbonates. The more northward-directed flow suggested at the elevation of the model base appears to reflect head conditions at a vertical position between the regional flow in the deeper volcanic section (with a coincident upward component) and local basin flow in the alluvium. Using the maps of kriged heads and an area within 2 km of the HTH-1 data point, the gradient at the domain top was estimated to have a magnitude of 4.4×10^{-3} and an orientation almost directly south. Similarly, the gradient at the base was estimated to have a magnitude of 4.6×10^{-3} and an orientation to the north-northeast. The similarity

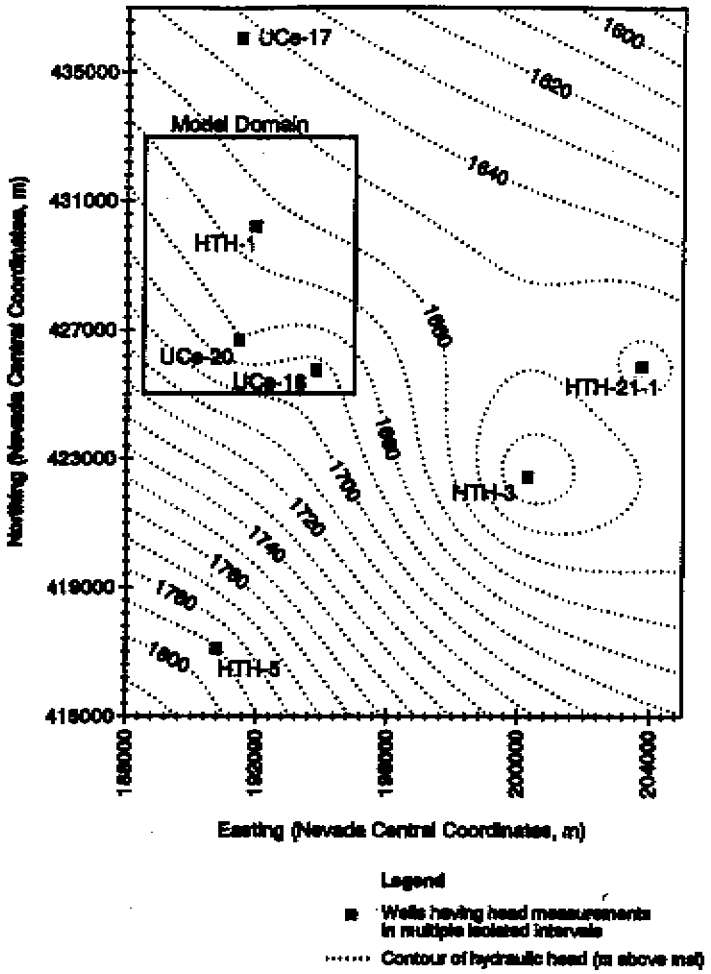

Figure 5.12. Contour map showing results of kriging hydraulic heads estimated at the elevation of the base of the model domain using the wells shown. A north-northeast direction of groundwater flow is suggested near HTH-1. Contour interval is 10 m.

between these values and the values estimated from the three wells alone provided confirmation that the gradients used in the model generally agree with regional trends.

5.4.2 Boundary Conditions

The three-dimensional head configuration described above results in potential components of flow in both the horizontal and vertical directions. To simulate this complicated pattern of flow, specified-head boundary conditions consistent with the ambient hydraulic gradients and measured heads were prescribed at the north, south, and bottom faces. Heads and gradients observed in northern Hot Creek Valley (particularly in wells at the UC-1, UC-3, and UC-4 land withdrawal areas) were given the greatest weight during this process, as heads in other wells are influenced by different hydrogeologic conditions. Thus, boundary heads were specified so that the mean horizontal hydraulic gradients were oriented in the north-south direction and parallel to the east-west faces of the model, which were specified as no-flow boundaries. Configuration of the head boundaries in this way results in prescribed mean flow directions at the top and bottom of the model

that differ slightly from the directions suggested by wells outside the model domain, but that are consistent with heads in wells inside the model domain. An alternative would have been to prescribe the heads on all four sides (and the base) thereby allowing mean flow in directions other than parallel to the model grid. This option was considered to overconstrain the flow simulations, especially considering the limited head data available at the boundaries, and was not implemented. Furthermore, the simulated transport distances presented in this report are well short of the model boundaries, such that slightly modifying the directions of mean horizontal gradients would have only minor effects on pathways of migration. Although the alluvial aquifer is considered to be unconfined, the top face was specified as a no-flow boundary, causing the aquifer to be simulated as confined. This was justified because as a steady state model there were no storage effects, and because the change in head across the top was small (less than three percent) compared to the domain thickness.

The heads at the upper and lower edges of the north and south specified-head boundaries were extrapolated from HTH-1 using the gradients determined from HTH-1, UCe-18, and UCe-20. The initial estimates of the heads in the remainder of the cells comprising the three specified-head boundaries were determined using linear interpolation. These boundary heads were then adjusted to reduce the imposed vertical gradients, and consequent vertical flow, in cells just below the upper boundary. To accomplish this, the heads in the three rows of cells below the top row of cells of the north and south specified-head boundaries were adjusted to obtain vertical gradients equal to five percent of the overall vertical gradient at each boundary. The resulting heads were smoothed using a moving average to obtain the distribution of heads on the specified-head boundaries shown in Figure 5.13. The configuration of heads on the boundaries allowed flow to freely enter or exit the domain at the north, south, and bottom faces in response to both horizontal and vertical hydraulic gradients. Flow did not cross the east, west, and top faces because they were treated as no-flow boundaries.

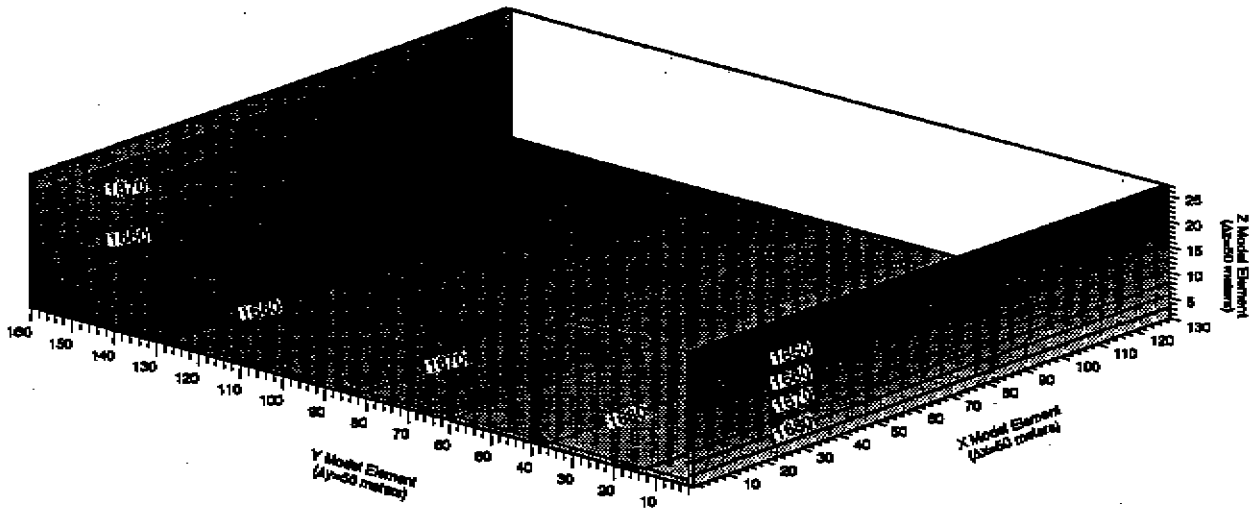

Figure 5.13. Contour plot showing the distribution of hydraulic heads assigned to cells on the specified-head boundaries of the groundwater flow model. Contour interval is 5 m.

Areally distributed recharge was not applied to the top boundary in the base-case model, though the effect of recharge at higher elevations was included by implication as the strong vertically downward hydraulic gradient at the northern edge of the domain. The effects of applying recharge to the top boundary were investigated during model development. In the absence of site data, an annual precipitation rate of 0.15 m (6 inches) was assumed for the UC- 1 area, based on the estimate of precipitation for elevations less than 2134 m in Hot Creek Valley (Rush and Everett, 1966). Although they suggested that no recharge occurs below this elevation, we assumed that the recharge rate is three percent of the precipitation rate, a figure suggested by Prudic *et al.* (1993) as representing a general percentage of precipitation that becomes recharge in aquifers in the Great Basin Province. Application of the resultant recharge rate of 4.5×10^{-3} m/yr uniformly across the top boundary resulted in vertical gradients at the site that greatly exceeded the gradient observed at HTH-1, both in the alluvium and in the tuffaceous sediments. Dinwiddie and Schroder (1971) reported a slightly upward head gradient from the base of the alluvium, and measured upward borehole flow from the base of the alluvium during a static flow meter test. Because the model could not match the established observations of gradients between the volcanics and alluvium when areal recharge was incorporated, it was excluded from the base case. In the base case, recharge is included as underflow into the lateral model boundaries on the upgradient side, consistent with the bulk of recharge occurring at higher elevations through the alluvial fans and along the range front.

5.4.3 Flow Model Parameters

The groundwater flow model of CNTA utilized the MODFLOW-88 code (McDonald and Harbaugh, 1988) in a steady-state and fully three-dimensional mode. The model included the entire 8 km by 6.5 km by 1.35 km volume of the *K* maps and used the same 50-m discretization. Flow was simulated for 225 realizations of the *K* maps. Flow into and out of the model occurred only at the north, south, and bottom faces; no additional groundwater sources or sinks were included.

The preconditioned conjugate-gradient program was parameterized to use 20 inner iterations per outer iteration, a maximum of 5000 outer iterations, a head change criterion of 0.001 m, a per-cell mass-balance residual criterion of 0.1 m^3/d, and a relaxation parameter value of 0.99. Of the 250 base-case flow realizations, the average overall mass balance discrepancy was 0.08 percent, and the maximum mass-balance discrepancy was 0.29 percent.

5.4.4 Calibration of the Flow Model

The calibration process is designed to ensure that the flow model adequately simulates the observed behavior of the flow system. Calibration is often achieved through refinement of the hydrogeologic framework, boundary conditions, and/or hydraulic properties, (ASTM, 1995). Two aspects of the CNTA model were adjusted during calibration; the vertical correlation length of *K* and the mean *K* of the alluvium (Category 1).

The vertical correlation length of *K* was adjusted during calibration as it was considered critical to the simulation of flow due to the presence of vertical gradients near the source. Because the principal objective of the flow model at CNTA was to simulate steady-state groundwater fluxes for

input to the transport model, the magnitude and orientation of the hydraulic gradients and the distribution of K were the most critical elements of the model. The overall gradients across the model were established using specified-head boundaries and were not adjusted during calibration. Likewise, the means and variances of K were assumed to be known based on the hydraulic information from the packer tests, and, with the exception of K of the alluvium, were not adjusted during calibration. However, the sparse spatial distribution of the K data introduced uncertainty into the estimates of the correlation lengths of K and thus was adjusted during calibration. The K value of the alluvium was the second calibration parameter and was adjusted based on a value of K estimated from a pumping test in HTH-1 with observations in HTH-2. As discussed in Section 2.4.1, the K estimated from this single pumping test is higher than the values of K estimated from packer tests in HTH-1 and in other wells in the alluvium.

The other aspects of the general hydrogeologic framework at CNTA were considered finalized prior to the development of the flow model and were therefore not modified during calibration. Boundary types were investigated during early phases of model development to best fit the conceptual model of flow, but no further modifications to the boundaries were made during calibration. The specified-head boundaries on the north, south, and bottom faces; the no-flow boundaries on the east and west faces; and the orientation of the mesh were chosen to approximate the north-south pattern of flow. Thus, only the boundary type of the top face was free to be modified, and was done so through changing from specified head to no-flow. The no-flow boundary was chosen for the final model because it eliminated the simulation of unrealistically high flow rates through the top boundary. Head values on the specified-head boundaries were chosen to reproduce the hydraulic gradients indicated by field measurements in packer-isolated borehole zones, and therefore were considered known and were not adjusted during the calibration process.

The calibration targets were measured hydraulic heads in the uppermost packer interval of HTH-1, UCe-18, and UCe-20. These targets were chosen only at the top of the model where simulated heads were free to change the most. The fixed heads at the base constrained head fluctuations near the bottom of the model, making heads there less sensitive to refinements made within the model. The head estimated for the top of the model domain at UC-1, based on the estimated horizontal gradient, was included as an additional calibration target. This point was particularly important to the calibration process because it governed the vertical gradient at the source, the head at the base being fixed. The calibration was evaluated using the root mean square (RMS) residual between the measured head h_m and simulated head h_s at the four calibration targets:

$$\mathrm{RMS} = \left[\frac{1}{n}\sum_{i=1}^{n}(h_m - h_s)_i^2\right]^{0.5} \qquad (5.1)$$

where n is the number of calibration targets. The model was considered reasonably calibrated when the RMS residual for 250 realizations was less than 5 m (0.37 percent of the saturated thickness of the model). In addition to heads simulated at the top of the model, vertical gradients, simulated at

locations where well data were available, were monitored to ensure that these gradients were consistent with the field data.

The results of two calibration trials are shown in Table 5.3. The first trial reduced the vertical correlation length from the 150-m maximum value estimated from the spatial analysis of the K data to a value of 50 m, which improved the calibration and resulted in an RMS residual of less than 5 m. Further reduction in the vertical correlation was not possible due to the constraint imposed by the 50-m cell size; therefore, the base-case flow simulations utilized a value of 50 m. The impacts on transport of the 150-m value were investigated in a separate transport sensitivity analysis. The second calibration trial increased the mean K in the alluvium by two orders of magnitude, resulting in further improvement of the calibration. This scenario was based on the K value of the alluvium estimated from the pumping test in wells HTH-1 and HTH-2, rather than the K estimated from the packer tests in HTH-1 and other wells. In an effort to maintain consistency within the K dataset, however, this scenario was not used as the base case despite the superior calibration. It should be pointed out that simulation of a higher mean K in the alluvium did not alter the modeled directions of flow between the volcanics and overlying alluvium (refer to Section 7.4.2). A separate transport sensitivity analysis was conducted to investigate the impacts on transport of higher K in the alluvium.

Table 5.3. Results of Two Calibration Trials of the Groundwater Flow Model.

Trial	RMS
$\lambda_z = 150$ m	5.43 m
Alluvium $\mu \log_{10} K = -0.6$	3.16 m
Base Case	4.65 m

5.4.5 Simulated Flow Fields

Profiles of hydraulic head simulated by the flow model are compared to measured heads in Figure 5.14. The head profile near Faultless is simulated to be near vertical as indicated by heads at the location of HTH-1. The model was not able to resolve the slightly higher head reported by Dinwiddie and Schroder (1971) in the section of densely welded tuff at elevation 1,079.7 m to 1,103.5 m. The head measured in this unit was 0.3 to 1.8 m higher than heads measured in the overlying alluvium, and 1.2 to 3.3 m higher than heads measured in the underlying tuffaceous sediments (Appendix 2). However, a downward head gradient is simulated from the densely welded tuff to the base of the model, which is consistent with the ambient conditions of the downward head gradient and downward borehole flow reported in the volcanic section by Dinwiddie and Schroder (1971). The mean gradient simulated in the alluvium is slightly downward (magnitude of 6.7×10^{-4}) although individual realizations simulated flow upward into the alluvium from the volcanic section. And although the base case did not simulate significant groundwater flow from the cavity horizon upward to the alluvium, this scenario was investigated as a sensitivity case with prompt injection of radionuclides upward in the chimney and subsequent migration out into the alluvium.

Groundwater specific discharges were calculated from the MODFLOW-simulated heads and the hydraulic conductivity fields described above using Equation (4.8). The simulated flow field is

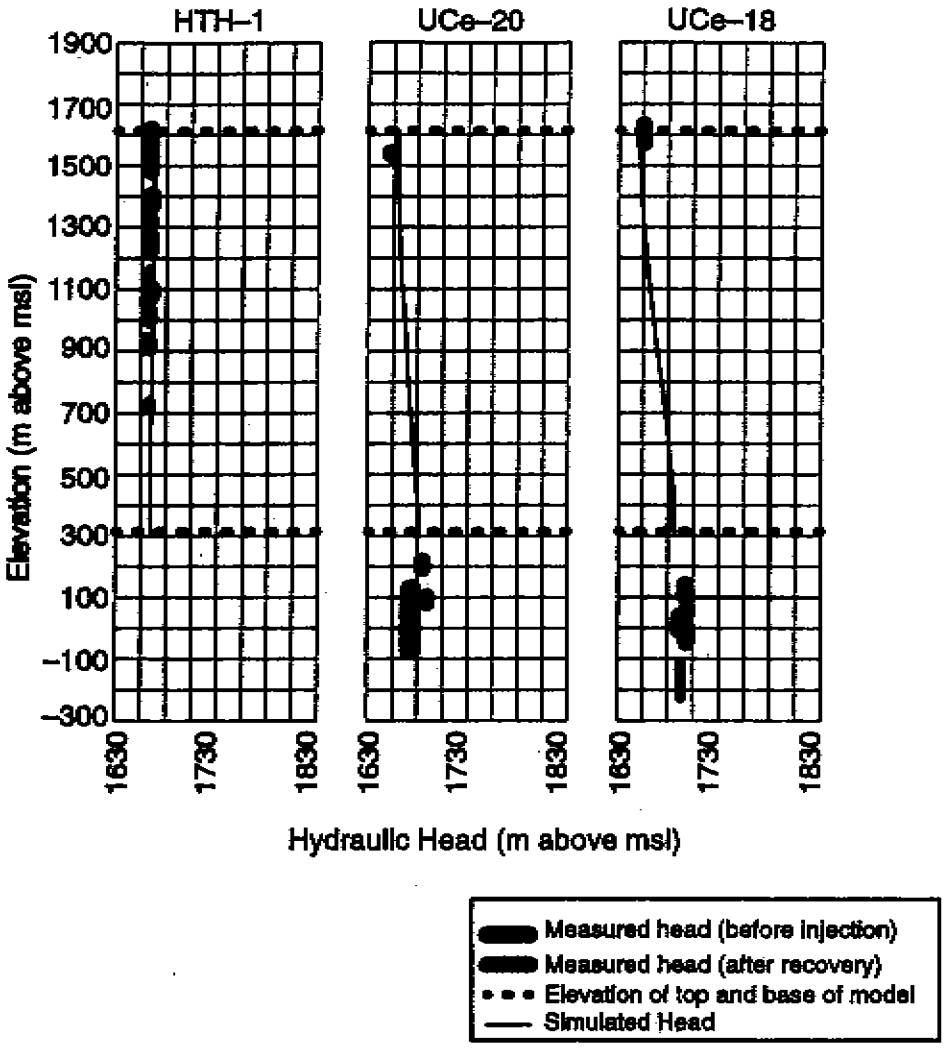

Figure 5.14. Profiles of hydraulic head simulated by the flow model compared to heads measured using straddle packers in CNTA exploratory wells located within the model domain. The simulated head profiles represent the mean of 225 flow realizations in the base case.

dominated by strong horizontal flow in the lower portion of the domain, strong vertical flow near the northern and southern ends, and a zone of low flow in the center (Figure 5.15(a)). The concentration of horizontal flow near the base and in the northern half of the domain corresponds to the high proportion of high-K volcanic rocks simulated in the lower half of the volcanic section. These thick sections of high-K volcanic rocks (i.e., densely welded tuffs) have not been observed at Faultless, but are included in the model because there is no evidence that they do not exist between the deepest extent of drilling at the site and the base of the model domain. In the model, these rocks provide a high-conductivity pathway for flow that is driven by the high hydraulic gradient toward the north at the base of the domain. The tuffaceous sediments, which have a much lower mean K,

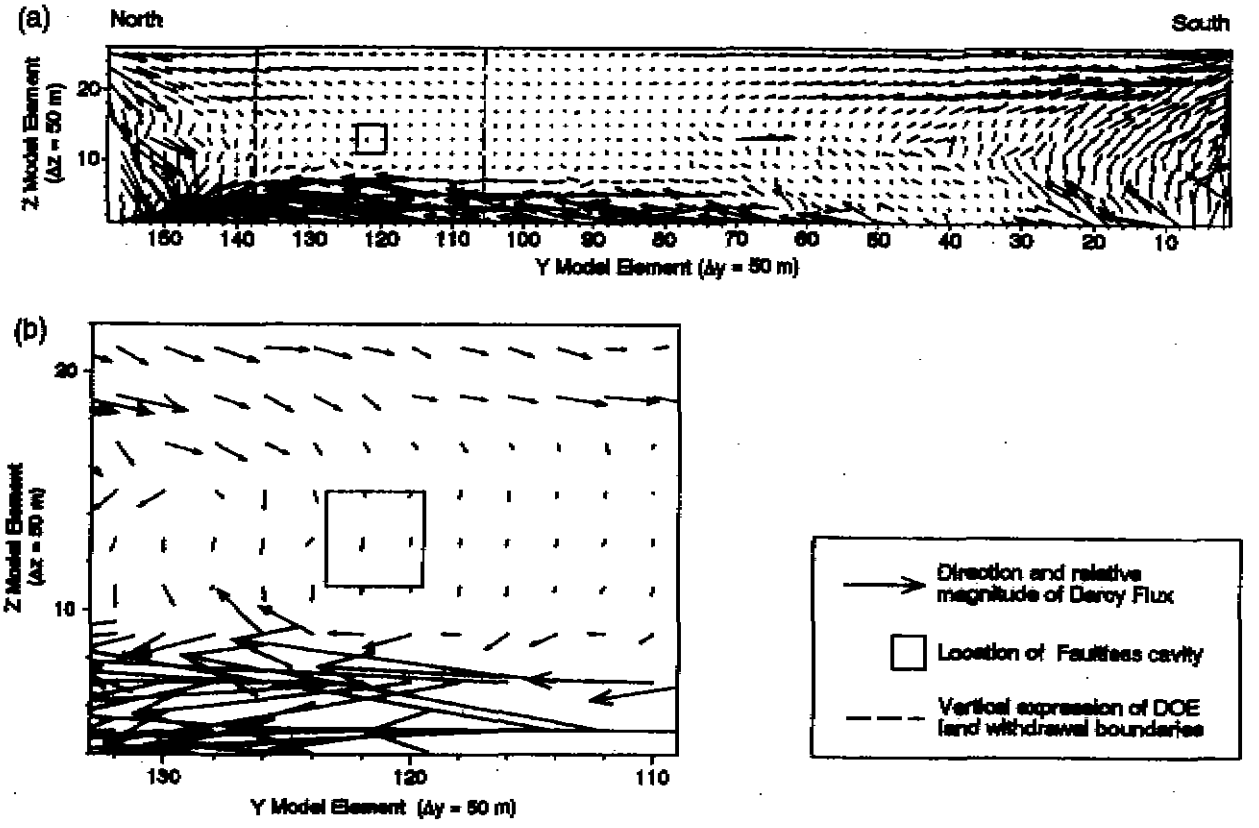

Figure 5.15. Diagram showing the directions and relative magnitudes of Darcy fluxes in a vertical cross section through the Faultless cavity. The flux vectors represent the ensemble mean of all flow realizations and are shown for every other cell. Part (b) shows a detail of the vicinity around the Faultless cavity.

also appear to contribute to this flow pattern by acting as a boundary to upward flow that is driven by the vertically upward component of the gradient in the southern portion of the domain.

The strong vertical flow simulated at the northern and southern ends of the domain is a response to the vertical gradients specified at these boundaries. Vertical flow diminishes toward the center of the domain as the magnitudes of the vertical gradients are reduced and the impact of the vertical anisotropy of K correlation scale increases. The zone of lowest vertical flow, as well as lowest horizontal flow, is simulated in the portion of the volcanic section simulated as low-K tuffaceous sediments and non-welded tuffs (Category 2). This region acts as an aquitard between the higher-K densely welded tuffs at the base and the higher-K alluvium at the top of the model.

The UC-1 cavity is located in the zone of lowest simulated flow, and in an area where the flow is directed downward and slightly to the north (Figure 5.15(b)). Thus, flow that passes through the cavity region moves down through the low-K tuffaceous sediments before reaching the simulated high-K pathways in the welded tuffs. Vertical velocities simulated in the source volume range from 3.2×10^{-9} to 5.8×10^{-6} m/d (using a homogeneous effective porosity value of 0.18), so the time of transport from the source to the welded tuffs is very long.

Overall, the patterns of groundwater flow simulated here are consistent with hydrogeologic evidence available in the Faultless area. The simulated low vertical flow rates at UC-1 support the presence of distinct flow systems that have very limited vertical interaction, as suggested by chemical and isotopic distinctions between groundwater in the alluvium and in the volcanic units. Low vertical flow rates are also indicated by the low vertical gradients of hydraulic head and borehole flows measured in HTH-1. Furthermore, the low velocities simulated in the center of the model support the very long residence times for groundwater in the volcanic units indicated by the ^{14}C data (30,000 to 50,000 years since time of recharge).

Groundwater velocities were calculated from the flow fields within the contaminant transport simulations. Measurements of effective porosity are not available from the site, but measurements of total porosity made on core samples during CNTA exploration are available for wells UC-1-I-1, UCe-17, UCe-18, and UCe-20, and are summarized by category in Table 5.4. Total porosity is likely to be a good approximation of effective porosity in Categories 1 and 2, which are composed primarily of unconsolidated clastic sediments, but probably overestimates effective porosity in the fractured densely welded tuffs of Category 3. This issue was addressed through development of a sensitivity case that has the porosity of Category 3 reduced to 0.005, a value representative of fracture porosity in densely welded tuffs, and includes matrix diffusion. This sensitivity case is described in a later section of this report. A value of 0.18 was used for all three categories in the base case, owing to the similarity of the mean values of the three categories and the high degree of overlap between categories.

Table 5.4. Values of Porosity Estimated from Measurements on Core Samples from Wells UC-1-I-1, UCe-17, UCe-18, and UCe-20 (Data reported in Barnes and Hoover, 1968; Hoover, 1968a; Hoover 1968b; and Snyder, 1967).

Hydrogeologic Category	Mean (%)	Standard Deviation (%)	Number of Measurements
1	19.3	6.31	14
2	17.5	7.22	23
3	15.7	6.21	57

6.0 Transport Model

6.1 Source Term

Contaminants from underground nuclear testing can be divided into two broad categories: radionuclides and non-radionuclides. Primary radionuclides can be attributed to three possible origins: 1) residual nuclear material that has not undergone a fission or thermonuclear reaction, 2) direct products of the nuclear reactions (fission products and tritium), and 3) activation products induced by neutron capture in the immediate vicinity of the explosion (Borg *et al.*, 1976). In addition, radionuclide daughter products are produced by decay of many of the primary radionuclides.

Non-radionuclide hazardous materials have been identified for some tests at the NTS (Bryant and Fabryka-Martin, 1991). No information is available regarding testing details (*e.g.*, stemming

plans) for the Faultless test. Given this, as well as the fact that the volume of such material is necessarily small due to the emplacement hole diameter (0.66-m-diameter casing string cemented within a 1.07-m hole; U.S. Atomic Energy Commission, 1973), non-radionuclide hazardous materials are not considered in the transport analysis.

6.1.1 Radionuclide Source Term

The Faultless radionuclide source term is included in an inventory prepared by Los Alamos and Lawrence Livermore national laboratories for nuclear tests conducted at non-NTS locations (Goishi *et al.*, 1995). This inventory represents the total radionuclide source term, given one constraint: radionuclides were excluded from the inventory if they were produced in such low amounts or decayed so rapidly that if the total amount produced during the test were dissolved into a volume of water equal to the volume of the cavity and allowed to decay for 100 years, the resulting aqueous concentration would be less than one-tenth of the maximum permissible concentration (MPC) (Smith *et al.*, 1995). This effectively eliminates radionuclides with half-lives less than about ten years from the inventory.

A shorter list of radionuclides of significance for remedial investigations at the NTS was compiled considering the 56 radionuclides presented by Goishi *et al.* (1994) for the NTS, and eight additional radionuclides with half-lives less than ten years (Smith, 1997). The criteria used in creating the short list were as follows: 1) the production of a radionuclide on a nuclear test, 2) the relative mobility of the radionuclide determined from historical observations, and 3) the health effects of the radionuclide relative to a total body or organ dose. This list contains 22 radionuclides (Table 6.1), and forms the basis for the source term considered in this work. Given the transport conditions simulated, the radionuclides with half-lives less than ten years decay too rapidly to be considered in the simulations. The remaining radionuclides cover the gamut of release functions and retardation properties (discussed in following sections) and thus can be considered representative of the full radionuclide source term.

The initial mass data for the radionuclides produced by Faultless remain classified (Goishi *et al.*, 1995) and cannot be presented in a public document. The transport calculations presented in this report were performed using a unit value for starting mass. The unit-mass-based transport analyses can be converted to true mass in a classified companion document, when the need arises.

Rough estimates of the initial masses of three important radionuclides, ^{3}H, ^{90}Sr, and ^{137}Cs, were made so that the general results of the transport modeling could be publicly related, and to provide a basis for understanding the uncertainties evaluated through the sensitivity analyses. The tritium mass was estimated based on the highest concentration measured for a water sample from the post-shot well, UC-1-P-2SR. This concentration, 9.2×10^{8} pCi/L was applied to a volume of water equivalent to the estimated chimney size. Based on generic relationships related to depth of burial (Glasstone and Dolan, 1977), the cavity radius for Faultless is estimated as 100 m. Chimney heights are typically four to six times the cavity radius. In this case, 500 m was used as the height because this also approximated the degree of saturation at the time the highest concentration sample was collected in 1976. The chimney porosity was estimated at 0.18, the same as that estimated for

the surrounding material. This reflects an assumption that the surface collapse volume met or exceeded (because of the inferred tectonic movement) the cavity volume, an assumption supported by estimates of the collapse volume (McKeown *et al.*, 1968) and calculations of cavity size based on depth of burial (Glasstone and Dolan, 1977). The resulting volume of water, 2.83×10^9 liters, and the above concentration, lead to a tritium mass estimate of 2.6×10^{18} pCi.

Table 6.1. List of Radionuclides Considered Most Significant for Remedial Investigations of Underground Nuclear Test Areas (Smith, 1997). Radionuclides with half-lives less than ten years are not considered in the Faultless analysis.

Radionuclide	Half-life, years	MPC, pCi/L
^{3}H	12.3	20,000
^{14}C	5730	2,000
^{36}Cl	3.01×10^5	700
^{60}Co	5.27	100
^{85}Kr	10.73	NA
^{90}Sr	29.1	8
^{99}Tc	2.13×10^5	900
^{106}Ru	1.02	30
^{125}Sb	2.758	300
^{129}I	1.57×10^7	1
^{134}Cs	2.065	80
^{137}Cs	30.17	200
^{151}Sm	90	1,000
^{152}Eu	13.48	200
^{154}Eu	8.59	60
^{155}Eu	4.71	NA
^{234}U	2.46×10^5	90
^{238}U	4.47×10^9	100
^{237}Np	2.14×10^6	5
^{239}Pu	2.41×10^4	8
^{240}Pu	6.56×10^3	8
^{241}Am	432.7	10

Without any measured concentrations of ^{90}Sr and ^{137}Cs, these radionuclides were estimated using rough relationships between radionuclide production and yield. Borg *et al.* (1976) estimated that 1.50×10^{14} pCi of ^{90}Sr and 1.80×10^{14} pCi of ^{137}Cs are produced per kiloton of test yield. Using these relationships and the upper bound of 1,000 kt from the announced Faultless yield range (U.S. DOE, 1994) gives an estimate of ^{90}Sr mass of 1.5×10^{17} pCi and of ^{137}Cs mass of 1.8×10^{17} pCi. It should be emphasized that these values, as well as the tritium value given above, are rough estimates for discussion purposes only, and that final calculations must rely on the classified data in Goishi *et al.* (1995).

6.2 Release Functions

Radionuclides produced by an underground nuclear test are present in three basic forms: gases, surface deposits, and volume deposits (Smith *et al.*, 1995), the proportions of which can change with time after the detonation. Immediately after the detonation, essentially all of the radionuclides are part of a superheated, expanding gas (Borg *et al.*, 1976). When the temperature and pressure start to drop, many of the gases condense. The condensation occurs based on the boiling point of the nuclide, with the higher-boiling points (first to condense) referred to as refractory nuclides, and the lower-boiling point species referred to as volatile. A high percentage of the refractory species are trapped in the solidifying melt, much of which collects at the base of the cavity as "puddle glass." These are the volume deposits, whose release is controlled by dissolution of this glass.

Nuclides with somewhat lower boiling points (*e.g.*, Cl, I) remain volatile longer and are able to migrate upward through cracks in the rubble chimney. Some portion of these are included within the solidifying puddle glass, but a portion is also deposited as coatings on chimney rubble surfaces. Nuclides included in these surface deposits can be released by relatively rapid processes such as ion exchange, as well as by dissolution, and thus the surface deposits are more susceptible to leaching than the radionuclides that are volume deposited. Ion exchange and dissolution of these surface coatings are dependent upon the mineralogy of the precipitates and their controlling thermodynamics. The specific form that these surface deposits take at Faultless is unknown, and even if it were, it is unlikely that thermodynamic data are available for some of the uncommon forms, much less definition of the transient temperature and pressure conditions under which the reactions will occur. For these reasons, no attempt was made to formulate a geochemical release function for the surface-deposited radionuclides. Rather, it was assumed that the surface deposits were immediately dissolved upon contact with groundwater and available for migration through the groundwater system. This assumption results in an overestimation of the availability of the surface-deposited radionuclides for transport, as the dissolution and exchange processes described above may be considerably smaller in magnitude and slower in occurrence than modeled. With no geochemical component to the release, the migration from the cavity of the surface-deposited nuclides is governed by the "hydraulic release." The hydraulic release defines the process of re-equilibration of the hydraulic head within the cavity (recovery to static water level from the depressed condition caused by the test), as well as flushing of contaminants from the cavity by the flow-through of groundwater.

Some of the radionuclides produced remain in gaseous form (*e.g.*, Kr and Xe) and may be incorporated in solidifying phases, dissolved in groundwater, or escape the saturated zone to migrate through the unsaturated section. That portion dissolved in groundwater will migrate as controlled by the hydraulic release described above. Other nuclides are gaseous, but then decay to a non-gaseous nuclide. In these cases, the preceding decay-chain behavior is an important control on the distribution and release of daughter nuclides. For example, both ^{137}Cs and ^{90}Sr can be found in surface deposits throughout the chimney, as well as in the puddle glass, because of gaseous precursors. Prompt injection is another release process that may transport gaseous species under early cavity conditions. Gaseous tritium and strontium and cesium precursors may be forced several

cavity radii away from the detonation point through explosion-induced fractures arranged radially away from ground zero (Smith, 1995). It is uncertain whether refractory species are transported by prompt injection.

Several of the processes described above require elaboration to understand how they were implemented in the transport analysis. Following are additional discussions of the apportioning of radionuclides between volume and surface deposits, the hydraulic release function, nuclear melt glass dissolution, and prompt injection.

6.2.1 Volume/Surface Mode Designation

Refractory and volatile behavior designations were culled from literature references (Borg *et al.*, 1976; Borg, 1975; Kersting, 1996; Smith, 1995) whenever possible. For those nuclides with no specific literature reference, volatilities of oxides (Bedford and Jackson, 1965; Krikorian, 1981) and melting point temperatures were used to assign a behavior consistent with the volatilities and melting points of known refractory and volatile nuclides.

A small proportion of nuclear melt glass is not incorporated in the bottom puddle, but is distributed through the collapsing chimney as a result of splashes caused by blocks of rock falling into the puddle, or as fine droplets entrained with escaping cavity gases (Smith, 1995). The exact amount distributed in this way is not known. Based on broad experience at Lawrence Livermore National Laboratory examining glass samples from underground testing, Borg (1975) estimates that at most, only two to three percent of refractories are lost from puddle glass. Rabb (1970) found that isotopes other than ^{137}Cs, ^{125}Sb, $^{95}Zr/^{95}Nb$, ^{147}Pm, and ^{185}W were 95 percent or more in the glass with the remainder elsewhere for the Pile Driver test. Based on this information, it is assumed here that five percent of the total mass of even the refractory species is lost from the puddle glass. Thus, the designated refractory radionuclides have five percent of their mass considered surface deposited, with the remaining 95 percent volume deposited (Table 6.2).

The distribution of ^{90}Sr and ^{137}Cs is assigned based on fractionation data compiled by Borg *et al.* (1976). Their Table 21 lists the fractionation index for several radionuclides from tests in different rock types. The lowest value measured from deeply buried underground tests (neglecting results from shallowly buried tests in alluvium) for incorporation in the glass was applied to the Faultless evaluation. Thus, it is assumed that 20 percent of the ^{137}Cs is contained within the puddle glass and 80 percent is surface deposited through the cavity and chimney, and 40 percent of the ^{90}Sr is in the puddle glass and 60 percent is surface deposited. The higher proportion of ^{90}Sr in the glass as compared to ^{137}Cs is consistent with the difference in the half-life of their gaseous precursors. The ^{90}Kr half-life is 33 seconds, whereas the ^{137}Xe half-life is 3.9 minutes, allowing more time for migration of the mass-137 chain to migrate out of the puddle glass.

The halogens, ^{36}Cl and ^{129}I, can be expected to have volatile behavior in the early time, but there are also natural analogs in the geologic environment whereby halogens are included in volcanic glass (Hampton and Bailey, 1984). As the steam condenses in the cavity, some of the volatiles will be trapped and incorporated in the glass. It is assumed here that half of the ^{36}Cl and ^{129}I is included in the glass, and half is surface deposited.

Table 6.2. Release Functions Assigned to Source Term Nuclides, based on Literature References Described in the Text.

Element	Hydraulic Release (%)	Volume (Glass) Release (%)
H (Hydrogen)	100	0
C (Carbon)	100	0
Cl (Chlorine)	50	50
Kr (Krypton)	100	0
Sr (Strontium)	60	40
Tc (Technetium)	5	95
I (Iodine)	50	50
Cs (Cesium)	80	20
Sm (Samarium)	5	95
Eu (Europium)	5	95
U (Uranium)	5	95
Np (Neptunium)	5	95
Pu (Plutonium)	5	95
Am (Americium)	5	95

By a similar process, other volatile nuclides are probably entrained in the melt. For example, the French report that more than 50 percent of the available tritium is captured by their glasses (Dupuis, 1970, as reported by Borg, 1975). Borg (1975) reports that only a small (but unquantified) portion of the total tritium produced can be recovered from glasses of tests conducted in saturated alluvium and tuff. At Pile Driver, Borg (1975) estimates that 1.53 g of a total 1.8 g produced by activation was contained in the melt, but notes that this was considerably less than the total tritium available. Given these uncertainties and the importance of tritium to the transport calculations, no incorporation in the melt glass is assumed here. The size of the carbon dioxide molecule can limit its inclusion in volcanic glasses, (though carbon monoxide may dissolve; Hampton and Bailey, 1984), and krypton is noncondensable, so these nuclides are also considered subject only to the hydraulic release function.

6.2.2 Cavity Infill

It is well established that nuclear cavities and chimneys are dewatered and subsequently refilled, though the process through which the dewatering occurs in largely inferred (Borg *et al.*, 1976). Within the cavity itself, the depressed water levels probably result from thermal and compressional forces generated by the nuclear reaction. Following the desaturation immediately after the test, the cavity and chimney will infill with groundwater flowing radially from the surrounding saturated rock.

The infill of the Faultless chimney with groundwater has been well recorded by water level measurements in UC-1-P-2SR through the years (Thordarson 1987; Chapman *et al.*, 1994). An apparent initial delay in infilling has been attributed to a zone of perched water, with measurements after 1974 representative of the rise of groundwater to the pre-test level. The pre-test level is a matter

of speculation. Thordarson (1987) estimated the pre-test level as occurring at a depth of about 168 m (hydraulic head of 1687 m). Given the hydraulic head measured at wells HTH-1 (1668.4 m) and HTH-2 (1667.1 m), this pre-test estimate appears high, requiring a gradient of about 0.025. Using the pre-test estimate of 1687 m, Thordarson (1987) predicted that the hydraulic head in the chimney would be fully recovered between 1993 and 2018. As of late 1997, the hydraulic head in the chimney was at 1660.7 m, over 26 m below the pre-test estimate, and almost 8 m below that measured in HTH-1. The recovery should bring the water level in UC-1-P-2SR above that in HTH-1 during 1999, while the pre-test estimate is predicted to be reached no sooner than 2001 (Appendix 3).

While hydraulic head within the chimney is depressed below that in the surrounding aquifer, there is no hydraulic force to drive contaminant migration. Given this, radionuclides are not allowed to exit the cavity and begin transport through the aquifer until 30 years after the nuclear test. The effect of this is to allow 30 years of radioactive decay, reducing the starting masses of those radionuclides with short half-lives.

Though there is no hydraulic force driving migration, there is a large chemical gradient between the cavity and surrounding areas that can drive diffusion of contaminants away from the cavity. The relative magnitudes of advective transport of clean groundwater toward the cavity and of diffusive movement of contaminated water away determines whether diffusion can cause migration to occur prior to cavity infilling. An analysis of these processes determined that advection dominates until very late time, and only during the last several months prior to full recovery can diffusion overcome advective flow and begin transporting radionuclides (Appendix 3).

The nuclear test also sets up a substantial, though temporary, thermal gradient. Analysis of the hydrologic impact of pluton emplacement concluded that waters in natural pluton systems move away from their points of origin to positions several kilometers away in a few hundred thousand years (Norton and Knight, 1977). However, the Faultless test had a much lower sustained temperature, and it is decaying toward the geothermal gradient very rapidly, compared to the pluton example. In early time, elevated temperatures in the cavity may have retarded groundwater inflow until the temperature dropped low enough to condense the steam into liquid water. That condensation process was postulated by Thordarson (1987) to be a possible contributor to the creation of the perched water level monitored in UC-1-P-2SR, as steam rose in the chimney and condensed at higher, cooler, levels. The impact of temperature on groundwater flow after condensation is through free convection, which is controlled principally by the hydraulic conductivity. In low conductivity material, very large temperature gradients are necessary to establish convection. Given the relatively low conductivity of the surrounding aquifers, particularly in the vertical direction, and the relatively high conductivity within the cavity and chimney, it is likely that the thermal impact on groundwater movement in the years after the test is confined to the cavity and chimney.

6.2.3 Nuclear Melt Glass Dissolution

The rock, fission products, and device components that are vaporized by the tremendous heat and pressure of a nuclear reaction quickly begin to condense and coalesce into nuclear melt glass.

This glass (a solid with no crystalline structure) contains much of the radioactivity produced by a nuclear test. Radionuclides must be removed from the melt glass to be transported by groundwater.

Available data for predicting nuclear melt glass dissolution are presented in a transport analysis performed for the Shoal underground nuclear test (Pohll *et al.*, 1998). The approach selected for that site, and also applied here, is to use dissolution rates based on analogy to the dissolution of volcanic glass. This approach avoids the significant problems inherent in trying to use data from nuclear melt glass leaching experiments, such as data collected during nonequilibrium conditions.

Dissolution of glass under the geochemical conditions of the CNTA area is expected based on thermodynamic considerations. The log of the ion activity product to the equilibrium constant (log IAP/K_T) for amorphous silica is -0.75 for groundwater collected from the chimney in well UC-1-P-2SR, indicating that the chimney water is undersaturated with respect to glass. The rate equation used to calculate nuclear melt glass dissolution follows a linear rate law (White, 1983):

$$Q = Q_0 + k_l t \qquad (6.1)$$

where Q is the mass transfer of a chemical species into aqueous solution per unit surface area of solid (moles/cm^2), Q_0 is the initial surface ion exchange (moles/cm^2), k_l is the linear rate constant (moles/cm^{2}s), and t is the time (s).

The bulk composition of volcanic glass and analyzed nuclear melt glass is similar (Table 6.3). Though there are no analyses of the bulk elemental composition of Faultless nuclear melt glass, there is no appreciable migration of major elements from a cavity region, such that nuclear melt glass tends to resemble the bulk rock composition (Schwartz *et al.*, 1984). Mineralogic analysis of tuffaceous sediments collected from UC-1-I-1 (an instrument hole adjacent to UC-1) reveals an orthoclase, plagioclase, and quartz-dominated material with approximately 71 percent SiO_2 and 16 percent Al_2O_3 (Appendix 5). This composition is closest to that of the perlite used by White (1983) in his dissolution experiments, so that the dissolution constant used here is the one determined from his experiment P-12, with a K_l of 0.45 x 10^{-15} moles/cm^{2}s and an initial exchange value, Q_0 of 0.48 x 10^{-9} moles/cm^2.

With the dissolution rate constant given on a per unit surface area basis, the specific surface area is a very sensitive term in the dissolution equation. It is also a parameter that is poorly known from experimental work and wholly unknown for *in situ* cavity conditions (Pohll *et al.*, 1998). The value used here, 0.05 m^2/g, is that reported by Essington and Sharp (1968) for larger particle sizes of nuclear melt glass collected from the Rainier test. Recent work evaluating the melt glass produced by the Cambric test (W. Bourcier, personal communication, 1998) applied studies of nuclear waste glass surface area to postulate much lower values of specific surface area (approximately 5.2 x 10^{-5} m^2/g). These lower surface areas, with resultant much slower glass dissolution rates, were planned to be included in the Faultless analysis until the transport analysis indicated very slow migration times. As discussed in a later section, the groundwater flow field and retardation play a much more significant role in contaminant migration at Faultless than the estimated glass dissolution rate.

Table 6.3. Comparison Between Chemical Composition of Natural Volcanic Glass and Nuclear Melt Glass. Major and trace element composition in terms of oxides, given as weight percents. Parentheses contain standard deviations, when available.

	SiO_2	Al_2O_3	FeO	MgO	CaO	Na_2O	K_2O
Perlite*	74.2	14.1	0.15	0.49	1.0	4.0	4.8
Obsidian*	76.0	13.8	0.40	0.011	0.21	4.4	4.5
Trachytic*	62.8	15.2	1.3	0.38	1.1	8.4	5.1
Nuclear Melt Glass†	73.1 (4.9)	14.2 (2.5)	1.18 (1.59)	0.22 (0.27)	1.06 (0.86)	3.49 (1.68)	6.6 (4.2)

*Glassy volcanic rocks, as reported by White (1983)
† Average of six nuclear melt glass samples, as reported by Smith (1995)

The total mass of glass available for dissolution is estimated based on a relationship of 700 metric tons of glass produced per kiloton yield (Smith, 1993), and a maximum estimate of 1,000 kt for Faultless. The resultant 7 x 10^5 metric tons of glass were assumed to have a gram formula weight of 60 and density of 2.65 g/cm^3. The dissolution was calculated iteratively to account for the continual reduction in dissolution as the total surface area is reduced. At each time step (of one year), the amount of dissolution is calculated. That lost mass is then subtracted from the initial mass of that time step to determine the new (reduced) total mass and related (reduced) specific surface area to use to determine the amount of mass lost in the next time step. As the mass and surface area get smaller, less dissolution occurs with each time step, with that reduction expressed as an exponential decline. Particles are released into the flow field according to the function $1\text{-}e^{kt}$ to approximate the glass dissolution process. Here, k is the release coefficient and is the product of the specific surface area and the dissolution rate constant. Multiplying the total mass (or number of particles) by the function reveals the amount to release at each time step (see Section 4.3 for additional discussion). This approach for handling glass dissolution assumes adequate flow of groundwater such that saturation with amorphous silica is not reached in the water. Given the low groundwater flow velocities in the model, this assumption may be violated and would result in even slower dissolution of the puddle glass than used here.

Using these parameters, 90 percent of the glass in the Faultless cavity is calculated to be dissolved after approximately 5500 years (Figure 6.1). Most of the mass is lost in early time (50 percent at 1660 years), with a trailing tail in later years. It is likely that these calculations over-predict dissolution because rate-reducing processes have been neglected (*e.g.*, protection of the glass from additional dissolution by the formation of a mantle of reaction products), and the specific surface area used may be too large. Using the surface area generated for Cambric, 5.2 x 10^{-5} m^2/g (W. Bourcier, personal communication, 1998), dissolution of half the glass mass requires approximately 1.5 million years.

6.3 Retardation

Radionuclides that are dissolved in groundwater and available for transport are subject to a variety of physical and chemical processes that can retard their movement relative to the movement of water. Together, these processes are referred to as retardation and include ion exchange,

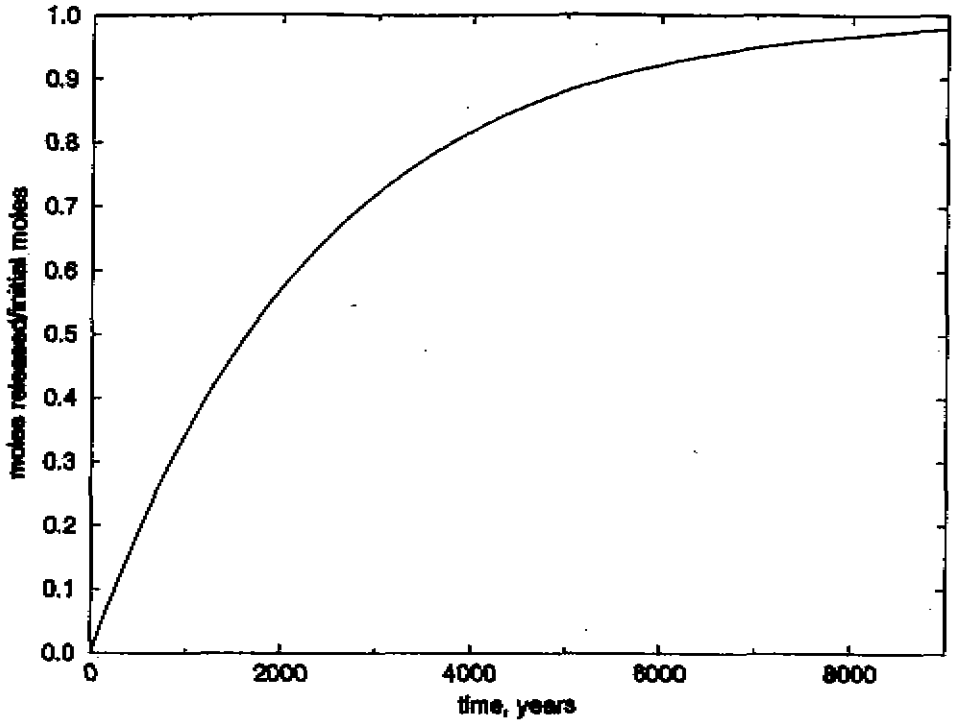

Figure 6.1. Dissolution of Faultless nuclear melt glass, assuming an analog to volcanic glass dissolution, using the parameters described in the text. Half of the starting mass is lost by 1660 years. The calculation used a specific surface area of 0.05 m^2/g and much smaller values indicated by other work discussed in the text were not used due to the very slow groundwater velocities at the site.

adsorption, and surface and bulk precipitation. Sorption and matrix diffusion are powerful retardation mechanisms that need to be incorporated in the transport analysis. The data necessary to consider individual reactions are not available for the Faultless test; instead, a bulk sorption approach is used to approximate chemical processes. This approach is limited to equilibrium-controlled processes. Kinetic processes, particularly diffusion, can be important in controlling the rate of other retardation processes and may result in additional significant inhibition of radionuclide transport. The supporting data for sorption, and how it was applied to the modeling is presented first, followed by a discussion of the treatment of matrix diffusion.

The distribution coefficient, K_d, is a measure of partitioning of an ion between the solution and the solid under equilibrium conditions. Distribution coefficients were estimated for the aquifer materials of the CNTA by Nork *et al.* (1971). They report K_d values for ^{45}Ca, ^{85}Sr, and ^{137}Cs for three different size fractions of tuff, welded tuff, lakebeds and gypsum, rhyolite, alluvium, and tuffaceous sediments in contact with groundwater from UCe-17, UCe-18, and HTH-1. The K_d values are very large (Table 6.4) and indicate significant potential for retardation of radionuclides in contact with the aquifer material near Faultless.

Extensive studies of sorption on materials from Yucca Mountain provide another source of information. Though alluvium is not of concern to that site, sorption to welded and non-welded tuffs

Table 6.4. Distribution Coefficients of Some Central Nevada Test Site Water-Mineral-Radionuclide Systems (Nork *et al.*, 1971).

Sample Designation	Rock Type	Sample Type	Water Designation	Distribution Coefficients (K_d), cm^3/g								
				Calcium-45*			Strontium-85*			Cesium-137*		
				500-4000 micron	62-500 micron	< 62 micron	500-4000 micron	62-500 micron	< 62 micron	500-4000 micron	62-500 micron	< 62 micron
UCe-17A	Various Tuffs	Cuttings	UCe-17 Zone 14	43.7	60.8	86.2	62.1	73.9	93.5	449.2	984.0	2604.0
		Cuttings Washed	UCe-17 Zone 14	131.3	106.4	131.4	104.3	95.5	124.8	554.6	807.4	1447.0
UCe-17B	Partly to Densley Welded Tuff	Core 23	UCe-17 Zone 5	213.3	216.6	284.3	143.8	139.6	265.3	107.5	167.9	428.8
UCe-18A	Lakebeds and Gypsum	Core 13	UCe-18 Zone 9	529.1	425.3	495.7	563.3	497.2	599.6	1254.0	1003.0	1645.0
UCe-18B	Rhyolite	Core 14	UCe-18 Zone 12	29.8	47.8	53.6	54.1	64.0	84.2	69.3	121.9	1347.0
UCe-11A	Alluvium	Cuttings	UCe-11 Composite	71.5	77.1	90.9	99.3	130.6	120.9	786.9	1519.0	759.2
		Cuttings Washed	UCe-11 Composite	75.6	94.9	136.4	138.1	148.1	235.0	1349.0	1324.0	4404.0
UCe-11B	Tuffaceous Sediment	Core 2	UCe-11 Composite	185.1	169.5	245.5	228.9	205.5	294.9	888.6	1139.0	2782.0
HTH-1A	Alluvium	Cutting	HTH-1 Zone 10	32.0	31.1	42.0	48.3	38.0	24.8	180.4	138.1	84.2
		Cuttings Washed	HTH-1 Zone 10	354.6	278.8	211.7	516.6	428.1	309.9	454.7	542.1	710.2
HTH-1B	Tuffaceous Sediment	Cutting	HTH-1 Zone 3	182.2	110.0	67.8	225.0	104.3	79.0	284.4	139.7	93.4
		Cuttings Washed	HTH-1 Zone 3	487.7	514.1	301.2	621.1	656.2	405.7	458.9	391.7	628.0
UCe-1-I-1A	Alluvium	Core	HTH-1 Zone 10	1380.0	2065.0	2842.0	570.7	694.4	866.0	2048.0	2542.0	2642.0
UCe-1-I-1B	Tuffaceous Sediment	Core	HTH-1 Zone 3	893.0	794.4	1163.0	2454.0	1806.0	1933.0	2642.0	3165.0	5051.0

* Level of radioisotope in solution: ^{45}Ca 0.001 μCi/ml
^{85}Sr 0.005 μCi/ml
^{137}Cs 0.05 μCi/ml

was evaluated. Many of the radionuclides evaluated exhibited strong sorption (Triay *et al.*, 1997). Specifically, it was determined that niobium, tin, thorium, zirconium, actinium, americium, samarium, plutonium, cesium, and radium could be assigned a minimum sorption coefficient value of 100 ml/g for Yucca Mountain performance assessment calculations (actual sorption measurements are often many times greater). Several other metals also exhibited high affinities for most Yucca Mountain rocks under most conditions, but had somewhat more complex behavior that indicated additional research was needed.

Given the important role such K_d values would play in estimating migration, validation and refinement of the sorptive properties of the aquifer matrices of CNTA were performed through a new series of experiments. The experiments were conducted using cores from CNTA drillholes with simulated groundwater based on chemical analyses of groundwater from HTH-1. Three aquifer materials were investigated: alluvium, tuffaceous sediment, and densely welded tuff. Batch equilibrium studies using different size fractions, batch rate-of-uptake studies using different size fractions, and column experiments were all conducted. It was impractical to run individual sorption experiments for all of the elements in the nuclear source term, plus daughter products, especially given the hazardous and controlled nature of many of the elements. Rather, surrogates were identified to approximate the actual source term. Strongly and moderately binding cations (lead, cesium and strontium, respectively) and strongly and weakly binding anions (selenite and chromate, respectively) were evaluated for their affinity for the different aquifer materials. The laboratory results are summarized below, followed by a discussion of the retardation calculation as applied to the transport calculations. The details of the sorption experiments may be found in Appendix 5.

6.3.1 Laboratory Results

6.3.1.1 Characterization of Aquifer Material

The adsorbent used in the sorption experiments was core material collected during drilling boreholes at CNTA and stored for the last several decades at the U.S. Geological Survey Core Library in Mercury, Nevada. Five different horizons were sampled from three boreholes. The main interest was in material from UC-1-I-1, as it was closest to the emplacement hole. Alluvium from UC-1-I-1 was collected from 611 m and an interval from 546 to 551 m. Tuffaceous sediments from the same hole were collected from 985 to 987 m and from 1,065 m. Spatial variability in the alluvium was investigated by a sample from 1,074 to 1,077 m in UCe-18. Welded tuff was not encountered in any nearby core to UC-1, so that the welded tuff interval at 296 m in HTH-3 was used.

It was not possible to conduct laboratory experiments with all different materials. A rather extensive characterization, however, was performed on all materials, to evaluate possible differences and similarities. Based on the characterization, and to perform experiments with relevant aquifer material as diverse as possible, the experiments were conducted with one sample each of alluvium, tuffaceous sediments, and densely welded tuff. Specifically, the following three samples were used: UC-1-I-1 546-551 m (alluvium), UC-1-I-1 985-987 m (tuffaceous sediments), and HTH-3 296 m (densely welded tuff).

To perform batch and rate-of-uptake laboratory experiments, the core samples were reduced in size. Several size fractions were obtained by sieving. Although several experiments were performed with different size fractions, most experiments were performed with the size fraction consisting of particles smaller than 125 μm. The first phase of the laboratory work included a rather extensive characterization of the smaller size fraction. The characterization of the powders included particle size distribution, porosity, bulk and true density, specific surface area, average pore diameter, and micropore volume using the Brunauer, Emmett and Teller (BET) (1938) model.

Details of the characterization are presented in Appendix 5. In summary, however, it can be said that the results were fairly similar for the three samples, although the density of the tuffaceous sediments (2.56 g/cm^3) was slightly lower than the density of the other materials (2.67 g/cm^3). In addition, the BET surface area of the densely welded tuff (6.24 m^2/g) was lower than the surface area of the alluvium (13.8 m^2/g) and tuffaceous sediments (16.7 m^2/g). These results are consistent with the lower micropore volume of the densely welded tuff compared to the alluvium and tuffaceous sediments. It should be noted, however, that the BET values may be underestimating the total available surface area for sorption, if the sample contains swelling clays (smectites). Even if the percentage of clays by weight is low, the error in the reported total surface area may be significant because of the high specific surface area of smectites (600-800 m^2/g).

The morphology of the samples was examined by scanning electron microscopy (SEM). Analyses were performed both on the powders used in the experiments and small core fragments. In addition, the energy dispersive x-rays (EDX) attachment of the SEM allowed the identification of the composition of individual mineral grains. The mineralogical composition of the samples was determined based on a combination of techniques. Bulk mineralogy was determined by powder x-ray diffraction (XRD) of the crushed sample. In addition, a semi-quantitative mineralogical composition of the core was obtained from SEM/EDX analysis of thin sections of the core combined with image analysis.

The drawback of the bulk mineralogical composition based on powder XRD is that relatively minor components may be overlooked. These relatively minor components, however (*e.g.*, clays and iron oxides), may account for a substantial fraction of sorption sites. In addition, amorphous or disordered materials (*e.g.*, hydrous phyllosilicates) may yield very broad peaks not easily identified as a mineral phase. The SEM/EDX analysis of the thin sections mentioned above can provide some additional information. Based on a combination of the above techniques, the core samples consisted mostly of quartz and feldspars (albite, anorthite, orthoclase, plagioclase), although calcite, hydrous aluminosilicates, and clay minerals were also found in smaller concentrations.

6.3.1.2 Experimental Procedures

The batch sorption experiments were performed with two different size fractions of each type of material (material smaller than 125 μm and material between 212 and 595 μm). Samples were equilibrated in individual polypropylene 12-mL reactors. All experiments reported here were performed with synthetic groundwater simulating the composition of groundwater from well HTH-1 at 741 m depth. Because of the large number of experiments needed to be performed, it was

not possible to investigate the sorption of cations and anions as a function of ionic strength, although, at least for some of the elements, ionic strength may be affecting their sorption behavior. A few experiments, however, were conducted with synthetic groundwater of different composition (simulating groundwater from well HTH-2 at 229 m depth) and the results were not substantially different.

To derive sorption isotherm parameters, experiments at different concentrations had to be performed. Again, because of work scope limitations, only a limited range of concentrations could be used. The concentrations used in these experiments ranged from 10^{-6} to 10^{-4} M. At least two concentrations were used for each isotherm and a linear isotherm was assumed, so that the isotherm was forced through the origin of axes. Each isotherm, therefore, was drawn through at least three points. Details and figures showing the sorption isotherms are included in Appendix 5. The resulting linear isotherm is usually referred to as a distribution coefficient, K_d, and is given by:

$$K_d = \frac{S}{C_{eq}} \tag{6.2}$$

where S is the sorbed concentration of the adsorbate per mass of adsorbent and C_{eq} is the equilibrium concentration of the adsorbate in the aqueous solution.

It should be obvious from the above equation that sorption isotherms only provide a means of quantifying the amount of a substance sorbed onto aquifer material relative to the dissolved concentration, presumably under equilibrium conditions. These isotherms represent, therefore, a macroscopic and quantitative description of the partitioning of a substance between the solid and aqueous phases, but provide very little indication of the particular process responsible for the retardation of a contaminant. Parametric investigations as a function of pH and ionic strength can provide valuable information regarding the specific process involved.

Owing to the relatively constant pH of the groundwater in both the alluvial and volcanic aquifers (see discussion below), most experimental data were collected under slightly basic pH conditions (pH 7-9). Data at lower pH values were occasionally collected to help interpret the type of sorption process involved. Sorption of cations occurs either through cation exchange at permanent-charge sites of clay minerals and zeolites, or through sorption at amphoteric sites of oxide and hydroxide minerals, or through surface precipitation. More detailed information is given in Appendix 5; suffice it to say that pH-independent sorption is indicative of sorption at permanent charge sites of clay minerals and zeolites, while pH-dependent sorption is consistent with sorption at amphoteric sites of oxides and hydroxides or surface precipitation.

Experiments were performed with both cations and anions. The selection of the cations and anions used in this study was based on an attempt to achieve the following objectives: to study as many cations and anions, with sorption behavior as diverse as possible for all three adsorbent materials used in this study. At the same time, because of safety concerns and other regulatory restrictions, none of the ions used could be of a controlled nature, although mixed isotopes in their natural abundance could be used instead of a radionuclide of the same element.

Based on the above, the cations used were lead (Pb), strontium (Sr), and cesium (Cs), and the anions used were chromate (Cr in the +6 oxidation state, from now on referred to as Cr^{VI}) and selenite (Se in the +4 oxidation state, from now on referred to as Se^{IV}). Lead is known to sorb very strongly on both cation exchange and amphoteric sites and it was used to model strongly sorbing radionuclides. Cesium tends to bind more strongly than Sr on cation exchange sites, while Sr may have slightly higher affinity for binding on amphoteric sites. Owing to the importance of the radionuclides of these elements it was decided to perform experiments with both Cs and Sr.

The anions were used as a model for the sorption of not only pertechnetates (Tc in the +7 oxidation state) but also any other anionic contaminant in the groundwater. On most surfaces, Se^{IV} is thought to bind more strongly than Cr^{VI}. In addition, the sorption of Se^{IV} tends to be less dependent on ionic strength compared to the sorption of Cr^{VI}. The sorption of both anions would be almost negligible on smectites and zeolites, *i.e.*, minerals with very high sorption capacity for cations. On oxide surfaces, however, such as iron oxides, Se^{IV} sorption, in particular, is expected to be at least comparable to the sorption of many divalent and transition metal cations.

Experiments were performed with both particle size fractions to assess the dependence of the distribution coefficients on particle size (see discussion on the dependence of K_d on specific surface area below and in Appendix 5). The batch sorption experiments will be summarized here; more detailed discussion can be found in Appendix 5.

6.3.1.3 Experimental Results

Batch Experiments

The K_d values for the small particle size fraction of the three different materials are given in Table 6.5. The values for the larger size fractions are given in Appendix 5. In general, the batch sorption results were consistent with the expected behavior of the cations and anions studied and with the mineralogical composition of the aquifer materials. Lead was the more strongly binding cation, followed by Sr and Cs. With respect to the anions, Se^{IV} and Cr^{VI} showed fairly similar behavior, although a few differences on specific adsorbents were evident. Cation sorption was a combination of pH-dependent and pH-independent behavior, presumably because of sorption at both pH-dependent and pH-independent sites, while anion sorption was entirely pH dependent, because anions are not expected to bind on minerals with high cation-exchange capacities, whereas they may bind on amphoteric, pH-dependent sites of oxides and other minerals.

The degree of anion sorption was a function of both pH and adsorbent type. Sorption was more pronounced on the alluvium and the densely welded tuff samples, compared to the tuffaceous sediment sample. These results correlate well with the increased concentration of iron oxides in the alluvium and the densely welded tuff and the absence of iron oxides from the tuffaceous sediments. The limited sorption of anions, however, was obvious only at pH values generally below six. At the pH of the groundwater at CNTA (approximately eight), essentially no anion sorption is expected and therefore very little retardation.

As pointed out above, Pb was the most strongly binding cation in all aquifer materials. Compared to Sr and Cs, this behavior has been confirmed by numerous studies and is not surprising.

It is, however, interesting to note the type of sorption behavior as a function of mineral composition of the three adsorbents. Specifically, the degree of pH-dependent sorption varied among the three samples, presumably as a function of the relative abundance of permanent charge and amphoteric sites. The alluvium and densely welded tuff samples contained iron oxides, resulting in more pronounced pH-dependent sorption. The tuffaceous sediments contained essentially no iron oxides and the cation sorption was essentially pH independent. The presence of smectite clay minerals and possibly hydrous aluminosilicates could explain the relatively high cation exchange capacity of the tuffaceous sediments.

Table 6.5. Laboratory-Measured Distribution Coefficients, Calculated Distribution Coefficients Scaled According to the Specific Surface Areas, and Retardation Coefficients Calculated using the Scaled K_ds. The retardation used in the transport modeling is the lowest value for each ion, regardless of aquifer type. Also shown, in parentheses, are retardation values derived using a fracture-flow model for a sensitivity calculation regarding the welded tuff.

		Alluvium	Tuffaceous Sediments	Welded Tuff
Lead	K_d-Lab, m^3/g	1.86×10^{-2}	1.33×10^{-2}	1.39×10^{-2}
	K_d-Scaled, m^3/g	1.86×10^{-3}	7.44×10^{-4}	NA*
	Retardation Coef.	2×10^{4}	8×10^{3}	2×10^{5} (12**)
Strontium	K_d-Lab, m^3/g	1.33×10^{-2}	1.16×10^{-3}	6.11×10^{-4}
	K_d-Scaled, m^3/g	1.33×10^{-3}	6.5×10^{-5}	NA*
	Retardation Coef.	2×10^{4}	7×10^{2}	9×10^{3} (1.5**)
Cesium	K_d-Lab, m^3/g	5.18×10^{-4}	1.51×10^{-3}	5.4×10^{-4}
	K_d-Scaled, m^3/g	5.2×10^{-5}	8.4×10^{-5}	NA*
	Retardation Coef.	6×10^{2}	9×10^{2}	8×10^{3} (1.4**)
Chromate	K_d-Lab, m^3/g	2.04×10^{-5}	1.01×10^{-5}	No Sorption
	K_d-Scaled, m^3/g	2.04×10^{-6}	5.7×10^{-7}	
	Retardation Coef.	2×10^{1}	7×10^{0}	1
Selenite	K_d-Lab, m^3/g	1.02×10^{-4}	5.59×10^{-6}	4.18×10^{-5}
	K_d-Scaled, m^3/g	1.0×10^{-5}	3.1×10^{-7}	NA*
	Retardation Coef.	1×10^{2}	5×10^{0}	6×10^{2} (1.0**)

* NA refers to not available, as a grain-size analysis approach for specific surface area was not possible for the indurated welded tuff.
** Retardation value calculated using a surface-based sorption coefficient, with an assumed fracture aperture of 4×10^{-4}m, used in one sensitivity analysis.

Sorption reactions occur between ions in solution and active reaction sites on the solid surface. The distribution coefficients measured in laboratory experiments are highly dependent upon the number of surface sites available. A persistent difficulty in applying laboratory sorption data to problems of transport through aquifers is the potential inconsistency between the scales of measurement; *i.e.*, scaling the number of surface sites available in the laboratory experiment to the number of surface sites available as groundwater flows through an aquifer. Unfortunately, the number of active reaction sites at the field scale is unknown.

In an attempt to address this scaling issue, the laboratory K_d values were adjusted by considering the specific surface area of the adsorbent used in the experiment and that of the bulk aquifer material as collected from the cores. The K_d values used are from batch sorption experiments with the size fraction smaller than 125 μm. This material had a specific surface area of 13.8 and 16.7 m^2/g for alluvium and tuffaceous sediment, respectively, as measured with the Brunauer-Emmet-Teller (BET) gas adsorption technique (Table 6.6). A second methodology was used to estimate the surface area for the bulk core material. The cores were gently disaggregated, then subjected to a particle size analysis. Assuming a geometry of spheres for the larger size fraction and plates for the clay size (less than 2 μm), a geometric-based surface area was calculated. If the clay is assumed to be predominantly illite, the BET and geometric-based surface are in good agreement (Table 6.6), only differing by as much as a factor of two. When the clay is assumed to be kaolinite, the calculated surface area is approximately one order of magnitude lower than that measured by BET on the small size fraction.

Table 6.6. Specific Surface Area (A_{sp}) Measurements on Core Material, Performed in the Laboratory using BET and Compared to Estimates Based on Grain Size Analysis. The grain-size approach could not be used on the indurated welded tuff. The samples from UC-1-I-1 at 546-551 m, UC-1-I-1 at 985-987 m, and HTH-3 at 296 m were used in the batch sorption experiments.

Borehole	UC-1-I-1	UC-1-I-1	UCe-18	UC-1-I-1	UC-1-I-1	HTH-3
Aquifer material	alluvium	alluvium	alluvium	tuffaceous sediments	tuffaceous sediments	densely welded tuff
Depth, m	546-551	611	1,074-1,077	985-987	1,065	296
BET A_{sp}, m^2/g	13.8	13.4	22.4	16.7	17.7	6.24
Grain-size (kaolinite) A_{sp}, m^2/g	1.39	0.58	1.5	0.93	1.39	NA
Grain-size (illite) A_{sp}, m^2/g	10.5	4.45	11.3	7.1	10.9	NA
Grain-size (kaolinite) A_{sp}/BET A_{sp}	0.1	0.043	0.067	0.056	0.079	NA

The laboratory K_d values were scaled using the following relationship:

$$K_{d\text{-insitu}} = K_{d\text{-lab}}\left(\frac{A_{sp\text{-insitu}}}{A_{sp\text{-BET}}}\right) \qquad (6.3)$$

with A_{sp} the specific surface area, and $A_{sp\text{-insitu}}$ assumed to be approximated by the geometric estimate on the core using the kaolinite approach. For the alluvium, the scaling factor $A_{sp\text{-insitu}}/A_{sp\text{-BET}}$, is 0.1, while it is 0.056 for the tuffaceous sediments. This effectively reduces the laboratory-based distribution coefficient by one to two orders of magnitude, resulting in less sorption.

Rate-of-Uptake Experiments

Rate-of-uptake experiments were performed with all three materials to evaluate the rate of metal ion sorption and indirectly the degree of equilibrium vs. nonequilibrium sorption. The faster the reaction process compared to the groundwater velocity, the more likely it is that the local equilibrium assumption will be valid. Processes very slow compared to the groundwater flow may, on the other hand, suggest sorption under nonequilibrium conditions.

Experiments were performed with the larger size fraction particles (212-595 μm) to maximize the potential to observe any effects of diffusion-limited sorption. Experiments were performed with 10^{-5} and 10^{-6} M metal concentrations. Most experiments were performed with Pb, because of the limitations of using low Sr concentrations with the alluvium sample explained below. All experiments were conducted with synthetic groundwater at constant temperature (25° C).

Details of the experimental results and discussion are presented in Appendix 5. In summary, the rate-of-uptake experiments with Pb suggest very fast kinetics, especially for the tuffaceous sediment and densely welded tuff samples. Equilibrium was achieved within approximately two hours in the alluvium sample, while it was essentially instantaneous in the tuffaceous sediment and densely welded tuff samples. In the tuffaceous sediment sample in particular, the concentration of Pb in solution increased after the initial uptake.

These results seem counterintuitive and inconsistent with diffusion-limited sorption. Given the relatively high surface area of these samples and the relatively minor dependence of specific surface area with particle size, one must assume that these particles have substantial porosity. The only reason why this porosity would not influence the rate of uptake from solution is that a process other than diffusion followed by adsorption is controlling the sorption of Pb. A plausible explanation is surface precipitation. It is conceivable that even under the lower Pb concentration used (10^{-6} M), surface precipitation occurs. Under these conditions, Pb could be sorbing at the external, readily accessible surface area of the particles, resulting in instantaneous sorption.

Column Experiments

Column experiments were conducted with the tuffaceous sediments and the densely welded tuff. Experiments with the alluvium sample proved to be difficult because of the disintegration of the sample in the water. The accumulation of the clay-size particle fraction at the end of the column essentially prevents any flow through the column. Very long times would be required under these conditions to observe any contaminant migration.

Experiments with the tuffaceous sediments and densely welded tuff were conducted in 10-cm-long plastic columns with a diameter of 2.5 cm. The flowrate in the columns was kept constant using a constant head setup. The flowrate achieved this way is a function of the total hydraulic head and the losses in the column, a strong function of the particle size distribution and adsorbent type. The same particle size fraction was used for both columns, *i.e.*, the size fraction between 212 and 595 μm. Owing to the different mineralogical composition of the two materials, the resulting flowrates were different, even though the particle size distribution was presumably

very similar. Under these conditions, the linear velocity in the columns was approximately 8.6 m/d in the densely welded tuff column and 8.6 x 10^{-2} m/d in the tuffaceous sediment column. The latter velocity, although it may appear slow for a laboratory experiment, is still orders of magnitude higher than the groundwater velocity at CNTA.

Both columns were allowed to run for approximately 100 pore volumes (a more detailed explanation of the methodology and analysis of the column experiments is presented in Appendix 5). No breakthrough was observed for any of the columns and for any of the cations under these experimental conditions. These results are consistent with the high retardation factors obtained from batch equilibrium sorption experiments. It should be emphasized that nonequilibrium sorption may contribute to an apparently faster breakthrough compared to a breakthrough based on the equilibrium partitioning of an ion between the two phases. Under these experimental conditions, however, it appears that even if nonequilibrium sorption is occurring, the flowrate is slow enough compared to the time scale of the sorption process so that breakthrough is not observed.

6.3.1.4 Discussion of Experimental Results

These results have significant implications for the migration of contaminants at the CNTA. As mentioned above, the velocities employed in the column experiments were substantially higher than anticipated groundwater velocities. Despite the potential for nonequilibrium sorption, however, the apparent retardation factors were higher than 100, suggesting very strong retardation for these contaminants in the tuffaceous sediments and densely welded tuff. It should be remembered, however, that the particles used in these column experiments were relatively fine (smaller than 600 μm) and that the site-specific K_d, and therefore retardation factor, is a function of the true specific surface area exposed to the groundwater flow. As the particle size increases, the specific surface area decreases, leading to a decrease in the retardation factor. This is particularly important in the case of the densely welded tuff, as will be explained below.

6.3.1.5 Limitations

Use of a distribution coefficient to model contaminant partitioning at the mineral-water interface assumes that the isotherm is linear and that sorption is controlled by equilibrium, rather than by kinetics. Use of distribution coefficients without reference to the specific experimental conditions under which they were obtained can also result in significant errors. Use of a linear isotherm imposes limits on the application of the K_d values to conditions similar to those in the experiments. In addition, many of the reactions leading to sorption behavior are strongly pH dependent, and thus require knowledge of pH conditions for application to transport calculations.

pH values do not vary greatly in groundwater sampled from both the alluvial and volcanic aquifers, generally being in the range of 8.2 to 8.4. Consistent mineralogic controls and the great depth below land surface to the saturated zone suggest no reason to expect significant pH variations in either time or space. Values of pH for water samples are higher in UC-1-P-2SR, up to 9.86, but this reflects samples collected in the cemented section of the borehole and is believed to reflect reactions between borehole fluid and cement. A pH log of the well shows a sharp decrease in pH

below the cemented zone (Chapman *et al.*, 1994). A compilation of data from water samples collected from nuclear cavities and near cavities indicates pH values near neutral to slightly basic, consistent with regional groundwater in the testing areas (Smith *et al.*, 1997).

Ion-Specific Comments

A few additional limitations with respect to the ions used in this study, specifically Pb and Sr, should be mentioned. The aqueous chemistry of Pb is more complex compared to the chemistry of the other cations used in this study (Cs and Sr). Specifically, Pb readily forms several hydrolysis products in the pH range of interest for this study, even at relatively low concentrations. The increased tendency of Pb to hydrolyze explains the substantially lower solubility of this ion compared to Cs and Sr. At higher concentrations, therefore, Pb is certain to precipitate either as a carbonate or a hydroxide or a mixed phase. The onset of bulk precipitation as a function of total Pb concentration and pH can be easily estimated using a geochemical model.

Unfortunately, the maximum dissolved Pb concentration estimated using a thermodynamic equilibrium model may not be applicable when solid phases are present, because of the increased potential of surface precipitation (compared to bulk, homogeneous precipitation from aqueous solutions). The actual onset of surface precipitation may occur at concentrations either higher or lower than predicted from an equilibrium thermodynamic model and cannot be determined easily without additional elaborate spectroscopic experiments. In light of the above, the maximum Pb concentration used in these experiments was 10^{-5} M to minimize the tendency for precipitation. It should be remembered that the distribution coefficients derived from this study are only overall partition coefficients between the two phases and that, based on this macroscopic information alone, it is impossible to distinguish between possible sorption mechanisms.

While Pb concentrations had to be maintained as low as possible because of the potential for surface and bulk precipitation, the uncertainty of the results obtained with Sr increases with decreasing concentrations. The reason for the increased uncertainty is the potential dissolution of small quantities of naturally occurring Sr from the aquifer material. It should be remembered that Sr, an alkaline earth metal, is a relatively common element in the earth's crust. Specifically, the average abundance of Sr in the earth's crust is 384 ppm, making Sr the 15th most abundant element (more abundant than elements like sulfur and carbon). Fortunately, the alluvium sample was the only one with any measurable Sr concentration, resulting in total dissolved Sr approximately 10^{-6} M. Experiments with the alluvium sample below approximately 10^{-5} M Sr are not very meaningful because the concentration dissolved from the solid is on the same order of magnitude as the concentration added to the sample. At higher Sr concentrations, the relative contribution of the naturally occurring Sr decreases and the results can easily be used to estimate the retardation of Sr in the alluvium aquifer.

Modeling Based on Experimental Results: Linearity and Equilibrium

The linearity of an isotherm can be estimated by fitting the data to a nonlinear isotherm, typically the Freundlich isotherm, given by the following equation:

$$S = K_F C_{eq}^{1/n} \quad (6.4)$$

where K_F is the Freundlich parameter equivalent to a distribution coefficient and the exponent 1/n is a measure of the nonlinearity of the isotherm. Obviously, when 1/n equals 1, the Freundlich isotherm is reduced to the linear isotherm and K_F is reduced to K_d. Although, strictly speaking, the linear isotherm would be inappropriate if 1/n were different from 1, given the substantial numerical advantage of using a linear vs. a nonlinear isotherm and the inherent uncertainty in the experimentally determined distribution coefficients, it is often justified to use a linear isotherm and to account for the uncertainties in the distribution coefficients and nonlinearity by sensitivity analysis. Though values of the Freundlich parameter are less than one for Pb and Cs, and more than one for Sr, the non-linearity of the isotherms is not too severe, so that the linear approach is used here.

As was pointed out earlier, modeling the retardation of contaminants of concern in this study was based on equilibrium partitioning derived from equilibrium experiments. Several questions have been raised with respect to the applicability of equilibrium partitioning data derived from experiments with finely ground, large-surface-area aquifer material to modeling the transport of contaminants of concern in the field. The effect of total available surface area for sorption should be obvious. It is reasonable to assume that at the field scale, the specific surface area would be lower and therefore the amount of a contaminant sorbed per mass of sorbent would also be lower. Details on the methodology to account for differences in specific surface area are given in Section 6.3.1.3.

In addition to the surface area scaling issue, modeling the retardation of radionuclides using equilibrium distribution coefficients may lead to significant errors if under local flow conditions equilibrium is not reached. Such sorption is referred to as nonequilibrium sorption and we assume that the local equilibrium assumption does not hold. Obviously, as to which type of sorption, equilibrium or nonequilibrium, would better describe a system depends on the time scale for a particular sorption process compared to groundwater velocity.

The additional experiments performed during this study, *i.e.*, experiments with different size fractions, batch rate-of-uptake experiments, and column experiments, although not always conclusive, provide good evidence that the selected equilibrium distribution coefficients are not unreasonable model parameters. To summarize the results presented above and in Appendix 5, experiments with different size fraction particles do not show any dramatic qualitative differences. These results can be easily explained because the specific surface areas of the different size fractions do not vary significantly and are relatively high, suggesting that a significant portion of the surface area is internal. Although extrapolation to the field scale cannot be made from such a small particle size range, it would not be unreasonable to assume that a significant fraction of the total, field-scale surface area might be accessible. The batch rat-of-uptake experiments for both the tuffaceous sediments and the densely welded tuff shows very fast uptake, suggesting fast sorption on easily accessible surface sites. It is therefore reasonable to assume that these processes are fast compared to the slow groundwater velocity. Finally, the column experiments, although quantitative estimates of the retardation cannot be obtained in the absence of a breakthrough curve, also suggest a very large

retardation factor, consistent with the values obtained from the batch equilibrium sorption experiments.

6.3.2 Assignment of Distribution Coefficient

Distribution coefficients were only determined in laboratory tests for strontium, cesium, lead, chromate, and selenite. The radionuclide source considered here (Table 6.1) includes many more elements, with the total radionuclide source term even more. Those elements that were not subject to the experiments were assigned K_d values by assuming analogous sorptive behavior to those elements with data. This process required assumptions regarding the likely chemical forms to be found, and obviously includes substantial uncertainty. The resulting sorption assignments are given in Table 6.7.

The laboratory analogue for the strongly sorbing cation is lead. In comparative studies of laboratory sorption data, lead is generally weaker sorbing, often by an order of magnitude, compared to some of the elements assigned here (*e.g.*, U, Pu, Np, Am) (Stenhouse and Pottinger, 1994). However, it should be noted that uranium, and to a lesser degree neptunium, had lower sorption affinities under some conditions tested for Yucca Mountain (Triay *et al.*, 1997). The more reduced conditions likely in the confined aquifers at CNTA can be expected to promote stronger sorption affinity as compared to the oxidized unsaturated zone at Yucca Mountain. Data for chromate and selenite are used as the anion analogue for technicium. Strontium and cesium are the moderately sorbing cations. Both were used in the experiments and have no other analogous members in the abbreviated source term considered here.

Table 6.7. Assignment of Sorption Behavior to Radionuclide Source Elements.

Element	No Sorption	Moderately Sorbing Cation	Strongly Sorbing Cation	Anion Sorbing
H (Hydrogen)	X			
C (CO_3) (Carbon)	X			
Cl (Chlorine)	X			
Kr (Krypton)	X			
Sr (Strontium)		X		
Tc (Technetium)				X
I (Iodine)	X			
Cs (Cesium)		X		
Sm (Samarium)			X	
Eu (Europium)			X	
U (Uranium)			X	
Np (Neptunium)			X	
Pu (Plutonium)			X	
Am (Americium)			X	

To follow the in-growth of daughters along decay chains, it is necessary in the modeling process to use the same sorption behavior assigned to the parent for the daughter because radioactive

decay (and daughter ingrowth) are handled in post-processing (individual radionuclides are not tracked during transport, only six solute classes as discussed in Section 7.0). In several cases, this causes a retardation assignment that is contrary to the expected behavior (Table 6.8). For both ^{85}Rb (from the ^{85}Kr parent) and ^{90}Zr (from the ^{90}Sr grandparent), this assignment leads to less retardation than expected for the daughter isotope, and thus a conservative overprediction of transport. For the barium daughters of the cesium isotopes, however, little retardation is expected while they are of necessity modeled using the retardation value assigned for cesium. This assignment was used as the migration of cesium is considered to be of greater interest than that of barium.

Table 6.8. Retardation Coefficients Assigned to Radionuclide Daughter Products that are Contrary to their Expected Transport Behavior. Retardation values were of necessity constant from parent to daughter, resulting variously in over- and under-estimation of sorption for these eight isotopes.

Daughter Isotope	Assigned Retardation Due to Parent (in parenthesis)	Expected Retardation
^{85}Rb	non-sorbing (^{85}Kr)	weakly sorbing
^{90}Zr	moderately sorb (^{90}S)	strongly sorbing
^{134}Ba	moderately sorbing (^{134}Cs)	non-sorbing
^{137}Ba	moderately sorbing (^{137}Cs)	non-sorbing

6.3.3 Calculation of Retardation Factor

The dimensionless retardation factor (R) in cases of fast reversible adsorption with a linear isotherm can be represented by the following equation (Freeze and Cherry, 1979):

$$R = 1 + \frac{\varrho_b}{\theta} K_d \tag{6.5}$$

where K_d [L^3/M] is the distribution coefficient, ϱ_b is the bulk density [M/L^3], and θ is porosity. For the alluvium, a bulk density of 2.04 g/cm^3 is used, based on measurements on core material from UC-1-I-1 (Hoover, 1968a). The bulk density for the tuffaceous sediments is estimated at 2.01 g/cm^3, again based on the same source. The porosity used is that determined for the groundwater transport model, also based on core measurements, a value of 0.18.

Combining Equations (6.3) and (6.5) and using the bulk densities and porosities as discussed above results in a range of retardation values for each absorbate and adsorbent (Table 6.5). Given the interbedded nature of the alluvium and tuffaceous sediments and the hundreds of different realizations of their relative geometries that underlie the flow model, separate retardation mechanisms are not modeled for them. Instead, the lowest retardation coefficient, whether from alluvium or tuffaceous sediments, was applied to the calculations. Thus, the retardation for cesium is 600, for strontium is 700, and for strongly sorbing cations (from lead) is 8,000. Though a retardation for anions of 5 to 7 is indicated from the selenite and chromate distribution coefficients, there is uncertainty around those values (see Appendix 5) so that a conservative retardation of one (no retardation) is used.

These same retardation values are also applied to transport through welded tuffs for the porous medium case. The laboratory distribution coefficients for lead and cesium were similar to those measured in the other material, though the strontium and chromate values were lower in the welded tuff. The indurated nature of the welded tuff unit made it unsuitable for the grain-size distribution approach of scaling the K_d values, and in all cases the scaled alluvium and tuffaceous sediment K_d values that were used in the retardation calculation were at least an order of magnitude lower than the laboratory measured K_d for the welded tuff.

Despite the relatively large porosity indicated for the welded tuff from core data (0.16), the conceptualization of the aquifer considers the bulk of the flow to be through fractures. Transport under fracture flow conditions was also analyzed for the welded tuff. To be consistent with this conceptualization, the sorptive properties of the unit were also reformulated. The retardation factor in fracture flow systems is better represented by:

$$R = 1 + \frac{2K_a}{b} \tag{6.6}$$

where K_a [L] is a surface-based sorption constant ($K_a = K_d/A_{sp}$) and b [L] is the mean fracture aperture (Freeze and Cherry, 1979; Moreno *et al.*, 1988; Frick *et al.*, 1991). Equation (6.6) is only valid for fractured materials in which the porosity of the solid mass between fractures is insignificant (Freeze and Cherry, 1979), an assumption that may well be violated based on the porosity measurements for welded tuff core.

The A_{sp} was measured using BET for welded tuff during the lab experiments and found to be 6.24 m^2/g. No measurements exist for the fracture aperture, b. Welded tuffs are also of great interest to radionuclide transport studies at the NTS, where the units occur throughout the underground test areas. Scoping transport calculations for the NTS estimated fracture apertures for permeable tuffs to range from 2×10^{-4} to 6×10^{-4} m (GeoTrans, 1995). The midpoint of that range, 4×10^{-4} m, was arbitrarily picked as the fracture aperture of the CNTA welded tuffs for the fracture-flow case. Using these values and the laboratory K_d measurements yielded retardation coefficients for anions (chromate) of 1.0, for cesium of 1.4, for strontium of 1.5, and for strongly sorbing cations (lead) of 12. These are the retardation values used for the fracture-flow formulation alone.

6.3.4 Matrix Diffusion

Matrix diffusion is a potentially important mass transfer process by which solutes are removed from high-velocity fracture flowpaths into the surrounding matrix. With the decay of radionuclides, long residence times in the rock matrix actually reduce the mass of contaminant, as well as retard the effective velocity. The analytical approach taken here to include the matrix diffusion process relies on a matrix diffusion parameter, introduced in Section 4.3 and repeated here:

$$\kappa = \frac{\theta_m \sqrt{D_m^* R_m}}{b} \tag{6.7}$$

where D^*_m (m^2/yr) is an effective diffusion coefficient in the rock matrix, b (m) is the fracture half-aperture, θ_m (m^3/m^3) is the rock matrix porosity, and R_m is the dimensionless retardation

coefficient in the rock matrix. The approach to calculating *R* for sorbing radionuclides was described in the previous section.

Matrix diffusion can be expected to be a significant transport process through the welded tuffs at CNTA because the porosity of the matrix blocks is relatively high. Core measurements on 57 samples of welded tuff from CNTA boreholes have a mean porosity of 0.16 with a standard deviation of 0.06.

Effective diffusion coefficients have not been measured on materials from CNTA, but have been measured in a variety of studies reported in the literature. Diffusion coefficients for basically non-sorbing species in materials from Yucca Mountain and the Nevada Test Site range from 1.0×10^{-7} to 3.5×10^{-6} cm^2/sec (Triay *et al.*, 1993; Walter, 1982). These experiments were with fresh surfaces of various volcanic lithologies and involved matrix porosities between 0.06 and 0.4. The recent tracer experiments in the fractured lavas at the Bullion site on the NTS resulted in estimates of diffusion coefficients of 1.4×10^{-7} to 1.9×10^{-7} cm^2/sec (IT Corp., 1998). The diffusion of tritiated water through saturated devitrified tuffs was found to be on the order of 10^{-6} cm^2/sec, while large anions that are excluded from tuff pores due to size and charge still recorded diffusion coefficients on the order of 10^{-7} cm^2/sec (Triay *et al.*, 1997). The International Atomic Energy Agency, in its evaluation of radionuclide diffusion into volcanics at the South Pacific French underground testing sites, used a diffusion coefficient of 1×10^{-7} cm^2/s, referenced as being based on a wealth of non-site-specific laboratory measurements (IAEA, 1998). Given these data to consider, a diffusion coefficient of 1×10^{-7} cm^2/s was used for the CNTA calculations. This value is at the conservative end of the range measured on Great Basin volcanics, as determined through both laboratory and field tests.

The fracture half-aperture probably presents the largest uncertainty in the matrix diffusion calculation. Data are not only lacking on fracture aperture for materials at CNTA, they are lacking in general. Larger fracture apertures are more conservative in the calculation (inhibit matrix diffusion), but are difficult to justify at depths of hundreds of meters due to overburden pressure. Fracture apertures at Yucca Mountain are estimated from 6×10^{-6} to 6.7×10^{-5} m (Peters *et al.*, 1984). Snow (1968) evaluated igneous and metamorphic rocks to 120 m depth and concluded that openings larger than 4×10^{-5} m would be unusual. In the South Pacific work mentioned above, the IAEA used a fracture aperture of 1×10^{-3} m. A value of 5×10^{-4} m was selected as the best guess for a fracture half-aperture for CNTA. This implies fracture openings of 1 millimeter at depths in excess of 1,000 m.

Combining the values described above leads to a matrix diffusion parameter, κ of 0.3. Though it was the intention to select conservative values for the underlying parameters, great uncertainty remains due to lack of data. Given that matrix diffusion is a critical process, this uncertainty is addressed by taking the additional conservative step of reducing the matrix diffusion parameter an order of magnitude, to a value of 0.03.

7.0 Results

The transport calculations employed the random walk particle-tracking method and the three-dimensional Darcy flux fields $q(x)$ on the same grid discretization and domain size as the groundwater flow model. The values of the parameters used in all base-case calculations, as well as the preliminary analysis described below, are listed in Table 7.1. The radionuclide source was centered at the working point of the Faultless test, and was simulated as a cube having edge lengths of 200 m. The infill time necessary for the cavity to re-saturate was taken to be 30 years (Section 6.2.2). An initial source mass of 1.0 was specified owing to the classified status of the Faultless test data, and was divided evenly among 20,000 particles. The number of particles was chosen by comparing the simulation results using 20,000 particles to those using 10,000. This twofold increase in the number of particles was accompanied by a relatively small reduction in the second moment (flux and concentration variance), ensuring that increasing the number of particles by another factor of two would not significantly change the results. The dispersivity values were chosen to be very small for two reasons: 1) the smaller dispersivity leads to more conservative estimates of mass flux and concentrations, and 2) the effect of different sensitivity parameters may be smeared out by the local dispersion if a large value is used. This results from the fact that the dispersive step may become much larger than the advective step due to the very low flow velocities, and as a result, local dispersion may be the dominant mechanism affecting transport. However, different values for local dispersivity are employed in the sensitivity analysis and their impact is evaluated. Our initial analysis indicated that the length of the average advective step was much smaller than the grid size, ensuring that particles did not bypass a grid cell in a single time step (no overshoot problems). Molecular diffusion D^* was assumed negligible and was not included.

The 28 radionuclides (parents and daughters) chosen for investigation were grouped into six solute classes based on their ratio of hydraulic release to geochemical release (refer to Section 6.2.1), geochemical release coefficient (Section 6.2.3), and retardation factor (Section 6.3.3), and are listed in Table 7.2. The transport of the radionuclides in each solute class was simulated as a group, followed by application of the radioactive decay rate appropriate to each individual radionuclide. The total simulation time and the time step are scaled for each class using the appropriate retardation factor in such a way that the same fraction of the cell is traversed by particles as for the cases with no retardation.

The results of the transport simulations are presented in terms of the first two moments of the normalized mass flux and peak concentration breakthrough curves calculated at the UC-1 land-withdrawal boundaries (Figure 7.1).

Table 7.1. Values of Parameters used in the Base-Case Simulations of Transport.

Parameter	Value
Location of Source, Nevada Central Coordinates (m)	
Easting	191,675
Northing	431,075
Elevation (m above msl)	885
Size of Source, edge length of cube (m)	200
Mass of Source, M_0	1.0
Infill Time	30 years
Number of Particles	20,000
Longitudinal Dispersivity, T_L (m)	0.05
Transverse Dispersivity, T_T (m)	0.005
Molecular Diffusion, D^*	0
Effective Porosity	0.18
Number of Realizations	110

Table 7.2. Values of Parameters Specific to Individual Solute Classes*.

Parameter	Class 1	Class 2	Class 3	Class 4	Class 5	Class 6
Total Time, t (years)	1.37×10^6	1.37×10^6	9.59×10^8	1.37×10^6	8.22×10^8	1.10×10^{10}
Time Step, Δt (years)	110	110	7.67×10^4	110	6.58×10^4	8.77×10^5
Release Ratio, Hydraulic Release / Geochemical Release	1.0/0	.5/.5	.6/.4	.05/.95	.8/.2	.05/.95
Retardation Factor	1	1	700	1	600	8,000
Geochemical Release Coefficient (1/day)	NA	1.17×10^{-6}	1.17×10^{-6}	1.17×10^{-6}	1.17×10^{-6}	1.17×10^{-6}

*Class 1: ^{3}H, ^{14}C, ^{85}Kr and ^{85}Rb
Class 2: ^{36}Cl and ^{129}I
Class 3: ^{90}Sr, ^{90}Y and ^{90}Zr
Class 4: ^{99}Tc
Class 5: ^{134}Cs, ^{134}Ba, ^{137}Cs and ^{137}Ba
Class 6: ^{151}Sm, ^{151}Eu, ^{152}Eu, ^{152}Gd, ^{154}Eu, ^{154}Gd, ^{234}U, ^{238}U, ^{237}Np, ^{239}Pu, ^{240}Pu, ^{236}U and ^{241}Am

7.1 Preliminary Analysis

Before discussing the detailed results of the transport simulations, two sets of simulations are presented that aid in the choice of the base case and the number of realizations considered. In the first part, an analysis of the directions of transport from the Faultless cavity as they relate to computing breakthrough curves at the land-withdrawal boundaries is presented. The second part of this section presents a comparison between a porous medium approach for the entire domain with uniform porosity of 0.18, and a simulated fracture approach of a system with a fractured welded tuff unit (Category 3) having porosity of 0.005 plus matrix diffusion. The objective of these two sets of preliminary simulations is to identify the most critical scenario (most conservative) that should be

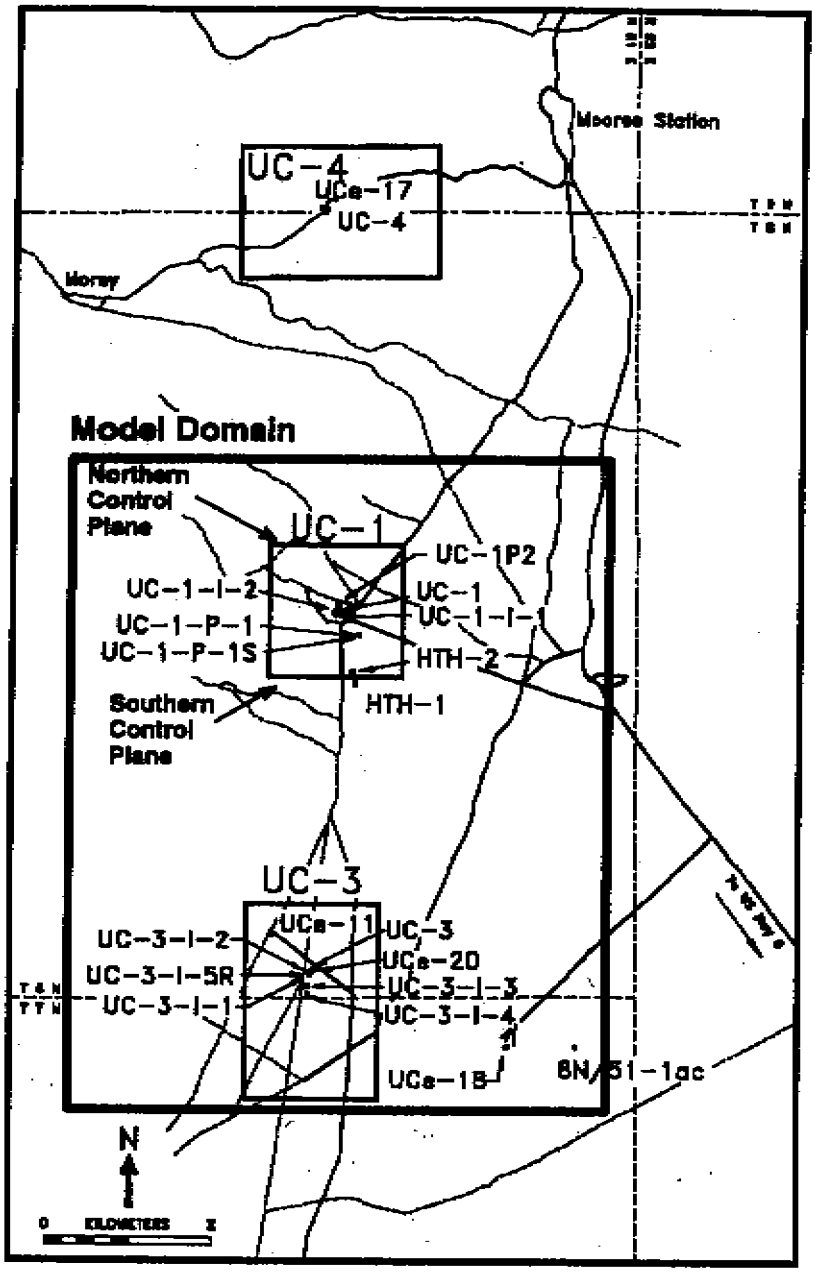

Figure 7.1. Map showing the locations of the breakthrough planes coincident with the northern and southern land-withdrawal boundaries.

considered as a base case and in the sensitivity analysis. Also, the choice of the flow realizations that represent the base case is determined by analyzing the transport results of the entire set of realizations including those showing no lateral breakthrough, but vertical movement across the domain's lower boundary.

7.1.1 Transport Directions and Number of Realizations

All the results presented in subsequent sections are based on 110 realizations of the flow field. Initially, 225 realizations of the conductivity field and thus the velocity field were generated. Preliminary transport simulations indicated that a large number of realizations did not show any breakthrough at the control plane. All the particles in these realizations moved vertically downward until they crossed the bottom of the modeled domain. Some other realizations showed weak breakthrough at the northern land-withdrawal boundary with most of the particles moving towards the domain bottom. These realizations were removed from subsequent analysis and the remaining 110 realizations, which were used in all transport simulations, were those cases that result in close to 100 percent mass breakthrough across the northern land-withdrawal boundary within the chosen simulation time (*e.g.*, 1.37×10^6 years for Class 1). This choice is considered conservative in the sense that it maximizes the mass flux and peak concentrations when only northern movement is considered. None of the initial 225 realizations showed any breakthrough at the southern land-withdrawal boundary.

To justify this choice and shed some light on the results of the total 225 realizations, a comparison is made of the results of simulations using the full set of realizations with those using only the 110 realizations with 100 percent northern breakthrough. All these simulations were performed for Case 1 with 100 percent hydraulic release and no retardation. For ^{14}C, Figure 7.2 shows the decayed mean and the mean plus one standard deviation of the total mass flux and peak concentration crossing the northern control plane using both the total 225 realizations and the selected 110 realizations. It is clear that using 110 realizations with full breakthrough to the north is more conservative than averaging over the full set of realizations including those with no or minimum breakthrough to the north. Analyzing the 110 realizations proves more conservative than using the full set of realizations.

There still exists the concern that the particles escaping the bottom of the simulation domain may reach a fast flowing region, which may carry these particles to the northern control plane. To alleviate this concern, Figure 7.3 plotsthe mean of the mass flux and the peak concentration of ^{14}C crossing the bottom boundary and compares it to the northern values using 225 and 110 realizations. The values of the mass flux and concentration across the domain's bottom are very small compared to those obtained at the northern control plane using the 110 realizations. For the mass flux, one may argue that when these particles crossing the bottom reach a fast flow region and then breakthrough to the north, they will add to the total mass flux crossing the northern land-withdrawal boundary. However, these particles still need some time to migrate to the north and therefore decay will reduce the total mass that eventually crosses the control plane. Even considering the unrealistic scenario that the mass flux across the bottom will just be mapped to the northern boundary, the peak value of this flux is about 10 percent of the peak value obtained using the 110 realizations, which lies within the uncertainty of the estimate. The peak concentration along the northern boundary would not be affected by the particles crossing the bottom and then migrating north. This is because these particles will eventually cross the control plane at a location below the boundaries considered in the modeling.

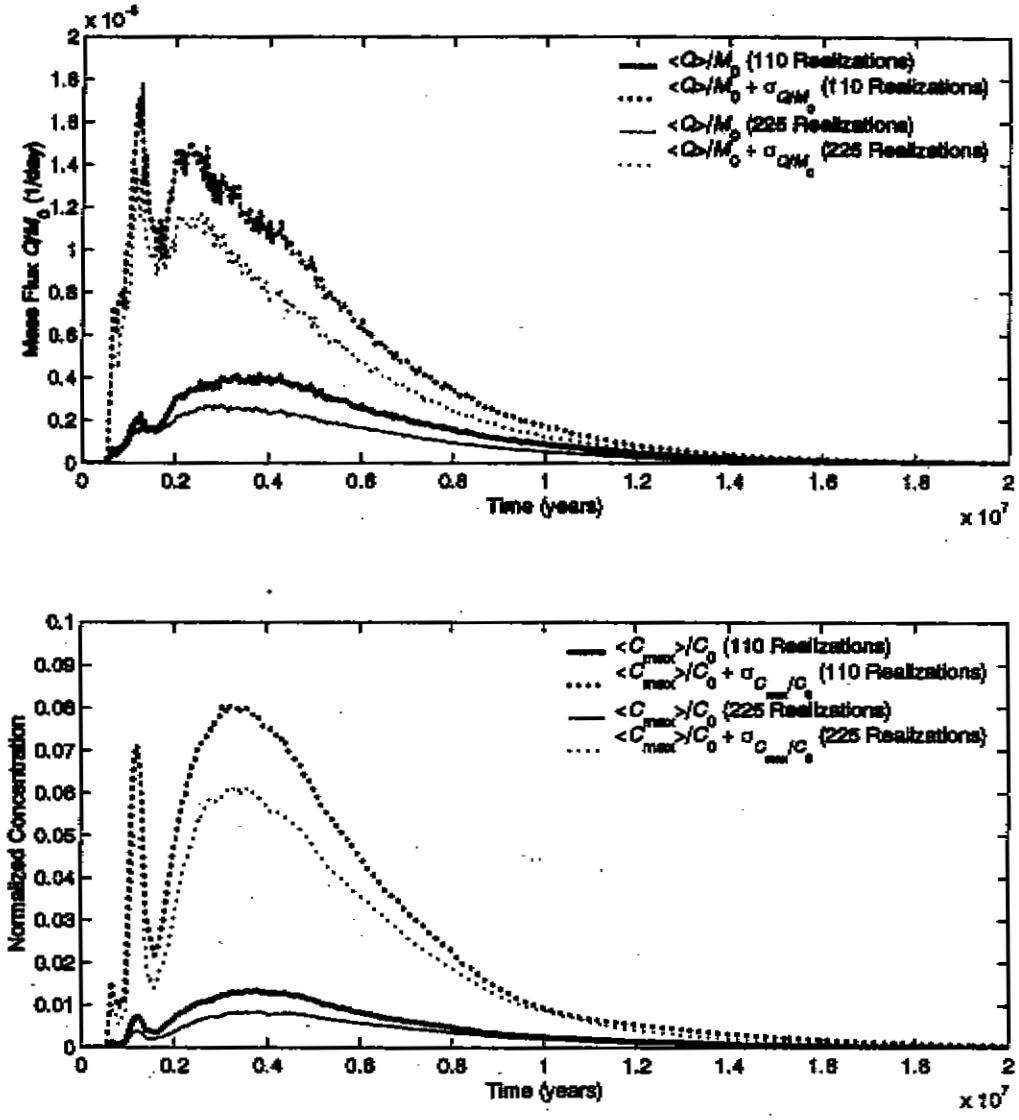

Figure 7.2. Plots showing decayed ^{14}C breakthrough at the northern land-withdrawal boundary using 110 realizations that showed 100 percent northern breakthrough as compared to using all 225 realizations of the flow field. All subsequent simulations of transport use the selected 100 realizations, thereby maximizing mass flux and concentration across the breakthrough plane.

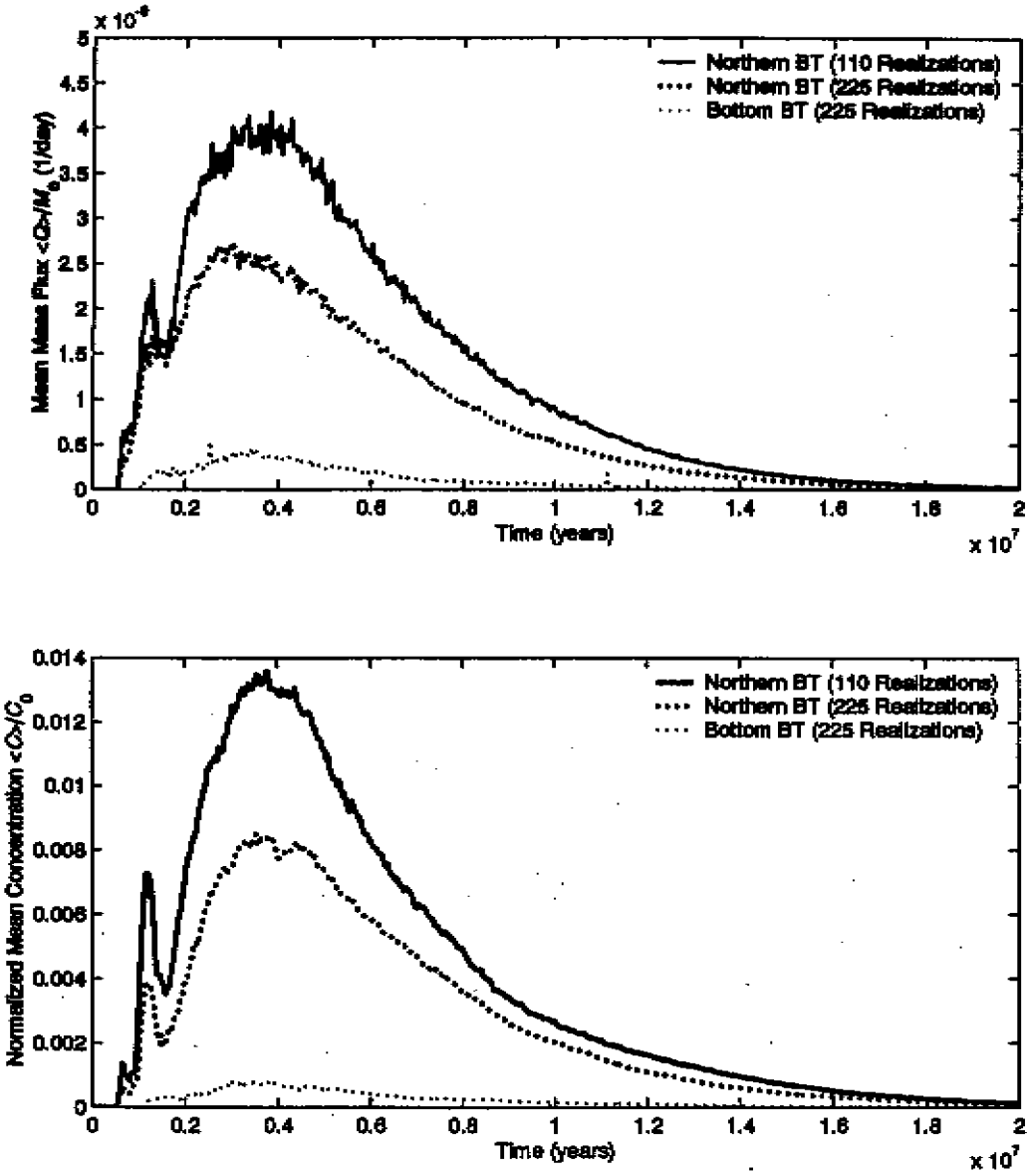

Figure 7.3. Plots showing decayed ^{14}C breakthrough at the northern land-withdrawal boundary (using the selected 100 and the full 225 realizations of the flow field) as compared to the breakthrough at the bottom of the model domain (using the full 225 realization of the flow field).

These particles will not contribute to the concentration values at the cells above the bottom of the domain, and therefore the estimate of peak concentration will not be affected.

These results indicate that focusing on the realizations that show 100 percent northern breakthrough is the most conservative choice. Neglecting those realizations with mostly vertical downward movement is not underestimating the predicted fluxes or concentration at the land-withdrawal boundary. In case these particles keep moving vertically downward, they will eventually decay while still within the land-withdrawal area. If these particles reach a fast moving flow region underneath the model domain, the magnitude of flux or concentration that may be added to the land-withdrawal boundary is very small, if any, and lies within the uncertainty of the estimate. Since none of the initial 225 realizations showed any breakthrough at the southern land-withdrawal boundary, the breakthrough curves at the northern land-withdrawal boundary are presented for all cases except for those involving prompt injection, as will be seen later.

7.1.2 Porous Medium Versus Fractured System

Measurements of total porosity on core samples from the site are likely to be representative of effective flow porosity in the unconsolidated and clastic sections of the alluvium, tuffaceous sediments, and nonwelded tuffs. However, these measurements may overestimate the effective flow porosity of the fractured densely welded tuffs, reported as a mean value of 0.16. For example, there is a single porosity value reported for a welded tuff in UCe-17 (outside the model domain) that was below the detection limit of 0.001 (Hoover, 1968a). This suggests that a lower porosity value than that used in the porous medium approach should be considered to represent the effective porosity in a fracture flow system through the densely welded tuffs. Therefore, a survey was conducted of published total and effective porosity values measured in densely welded tuffs at the NTS and the Yucca Mountain project. The Environmental Restoration Database of hydrologic parameters (Rehfeldt *et al.*, 1996) reports a range from 0.027 to 0.45 for porosity values for welded tuffs at the NTS, while Schenker *et al.* (1995) report a range from 0.004 to 0.48 for welded tuffs at Yucca Mountain. Blankennagel and Weir (1973) used a minimum effective fracture porosity of 0.005 for estimates of groundwater velocity beneath Pahute Mesa, NTS. For the fracture flow conceptualization, a value of 0.005 was selected for use as the effective flow porosity for all cells in Category 3; cells in Categories 1 and 2 remained at the 0.18 value used in the porous medium case. This value is two orders of magnitude lower than the mean of the CNTA porosity data for densely welded tuffs (0.16 average of 57 values), but is of the same order as the one outlier (reported as <0.001) given by Hoover (1968a).

The conceptualization of flow restricted to fractures for the welded tuff unit has implications not only for effective porosity, but also for retardation behavior. As described in Section 6.3, for the fracture flow case, the retardation factor was calculated using a surface-based sorption constant and an assumed mean fracture aperture, resulting in retardation coefficients of 1.03 for anions, 1.4 for cesium, 1.5 for strontium, and 12 for strongly sorbing cations, that are up to two orders of magnitude lower than those used in the porous medium case. It should be emphasized that under these conceptualized flow conditions (fracture flow), kinetic retardation processes, such as matrix

diffusion, are likely to play a significant role. As will be seen shortly, the effect of matrix diffusion serves to moderate (or dominate) the impact of the lower retardation and porosity values (higher velocities, short arrival times, and less decay), by allowing the removal of contaminants from the flow field (fractures) into the rock matrix while allowing decay.

For all six radionuclide groups shown in Table 7.2, two settings were considered. First a uniform-porosity porous medium was considered with 0.18 effective porosity applied to all categories in the simulated domain. Processes included in the transport simulations for this case were advection, local dispersion, retardation, glass dissolution, and radioactive decay. Secondly, model cells that belong to Category 3 (welded tuff) were assumed to behave like a fractured system and as such were assigned a fracture porosity of 0.005, whereas cells of the other two categories were assigned the 0.18 porosity value. In addition, retardation coefficients were also changed for cells in Category 3 as discussed above. The transport simulations for this case included the same processes as in the first setting with the additional process of matrix diffusion that was handled in a post-processing mode. The results of all six scenarios in both cases are presented in Appendix 6. Following is a discussion of some specific examples and comparisons between the two cases.

Figure 7.4 presents the total mass flux and the peak concentration breakthrough curves (mean and mean plus one standard deviation) for ^{3}H using a fracture flow system and two matrix diffusion parameters, 0.03 and 0.06. It should be noted here that Figure 7.4 has two different scales shown by the numbers at the left (for $\kappa = 0.06$) and the right (for $\kappa = 0.03$). It is clear that changing the matrix diffusion parameter by a factor of 2 leads to dramatic changes in the resulting concentrations and mass fluxes. By decreasing the matrix diffusion effect, the peak mass flux increased by about three orders of magnitude, and the peak concentration increased less than two orders of magnitude. The effect of matrix diffusion is usually manifest in a delayed mass arrival and a very long tail. This effect is not very clear for ^{3}H since it has a very short half-life. The short half-life and the slower velocity in the case with porous medium porosity of 0.18 result in no breakthrough for ^{3}H in that scenario. The short half-life of ^{3}H is magnifying the difference between the case of porous medium flow and fracture flow with matrix diffusion. It also shows a great sensitivity to the matrix diffusion coefficient, κ, in the fracture flow scenario. These findings and explanations are supported by the results of Figure 7.5 for ^{14}C. The figure displays the comparison between the porous medium case and the fracture flow scenario with two different matrix diffusion parameters, $\kappa = 0.03$, and 0.06. Three different scales for the vertical axis exist as shown by the numbers on the figure. The difference between the porous medium case and the fracture flow case is less dramatic than for ^{3}H. Carbon-14 mass flux and concentrations are two orders of magnitude higher for the porous medium case relative to fracture flow with $\kappa = 0.03$. The sensitivity of the flux and concentrations to the parameter κ is also less dramatic than for ^{3}H. There is only a factor of 4-6 reduction in mass flux and concentration of ^{14}C when κ is doubled. The long tail of the breakthrough curve is also more evident in this case.

The previous results show that the porous medium scenario may be more or less conservative than the fracture flow scenario depending on the half-life of the radionuclide considered. Transport of ^{3}H, with a short half-life, is more conservatively addressed within a fracture flow system, whereas

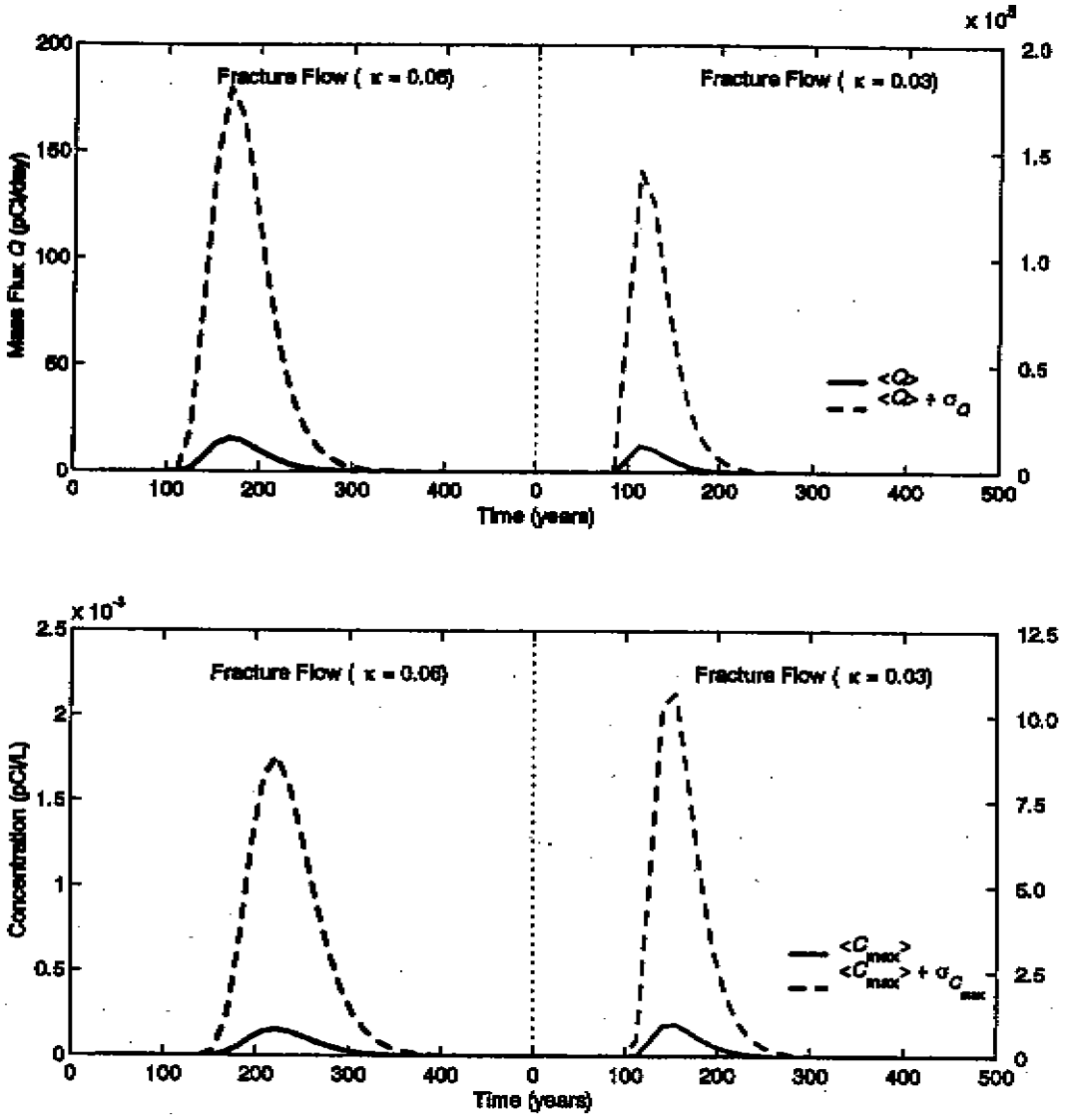

Figure 7.4. Plots comparing decayed ^{3}H breakthrough for two values of the matrix diffusion parameter, κ, in the fracture flow formulation. Note the different scales used on the vertical axes of these plots.

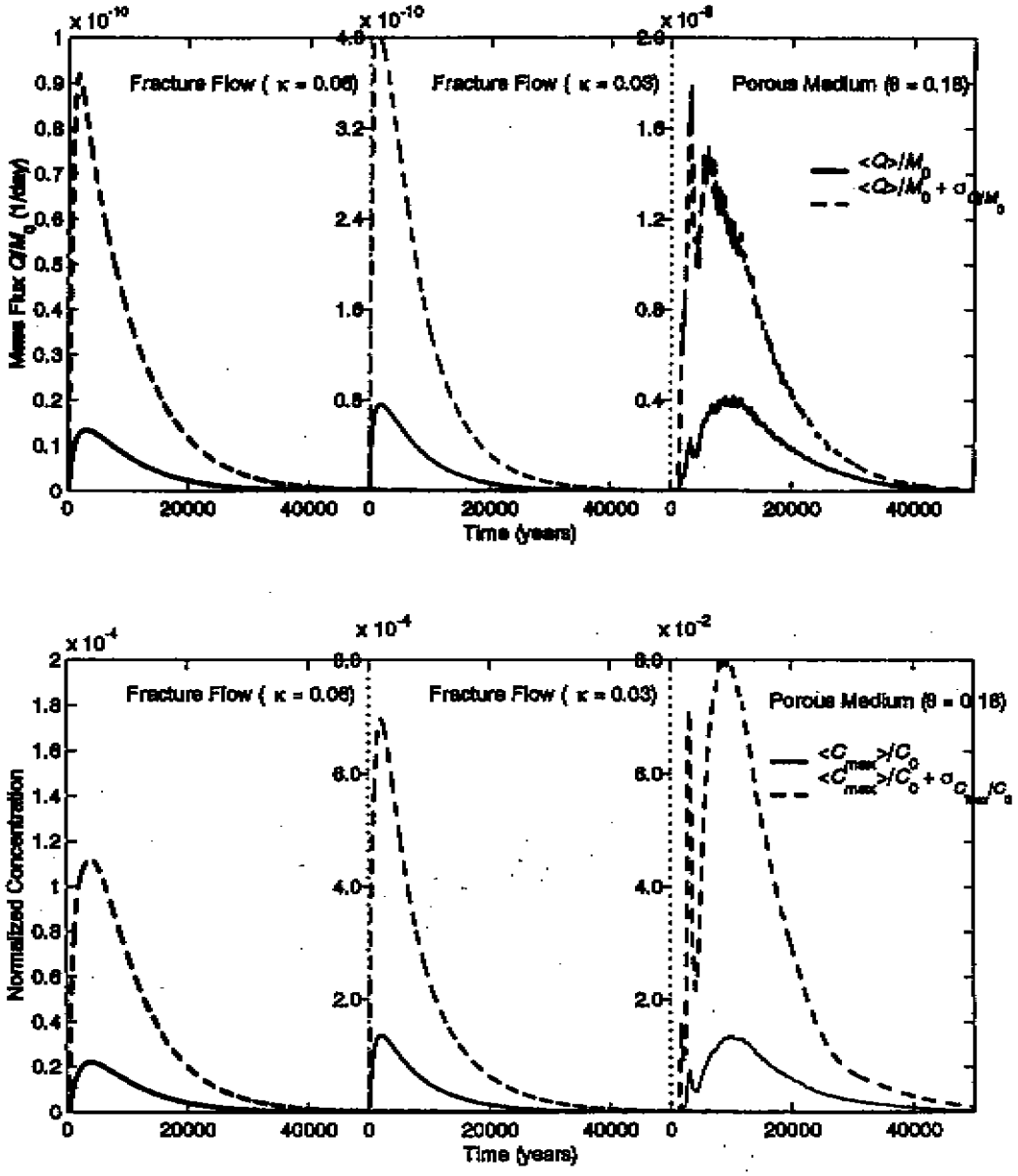

Figure 7.5. Plots showing the decayed ^{14}C breakthrough for two values of the matrix diffusion parameter, κ, in the fracture flow formulation as compared to breakthrough in the porous medium formulation. Note the different scales used on the vertical axes of these plots.

the porous medium approach is more appropriate for long lived nuclides such as ^{14}C, ^{36}Cl, and ^{99g}Tc. Table 7.3 shows the comparison between the porous medium scenario, the fracture flow scenario, and a fracture flow scenario without matrix diffusion ($\kappa = 0.0$). The latter scenario is only added for comparison purposes and to highlight the importance of the matrix diffusion process, which acts as a natural remediator for radionuclides. It is important to emphasize that this latter scenario is physically unrealistic especially with the very large matrix porosity of 0.16 inferred from the core data. The comparison in Table 7.3 is presented for one selected element from each of the six groups shown in Table 7.2 and discussed earlier in Section 6.1. It can be seen that only case 1, ^{3}H concentrations, are higher for the fracture flow with matrix diffusion than for the porous medium case. The rest of the radionuclides in Table 7.3 show higher concentrations and mass fluxes when studied with the porous medium assumption. When the retardation in the matrix rock is high (e.g., cases 3, 5, and 6), the matrix diffusion parameter, κ, becomes large. This enhances the effect of matrix diffusion, which eliminates the total mass by retaining it in the rock matrix for very long times allowing for the decay. For this reason, ^{90}Sr, ^{137}Cs, and ^{238}U do not show any breakthrough at the northern control plane. Neglecting matrix diffusion in a fracture flow scenario leads to the highest concentrations and mass fluxes in all cases presented in Table 7.3 and in Appendix 6. Again, this scenario is unrealistic and is considered here only for comparison purposes.

Based on the above analysis, it was found that the majority of the radionuclides considered in the source term were significantly affected by matrix diffusion to the extent that the effect of the accelerated flow in the fractures was counterbalanced by the diffusion, retardation and decay into the rock matrix. As a result, the final concentrations and mass fluxes at the land-withdrawal boundary were smaller than those resulting from the uniform-porosity, porous medium approach. Only two radionuclides with very short half-life have the fracture flow approach more critical than the porous medium. Therefore, the porous medium scenario is considered to be the base case, as it represents a more conservative approach for most of the radionuclides. The rest of the transport simulations and sensitivity analysis will utilize this formulation. The results in Appendix 6 show the fracture flow scenario for all the six groups with only ^{3}H (half-life = 4.49×10^{3} days) and ^{85}Kr (half-life = 3.91×10^{3} days) being critical for this case. It should be recalled that the fracture flow analysis uses a matrix diffusion parameter ($\kappa = 0.03$) that is 10 times smaller than the best estimate of 0.3, and thus is in itself a conservative depiction of fracture flow.

The following uses the selected base case of a porous medium with uniform effective flow porosity of 0.18. The analysis is performed using 110 realizations as discussed above and all scenarios are evaluated using the input data of Tables 7.1 and 7.2. The sensitivity analyses are performed on the same base case and the results of all cases considered in the transport simulations are summarized in Appendix 6.

7.2 Undecayed Breakthrough Curves

The effects of the hydraulic/geochemical release ratio, the retardation, and the geochemical release factor of the six solute classes are most effectively examined without the effects of radioactive decay. This is because the widely differing decay rates of the individual radionuclides

Table 7.3. Tabulation of Mass Flux and Concentration Results for the Porous Medium (PM) Formulation and the Fracture Flow (FF) Formulation with and without Matrix Diffusion. One radionuclide from each of the six solute classes is presented. The results include peak mass flux (Q_{max}), standard deviation of peak mass flux, $(\sigma Q)_{max}$, normalized peak mean concentration (C_{max}), standard deviation of normalized peak mean concentration $(\sigma C)_{max}$, and time of occurrence.

Radionuclide	Half-life (days)	Scenario	κ ($days^{-1/2}$)	Q_{max} (day^{-1})	Time (years)	$(\sigma Q)_{max}$ (day^{-1})	Time (years)	C_{max} (normalized)	Time (years)	$(\sigma C)_{max}$ (normalized)	Time (years)
^{3}H - Case 1	4.49E+3	PM	NA	0.0000E+000	NA	0.0000E+000	NA	0.0000E+000	NA	0.0000E+000	NA
		FF	0.03	4.7423E-015	1.1221E+002	4.9467E-014	1.1221E+002	6.2760E-010	1.5331E+002	5.3801E-009	1.5331E+002
		FF	0.00	8.4037E-012	8.4815E+001	8.6294E-011	7.1116E+001	8.8009E-006	8.4815E+001	9.1884E-005	8.4815E+001
^{36}Cl - Case 2	1.1E+08	PM	NA	2.4081E-008	3.0277E+004	2.8944E-008	1.4934E+004	9.7575E-002	4.9893E+004	2.7390E-001	1.9646E+004
		FF	0.03	5.6753E-011	3.9341E+003	2.2806E-010	3.9478E+003	1.2775E-004	3.4547E+003	4.9636E-004	3.4410E+003
		FF	0.00	3.3078E-008	2.0016E+004	4.7490E-008	4.3862E+003	1.4384E-001	2.8551E+004	2.8991E-001	1.7304E+004
^{90}Sr - Case 3	1.06E+4	PM	NA	0.0000E+000	NA	0.0000E+000	NA	0.0000E+000	NA	0.0000E+000	NA
		FF	0.79	0.0000E+000	NA	0.0000E+000	NA	0.0000E+000	NA	0.0000E+000	NA
		FF	0.00	2.4975E-011	1.1221E+002	2.2120E-010	1.1221E+002	4.4047E-005	1.3276E+002	4.5986E-004	1.3276E+002
^{99}Tc - Case 4	7.78 E+07	PM	NA	2.3411E-008	3.2123E+004	2.7004E-008	1.4260E+004	9.1750E-002	4.9438E+004	2.6000E-001	1.9739E+004
		FF	0.03	1.8729E-011	9.3285E+003	5.4909E-011	7.6846E+003	7.2722E-005	1.0972E+004	2.3447E-004	6.0408E+003
		FF	0.00	1.8256E-008	2.1164E+004	2.1475E-008	7.3559E+003	1.1532E-001	3.1794E+004	1.7572E-001	8.8342E+004
^{137}Cs - Case 5	1.10E+04	PM	NA	0.0000E+000	NA	0.0000E+000	NA	0.0000E+000	NA	0.0000E+000	NA
		FF	0.73	0.0000E+000	NA	0.0000E+000	NA	0.0000E+000	NA	0.0000E+000	NA
		FF	0.00	5.3421E-013	2.4920E+002	5.5773E-012	2.4920E+002	3.3953E-006	2.4920E+002	3.5448E-005	2.4920E+002
^{238}U - Case 6	1.64E+12	PM	NA	3.1013E-012	2.3233E+008	3.7869E-012	1.0606E+008	1.0301E-001	3.8400E+008	2.8147E-001	4.0329E+008
		FF	2.68	0.0000E+000	NA	0.0000E+000	NA	0.0000E+000	NA	0.0000E+000	NA
		FF	0.00	8.0227E-010	4.4136E+003	2.8125E-009	4.4136E+003	3.5487E-002	7.8578E+005	1.4452E-001	8.7971E+003

conceal the general release and retardation behavior. Analysis of the base-case flow realizations revealed that there was no breakthrough at the southern control plane during the simulation time of 1.1×10^{10} years. This is the result of the strong northward-directed flow simulated in the densely welded tuffs at the base of the model combined with the vertical downward flow around the test.

Figure 7.6 shows the undecayed breakthrough curves for the six solute classes. Note that the time scale begins at 1,000 years and extends to 1.0×10^{10} years. Even without decay, essentially no mass was simulated to pass the northern breakthrough plane earlier than 1,000 years after the test. It is clear that the shapes of the six curves are almost identical with only shifted location and peak height. As Table 7.2 indicates, the six classes differ in two aspects: the sorption characteristics reflected in the different retardation factors, and the hydraulic/geochemical release ratio. The latter has a minor effect on the rising limb of the breakthrough curve as can be seen if Classes 1 and 2 are compared. This is due to the fact that the travel time to the control pane is much longer than the time scale within which all glass dissolution occurs and therefore all particles are released to the domain. The effect of the retardation factor is evident in the delayed arrival of mass to the control plane as retardation increases. Careful examination of Figure 7.6 indicates that the area under each of the six curves is exactly the same, which should be equivalent to the initial mass, M_0. If Class 1 is compared to to Class 5, for example, it can be seen that the peak flux dropped from 2.6×10^{-8} in Class 1 to 4.0×10^{-11} in Class 5 with a factor of about 650. On the other hand, Class 5 is spanning a time frame of about 8.5×10^{8} years, which is about 650 times larger than that spanned by the breakthrough curve

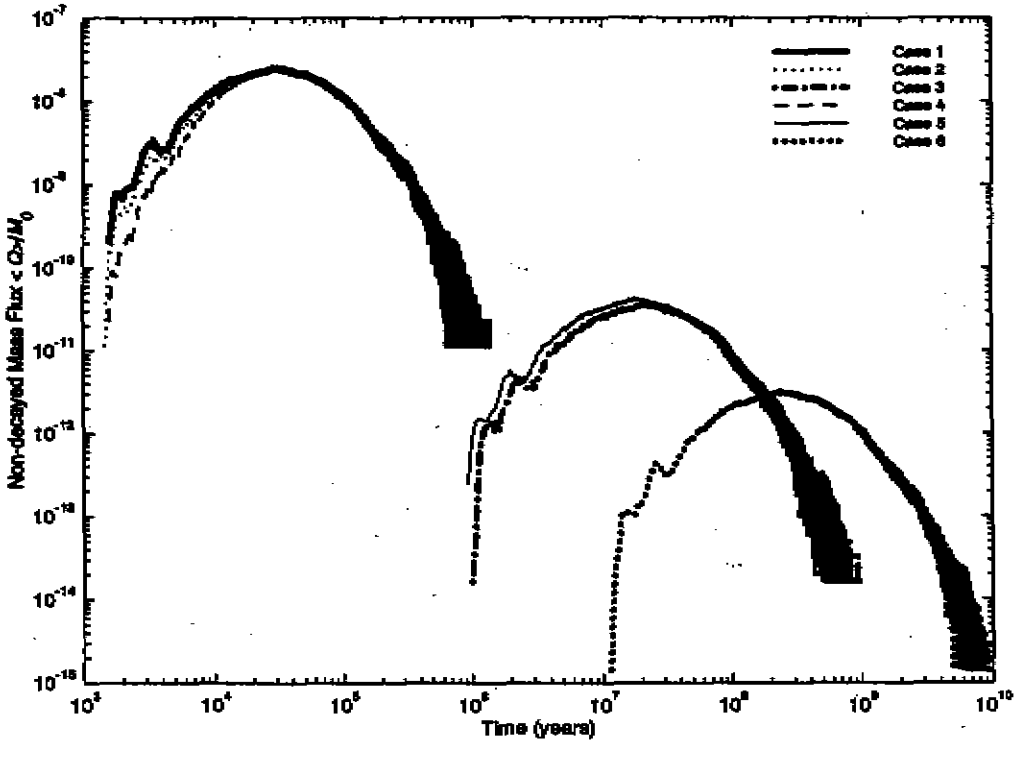

Figure 7.6. Plot of the undecayed breakthrough curves for the six solute classes.

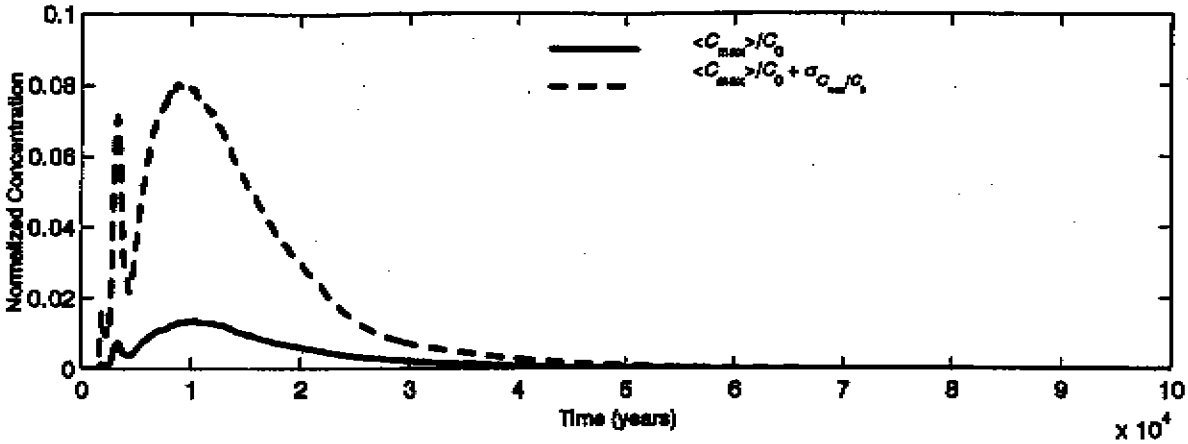

Figure 7.7. Plot of the decayed and normalized breakthrough curve for the base-case transport of ^{14}C, a member of Solute Class 1.

of Class 1 (about 1.5 x 10^6 years). Therefore, integrating the two breakthrough curves with time yields exactly the same total mass.

7.3 Breakthrough with Radioactive Decay

The normalized values of peak mass flux and concentration at the control plane, and their standard deviations, are listed for all radionuclides in Appendix 6. These values include radioactive decay and are based on unit mass at the source. Class 1 radionuclides have no retardation and 100 percent hydraulic release, which means that all particles are released to the flow field and allowed to move at the same time. The long travel times to the control plane result in essentially complete radioactive decay for nuclides with short half-lives. This includes ^3H in Class 1, ^{90}Sr in Class 3, and ^{137}Cs in Class 5. Classes 3 and 5 include a portion of slow release due to glass dissolution and retardation by sorption.

Carbon-14, with a half-life about three orders of magnitude longer than tritium, shows significant mass flux (Appendix 6) and peak concentration at the control plane (Figure 7.7). The peak of the mass flux is about 4.0 x 10^{-9} M_0 (mass/day) and occurs at about 10,400 years after detonation. The peak concentration is found to be about one percent of the initial concentration, as shown in Figure 7.8, and occurs at the same time as the peak mass flux. The uncertainty of the results is large due to the heterogeneous flow field and the limited number of realizations characterizing this heterogeneity. That is to say that as the variability in the hydraulic conductivity increases, more realizations are needed to properly sample the full distribution of the conductivity values. In addition, using a limited number of particles may lead to sampling errors (very large numbers or very low numbers of particles in the grid cells) that add to the uncertainty of the estimates. Increasing the number of realizations and the number of particles would dramatically reduce flux and concentration variances, a task that is computationally very demanding. The ensemble averages, however, are much less sensitive to the number of realizations and number of particles.

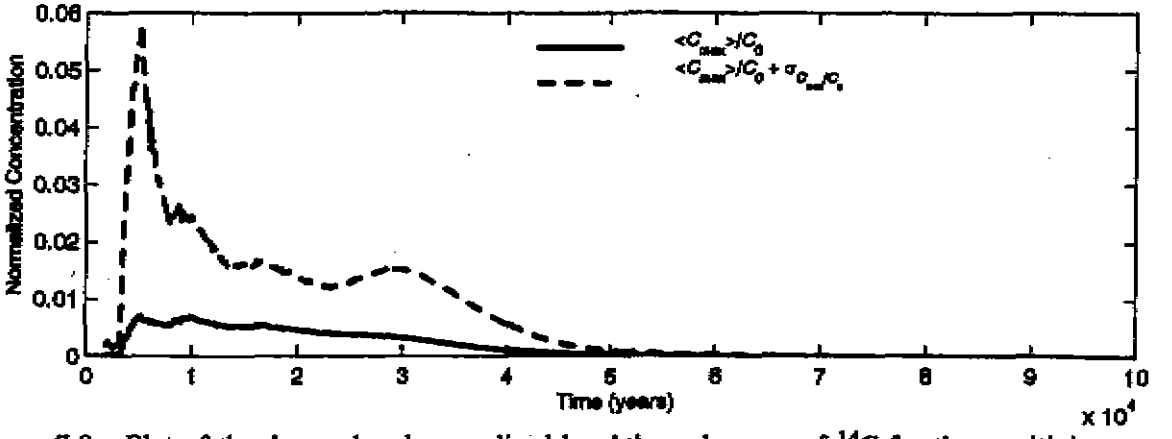

Figure 7.8. Plot of the decayed and normalized breakthrough curve of ^{14}C for the sensitivity case of increased vertical correlation length of $\log_{10} K$.

7.4 Sensitivity Analysis

All flow and transport models incorporate a degree of uncertainty in hydrogeologic parameters, boundary conditions, flow conceptualization, and model construction. Uncertainty in hydraulic conductivity was addressed in the CNTA model by using a stochastic approach to simulate the K fields based on multiple measurements of hydraulic conductivity. This quantitative approach incorporated both the spatial variability of K and the uncertainty in the K measurements. However, other elements of the flow and transport model incorporate uncertainty that could not be quantified in the same way, and sensitivity analyses were conducted for a selected number of these. The boundary conditions are an aspect of the model whose uncertainty was not tested, owing to limited site-specific data pertinent to the analysis. The selection and uncertainty in boundary conditions are discussed in detail in Section 5.4.

The ASTM Standard Guide for Conducting a Sensitivity Analysis D 5611-94 was used as a general guide for the sensitivity analysis. Model sensitivity was addressed by adjusting selected input parameters and/or model configurations and evaluating the resultant impacts on transport behavior. As with the base-case simulations, the same 110 flow realizations that showed 100 percent breakthrough at the control plane were used for the sensitivity simulations. The sensitivity cases included analysis of the vertical correlation of K, mean log K in the alluvium, prompt injection of radionuclides upon detonation, and local dispersivity.

7.4.1 Vertical Correlation Length of Hydraulic Conductivity

The spatial analysis of the K data indicated that the value of the vertical correlation length ranged from 50 to 150 m for all three categories. The value of 50 m was used in the base-case K maps because it improved the calibration of the flow model. The flow model results indicated that flow is primarily vertical near the Faultless cavity and therefore a sensitivity case was developed to evaluate the impacts on transport of increased hydraulic continuity in the vertical direction. For this case, the vertical correlation length of all three categories was increased to 150 m, the maximum value estimated during the spatial analysis of K.

The results show that transport toward the north slightly decreased, and breakthrough concentrations remained far below detectable levels. The results for ^{14}C illustrate how transport toward the northern control plane decreased slightly for long-lived radionuclides (compare Figure 7.7 and Figure 7.8). The normalized peak concentration of ^{14}C shows a small decline from 1.36 x 10^{-2} in the base case to 7.05 x 10^{-3} in the sensitivity case, while the time of the peak was reduced from 10,330 years to 5181 years. The mass passing the breakthrough plane also decreased in the sensitivity case (Appendix 6). The reduced concentration and the lower peak mass flux are the result of increased plume spreading in the vertical direction in response to the higher λ_z. This leads to increased numbers of particles reaching the bottom of the modeled domain faster than in the base case; vertical movement is increased in the sensitivity case, whereas horizontal transport is not significantly impacted. The end result is a smaller number of particles reaching the control plane as compared to the base case.

7.4.2 Hydraulic Conductivity of Alluvium

The mean $\log_{10} K$ value of -2.62 used for the alluvium in the base case was calculated from the packer-test data, all of which were collected in wells within the model domain. A pumping test conducted in HTH-1 and HTH-2 in the alluvium resulted in estimates of $\log_{10} K$ of -0.25 and -0.02, depending on the aquifer thickness used. To test the sensitivity of the model to higher K in the alluvium, the mean $\log_{10} K$ of cells in Category 1 was increased to -0.6 (a higher value was not used because the packer data clearly indicate a trend of declining K with increasing depth in the alluvium). The variance in Category 1 was not modified, nor were the K statistics of the other two categories. The higher K of this sensitivity case is considered unlikely to represent the field conditions, given the bulk of hydraulic conductivity data available.

It should be noted that despite the southward-directed hydraulic gradient in the alluvium, the base case indicated that no breakthrough occurred at the southern land-withdrawal boundary. This was related in part to the relatively low K of the alluvial sediments. More importantly, however, was the downward-directed hydraulic gradient that prevented groundwater movement up to the alluvium from the cavity. The simulation of a higher mean K in the alluvium did not alter the modeled direction of flow between the alluvium and underlying volcanics. Comparing the vertical head profiles (Figure 7.9) reveals an increase in upward vertical gradient within the alluvium itself for the case with higher hydraulic conductivity, but virtually no change between simulated heads in the lower alluvium and in the volcanics. As the source of the radionuclides is in the volcanic section, the transport calculations are insensitive to the mean K value assigned to the alluvium.

7.4.3 Prompt Injection

Prompt injection of particles upward into a hypothetical chimney was simulated in this sensitivity case. The chimney was assumed to have the same diameter as the cavity (200 m) and to extend 400 m above the cavity (total height of 600 m). This configuration caused the chimney to extend approximately 250 m above the volcanic section and into the alluvium. Particles were positioned in the chimney following an exponential distribution so that most of the mass was concentrated in the cavity (Figure 7.10). This is consistent with monitoring data in post shot well

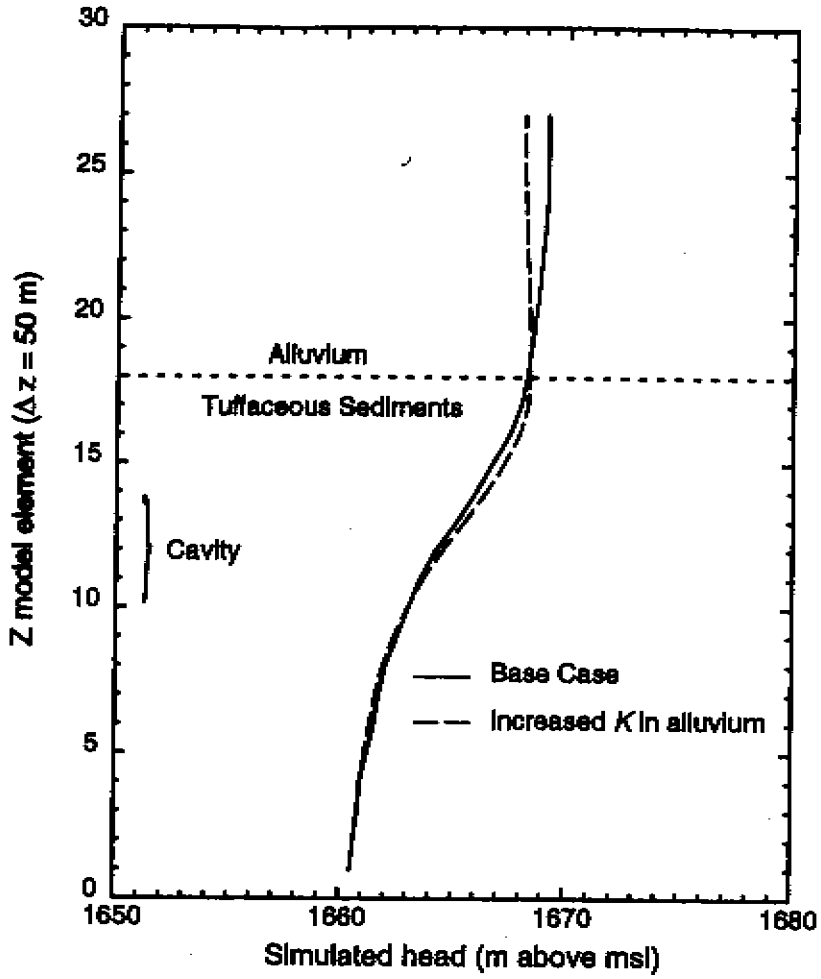

Figure 7.9 Comparison of simulated vertical head profiles at UC-1 for the base case and the sensitivity case having increased mean K in the alluvium.

UC-1-P-2SR, that records rapidly decreasing tritium concentrations in the well with decreasing depth below land surface (Mihevc *et al.*, 1996; Mihevc and Lyles, 1998).

Considering prompt injection into the base-case flow field does result in breakthrough at the southern boundary where there was none in the base case (Figure 7.11), but at insignificant concentrations of the order of 10^{-20} pCi/L (scaled value using the unclassified initial mass estimate).

The prompt injection scenario can be combined with the sensitivity case evaluating hydraulic conductivity in the alluvium. As noted in the previous section, transport is not sensitive to the hydraulic conductivity assigned to the alluvium because the radionuclide source is located in the underlying volcanics and the hydraulic gradient serves to move contaminants downward. If a portion of the radionuclides is injected into the alluvium by prompt injection, the significance of the hydraulic conductivity in the alluvium becomes greater. Simply combining the two sensitivity cases previously analyzed (a mean $\log_{10} K$ of -0.6 for the alluvium and an exponential distribution of tritium upward through the chimney) results in a peak ^3H concentration of 2.4×10^5 pCi/L, based

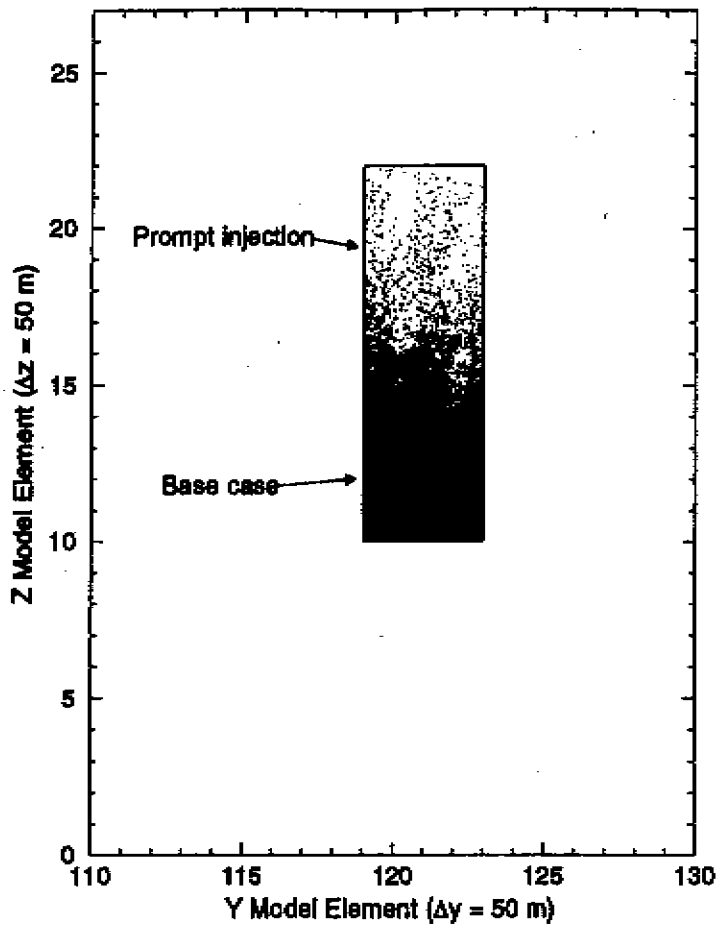

Figure 7.10. Plot showing a cross section of the cavity and chimney and the distribution of mass resulting from prompt injection. This distribution of initial mass was used for the sensitivity case of prompt injection and increased $\mu \log_{10} K$ in the alluvium.

on the estimated source concentration, occurring at the southern breakthrough plane at 57.4 years (Figure 7.11). The influence of increasing the mean $\log_{10}$ in the alluvium when source nuclides are present is dramatic because of the increased velocity toward the southern control plane and the early arrival time, which minimizes the effect of decay, as compared to the base case. However, the impact is likely to be over-represented here because the packer data suggest a decrease in hydraulic conductivity with increasing depth that is not reproduced in this sensitivity case, and the source, even for prompt injection, is located at the base of the alluvium. It should also be remembered that prompt injection is of possible importance only for volatile nuclides or radionuclides with volatile precursors.

7.4.4 Local Dispersivity

Local-scale dispersion accounts for the sub-grid velocity variability and the mixing process resulting from the random motion of particles in the liquid phase. The longitudinal dispersivity value of 0.05 m used in the base case was chosen based on the very low flow velocities encountered around

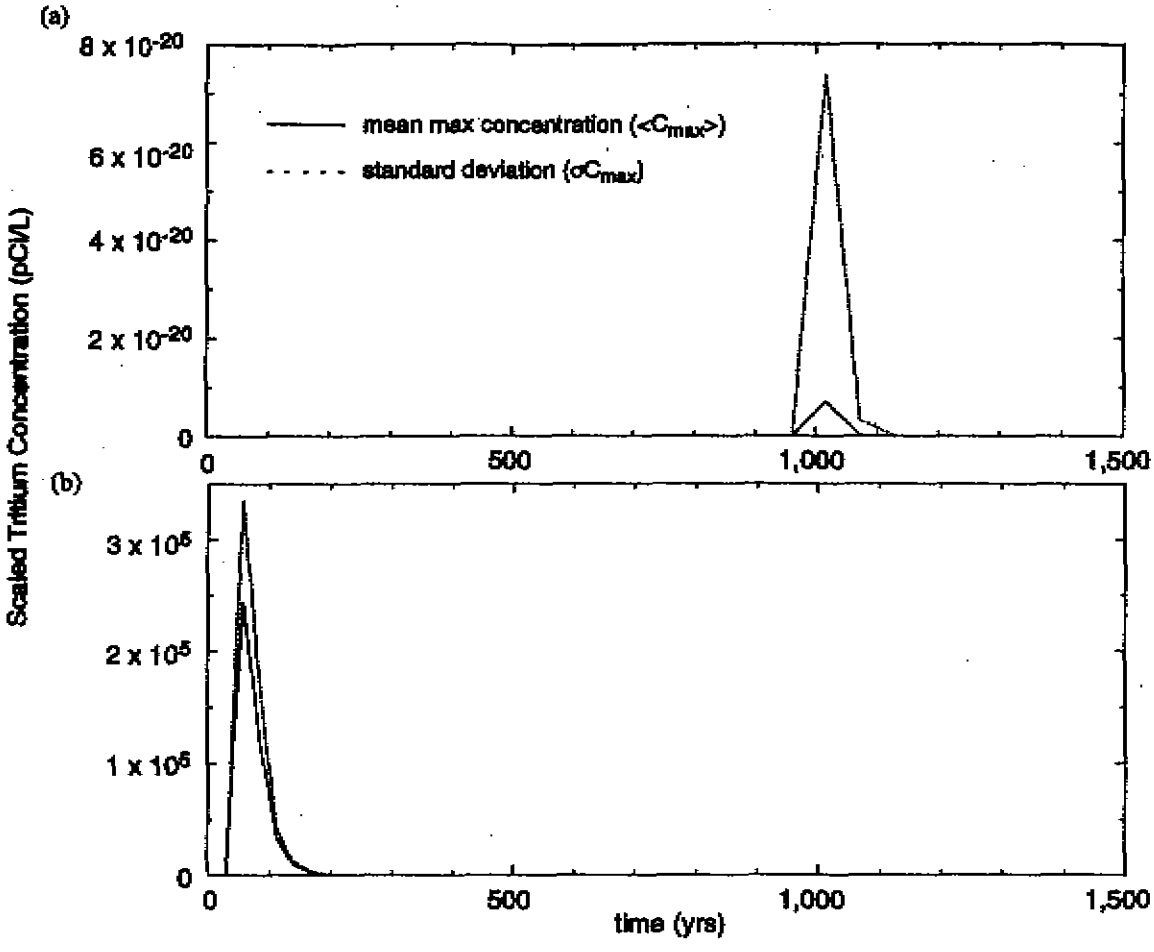

Figure 7.11. (a)Plot of the decayed breakthrough curve of ^{3}H (scaled using estimated source concentration) for the case of prompt injection into the base-case flow field. (b)Plot for the sensitivity case of prompt injection and increased $\mu \log_{10} K$ of the alluvium.

the source and also on the choice of the time step. As mentioned earlier, the choice of the dispersivity values was conservative and was directed toward minimizing the effect of local dispersion so as not to smear out the effect of the sensitivity parameters that may change the flow pattern. To achieve that, an attempt was made to keep (on an average sense) the advective step dictated by the velocity heterogeneity larger than the random step accounting for local-scale dispersion. Also, part of the sub-grid velocity variability is accounted for by the fact that particle velocity is obtained by interpolation of the eight surrounding velocities, and the concept of cell-constant velocity was not employed. Therefore, the choice of α_L= 0.05 m was thought to be reasonable and consistent with other transport parameters. In addition, with the very long travel times that maximized the effect of radioactive decay, focus was placed on those parameters and scenarios that accelerate transport not those delaying or inhibiting transport to the control plane.

To assess the impact of the local-scale dispersion, Figure 7.12 compares the mass flux and peak concentration of ^{14}C obtained using three dispersivity values; α_L = 0.05 m (base case), α_L =0.5 m

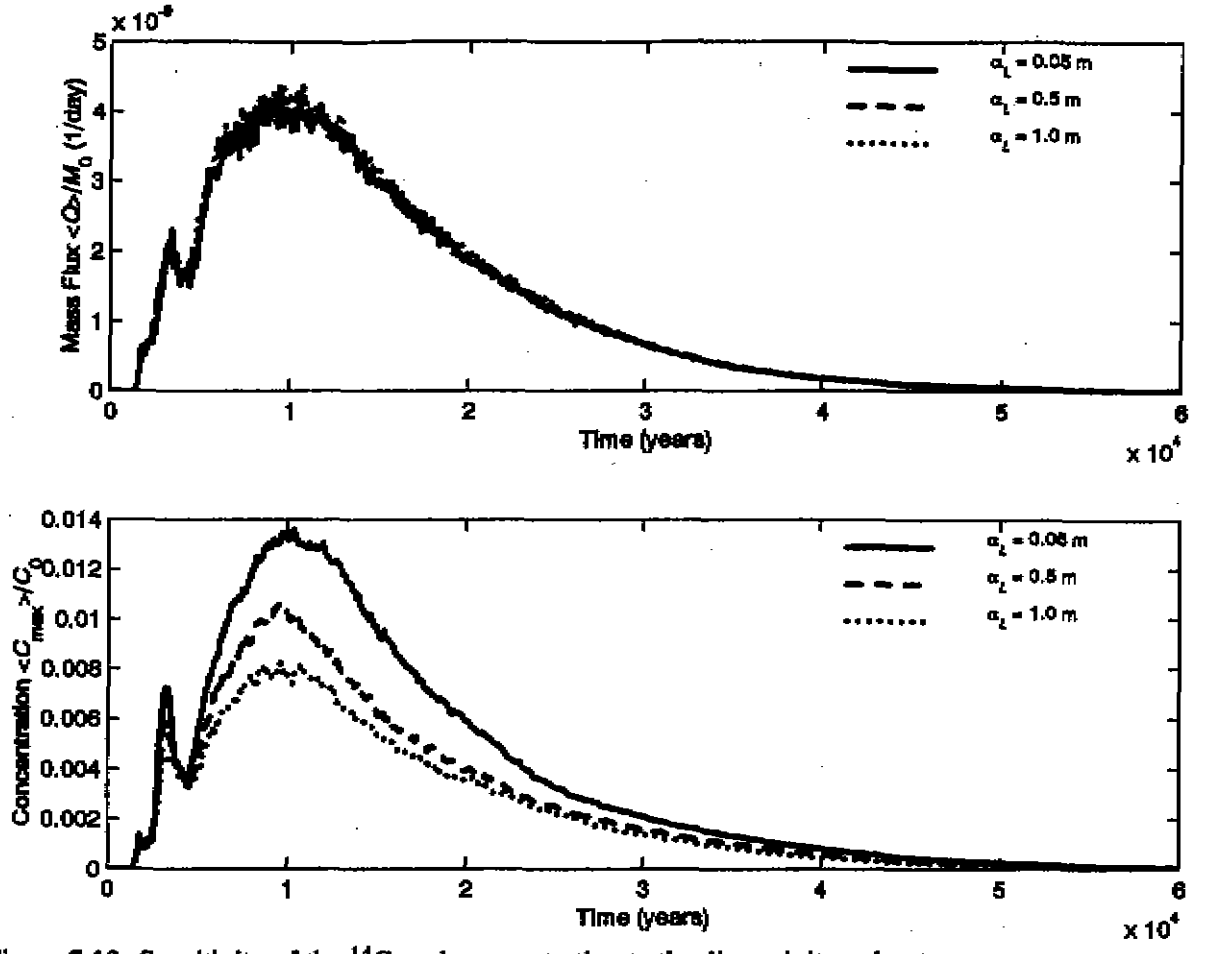

Figure 7.12. Sensitivity of the ^{14}C peak concentration to the dispersivity value.

and α_L =1.0 m. The transverse dispersivity, α_T, is taken as 1/10 α_L in all three cases. It can be seen from Figure 7.12 that the total mass flux crossing the control plane is not affected by the dispersivity value, whereas the peak concentration decreases as α_L increases. The effect of local dispersion is to smooth out the particle distribution that results from the highly heterogeneous velocity field. As can be seen from Figure 5.13, the horizontal velocity component in the lower portion of the domain is much higher than the vertical component. Thus, the increased local dispersion has a minor effect, if any, on the longitudinal movement of the particles and a significant effect on the transversal dispersion in the vertical and lateral directions. Therefore, total mass flux is not influenced by the increased dispersivity, whereas the peak concentration is reduced due to the wider distribution of the plume crossing the control plane.

8.0 Discussion

8.1 Base-Case Transport Results

Two fundamentally different conceptualizations of transport were evaluated: treating all three modeled aquifers as a porous medium with a mean porosity of 0.18, consistent with the core data;

and treating the welded tuff aquifer as a fracture flow unit with a flow porosity of 0.005 plus diffusion into a higher porosity matrix. The differences between these two approaches are easiest to predict for a non-decaying solute. Without the process of radioactive decay, fracture flow with matrix diffusion will experience an earlier peak mass flux, but at a lower mass flux value, followed by a long tail, than a higher porosity simulation. Conversely, the higher porosity approach with no matrix diffusion will have a greater delay before initial breakthrough, but when the breakthrough occurs it will happen over a shorter time span and result in higher peak mass flux values than occurs with matrix diffusion. The effect of radioactive decay depends on the length of the half-life relative to breakthrough. Long-lived radionuclides approximate the behavior of a non-decaying solute. Short-lived radionuclides, however, are much more time-dependent and thus sensitive to velocity.

With the significant retardation and mass distribution over very long times caused by matrix diffusion during fracture flow, the porous medium approach was found to be conservative (resulting in more mass breakthrough) for the vast majority of radionuclides. For two very short-lived nuclides with no sorption properties, ^{3}H and ^{85}Kr, the fracture flow formulation was more conservative, as the small portion of mass that is only slightly retarded by diffusion is the only breakthrough recorded before complete decay in either scenario (fracture flow or porous medium).

Considering the porous medium with uniform porosity of 0.18, essentially no breakthrough is calculated to occur across the UC-1 land-withdrawal boundary during the 1,000-year period of interest. Quantifying the breakthrough that is projected in the millennia after that is hampered by the classified nature of the initial source masses. Unclassified estimates, based on gross relationships with test yield, were made for tritium, ^{90}Sr, and ^{137}Cs; however, with their relatively short half-lives, none of these radionuclides "survived" to the breakthrough plane. Normalized fluxes of the remaining radionuclides in the source term appear to generally also be very low (Appendix 6), with many of the shorter-lived species also not surviving the base-case transport to the control plane. The significance, or lack thereof, of the long-lived radionuclides and daughter products that do break through can only be determined by scaling the results using the true classified masses. The peak mean breakthroughs of the surviving radionuclides occur between 2000 years for short-lived species with no retardation, out to 75 million years for long-lived radionuclides with significant retardation.

Applying a low porosity of 0.005 to simulate fracture flow in the welded tuff allows earlier breakthrough of a small portion of contaminant mass that is only slightly retarded by matrix diffusion. This formulation provided the largest mass breakthrough for ^{3}H and ^{85}Kr, as both of these short-lived nuclides completely decayed in the slower velocity field simulated by the 0.18 porosity. Using the unclassified estimate of initial tritium mass to scale the tritium breakthrough gives an estimated peak mean concentration of almost 1 pCi/L, and mean plus one standard deviation of 10 pCi/L, occurring at 153 years after the Faultless test. It should be noted that though the peak mass flux for the remaining radionuclides occurs with the higher porosity porous medium formulation, the initial breakthrough and timing of the peak mass flux occurs earlier (within the first several thousand years for non-sorbing nuclides) with the fracture flow parameters.

The low groundwater velocities modeled at the ground zero location that result from the complex hydrogeologic environment in Hot Creek Valley confine significant transport of

radionuclides from the Faultless test to the immediate land-withdrawal area for thousands of years. Breakthrough at the land-withdrawal boundary is further delayed by vertical movement modeled to occur from the test cavity, so that only upon encountering hypothesized welded tuff units somewhere below the test horizon does significant lateral movement toward the boundary occur. It is important to recall that densely welded tuffs were not encountered at the UC-1 drillhole or instrument holes, and that their presence somewhere below the test horizon is stochastically represented based on sparse regional data. The fracture flow conceptualization was based solely on a hypothetical model of how fractured, densely welded tuffs are predicted to behave hydraulically.

The groundwater system as modeled for either the porous medium or fracture flow formulation is consistent with both hydraulic and chemical data. Chemical and isotopic interpretations in the UC-1 area support the presence of isolated flow systems in the alluvium and underlying volcanics, with minimal vertical exchange between them. Carbon-14 data indicate very long residence times for groundwater in the volcanic units (30,000 to 50,000 years since time of recharge for groundwater collected from HTH-1), consistent with low velocities. However, without knowledge of the recharge area or multiple measurements along a flowpath, the actual groundwater velocity cannot be inferred from the single HTH-1 measurement. Hydrologic logging supports the presence of very low vertical flow rates in the area, and the long period of time required to recover to the pre-test water level attests to low hydraulic conductivities encountered by the Faultless cavity and chimney.

8.2 Impact of Sensitivity Analysis

By the very nature of our imperfect knowledge of the subsurface environment, numerical models of groundwater flow and transport encompass large uncertainties in both the conceptual model (including boundary conditions) and parameters upon which the results are based. The model of the Faultless test presented here is no exception. Given the very low rates of transport predicted for the base case, however, the sensitivity analysis was focused not on broadly evaluating the relative impact of each uncertain parameter, but rather on those uncertainties which presented the possibility of reduced travel times and thus enhanced transport. As such, the sensitivity analysis was skewed away from evaluating the impact of parameter uncertainties that would only serve to further inhibit transport.

A good example of this is the great uncertainty present in the geochemical release function used to model the release of radionuclides from the nuclear melt glass. Work currently being performed in support of radionuclide migration at the NTS uses glass dissolution rates orders of magnitude lower than that applied to Faultless. A sensitivity analysis of the transport results to this parameter was initially slated to be performed, similar to that presented by Pohll *et al.* (1998) for the Shoal site, but given that the impact would be to only further retard transport from the cavity, it was not performed for Faultless. The uncertainty in the boundary conditions of the flow model was also not analyzed, owing to limited site-specific head data. Boundary heads were chosen to be consistent with the patterns of hydraulic head observed in Hot Creek Valley, and to produce a head distribution near Faultless consistent with the available local data. Thus, the uncertainty in these boundaries could not be quantified.

None of the individual sensitivity cases studied (increasing the vertical correlation length of hydraulic conductivity, increasing the mean hydraulic conductivity of the alluvium, simulating prompt injection of tritium into the upper portions of the chimney, and increasing the local dispersion) significantly altered the base-case transport results during the 1,000-year period of interest. However, combining the prompt injection scenario with higher hydraulic conductivity in the alluvium created the only scenario with significant ^{3}H breakthrough at the southern control plane.

8.3 Contamination Boundaries

The purpose of this modeling is to characterize groundwater flow and transport at CNTA using site-specific hydrologic data. Ultimately, however, the calculations will support development of the Corrective Action Decision Document and provide a foundation for establishing areas that may contain contaminated groundwater. Appendix VI of the Federal Facility Agreement and Consent Order calls for establishing contaminant boundaries that define the aggregate maximum extent of contaminant transport at or above a concentration of concern, and in addition express modeling uncertainty through inclusion of a confidence interval in the boundary determination.

Examples of contaminant-concentration maps are presented here using the methodology developed by Pohll *et al.* (1998). The location of the boundary is determined through analysis of all transport realizations to identify the 50th percentile (*i.e.*, median) probability of an area that would be located within such a boundary. For each simulation and at each time step, the concentration level is determined for each model grid cell. If the concentration exceeds a specified limit at any one vertical location, then a "hit" is recorded for that x-y location. Each of the x-y locations is scanned to determine if the threshold is exceeded and the process is repeated up to 1,000 years or when all the simulated cell concentrations are less than the specified limit. The 50th percentile boundary is determined by including all cells that have at least 50 realizations that exceed the limit.

For these examples, the drinking water limits for ^{3}H, ^{90}Sr, and ^{137}Cs are considered for the boundary determination and the 90 percent confidence interval is presented using the base-case 110 transport realizations of the porous medium formulation. Given that the true initial masses of these nuclides are classified, the unclassified estimates based on test yield are used for scaling the transport results. All of the example contaminant-concentration boundaries are well within the land-withdrawal boundary surrounding UC-1 (Figures 8.1, 8.2, and 8.3). They all also essentially define the location of the source itself and reflect the very limited lateral migration that occurs over the 1,000-year time period. The slightly smaller extent of ^{90}Sr and ^{137}Cs reflects the retardation these radionuclides experience as compared to tritium. Downward vertical movement (Figure 8.4) is also limited over this time period, controlled by the low hydraulic conductivity values. The ^{3}H maps using the fracture flow formulation are essentially the same as the ^{3}H maps shown here, with the contaminant-concentration boundaries confined to the area around the source.

Owing to the manner in which these boundaries are produced, they are not snapshots in time. Instead, the boundaries probabilistically represent all the locations the plume may encounter during

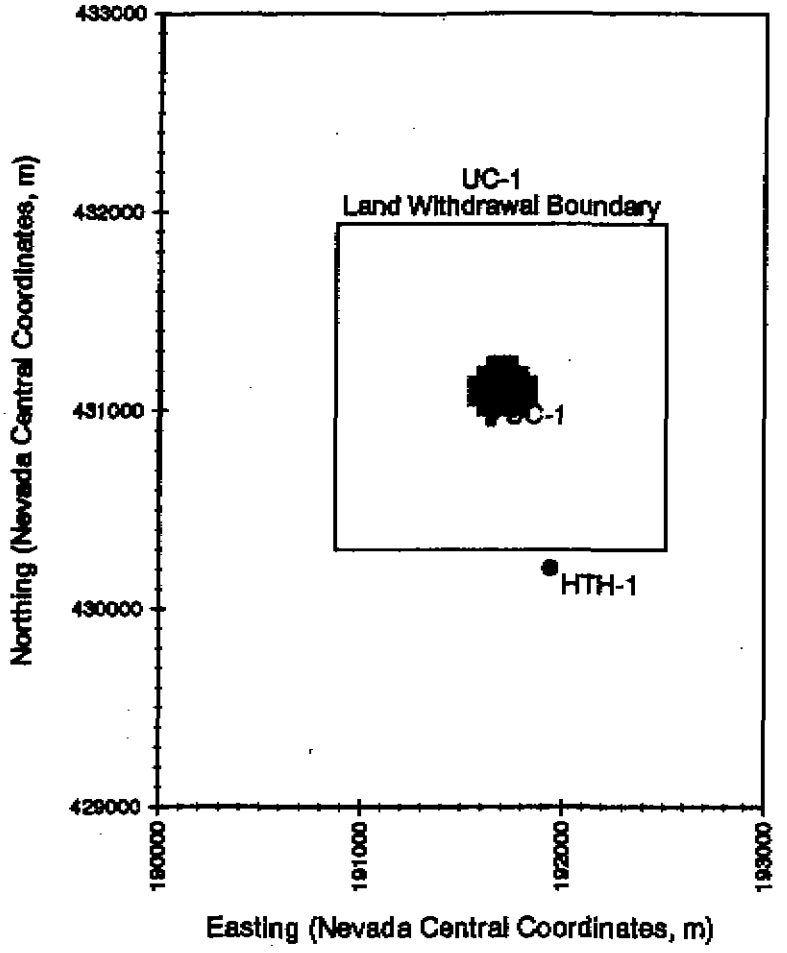

Figure 8.1. Map showing the area of ^{3}H exceedence of 20,000 pCi/L at the 90 percent confidence level.

the 1,000-year migration period. As can be seen, that location is confined to the area immediately adjacent to the nuclear cavity.

8.4 Interpretation of Contaminant Concentration Predictions

The radionuclide concentrations presented at the control plane, and the spatial representation of these concentrations discussed in the previous section, are subject not only to conceptual model and data uncertainty, but also to irreducible uncertainty caused by imperfect knowledge of the heterogeneous aquifer through which flow and transport occurs. Uncertainties in the data and conceptual model were addressed to some extent through the sensitivity analysis, with the irreducible uncertainty reflected in the standard deviation of the concentrations. These standard deviations are generally of the same order of magnitude as the mean itself, a problematic situation in terms of attempting to validate predictions of contaminant concentrations with field measurements.

Another difficulty presented by the Faultless modeling results is caused by the very long travel times predicted. Over the time frame available for validation, very little migration is predicted to

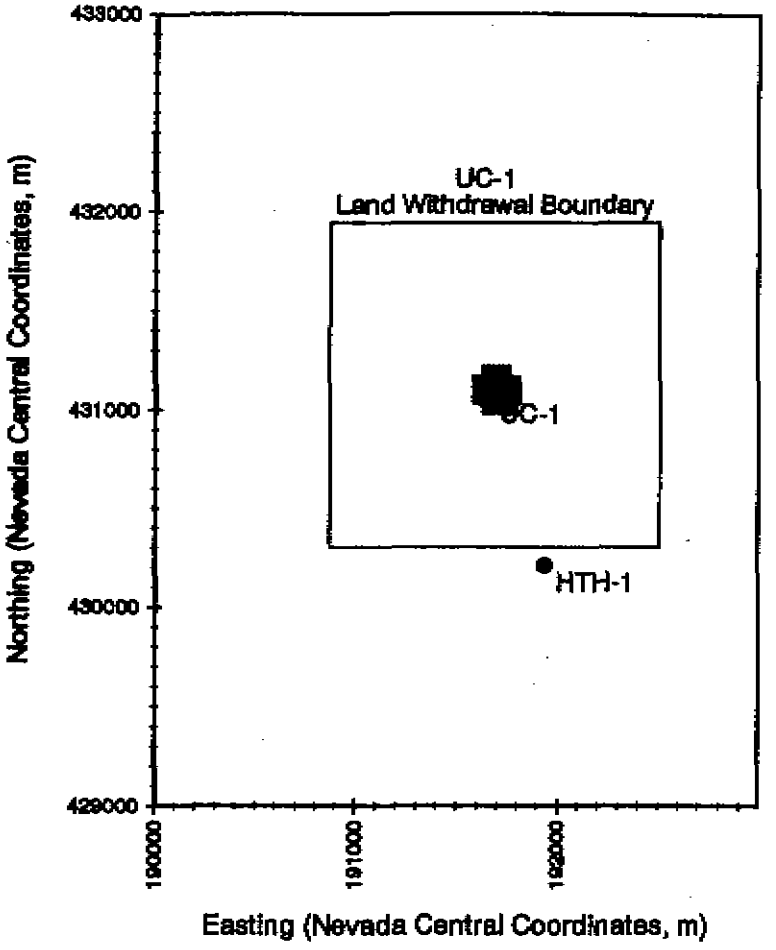

Figure 8.2. Map showing the area of ^{90}Sr exceedence of 80 pCi/L at the 90 percent confidence level.

occur. So little, in fact, that it is all contained within the "source" area of the model domain. This area has been subject to the extreme forces of the nuclear test, with geologic and hydrogeologic impacts that were not included in the modeling performed here. Specifically, the flow and transport modeling was based on pre-Faultless data, with the assumption that over the long-term, those data represented the flow field that would control transport. Over the short-term, and not included in the model, are near-source faulting and altered water levels that would render the model results inconsistent with near-field conditions.

In addition, it must be remembered that the contaminant concentrations presented here represent concentrations averaged over the volume of water contained in one model grid cell (2.25×10^7 L), and thus observations of solute concentration must be of the same scale for comparison. Solute concentrations measured in groundwater are volume averages of local concentration, and various sampling methods result in different amount of mixing of solute mass in sampled water volume. Small volume, point measurements, particularly near the source, can be expected to vary greatly from the predictions presented here for relatively large volumes.

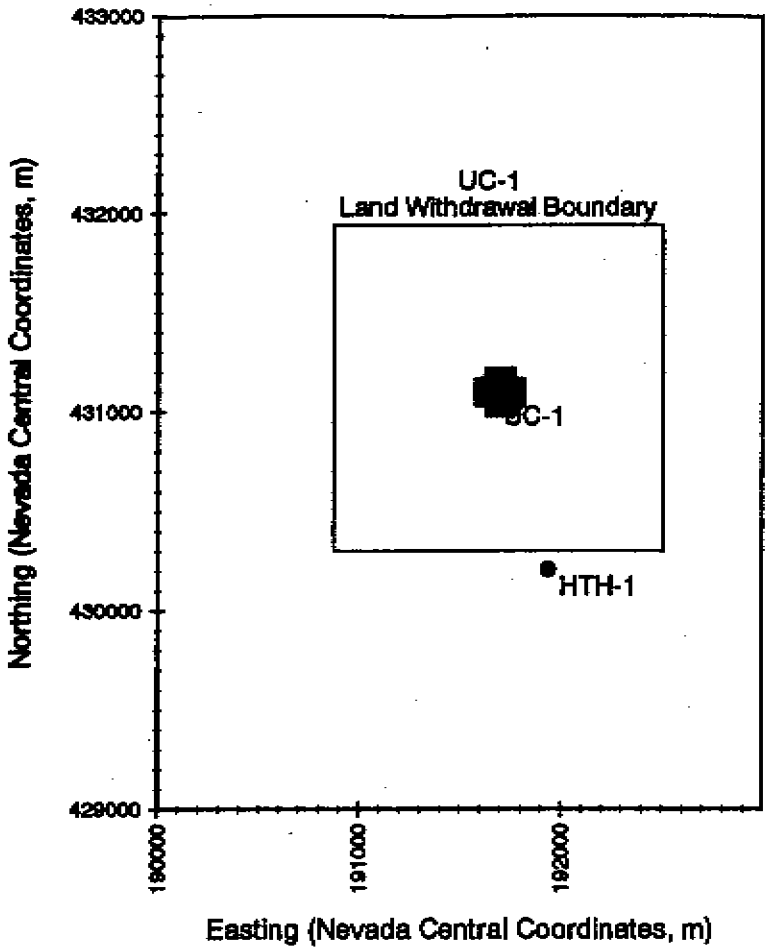

Figure 8.3. Map showing the area of ^{137}Cs exceedence of 200 pCi/L at the 90 percent confidence level.

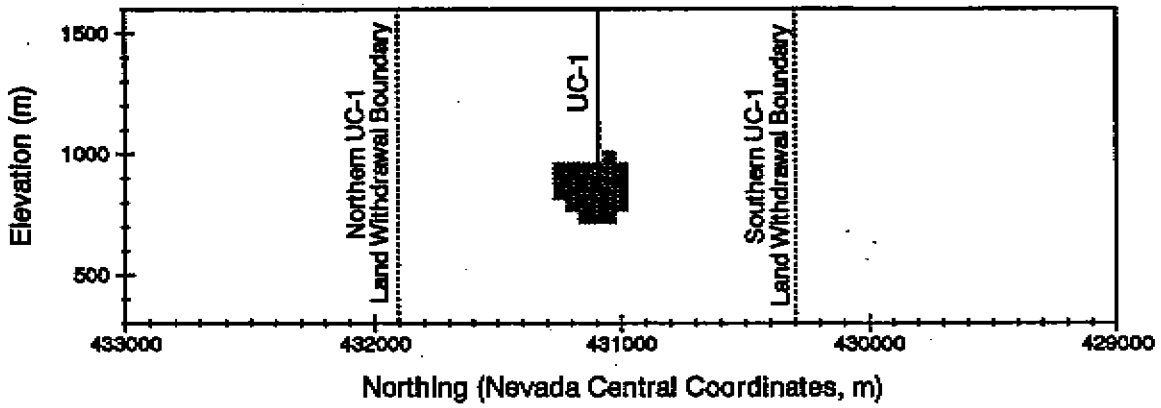

Figure 8.4. Vertical cross section showing the area of ^{3}H exceedence of 20,000 pCi/L at the 90 percent confidence level.

9.0 Conclusions

The volcanic section in which the Faultless test was detonated is dominated by tuffaceous sediments and nonwelded volcanic tuffs. Data from straddle-packer tests in exploratory wells, slug tests in a post shot hole, and water-level recovery in the cavity and chimney all indicate that these rocks have very low hydraulic conductivity. More rapid groundwater flow at CNTA may occur in Tertiary fractured and faulted densely welded volcanic tuffs, but these rocks were identified only in a single 24-m-thick section in one of the wells in the vicinity of Faultless. The database of hydraulic conductivity data available for CNTA allowed a quantitative measure of the uncertainty of this parameter to be incorporated in the model. This was accomplished through a stochastic approach that treated K as a random variable, producing three-dimensional maps of heterogeneous K fields conditioned on the available hard data. The absence of hard data below the Faultless cavity resulted in simulation of both low- and high-K rocks, reflecting the uncertainty in the lithology in that region of the model.

The flow model was based on hydrogeologic conditions prior to the Faultless test, under the assumption that transport over the long term would be controlled by these factors rather than the relatively short-term effects of the test. The flow system near Faultless is conceptualized to consist of a shallow system in the alluvium in which flow is directed southward toward southern Hot Creek Valley, and a deep volcanic section in which flow is directed northeastward toward southern Railroad Valley. Recharge from precipitation to the north of the modeled area causes hydraulic heads there to decrease with depth. In southern Hot Creek Valley, heads in the volcanic units are higher than the overlying alluvium leading to vertically upward hydraulic gradients. An important implication of these flow patterns is that the test cavity, which is located at a depth intermediate between the shallow alluvium and deeper volcanic tuff flow systems, lies in a zone of very low horizontal and vertical hydraulic gradients. Although data about vertical gradients at the emplacement hole UC-1 prior to the test are not available, vertically distributed head data and tracer-test data from HTH-1, 1,000 m southeast, indicate that vertical gradients are very low.

The combination of low hydraulic conductivity and low gradients of hydraulic head results in very low groundwater velocities simulated by the model in the section of tuffaceous sediments encompassing the source. Uncertainty in K was included in the model through the stochastic approach, but the uncertainty in the boundary conditions that control the magnitudes and directions of the hydraulic gradients was not directly addressed. The limited availability of head data within the model domain meant that boundary heads were chosen to be consistent with the patterns of head in Hot Creek Valley, rather than based on measurements at the boundaries. Therefore, although the gradients simulated by the model in the vicinity of the test are consistent with the available data, some uncertainty in this aspect of the model remains.

Two transport formulations were evaluated: a uniform porosity of 0.18 in all three aquifers, and a lower porosity of 0.005, approximating a fracture system, for the welded tuff aquifer. Despite the higher groundwater velocity in the fracture formulation, peak mass flux values for most radionuclides are lower in the fracture case than for the uniform porosity approach because

radionuclides are retarded by diffusion into the aquifer matrix. Laboratory studies indicate that sorption properties of CNTA aquifer materials are quite high, further serving to retard transport of reactive radionuclides. The sensitivity analysis showed that the transport results were relatively insensitive to increasing the vertical correlation length of hydraulic conductivity, increasing the mean hydraulic conductivity of the alluvium, simulating prompt injection of tritium into the upper portions of the chimney, and increasing the local dispersion, though by combining the prompt injection scenario with higher hydraulic conductivity in the alluvium created the only scenario with significant ^{3}H breakthrough at the southern control plane.

Considering the porous medium formulation, essentially no breakthrough is calculated to occur across the UC–1 land–withdrawal boundary during the 1,000–year period of interest. Transport was investigated at much longer time frames, with relatively short–lived radionuclides (such as ^{3}H, ^{90}Sr, and ^{137}Cs) essentially completely decaying before breakthrough. Breakthrough of long–lived radionuclides does occur, at times varying from 2000 to 75 million years, but the significance of breakthrough cannot be evaluated until the results are scaled by the classified masses. The highest peak mass fluxes for ^{3}H and ^{85}Kr occur in the fracture flow simulations as the early breakthrough of the small portion of mass that is only slightly retarded by matrix diffusion is the only breakthrough that occurs prior to decay in either the porous medium or fracture cases. Scaling the results using an unclassified estimate of initial tritium mass gives an estimated peak concentration of almost 1 pCi/L, occurring 153 years after the Faultless test under conditions of fracture flow. Though the highest peak mass fluxes are calculated to occur with the porous medium approach for all radionuclides except ^{3}H and ^{85}Kr, the initial breakthrough and time of the peak mass flux for all nuclides occurs earlier (within the first several thousand years for non–sorbing nuclides) in the fracture flow scenario. Lithologic and porosity data from the site support the porous medium scenario for groundwater transport from the Faultless test, with the fracture formulation presented in response to uncertainty in aquifer characteristics below the depth of the test and hypotheses of the nature of groundwater flow in welded tuff units.

10.0 Bibliography

Ahlstrom, S.W., H.P. Foote, R.C. Arnett, C.R. Cole and R.J. Serne, 1977. Multicomponent mass transport model: Theory and numerical implementation (discrete-parcel-random walk version). Rept. BNWL-2127, Battelle Pacific. Northwest Laboratory, Richland, Washington.

Alabert, A., 1987. Stochastic imaging of spatial distributions using hard and soft information. M.S. Thesis, Applied Earth Science Department, Stanford University, 184 p.

Anderson, R.E., F.M. Byers Jr., G.L. Dixon, E.B. Ekren, D.C. Hedlund, E.N. Hinrichs, D.L. Hoover, F.N. Houser, F.J. Kleinhampl, P.P. Orkild, C.L. Rogers, K.A. Sargent and R.P. Snyder, 1967. Preliminary reconnaissance geologic map of central Nevada, U.S. Geological Survey Technical Letter: Central Nevada-1.

Andricevic, R., T. Brikowski, E. Jacobson and K. Pohlmann, 1995. Improved Methods for Aquifer Characterization and WHPA Delineation in Complex Hydrogeologic Settings: Interim Report. Desert Research Institute, Water Resources Center, prepared for U.S. Environmental Protection Agency, Environmental Monitoring Systems Laboratory.

Arteaga, F.E., 1980. Mathematical Model Analysis of the Eagle Valley Ground-Water Basin, West Central Nevada. U.S. Geological Survey Open-File Report 80-1224.

ASTM (American Society for Testing and Materials), 1995. Standard Guide for Calibrating a Ground-Water Flow Model Application, Section D18.21.10, Designation C-7, Draft No. 4, September 21. ASTM, Philadelphia, PA, 14 p.

Avon, L. and T.J. Durbin, 1992. Evaluation of the Maxey-Eakin Method for Calculating Recharge to Ground-Water Basins in Nevada. Las Vegas Valley Water District, Cooperative Water Project, Series Report No. 7, 44 p.

Banister, J.R. and R.A. Johnson, 1969. Preliminary Effects Evaluation for Event Adagio, U.S. AEC, NVO-46 (Preliminary), Confidential, 45 p. + Appendices.

Barnes, W. and D.L. Hoover, 1968. Preliminary Lithologic Log of Drill Hole UCe-20, Hot Creek Valley, Nye County, Nevada. U.S. Geological Survey, Special Projects Branch, Technical Letter: Central Nevada-15, 13 p.

Bedford, R.G. and D.D. Jackson, 1965. Volatilities of the Fission Product and Uranium Oxides. Lawrence Livermore National Laboratory, UCRL-12314, 37 p.

Blankennagel, R.K. and J.E. Weir, 1973. Geohydrology of the Eastern Part of Pahute Mesa, Nevada Test Site, Nye County, Nevada. U.S. Geological Survey Professional Paper 712-B.

Borg, I.Y., R. Stone, H.B. Levy and L.D. Ramspott, 1976. Information pertinent to the migration of radionuclides in ground water at the Nevada Test Site Part 1: Review and analysis of existing information. Lawrence Livermore National Laboratory, Report UCRL-52078 Part 1, 216 p.

Borg, I.Y., 1975. Radioactivity trapped in melt produced by a nuclear explosion. *Nuclear Technology*, 26:88-100.

Boucher, G., A. Ryall and A.E. Jones, 1969. Earthquakes associated with underground nuclear explosions. *Journal of Geophysical Research*, Vol. 74, No. 15, 3808-3820.

Brunauer, S., P.H. Emmett and E. Teller, 1938. Adsorption of gases in multimolecular layers. *Journal of American Chemical Society*, 60:309–319.

Bryant, E.A. and J. Fabryka-Martin, 1991. Survey of Hazardous Materials used in Nuclear Testing. Los Alamos National Laboratory, LA-12014-MS, 12 p.

Carrol, R.D., 1990. Electric Logging and Electrical Properties of Rocks in Rainier Mesa Area, Nevada Test Site, Nevada. U.S. Geological Survey Open-File Report 90-31.

Chapman, J.B., T.M. Mihevc and B.F. Lyles, 1994. The application of borehole logging to characterize the hydrogeology of the Faultless site, Central Nevada Test Area. Desert Research Institute, Water Resources Center, Publication #45119, DOE/NV/10845-35, 36 p.

Claassen, H.C., 1978. Hydrologic Processes and Radionuclide Distribution in a Cavity and Chimney Produced by the Cannikin Nuclear Explosion, Amchitka Island, Alaska. U.S. Geological Survey Professional Paper 712–D, 28p.

Cooper, H.J., J. Bredehoeft and I. Papadopulos, 1967. Response of a finite-diameter well to an instantaneous charge of water. *Water Resources Research*, 3(1):263-269.

Corchary, G.S., 1967. Lithologic logs of six exploratory holes (UCe–9, –10, –11, 12a, –13, and –14) drilled in alluvium in central Nevada. U.S. Geological Survey Interagency Report: Central Nevada–1, USGS–474–2, 20 p.

Cvetkovic, V., and G. Dagan, 1994. Transport of kinetically sorbing solute by steady random velocity in heterogeneous porous formations. *Journal of Fluid Mechanics*, 265:189–215.

Cvetkovic, V., J. O. Selroos, and H. Cheng, 1999. Transport of reactive tracers in rock fractures *Journal of Fluid Mechanics*, 378:335–356..

Dagan, G., 1986. Statistical theory of groundwater flow and transport pore to laboratory, laboratory to formation, and formation to regional scale. *Water Resources Research*, 22(9):120S-135S.

Davisson, M.L., G.J. Nimz, G.B. Hudson, D.K. Smith, J.H. Rego and J.M. Kenneally, 1994. FY-92 report on the isotope hydrology characterization of the Faultless test site, Nye County, Nevada. Lawrence Livermore National Laboratory, Report UCRL-ID-116133, 17p.

Delhomme, J.P., 1979. Spatial variability and uncertainty in groundwater flow parameters: A geostatistical approach. *Water Resources Research*, 15(2):269-280.

Deutsch, C.V. and A.G. Journel, 1998. *GSLIB Geostatistical Software Library and User's Guide*. Second Edition. Oxford University Press.

Dinwiddie, G.A., 1972. Summary of recent hydrologic data, Faultless site, Hot Creek Valley, Nevada. U.S. Geological Survey letter report, 21 p.

Dinwiddie, G.A. and L.J. Schroder, 1971. Summary of Hydraulic Testing in and Chemical Analysis of Water Samples from Deep Exploratory Holes in Little Fish Lake, Monitor, Hot Creek, and Little Smoky Valleys, Nevada. U.S. Geological Survey Open-File Report USGS-474-90, 69 p.

Dinwiddie, G.A. and S.W. West, 1970. Hydrologic phenomena at the Faultless site, Hot Creek Valley, Nevada. U.S. Geological Survey letter report, 24 p.

Dinwiddie, G.A., 1970a. Hydraulic testing of well HTH-4 in central Nevada. U.S. Geological Survey Technical Letter: Central Nevada-34, USGS-474-31, 20 p.

Dinwiddie, G.A., 1970b. Hydraulic testing of well HTH-5 in central Nevada. U.S. Geological Survey Technical Letter: Central Nevada-37, USGS-474-39, 14 p.

Dinwiddie, G.A., 1970c. Hydraulic testing and sampling of hole Ue-1, in central Nevada. U.S. Geological Survey Technical Letter: Central Nevada-7, USGS-474-77, 25 p.

Dinwiddie, G.A., 1970d. Analysis of hydraulic tests in Hot Creek Valley, Nevada. U.S. Geological Survey Technical Letter: USGS-474-82.

Dinwiddie, G.A., 1969a. Hydraulic testing of well HTH-23 in central Nevada. U.S. Geological Survey Technical Letter: Central Nevada-32, USGS-474-23, 34 p.

Dinwiddie, G.A., 1969b. Hydraulic testing of well HTH-3 in central Nevada. U.S. Geological Survey Technical Letter: Central Nevada-35, USGS-474-34, 23 p.

Dinwiddie, G.A., 1968. Hydraulic testing of well HTH-21-1 in central Nevada. U.S. Geological Survey Technical Letter: Central Nevada-22.

Dixon, G.L. and R.P. Snyder, 1967. Preliminary lithology and physical properties data, drill hole Ue-18, Hot Creek Valley, central Nevada. U.S. Geological Survey Technical Letter: Central Nevada-2, USGS-474-256, 5 p.

Drellack, S.L., 1994. An Introduction to NTS Geology and Geophysical Log Characteristics. Raytheon Services Nevada.

Dupuis, M., 1970. Distribution and Evolution of Radioelements After a Nuclear Explosion. Bull. Infor. Sci. Tech., 149: Lawrence Livermore National Laboratory, 1972, UCRL-Trans-10617-5.

Eakin, T.E., G.B. Maxey, T.W. Robinson, J.C. Fredericks and O.J. Loeltz, 1951. Contributions to the hydrology of eastern Nevada. Nevada State Engineer's Office, Water Resources Bulletin, no. 12, 171 p.

Ekren, E.B., C.L. Rogers and G.L. Dixon, 1973a. Geologic and Bouger gravity map of the Reveille quadrangle, Nye County, Nevada. U.S. Geological Survey: Miscellaneous Geologic Investigations Map I-806.

Ekren, E.B., E.N. Hinrichs, W.D. Quinlivan and D.L. Hoover, 1973b. Geologic map of the Moores Station quadrangle, Nye County, Nevada. U.S. Geological Survey: Miscellaneous Geologic Investigations Map I-756.

Ekren, E.B., F.M. Byers Jr., W.J. Carr, G.L. Dixon, H.W. Dodge, D.C. Helund, E.N. Hinrichs, D.L. Hoover, W.D. Quinlivan, C.L. Rogers and R.P. Snyder, 1968. Preliminary geologic map of the Hot Creek Valley area, Nye County, Nevada. U.S. Geological Survey: Interagency Report Central Nevada-3.

Essington, E.H. and J.V.A. Sharp, 1968. Some Aspects of Ground-Water Solution Chemistry, Underground Nuclear Explosion Zones, Nevada Test Site. *In* Eckel, E.B., Nevada Test Site, Geological Society of America Memoir 110, pp. 263-273.

Faure, G., 1977. Principles of Isotope Geology. John Wiley and Sons, New York, 464 p.

Fiero Jr., G.W., J.R. Illian, G.A. Dinwiddie and L.J. Schroder, 1974. Use of hydrochemistry for interpreting ground-water flow systems in central Nevada. U.S. Geological Survey Open-File Report, USGS-474-178.

Fiero Jr., G.W. and J.R. Illian, 1969. Regional Hydrology Hot Creek Valley Flow System, Nye County, Nevada. Desert Research Institute, Water Resources Center, Interim Report, 17 p.

Fiero, G.W., A.L. Mindling and J.R. Illian, no issue date given. Section B: Regional groundwater flow systems of central Nevada. Desert Research Institute, Water Resources Center, Publication #44005.

Freeze, R.A. and J.A. Cherry, 1979. Groundwater, Prentice-Hall, Inc., Englewood Cliffs, New Jersey.

Frick, U., W. Alexander, B. Baeyens, P. Bossart, M.H. Bradbury, Ch. Bühler, J. Eikenberg, Th. Fierz, W. Heer, E. Hoehn, I.G. McKinley and P.A. Smith, 1991. Grimsel Test Site - The Radionuclide Migration Experiment - Overview of Investigations 1985-1990. National Cooperative for the Disposal of Radioactive Waste Technical Report 91-94.

Gelhar, L.W., 1986. Stochastic subsurface hydrology from theory to applications. *Water Resources Research*, 22(9)1355:1455.

GeoTrans, Inc., 1995. A fracture/porous media model of tritium transport in the underground weapons testing areas, Nevada Test Site. Report prepared for the U.S. Department of Energy, 39 p.

Glasstone, S. and P.J. Dolan, 1977. The effects of nuclear weapons, 3rd edition. U.S. Department of Defense and U.S. Department of Energy, 653 p.

Goishi, W., J.W. Meadows, N. Namboodiri, D.K. Smith and J.F. Wild, 1995. Radionuclide Inventory for U.S. Nuclear Tests Conducted off the NTS and Hydronuclear and Safety Experiments Conducted on the NTS, Lawrence Livermore National Laboratory, UCRL-ID-121901, Secret-Restricted Data.

Goishi, W., B. Esser, J. Meadows, N. Namboodiri, D. Smith, J. Wild, S. Bowen, P. Baca, L. Olivas, C. Geoffrion, J. Thompson and C. Miller, 1994. Total Radionuclide Inventory Associated with Underground Nuclear Tests Conducted at the Nevada Test Site 1955-1992. Los Alamos National Laboratory, LA-CP-94-0222, Secret-Restricted Data, 242 p.

Gonzalez, D.D., 1977. Hydraulic effects of underground nuclear explosions, Amchitka Island, Alaska. Ph.D. Dissertation, Colorado State University, Fort Collins, Colorado, 141 p.

Hampton, C.M. and D.K. Bailey, 1984. Gas Extraction experiments on volcanic glasses. *J. Non-Crystalline Solids*, 67:147-168.

Hassan, A.E., R. Andricevic, and V. Cvetkovic, in review, 1999. Analysis of absolute and relative dispersion for solute flux in heterogeneous media, Water Resour. Res.

Healey, D.L., 1968. Gravity survey of northern Hot Creek Valley, Nye County, Nevada. U.S. Geological Survey Technical Letter: Central Nevada-18, 21 p.

Hess, K.M., S.H. Wolf and M.A. Celia, 1992. Large-scale natural gradient tracer test in sand and gravel, Cape Cod, Massachusetts, 3. Hydraulic Conductivity Variability and Calculated Macrodispersivities, *Water Resources Research*, 28(8):2011-2027.

Hill, M.C., 1990. Preconditioned Conjugate-Gradient 2 (PCG2), A computer program for solving ground-water flow equations. U.S. Geological Survey, Denver, Colorado.

Hoeksema, R.J. and P.K. Kitanidis, 1985. Analysis of the spatial structure of properties of selected aquifers. *Water Resources Research*, 21(4):563-572.

Holmes and Narver, Inc., 1974. Summary report Central Nevada Test Area demobilization and restoration activities. U.S. Atomic Energy Commission report NVO-152, 61 p.

Hoover, D.L., 1968a. Lithologic log of drill hole UCe-17, and general geology of the UCe-17 area, Hot Creek Valley, Nevada. U.S. Geologic Survey Technical Letter: Central Nevada-13, USGS-474-258, 14 p.

Hoover, D.L., 1968b. Lithologic logs of drill holes in the Faultless area, Hot Creek Valley, Nevada. U.S. Geological Survey Technical Letter: Central Nevada-17.

Hvorslev, M.J., 1951. Time lag and soil permeability in groundwater observations. U.S. Army Corps of Engr., Waterways Exp. Sta. Bull 36.

Ingraham, N.L., B.F. Lyles, R.L. Jacobson, and J.W. Hess, 1991. Stable isotope study of precipitation and spring discharge in southern Nevada. *Journal of Hydrology*, 125, pp.243–258.

International Atomic Energy Agency (IAEA), 1998. The Radiological Situation at the Atolls of Mururoa and Fangataufa, Volume 4, Releases to the Biosphere of Radionuclides From Underground Nuclear Weapons Tests at the Atolls, IAEA, Austria, 270p.

IT Corporation, 1998. Report and Analysis of the BULLION Forced–Gradient Experiment. Prepared for DOE/NV. Report DOE/NV/13052–042. Variable paging. Las Vegas, NV.

Johnson, N.M. and S.J. Dreiss, 1989. Hydrostratigraphic interpretation using indicator geostatistics. *Water Resources Research*, 25(12):2501-2510

Journal, A.G. and F.G. Alabert, 1990. Non-Gaussian data expansion in the earth-sciences. *Terra Nova*, 1(2):123-134.

Kersting, A.B., 1996. The State of the Hydrologic Source Term. Lawrence Livermore National Laboratory, UCRL-ID-126557, 30 p.

Keys, W.S., 1990. Borehole Geophysics Applied to Groundwater Investigation. U.S. Geological Survey T.W.R.I.-2-E2, 150 p.

Kinzelbach, W., 1988. The random walk method in pollutant transport simulation. In *Groundwater Flow and Quality Modeling*, edited by E. Custodio *et al.*, pp. 227-246, D. Reidel, Norwell, Mass.

Krikorian, O.H., 1981. Predictive Calculations of Volatilities of Metals and Oxides in Steam-Containing Environments. Lawrence Livermore National Laboratory, UCRL-85553, 27 p.

McDonald, M.G. and A.W. Harbaugh, 1988. A Modular Three-Dimensional Finite-Difference Ground-Water Flow Model. U.S. Geological Survey, Techniques of Water Resources Investigations, Book 6, Chap. A1, 586 p.

McKeown, F.A. and D.D. Dickey, 1969. Fault displacements and motion related to nuclear explosions. Bulletin of the Seismological Society of America, Vol. 59, No.6, pp. 2253-2269.

McKeown, F.A., D.D. Dickey and W.L. Ellis, 1968. Preliminary report on the geologic effects of the Faultless event. U.S. Geological Survey, Central Nevada-16, USGS-474-65, 20 p.

Mihevc, T.M. and B.F. Lyles, 1998. Summary of field activities at the Faultless site, Nevada. Desert Research Institute, Water Resources Center, letter report, 14 p.

Mihevc, T.M., J.B. Chapman and B.F. Lyles, 1996. The application of borehole logging to characterize the hydrogeology of the Faultless nuclear test site, Nevada. *Hydrogeology Journal*, v.4, no.4, 83-97.

Moltyaner, G.L., M.H. Klukas, C.A. Wills and W.D. Killey, 1993. Numerical simulation of Twin Lake natural-gradient tracer tests: A comparison of methods. *Water Resources Research*, 29(10): 3433-3452.

Moreno, L., Y. Tsang, C. Tsang, F. Hale and I. Neretnieks, 1988. Flow and tracer transport in a single fracture: A stochastic model and its relation to some field observations. *Water Resources Research*, 24(12):2033-2048.

NAGRA (National Cooperative for the Disposal of Radioactive Waste), 1994. Kristallin–I Safety Assessment Report. National Cooperative for the Disposal of Radioactive Waste, Technical Report 93–22, 396p.

Nork, W.E., E.J. Forslow and E.H. Essington, 1971. Radioactivity in water, Central Nevada Test Area. Teledyne Isotopes Report, NVO-1229-175, 84 p.

Norton, D. and J. Knight, 1977. Transport phenomena in hydrothermal systems: cooling plutons. *Amer. J. Sci.*, 277:937–981.

Peters, R.R., E.A. Klavetter, I.J. Hall, S.C. Blair, P.R. Heller, and G.W. Gee, 1984. Fracture and Matrix Hydrologic Characteristics of Tuffaceous Materials from Yucca Mountain, Nye County, Nevada. Sandia National Laboratories Report SAND84–1471.

Pohll, G., J. Chapman, A. Hassan, C. Papelis, R. Andricevic and C. Shirley, 1998. Evaluation of groundwater flow and transport at the Shoal underground nuclear test: an interim report. Desert Research Institute, Water Resources Center, Publication #45162, DOE/NV/11508-35, 123 p.

Pohlmann, K., C. Shirley and R. Andricevic, 1996. Near-Field Modeling in Frenchman Flat, Nevada Test Site. Desert Research Institute, Water Resources Center, Publication #45154, 26 p.

Pohlmann, K., J. Chapman and R. Andricevic, 1995. Exposure assessment of groundwater transport of tritium from the Central Nevada Test Area. Desert Research Institute, Water Resources Center, Publication #45133, DOE/NV/11508-02, 22 p.

Prudic, D.E., J.R. Harrill and T.J. Burbey, 1993. Conceptual Evaluation of Regional Ground-Water Flow in the Carbonate Rock Province of the Great Basin, Nevada, Utah, and Adjacent States. U.S. Geological Survey, Open-File Report 93-170, 103 p.

Purvance, D.T., 1999. Use of the Geoelectric Signal to Estimate Hydraulic Conductivity Fields and Spatial Structures at Variable Scales. Ph.D. Dissertation, University of Nevada, Reno. 126 p.

Quinlivan, W.D. and C.L. Rogers, 1974. Geologic map of the Tybo quandrangle, Nye County, Nevada. U.S. Geological Survey Miscellaneous Geologic Investigations Map I-821.

Rabb, D.D., 1970. Particle-Size Distribution Study: Piledriver Event. Proc. Symp. Engineering with Nuclear Explosives, CONF-700101, Vol. 2, pp. 888-908.

Rehfeldt, K., O. Drici, J. Renier and J. Marie, 1996. Hydrologic Parameter Data Documentation Package, Underground Test Area Subproject, Phase I Data Analysis Task, Volume IV. IT Corporation, prepared for U.S. Department of Energy, Env. Rest. Program, 21 p.

Ross, C.S. and R.L. Smith, 1961. Ash-flow tuffs – Their origin, geologic relations, and identifications. U.S. Geological Survey Professional Paper 366, 81 p.

Rush, F.E. and D.E. Everett, 1966. Water-resources appraisal of Little Fish Lake, Hot Creek, and Little Smoky valleys, Nevada. State of Nevada Department of Conservation and Natural Resources, Water Resources–Reconnaissance Series Report 38.

Schenker, A.R., D.C. Guerin, T.H. Robey, C.A. Rautman and R.W. Barnard, 1995. Stochastic Hydrogeologic Units and Hydrogeologic Properties Development for Total-System Performance Assessments. Sandia National Laboratories, SAND94-0244, 89 p. + Appendices.

Schwartz, L., A. Piwinskii, F. Ryerson, H. Tewes and W. Beiriger, 1984. Glass produced by underground nuclear explosions. *J. Non-Crystalline Solids,* 67:559-591.

Shirley, C., K. Pohlmann and R. Andricevic, 1996. Three-dimensional Mapping of Equiprobable Hydrostratigraphic Units at the Frenchman Flat Corrective Action Unit, Nevada Test Site. Desert Research Institute, Water Resources Center, Publication #45152.

Shirley, C.T., 1995. Hydrostratigraphic units within the alluvium and tertiary volcanics of east central Yucca Flat, Nevada Test Site. M.S. Thesis, Water Resources Management, Department of Geosciences, University of Nevada, Las Vegas.

Smith, D.K., A.B. Kersting, J.M. Kenneally, J.H. Rego and J.L. Thompson, 1997. Hydrologic Resources Management Program FY 1996 Progress Report. Lawrence Livermore National Laboratory, UCRL-ID-126886, 40 p.

Smith, D.K., 1997. Radionuclides recommended by the UGTA Source and Transport Subcommittee of significance for remedial investigations at the Nevada Test Site. Memorandum from Lawrence Livermore National Laboratory to Janet Wille, IT Corporation, copied to Robert Bangerter, DOE, dated April 2, 1997.

Smith, D.K., B.K. Esser and J.L. Thompson, 1995. Uncertainties Associated with the Definition of a Hydrologic Source Term for the Nevada Test Site. Lawrence Livermore National Laboratory, UCRL-ID-120322, 21 p.

Smith, D.K., 1995. Characterization of nuclear explosive melt debris. *Radiochimica Acta,* 69:157-167.

Smith, D.K., 1993. A Review of Literature Pertaining to the Leaching and Sorption of Radionuclides Associated with Nuclear Explosive Melt Glasses. Lawrence Livermore National Laboratory, UCRL-ID-113370, 26 p.

Smith, R.L., 1960. Zones and zonal variations in welded ash flows. U.S. Geological Survey Professional Paper 354-F, pp. F149-F159.

Snow, D.T., 1968. Rock fracture spacings, openings, and porosities. *J. Soil Mech. Found. Div.*, Proc. Amer. Soc. Civil Engineers, 94, pp. 73–91.

Snyder, R.P., 1967. Preliminary lithologic report on drill hole UCe-18, Hot Creek Valley, Nye County, Nevada. U.S. Geological Survey Technical Letter: Central Nevada-10, 10 p.

State of Nevada, 1988. Hydrographic Basin Statistical Summary – Ground Water Basins 001–232, Carson City, Nevada. State of Nevada Department of Conservation and Natural Resources, Division of Water Resources and Water Planning.

Stenhouse, M.J. and J. Pottinger, 1994. Comparison of sorption databases used in recent performance assessments involving crystalline host rock. *Radiochemical Acta,* 66/67:267-275.

Sudicky, E.A., 1986. A natural gradient experiment of solute transport in a sand aquifer: Spatial variability of hydraulic conductivity and its role in the dispersion process. *Water Resources Research*, 22(13):2069-2082.

Thordarson, W., 1987. Hydrogeology of the Faultless site, Nye County, Nevada. U.S. Geological Survey, Water-Resources Investigations Report 86-4342, 40 p.

Thordarson, W., 1985. Hydrogeologic monitoring at the Faultless site, Nye County, Nevada. U.S. Geological Survey, Open-File Report 84-580, 37 p.

Tompson, A.F.B. and L.W. Gelhar, 1990. Numerical simulation of solute transport in three-dimensional, randomly heterogeneous porous media. *Water Resources Research*, 26(10):2541-2562.

Triay, I.R., A. Meijer, J.L. Conca, K.S. Kung, R.S. Rundberg, B.A. Strietelmeier, C.D. Tait, D.L. Clark, M.P. Neu and D.E. Hobart, 1997. Summary and Synthesis Report on Radionuclide Retardation for the Yucca Mountain Site Characterization Project. Los Alamos Report LA–13262–MS, 274 p.

Triay, I.R., K.H. Birdsell, A.J. Mitchell, and M.A. Ott, 1993. Diffusion of Sorbing and Non–Sorbing Radionuclides. In Proceedings of the Fourth Annual International High Level Radioactive Waste Management Conference, Las Vegas, NV, April 26–30, Vol. 2. American Nuclear Society, pp.1527–1532.

U.S. Atomic Energy Commission, 1973. Planning directive demobilization, restoration, and monitoring Central Nevada Test Area. Nevada Operations Office report NVO-90, variable paging.

U.S. Department of Energy, 1994. Announced United States Nuclear Tests. Nevada Operations Office report DOE/NV—209 Rev. 14.

Walter, G.R., 1982. Theoretical and Experimental Determination of Matrix Diffusion and Related Solute Transport Properties of Fractured Tuffs from the Nevada Test Site. Los Alamos National Laboratory Report LA–9471–MS.

White, A.F., 1983. Surface chemistry and dissolution kinetics of glassy rocks at 25°C. *Geochim. et Cosmochim. Acta*, 47:805-815.

Winograd, I.J. and W. Thordarson, 1975. Hydrogeologic and Hydrochemical Framework, South-Central Great Basin, Nevada-California, with Special Reference to the Nevada Test Site. U.S. Geological Survey Professional Paper 712-C, 126 p.

APPENDIX 1

REGIONAL HYDRAULIC HEAD MEASUREMENTS IN THE HOT CREEK VALLEY

prepared by
Todd Mihevc and Brad Lyles
September 30, 1997

In preparation for the construction of a groundwater flow model, the need arose to confirm regional water levels in the Hot Creek Valley. Previous hydraulic head measurements to determine valley-wide gradients were conducted in the mid-1960s, and although present groundwater withdrawals are not excessive, a re-evaluation of the gradient is a necessary step in the groundwater modeling effort.

To determine possible well locations, several data sources were accessed which include: tabulated data from the State Engineers Office, a Fenix & Scission report to the U.S. Atomic Energy Commission (AEC) entitled "The Abandonment of Drill Holes, Central Nevada Test Area," and a Department of Air Force report entitled "M-X Multiple Protective Shelter, Water Resources Program - Nevada, A Summary." The State Engineers office produced a printout of water rights for the Hot Creek Valley. Although this list included all the certified water rights, it also included all applications for water rights, most of which had no wells associated with them. The Fenix & Scission report described which of the hydrologic exploration wells for the Central Nevada Test Area were abandoned, how they were abandoned, and which wells were turned over to the Bureau of Land Management. The Air Force report listed the production and monitoring wells that were drilled for characterization of hydraulic properties, as well as the shallow ground-water monitoring borings that were used for valley-wide hydrologic characterization. The locations of all potential wells were transferred to 1:100,000 scale topographic maps that were used in the field to aid in well location.

Water levels were determined from available wells in Hot Creek Valley, the northern portion of Revellie Valley, and the southern portion of Big Sand Springs Valley between August 11, 1997 and August 17, 1997. In most wells, the depth to water was determined with an Olympic well probe, however, at the UC-1 site, a logging truck with a water level indicator was used. Several of the wells surveyed had pumps installed in such a way that access for measuring equipment was precluded. Also in the southern end of Hot Creek Valley, adjacent to Base Camp, large capacity irrigation wells had been pumping for much of the spring and summer, making water level measurements in that area unreliable for valley-wide gradient calculation.

Several of the wells in Hot Creek and Big Sand Springs valleys that were abandoned by the AEC have been re-completed to supply water for cattle. The wells were abandoned by setting a wooden plug at 10 feet below the land surface and filling the casing with cement from the surface to the plug. The wells were re-completed by digging below the cement filled portion of the casing, cutting off that portion and welding on a new section of casing. These wells include: UCE-18, HTH-21, HTH-21-1, HTH-3, and HTH-23. Of these wells, HTH-21 and HTH-3 were both dry. UCE-17, which was supposed to have access to the water table, was plugged, probably by a rock at 425 feet below the top of the casing.

Of the wells that were located within the study area, Table 1 lists the ones that were determined to be dry. The total depth of these wells was not determined.

TABLE 1. WELLS THAT WERE DETERMINED TO BE DRY IN 1997.

Well	Easting* (meters)	Northing* (meters)
HTH-21	203,750	425,861
HTH-3	200,280	422,400
Pedros Well	178,125	401,990
Hot Creek Ranch	180,945	417,549

*All locations are presented in Nevada State Plane Coordinates (meters)

During the field visit several of the wells investigated did not have access for equipment for water level determination because of the way the pumps were installed or the wells were abandoned. Table 2 is a list of these wells.

TABLE 2. WELLS THAT DID NOT HAVE ACCESS FOR MEASURING EQUIPMENT IN 1997.

Well	Easting (meters)*	Northing (meters)*	Status
UCE-11	190,940	427,110	Plugged
6 Mile Well	191,000	417,000	Pump installed
HTH-5	190,773	417,075	Plugged
HTH-4	209,077	422,427	Pump installed
Keystone Well	182,663	404,547	Pump installed
Joes Well	188,141	380,013	Pump installed
Warm Spring Trailer Park	178,670	381,620	Pump Installed
Base Camp	186,101	395,053	Pump installed
UCE-23	208,440	417,258	Plugged
UCE-17	191,457	436,032	Rock @ 425'

*All locations are presented in Nevada State Plane Coordinates (meters)

Table 3 is a list of the wells where water level measurements were successfully obtained. Water elevations in Table 3 were determined by subtracting depth to water measurements from surface elevation of the wells. Surface elevations were estimated from 7.5 minute topographic maps or from reported elevations. The locations of these wells are shown in Figure 1.

A contour map of groundwater heads was produced for Hot Creek Valley from the measurements of composite hydraulic head (Figure 2). Wells outside Hot Creek Valley (i.e. HTH–23 and HTH–21–1) were not included in the contouring as they represent hydrogeologic conditions in a separate valley. Figure 2 indicates that the gradient is steep in the northern portion of the valley and becomes flatter south of the UC–1 site. The contour map shown in Figure 3 focuses on the area where the hydraulic gradients are low, and utilizes a finer contour interval. These maps show a general decrease in hydraulic gradient from the north end of the valley to the south end.

TABLE 3. LIST OF WELLS, WHERE HYDRAULIC HEAD MEASUREMENTS WERE MADE AND THE WATER SURFACE ELEVATION.

Well	Easting (m)	Northing (m)	Water Elevation (m)	Surface Elevation Source
MX Obs (375)	190,097	383,514	1568.4	1
MX Well Reveille	181,773	372,800	1574.4	1
Fallini Ranch	196,309	383,011	1557.7	3
E.W. Fallini	192,487	386,230	1566.8	3
NDOT Maint.	191,002	401,973	1587.9	3
MX Obs (Tybo)	185,193	395,837	1569.7	1
Tybo Well	183,684	398,352	1572.1	3
MX Well (Tybo)	182,175	399,559	1595.4	1
MX Obs (valley)	187,708	403,155	1595.9	1
9 Mile Ranch	185,092	411,480	1632.2	3
UCE–18	193,804	425,754	1656.5	2
HTH–21–1	203,760	425,912	1637.6	2
HTH–23	208,555	416,992	1617.2	2
North Well	192,536	445,078	1913.9	3
North Artesian Well	193,843	443,066	1882.5	3
MX Well (north)	189,896	415,302	1634.8	1
HTH–1	191,838	430,207	1668.1	2
HTH–2	191,898	430,355	1666.4	2
UC–1–P–1S	191,974	430,805	1755.9	2
UC–1–P–2SR	192,018	431,179	1659.9	2

[1]U.S. Geological Report
[2]Fenix & Sisson Report
[3]Estimate from 7.5 minute topographic map

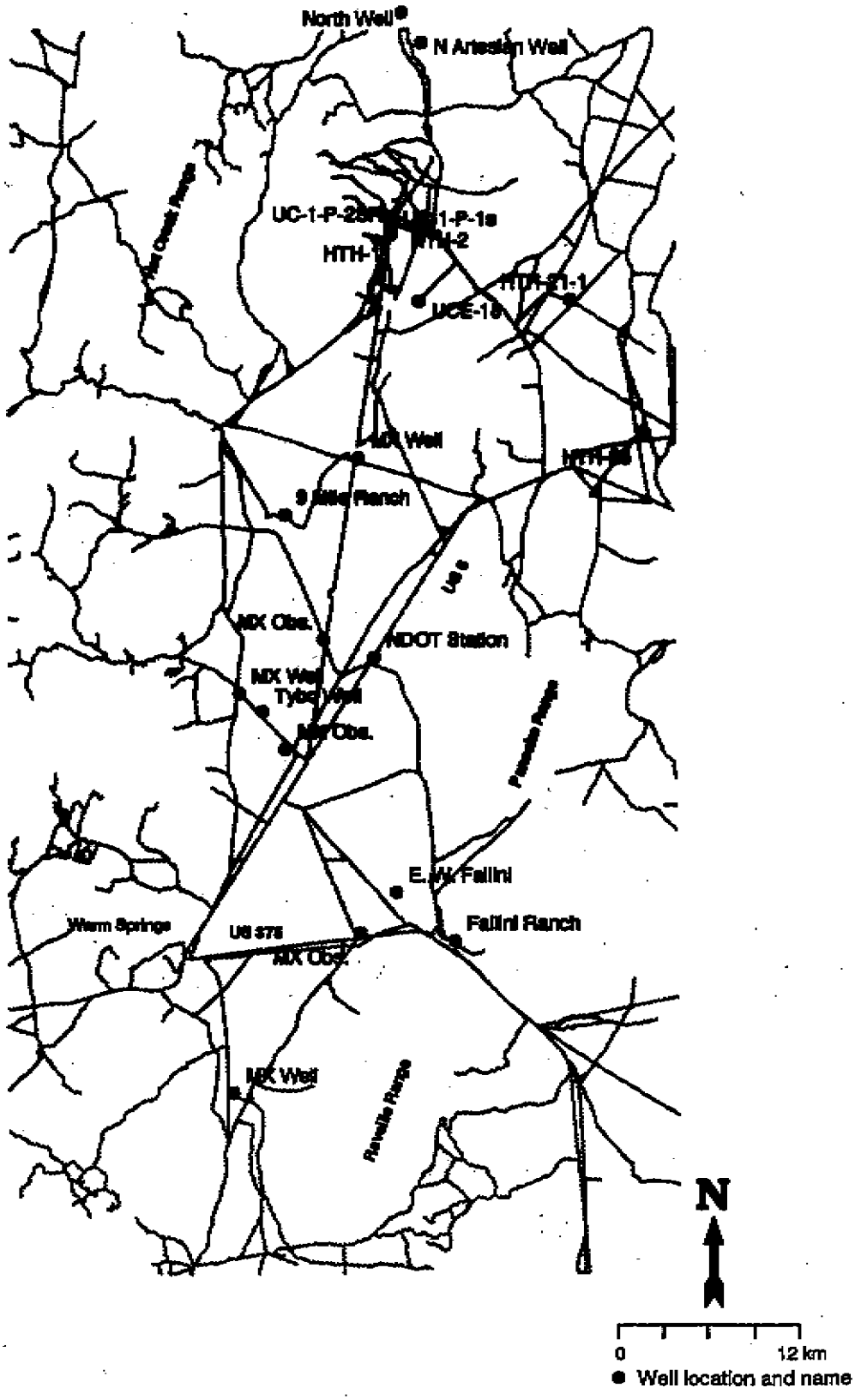

Figure 1. Location of wells where water level measurements were made.

Figure 2. Contour map of composite groundwater heads in Hot Creek Valley.

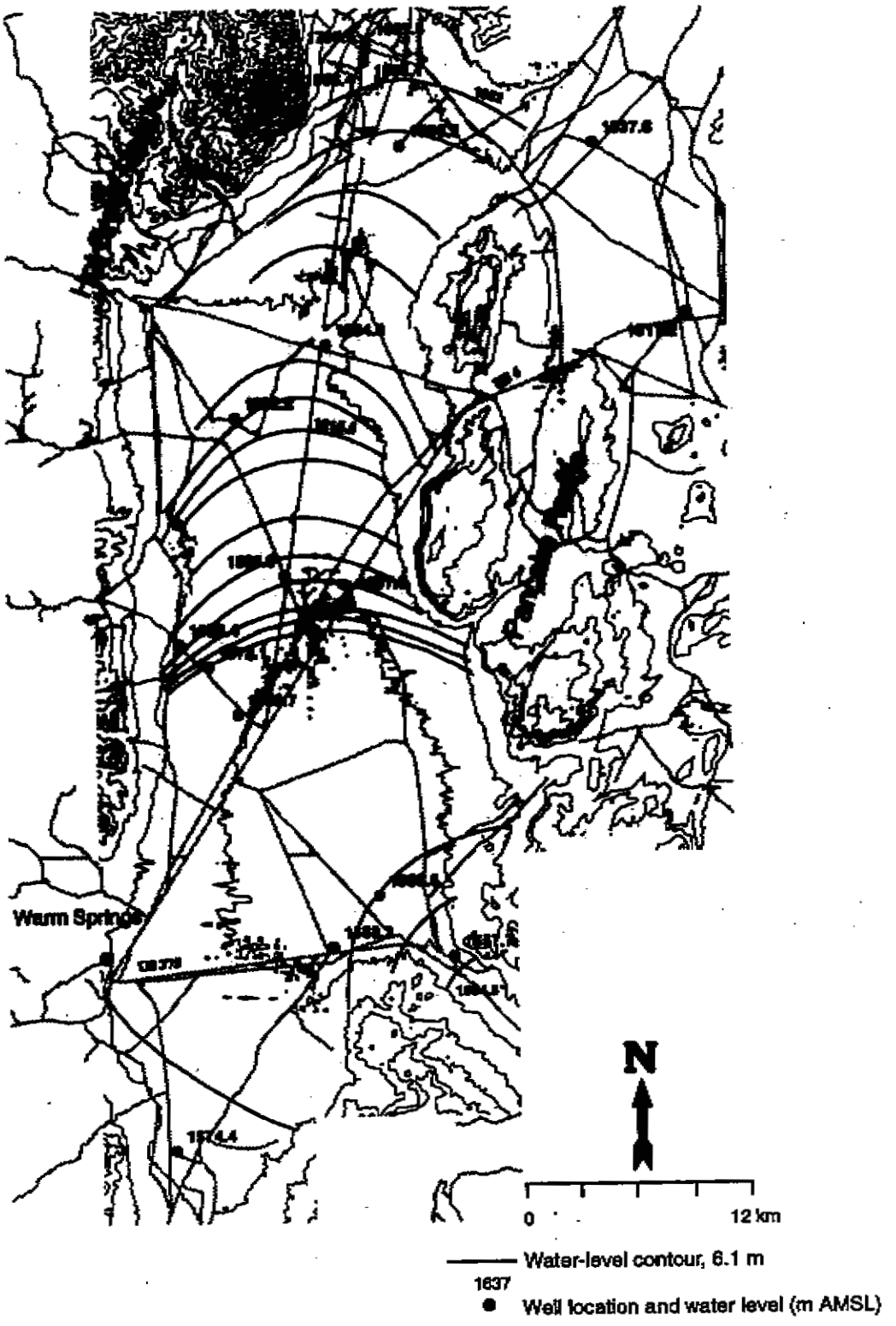

Figure 3. Contour map of composite groundwater heads in Hot Creek Valley, focusing on the area where hydraulic gradients are lowest.

APPENDIX 2

SUMMARY OF HYDRAULIC DATA FROM CNTA PACKER TESTS

The data contained in this appendix summarize the results of straddle packer tests conducted in the CNTA exploratory holes as reported by Dinwiddie and Schroder (1971).

Explanation

nc	–	data not collected for interval
e	–	estimated
lsd	–	land surface datum
m	–	meters
m3 pd	–	cubic meters per day
dd	–	drawdown
m2	–	square meters
High	–	recovery too rapid to measure
Low	–	time-interval measurement of water-level change too small to measure accurately

Note

There are two columns of values for Static Water Level and Relative Specific Capacity. The values in the first column are from injection, the values in the second column are from recovery after swabbing.

HTH-1

Northing(ft)		1411443							
Easting(ft)		629720							
Elevation(m)		1832							
Zone	Interval Tested		Static Water Level		Relative Specific Capacity		Transmissivity	Hydraulic Conductivity	Rock Type
	(m below lsd)		(m below lsd)		(m3 pd per m of dd)		(m3 pd per m)	(m3 pd per m2)	
10	213	259	168	167.4	High	High	e16.4	e3.60E-01	Alluvium
9	290	350.5	168	167.7	1.79	nc	3.1	5.10E-02	Alluvium
8	426.7	457.2	167.1	167.4	0.54	0.18	6.00E-01	2.00E-02	Alluvium
7	506	524.2	168.6	nc	0.054	0.072	7.30E-02	4.00E-03	Alluvium
6	563.9	603.5	nc	168	0.054	0.089	8.20E-02	2.10E-03	Alluvium
5	670.6	701	nc	e168	e0.018	nc	1.90E-03	6.20E-05	Alluvium
4	731.4	749.8	166.8	nc	0.18	nc	3.30E-01	1.80E-02	Welded tuff
3	804.7	826	169.2	nc	0.54	nc	1.2	5.60E-02	Tuffaceous sediments
2	899.2	917.4	170.1	nc	1.07	nc	4.9	2.70E-01	Tuffaceous sediments
1	1094	1117	nc	e168	e0.0036	e0.0054	nc	nc	Tuffaceous sediments

HTH-3

Northing(ft)		1385943.94							
Easting(ft)		657118.89							
Elevation(m)		1803							
Zone	Interval Tested		Static Water Level		Relative Specific Capacity		Transmissivity	Hydraulic Conductivity	Rock Type
	(m below lsd)		(m below lsd)		(m3 pd per m of dd)		(m3 pd per m)	(m3 pd per m2)	
1	16	197	169.5	nc	nc	nc	nc	nc	Welded tuff
3	1056	1114	169.8	nc	4.8	nc	1.20E+01	2.10E-01	Welded tuff
2	1119	1171	171.2	nc	8.4	nc	1.20E+01	2.30E-01	Welded tuff
6	1432	1526	172.8	nc	0.34	nc	9.70E-01	1.00E-02	Welded tuff, tuffaceous sandstone and claystone
5	1570	1667	172.5	nc	0.61	nc	2.4	2.80E-02	Welded tuff
4	1673	1771	172.9	nc	1.1	nc	2.9	3.00E-02	Welded tuff
7	1434	1831	172.7	nc	nc	nc	nc	nc	Welded tuff, tuffaceous sandstone and claystone

HTH-4

Northing(ft)		1379469.45							
Easting(ft)		683276.08							
Elevation(m)		1776							
Zone	Interval Tested (m below lsd)		Static Water Level (m below lsd)		Relative Specific Capacity (m3 pd per m of dd)		Transmissivity (m3 pd per m)	Hydraulic Conductivity (m3 pd per m2)	Rock Type
2	0	219	144.5	nc	nc	nc	nc	nc	Alluvium and rhyolite
1	265	271	151.1	nc	0.75	nc	7.30E-01	1.20E-01	Partially to densely welded tuff
3	615.7	624.8	164.3	nc	3.6	nc	7.3	8.00E-01	Partially to densely welded tuff
7	1061	1070	nc	nc	nc	nc	nc	nc	Partially to densely welded tuff
6	1347	1356	e258	nc	e0.036	nc	e7.30E-01	e8.00E-01	Partially to densely welded tuff
5	1661	1670	nc	nc	nc	nc	nc	nc	Partially to densely welded tuff
4	1783	1792	nc	nc	e0.002	nc	nc	nc	Partially to densely welded tuff

HTH-5

Northing(ft)	1368424.47						
Easting(ft)	625928.65						
Elevation(m)	1675						
Zone	Interval Tested (m below lsd)		Static Water Level (m above (+) or m below (-) lsd)		Relative Specific Capacity (m3 pd per m of dd)		Rock Type
7	174	180	-30.2	nc	nc	nc	Alluvium
1	138	635.5	-38.42	nc	0.18	nc	Alluvium, [illegible] sandstone and siltstone, and welded tuff
3	635.2	791	5.79	nc	nc	nc	Welded tuff with thin intervals of bedded tuff
2	794	1008	e+13	nc	nc	nc	Welded tuff with thin intervals of bedded tuff
4	1008	1085	nc	nc	e0.004	nc	Welded tuff with thin intervals of bedded tuff
6	1635	1704	e+97	nc	e0.00006	nc	Welded tuff with thin intervals of bedded tuff
5	1705	1831	136.5	nc	0.002	nc	Welded tuff with thin intervals of bedded tuff

HTH-21-1

Northing(ft)		1397250.13							
Easting(ft)		668505.56							
Elevation(m)		1787							
Zone	Interval Tested		Static Water Level		Relative Specific Capacity		Transmissivity	Hydraulic Conductivity	Rock Type
	(m below lsd)		(m below lsd)		(m3 pd per m of dd)		(m3 pd per m)	(m3 pd per m2)	
14	408.4	624.8	154.2	nc	nc	nc	nc	nc	Alluvium
12	694.6	706.5	151.5	nc	12	nc	23.1	1.94	Welded tuff
13	709.8	749.2	150	nc	12	nc	23.1	0.58	Welded tuff
9	1109	1167	151.6	nc	6.8	nc	17.3	0.30	Welded tuff
8	1358	1416	147.8	nc	3.6	nc	23.1	0.40	Tuffaceous sediment
10	1418	1468	153.4	nc	7.7	nc	13.8	0.28	Welded tuff
7	1471	1528	127.9	nc	0.55	nc	0.69	0.012	Welded tuff
5	1535	1593	129.5	nc	8.8	nc	23.1	0.40	Welded tuff
6	1596	1981	129.5	nc	nc	nc	nc	nc	Welded tuff
11	1608	1699	nc	nc	e0.007	nc	e1.40E-05	e1.50E-07	Welded tuff
3	1703	1760	nc	nc	e0.006	nc	e6.90E-04	e1.20E-05	Welded tuff
4	1763	1981	e115	nc	e0.5	nc	nc	nc	Welded tuff
1	1822	1880	nc	nc	Low	nc	nc	nc	Welded tuff
2	1883	1981	nc	nc	Low	nc	nc	nc	Welded tuff

HTH-23

Northing(ft)		1368067							
Easting(ft)		684237							
Elevation(m)		1786							
Zone	Interval Tested		Static Water Level		Relative Specific Capacity		Transmissivity	Hydraulic Conductivity	Rock Type
	(m below lsd)		(m below lsd)		(m3 pd per m of dd)		(m3 pd per m)	(m3 pd per m2)	
1	379.2	750.1	132.5	nc	nc	nc	nc	nc	Welded tuff
6	1413	1486	130.7	nc	0.07	nc	2.90E-01	4.00E-03	Welded tuff
5	1489	1562	142.3	nc	0.02	nc	2.40E-02	3.30E-04	Welded tuff
7	1550	1598	142.8	nc	0.89	nc	9.10E-01	1.90E-02	Welded tuff
4	1596	1669	nc	nc	e0.07	nc	e6.10E-02	e8.30-04	Welded tuff
8	1671	1719	143.6	nc	1.6	nc	4.8	1.00E-01	Welded tuff
9	1722	1795	nc	nc	e0.04	nc	e1.00E-03	e1.40E-05	Welded tuff
3	1777	1850	nc	nc	e0.02	nc	e6.20E-04	e8.40E-06	Welded tuff
2	1853	1899	144.6	nc	2.1	nc	5.8	1.30E-01	Welded tuff
11	1852	1908	136.6	nc	nc	nc	nc	nc	Welded tuff
10	1911	1944	136.6	nc	3.8	nc	4.8	1.80E-01	Welded tuff

UCe-16

Northing(ft	1499400						
Easting(ft)	487000						
Elevation(	2095	+ 7.6					
Zone	Interval Tested		Static Water Level		Relative Specific Capacity		Rock Type
	(m below lsd)		(m above (+) or m below (-) lsd)		(m3 pd per m of dd)		
1	514.2	563.9	5.88	nc	High	nc	Rhyolite
2	1078	1138	-16	nc	0.018	nc	Rhyolite
3	1150	1210	-2	nc	e0.0054	nc	Rhyolite
4	1263	1327	between -25 and -42	nc	Low	nc	Rhyolite

UCe-17

Northing(ft)	1430622								
Easting(ft)	628172								
Elevation(m)	1998								
Zone	Interval Tested		Static Water Level		Relative Specific Capacity		Transmissivity	Hydraulic Conductivity	Rock Type
	(m below lsd)		(m below lsd)		(m3 pd per m of dd)		(m3 pd per m)	(m3 pd per m2)	
15	239	279	145	145	High	High	nc	nc	Alluvium
14	539.5	560.8	145	145	nc	nc	nc	nc	Alluvium
1	956.7	1018	269	nc	0.89	nc	e2.63	e4.31E+02	Welded tuff
2	1158	1219	nc	nc	nc	nc	nc	nc	Welded tuff
3	1223	1284	nc	nc	nc	nc	nc	nc	Welded tuff
4	1367	1428	nc	nc	e0.02	nc	e1.31E-01	e2.15E-03	Welded tuff
5	1408	1469	272	nc	4.1	nc	e8.76	e1.44E-01	Welded tuff
6	1597	1658	nc	nc	e0.005	nc	e2.63E-03	e4.31E-05	Welded tuff
8	1868	1929	nc	nc	e0.036	nc	2.63E-03	4.31E-05	Tuffaceous sediments
9	1960	2021	nc	nc	e0.02	nc	8.47E-04	1.39E-05	Tuffaceous sediments
10	2056	2117	e351	nc	e0.05	nc	6.57E-02	1.08E-03	Welded tuff
11	2149	2210	nc	nc	e0.04	nc	2.39E-02	3.92E-04	Welded tuff
12	2212	2273	nc	nc	e0.007	nc	1.75E-03	2.87E-05	Welded tuff

UCe-18

Northing(ft)		1396833							
Easting(ft)		635840							
Elevation(m)		1756							
Zone	Interval Tested (m below lsd)		Static Water Level (m below lsd)		Relative Specific Capacity (m3 pd per m of dd)		Transmissivity (m3 pd per m)	Hydraulic Conductivity (m3 pd per m2)	Rock Type
11	124	182	101	nc	High	High	nc	nc	Alluvium
10	1237	1277	nc	nc	Low	nc	e4.00E-03	e1.00E-04	Alluvium
9	1388	1447	nc	nc	nc	nc	nc	nc	Rhyolite
12	1461	1522	nc	nc	nc	nc	nc	nc	Rhyolite
5	1530	1579	nc	nc	High	High	nc	nc	Rhyolite
8	1615	1649	59.3	nc	nc	nc	nc	nc	Rhyolite
7	1685	1719	nc	e58	nc	0.36	nc	nc	Rhyolite
4	1717	1766	e64	e64	High	High	nc	nc	Rhyolite
6	1769	1802	nc	e58	nc	3.6	nc	nc	Rhyolite
3	1804	1853	nc	nc	nc	e0.018	nc	nc	Rhyolite
2	1874	1985	nc	64	nc	nc	nc	nc	Rhyolite and bedded tuff
1	1948	1985	nc	nc	nc	nc	nc	nc	Rhyolite and bedded tuff

UCe-20

Northing(ft)		1399868.46							
Easting(ft)		628092.75							
Elevation(m)		1755							
Zone	Interval Tested (m below lsd)		Static Water Level (m below lsd)		Relative Specific Capacity (m3 pd per m of dd)		Transmissivity (m3 pd per m)	Hydraulic Conductivity (m3 pd per m2)	Rock Type
13	213	219	104	nc	0.089	nc	7.78E-03	1.27E-03	Alluvium
14	671	677	nc	nc	e0.0007	nc	e6.25E-04	e1.02E-04	Alluvium
5	1481	1503	nc	nc	e0.002	nc	e2.48E-04	e1.18E-05	Welded tuff
1	1481	1618	nc	nc	e1.27	nc	1.35E-01	9.90E-04	Welded tuff
4	1503	1538	nc	nc	e0.009	nc	4.38E-03	1.22E-04	Welded tuff
10	1521	1539	nc	nc	e0.005	nc	2.19E-03	1.20E-04	Welded tuff
11	1539	1558	69.5	66.8	0.32	0.39	1.31E-01	7.16E-03	Welded tuff
3	1539	1618	nc	nc	e0.2	nc	9.38E-02	1.20E-03	Welded tuff
2	1579	1618	nc	nc	e0.0003	nc	e8.75E-04	e2.26E-05	Welded tuff
9	1625	1829	82.6	79.9	6.44	nc	e43.8	e2.10E-01	Welded tuff
12	1653	1671	65.5	65.6	High	High	e37.5	2.05	Welded tuff
8	1680	1829	84.5	82.9	nc	0.14	e26.3	1.76E-01	Welded tuff
7	1799	1829	nc	nc	e0.04	nc	1.73E-02	5.67E-04	Welded tuff

APPENDIX 3

ANALYSIS OF CAVITY INFLOW FLUX RELATIVE TO DIFFUSIVE FLUX FOR THE FAULTLESS EVENT

Prepared by Dr. Bill Hu

A significant depression in potentiometric levels in the cavity area was caused by the Faultless test. The subsequent recovery to pre–test levels is taking decades to complete. During this period, no advective movement of contaminants from the Faultless chimney can occur because the hydraulic gradient is radially directed toward, rather than away from, the test cavity. Though advective movement is not possible, the strong concentration gradient between the highly radioactive cavity and the surrounding low radioactivity groundwater creates the potential for diffusive flux of contaminants away from the cavity. The following analysis quantitatively examines the magnitude of the advective flux of non–contaminated water toward the cavity relative to the diffusive flux of contaminated water away. The conclusion is that the advective flux is much larger than the diffusive flux until very late time, so that significant diffusion–driven migration from Faultless is unlikely.

Water Level Equation (in meters)

$$h(t) = 857.43 + 0.195 * t - 1.722 * 10^{-5} * t^2 + 5.587 * 10^{-10} * t^3 \qquad (1)$$

The above equation is only valid for t>5000 days from the beginning of 1968. From the fit, the water level will be 1687 m about 12,130 days from January 1, 1968. That means the water level will be totally recovered in March, 2001.

Process Analysis

Dispersion Equation

$$\frac{\partial C}{\partial t} = D\nabla^2 C - \nabla \cdot (VC) \qquad (2)$$

$\partial C/\partial t>0$ means convective transport of solute into the cavity is larger than the dispersion from the cavity; and vice versa. Initially, $\nabla \cdot (VC) >> D\nabla^2 C$. Basically speaking, $D\nabla^2 C$ is unchanged, but $\nabla \cdot (VC)$ decreases with the water level recovering in the cavity. At some date, the water level reaches a height where $\nabla \cdot (VC) = D\nabla^2 C$. After that date, solute will begin to disperse out of the cavity. Here we will calculate the water level and the date, which start from the following equation.

$$D\nabla^2 C - \nabla \cdot (VC) = \nabla \cdot (D\nabla C - VC) = 0 \qquad (3)$$

Which means the mass flow–in equals the mass flow–out. Equation (3) can be written as

$$D\nabla C = VC$$

Or

$$V = \frac{D\nabla C}{C} \qquad (4)$$

Basic Assumptions:

1. homogenous and isotropic medium
2. no recharge (pure recovering process)
3. solute concentration in the cavity is uniform and constant
4. there is a concentration decrease ring, where the solute concentration decreases from C_0 (the concentration inside the cavity) to zero. The ring's length is assumed to be L (meter)
5. isothermal conditions are assumed.

Calculation

1. Concentration distribution within the ring

$$D\left[\frac{1}{r}\frac{\partial}{\partial r}\left(r\frac{\partial C}{\partial r}\right)\right] = 0 \qquad (5)$$

The solution of (5) is

$$C = \frac{C_0}{\ln(1 + L/r_0)}[\ln(r_0 + L) - \ln r] \qquad where(r_0 < r < r_0 + L) \qquad (6)$$

where r_0 is the radius of the cavity and is known to be 100 m.

2. Water level distribution and hydraulic gradient

Since no recharge is assumed in the vertical direction, the flow rate in a cylindrical cross–section is

$$Q = -2\pi T\frac{dh}{dr} \qquad (7)$$

where Q is the flow rate into the cavity, and T=KM is the transmissivity, K is the conductivity, and M is the aquifer thickness.

Let R represent the hydraulic funnel's radius caused by the cavity and assume R=600m (from the center of the cavity).

(7) can be solved as

$$H - h = \frac{H - h_0}{\ln(600/100)}(\ln 600 - \ln r) \qquad (8)$$

where h_0 is the water level in the cavity, H is the water level beyond the hydraulic funnel, which is known as 1687 m (the pre–test water level).

The hydraulic gradient is

$$\frac{dh}{dr} = \frac{H - h_0}{\ln(600/100)}\frac{1}{r} \qquad (9)$$

3. Solute diffusion and mass convective flux

Solute diffusion out of the cavity

$$q_{out} = -D\frac{\partial C}{\partial r} = \frac{DC_0}{\ln(1 + L/r_0)}\frac{1}{r} \quad (r_0 < r < r_0 + L) \tag{10}$$

Mass convective flux into the cavity

$$q_{in} = -CV = CK\frac{dh}{dr} = K\frac{H - h_0}{\ln(600/100)}\frac{C}{r} \tag{11}$$

Let q_{in} equal q_{out} at the middle of the ring (r=100+L/2 m).

$$\frac{DC_0}{\ln(1 + L/r_0)}\frac{1}{r_0 + L/2} = K\frac{H - h_0}{\ln(600/100)}\frac{C_{r_0+L/2}}{r_0 + L/2} \tag{12}$$

From (6) we have

$$C_{r_0+L/2} = \frac{C_0}{\ln(1 + L/r_0)}[\ln(r_0 + L) - \ln(r_0 + L/2)] \tag{13}$$

Substitute (13) into (12) to yield

$$h_0 = H - \frac{D\ln 6}{K[\ln(r_0 + L) - \ln(r_0 + L/2)]} \tag{14}$$

$K = 3.9\times10^{-8}$ m/s

$D=2.939\times10^{-9}$ m^2/s

If the ring length is chosen as L=5m, then

h_0=1687–4.87=1682.13 m. This is the recovered water level where the flux inward and outward will be equal. This is projected to occur in September, 2000 (11,900 days from January 1, 1968).

If the ring length is chosen to be L=10m, then

h_0=1687–2.9=1684.1 m, which is projected to occur in November, 2000 (12,000 days from January 1, 1968).

If the ring length is chosen to be L=100m, then

h_0=1687–0.47=1686.53m, which is projected to occur in January, 2001 (12,060 days from January 1, 1968).

With the assumption of ring length, and the other assumptions listed earlier, diffusion is not expected to overcome advective flux into the cavity until two to five months prior to full hydraulic recovery. Once full recovery is achieved, contaminant migration will again be dominated by advective flux (during this time, away from the cavity).

APPENDIX 4

ELECTRICAL RESISTIVITY LOGS

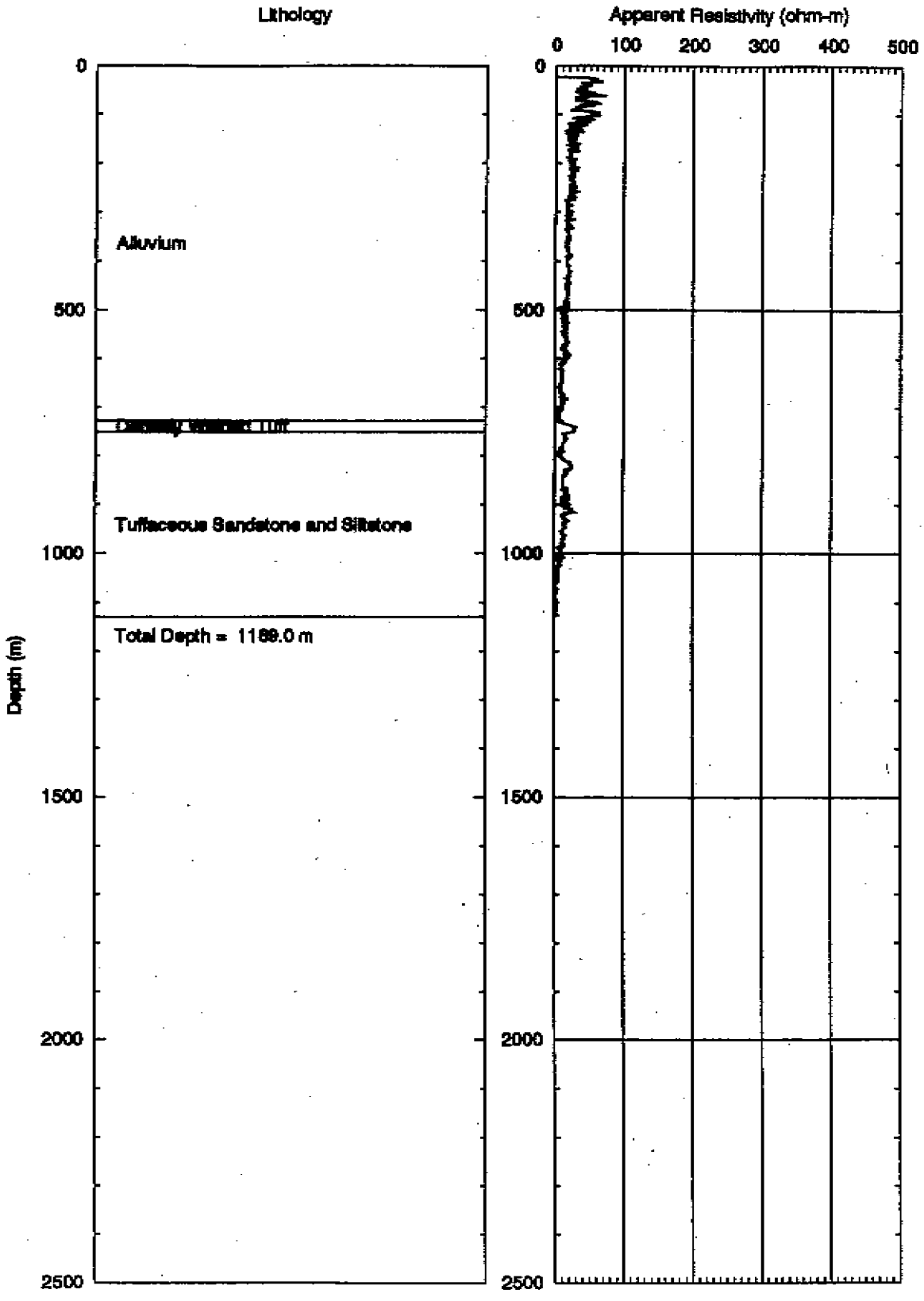

Figure 4–1. Lithologic log and lateral log for HTH-1.

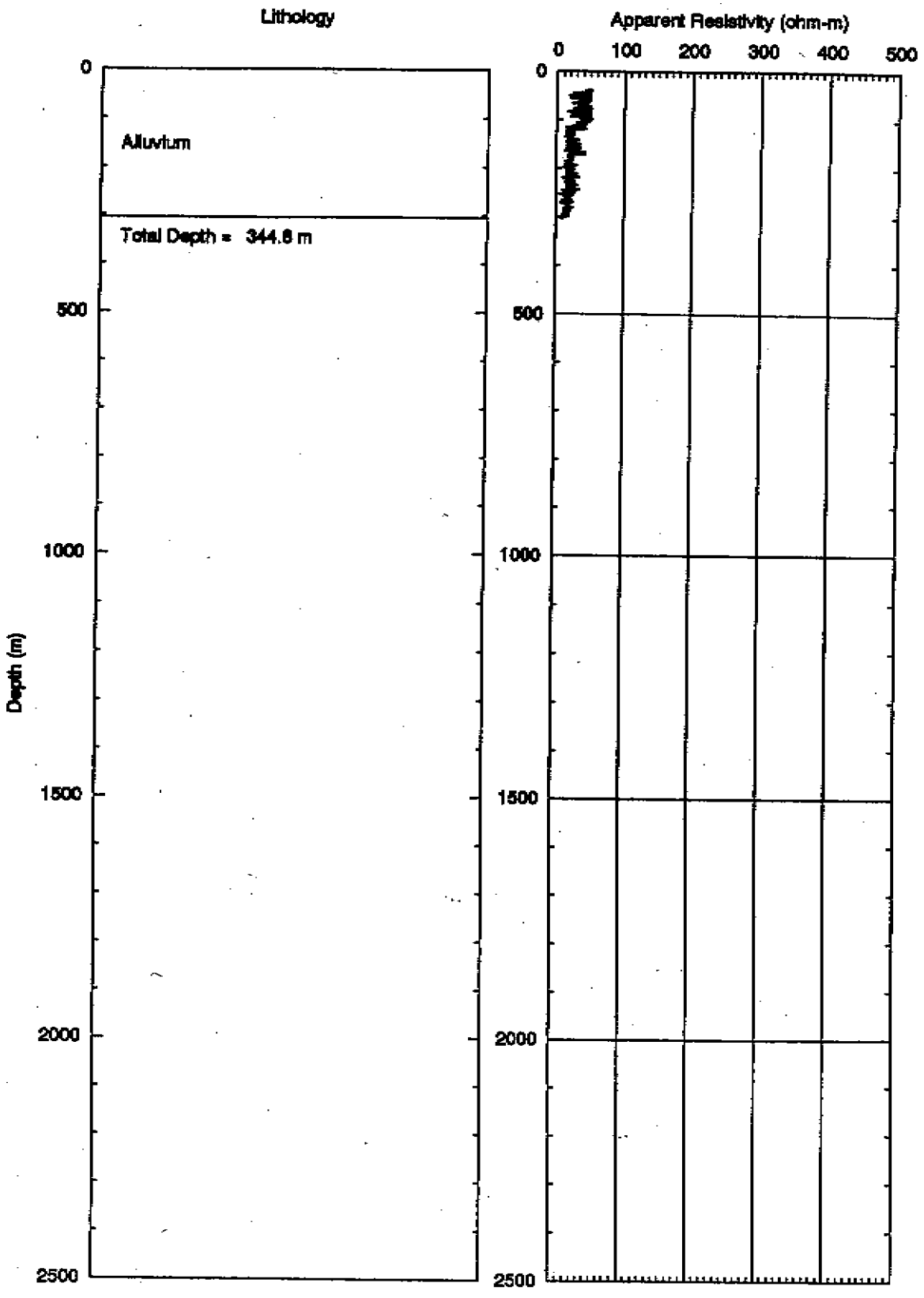

Figure 4–2. Lithologic log and lateral log for HTH-2.

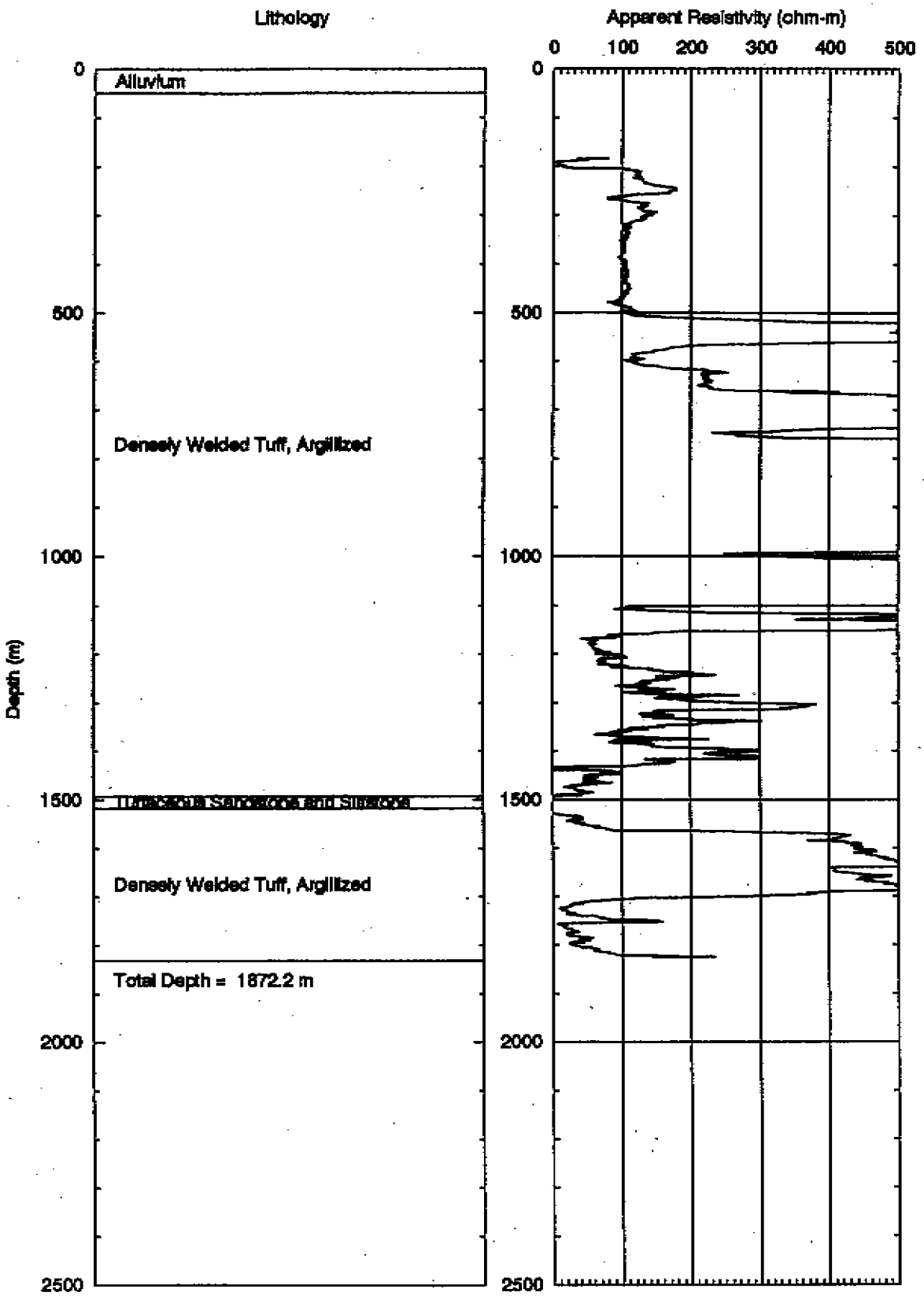

Figure 4–3. Lithologic log and lateral log for HTH-3.

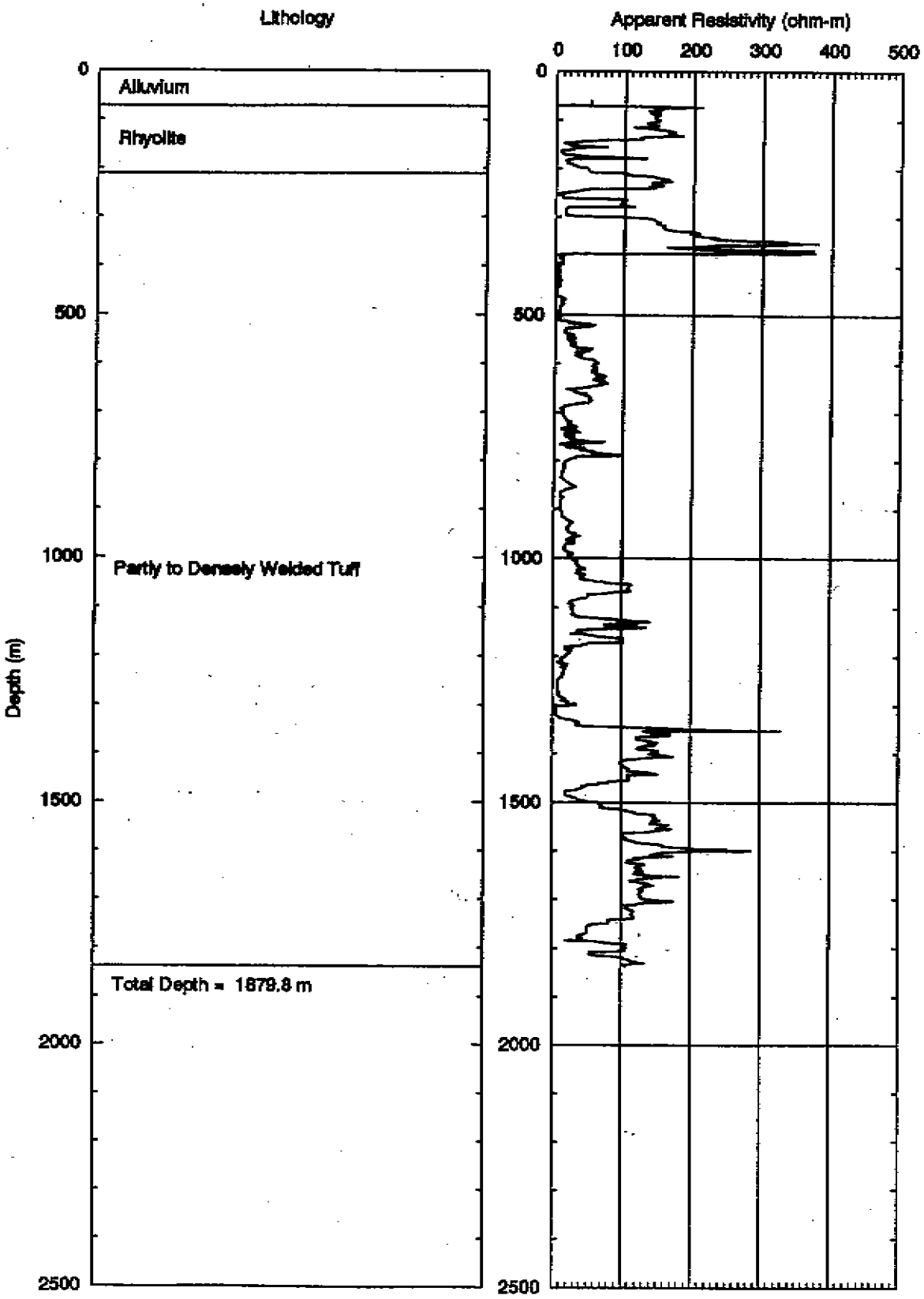

Figure 4–4. Lithologic log and lateral log for HTH-4.

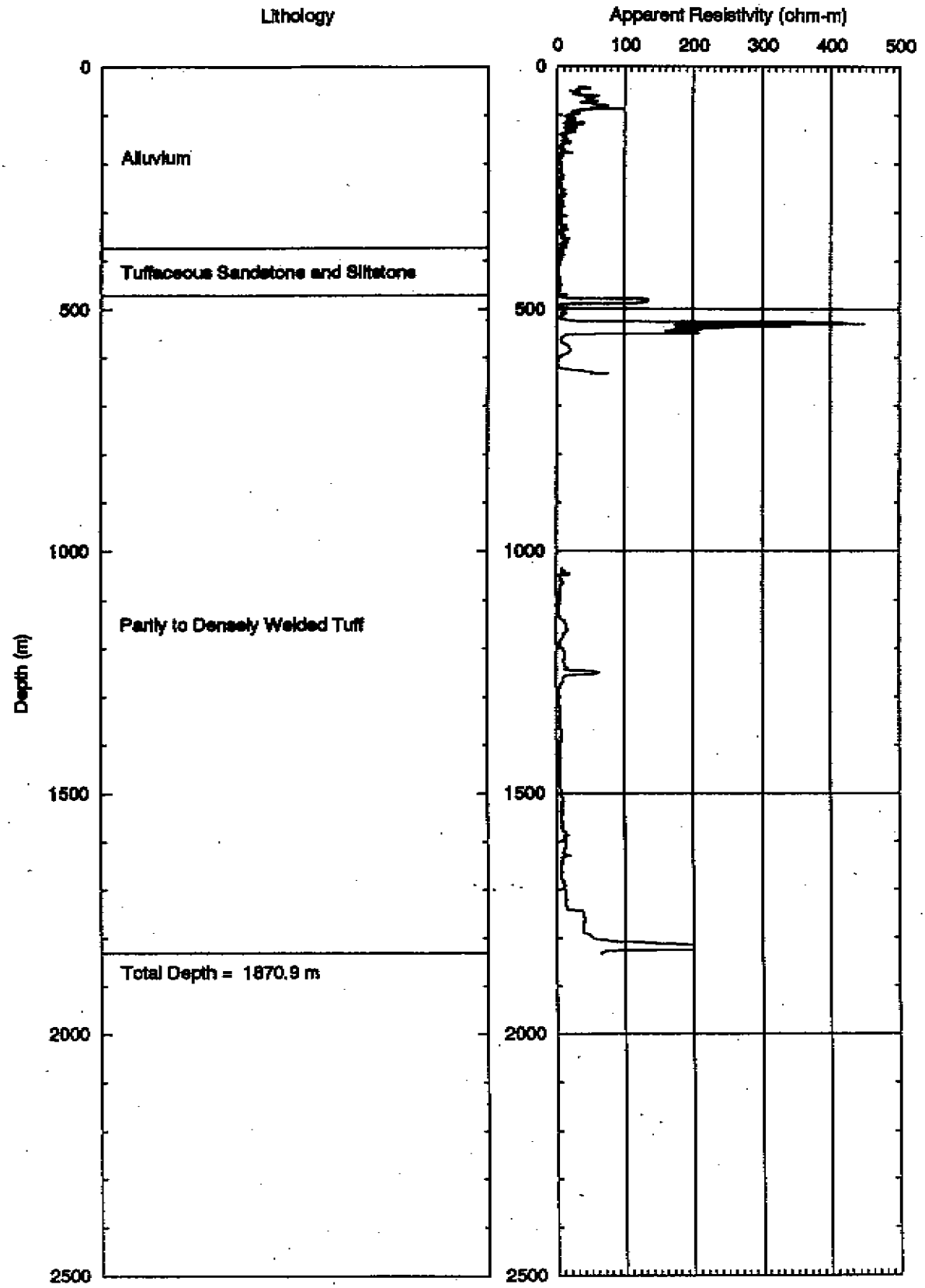

Figure 4–5. Lithologic log and lateral log for HTH-5.

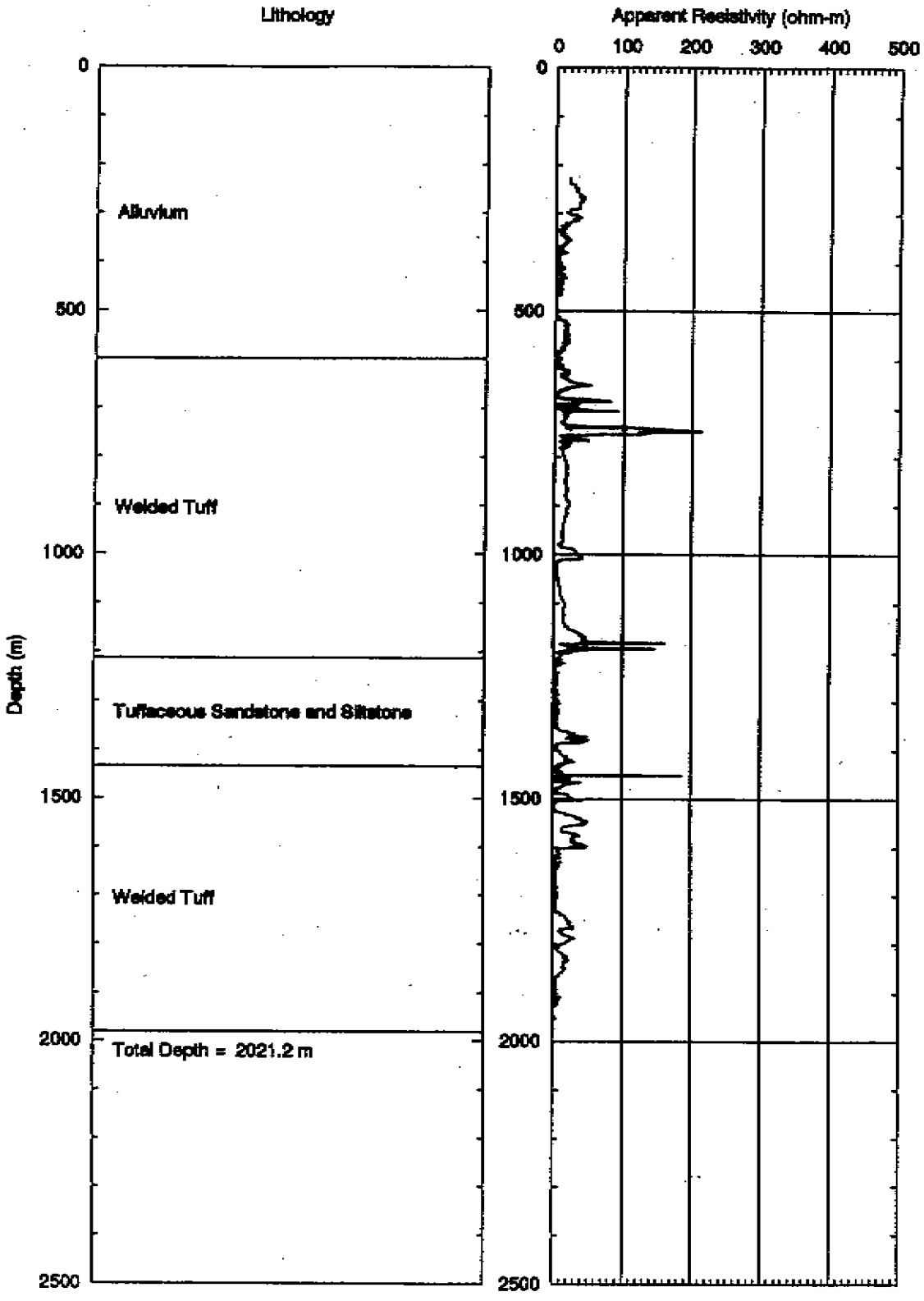

Figure 4–6. Lithologic log and lateral log for HTH-21-1.

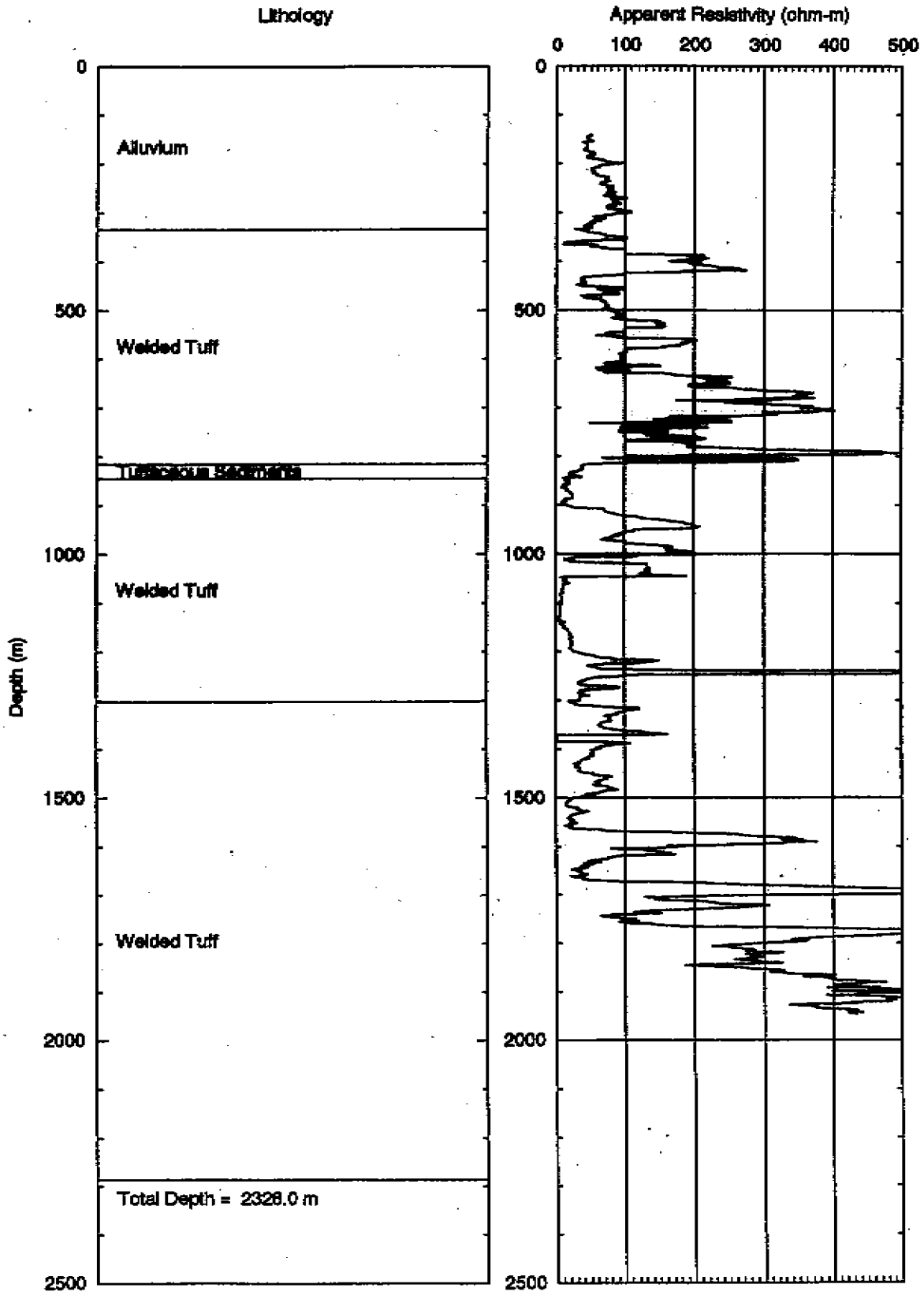

Figure 4–7. Lithologic log and lateral log for HTH-23.

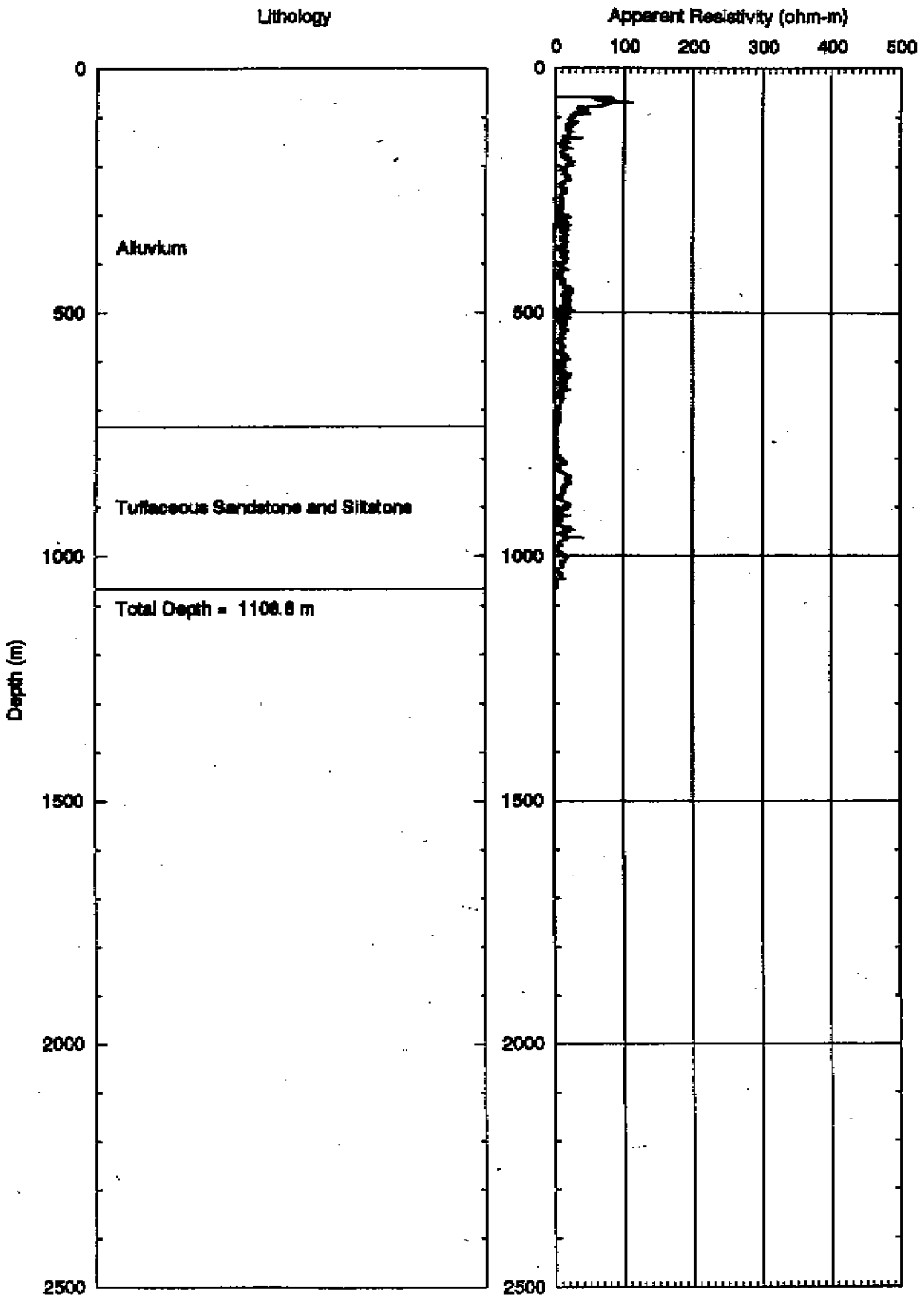

Figure 4–8. Lithologic log and lateral log for UC-1-i-1.

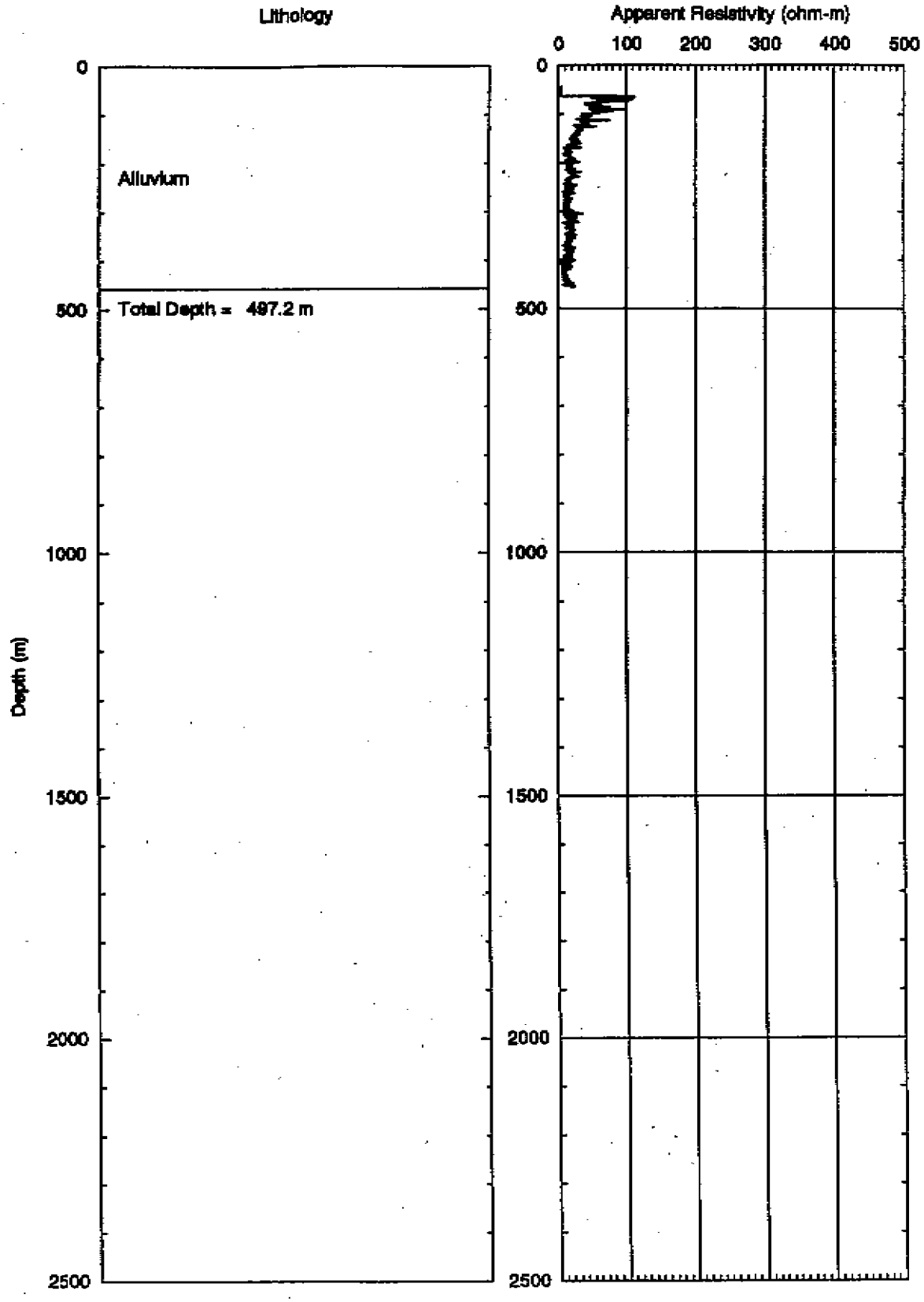

Figure 4–9. Lithologic log and lateral log for UC-1-i-2.

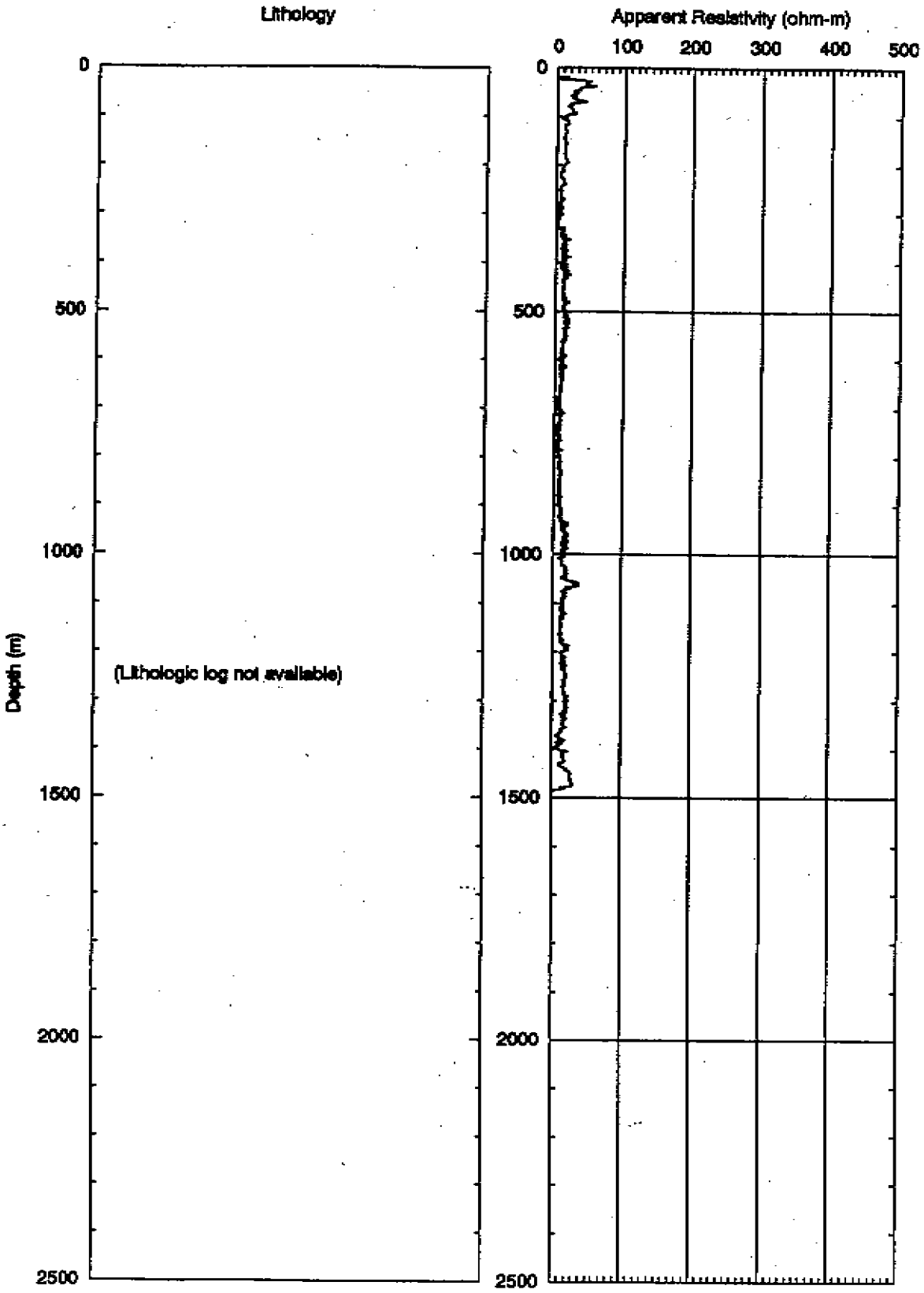

Figure 4–10. Lithologic log and lateral log for UC-3-i-1.

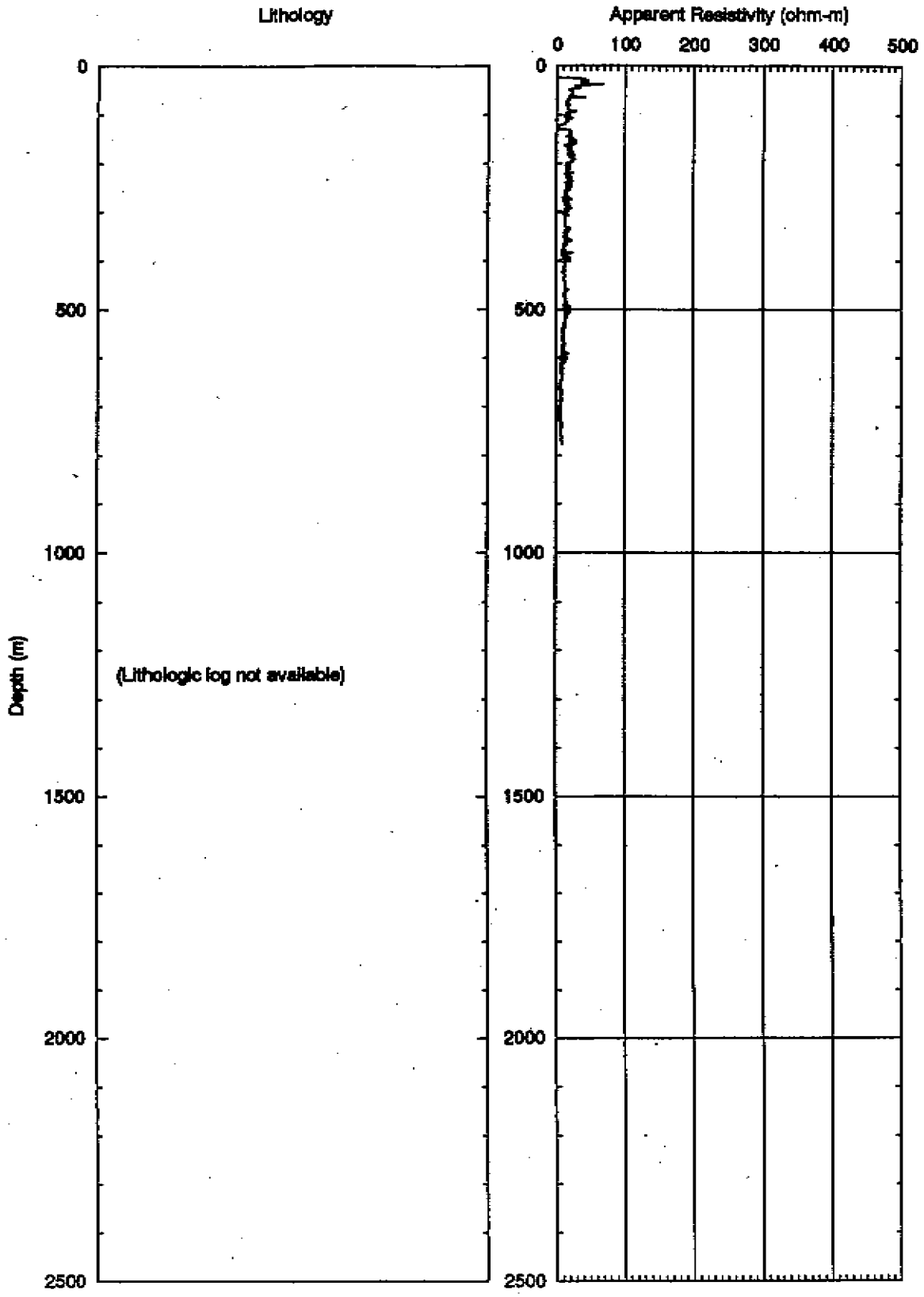

Figure 4–11. Lithologic log and lateral log for UC-3-i-2.

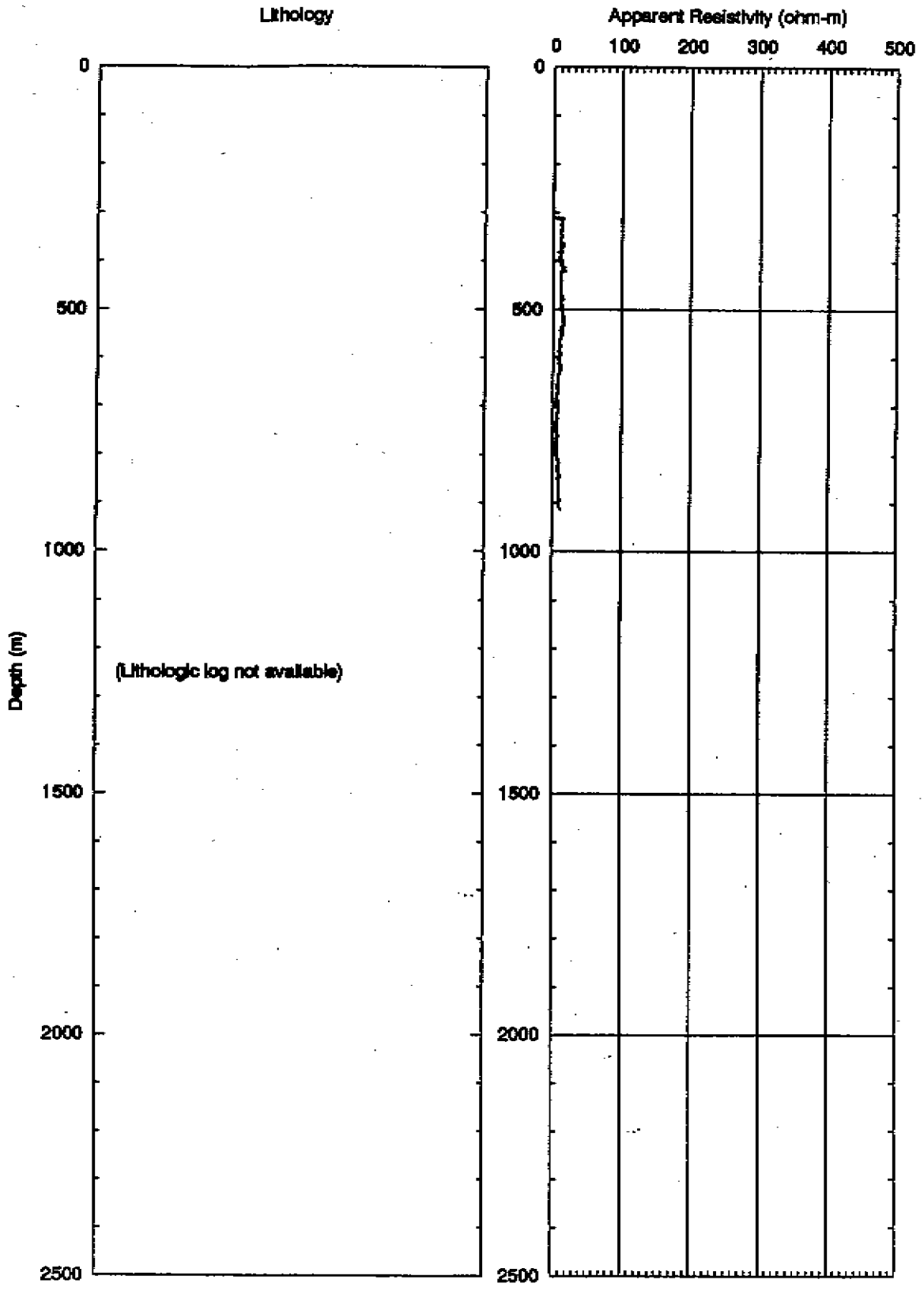

Figure 4–12. Lithologic log and lateral log for UC-3-i-3.

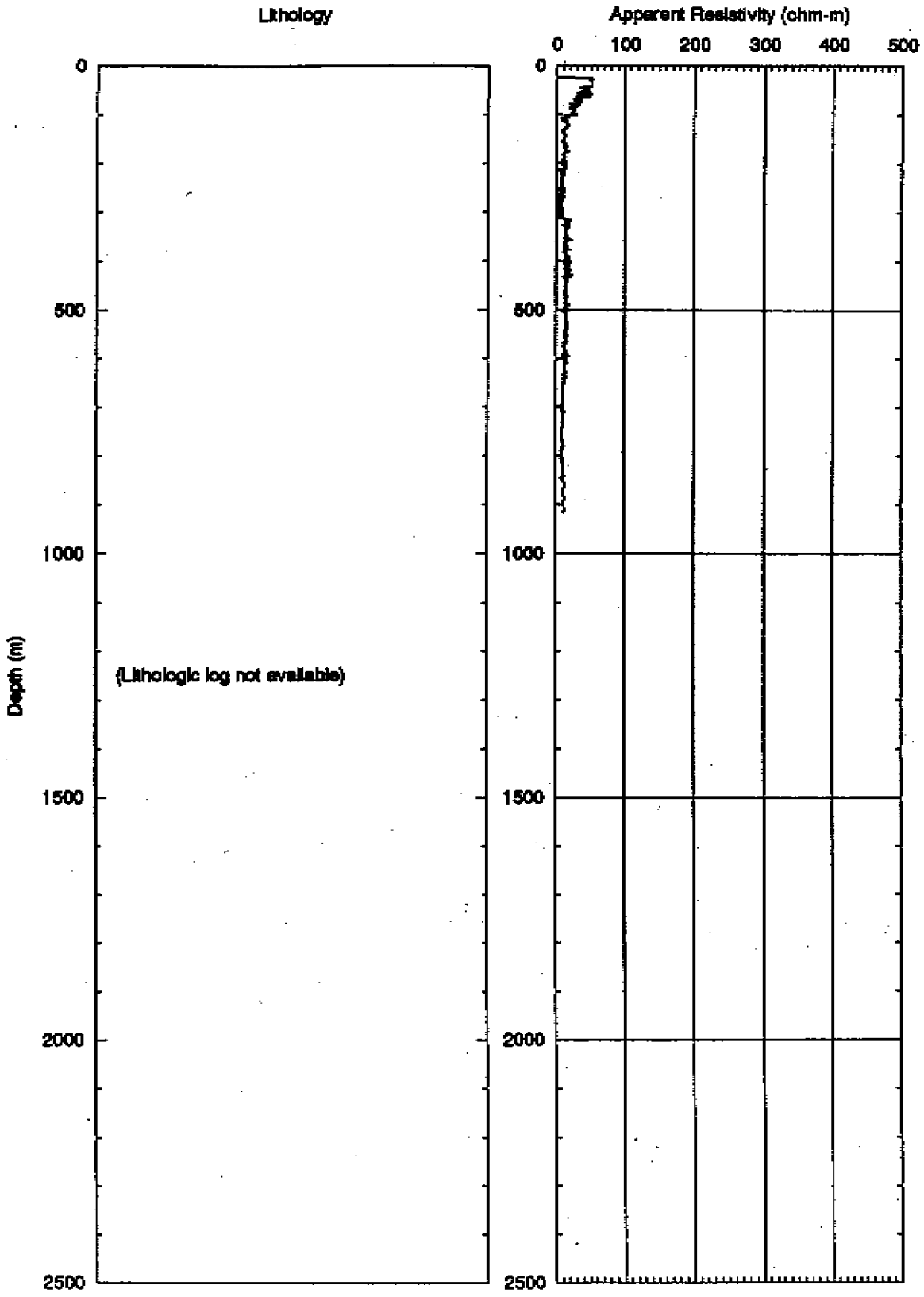

Figure 4–13. Lithologic log and lateral log for UC-3-i-4.

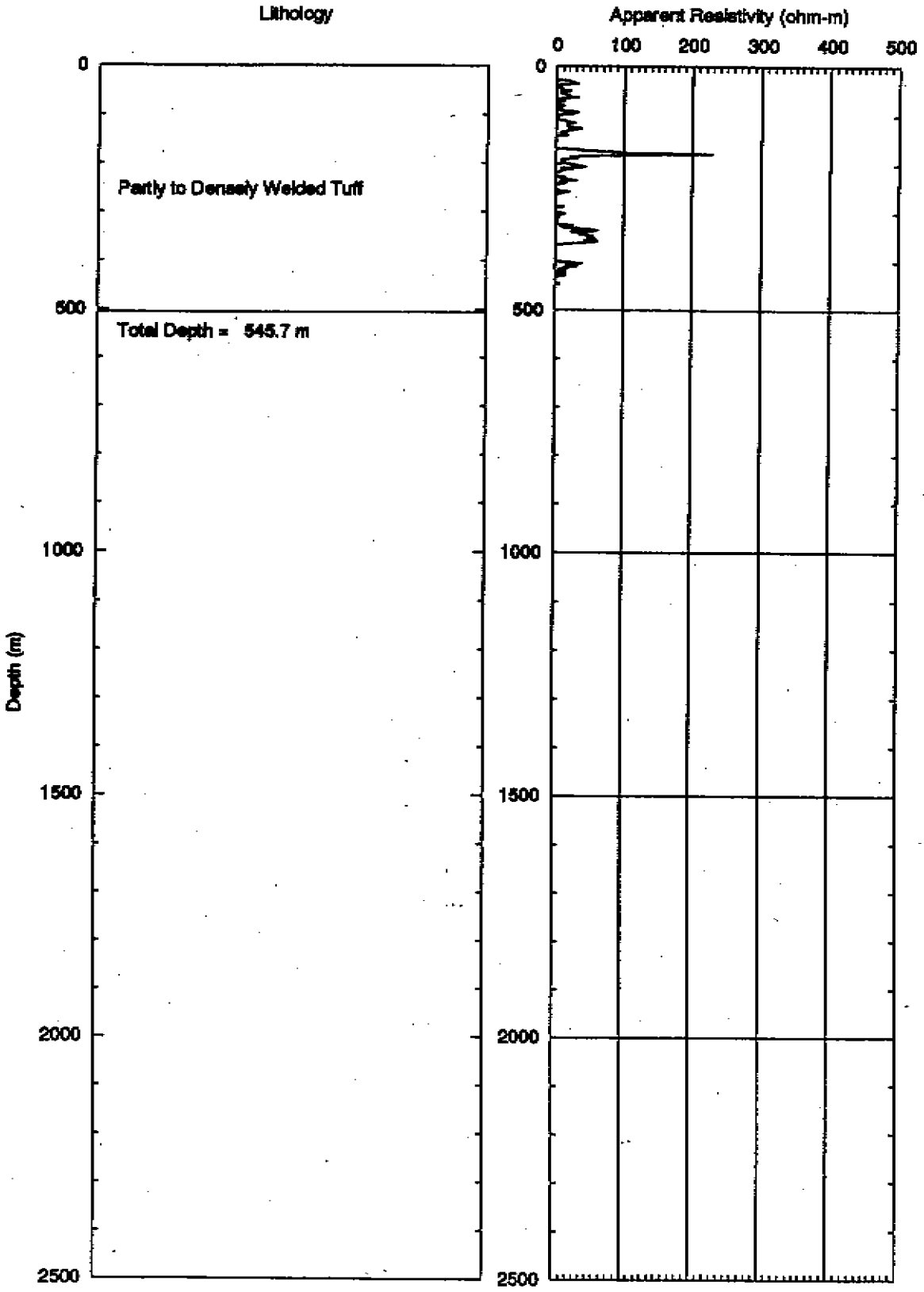

Figure 4–14. Lithologic log and lateral log for UCe-2.

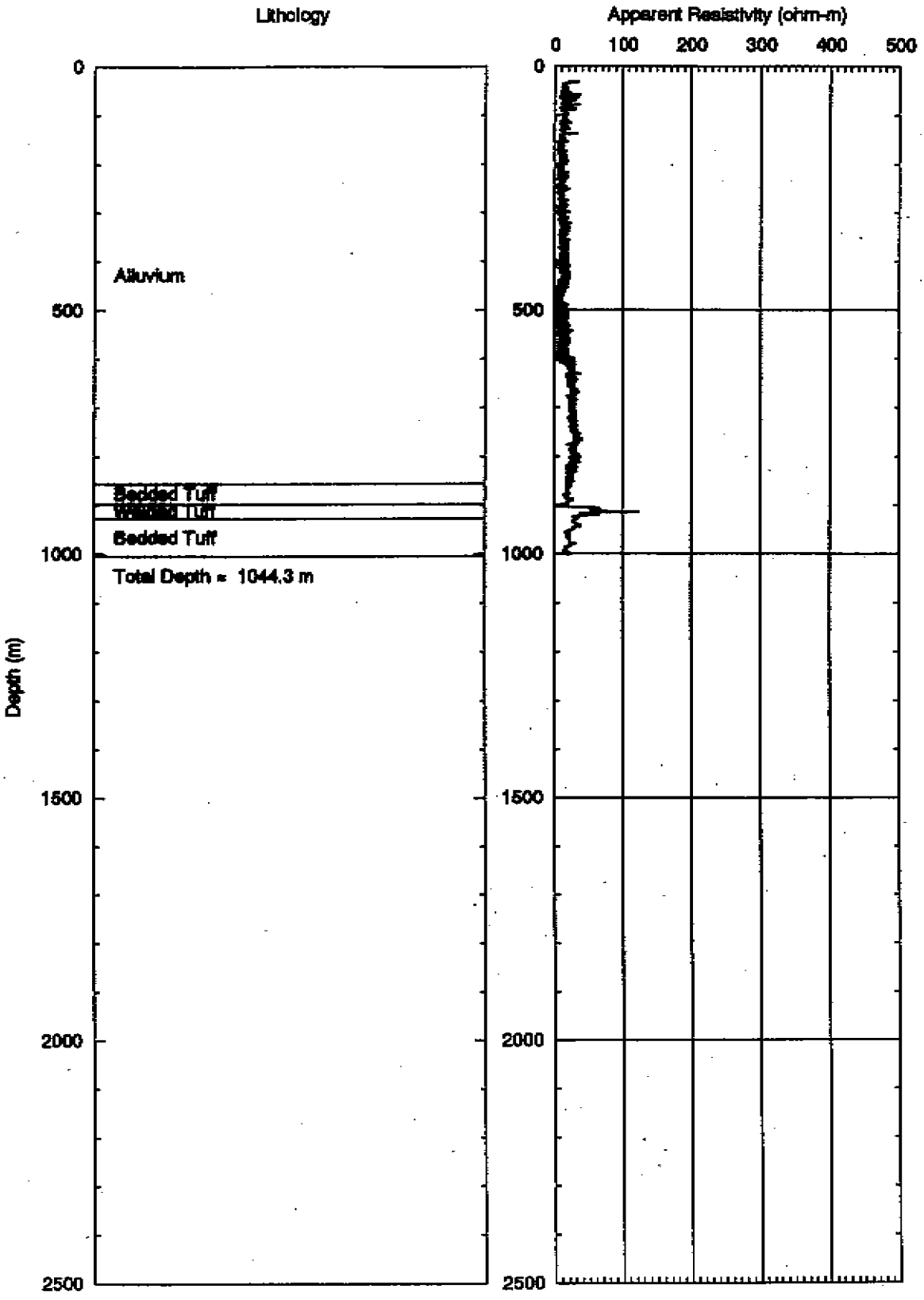

Figure 4–15. Lithologic log and lateral log for UCe-9.

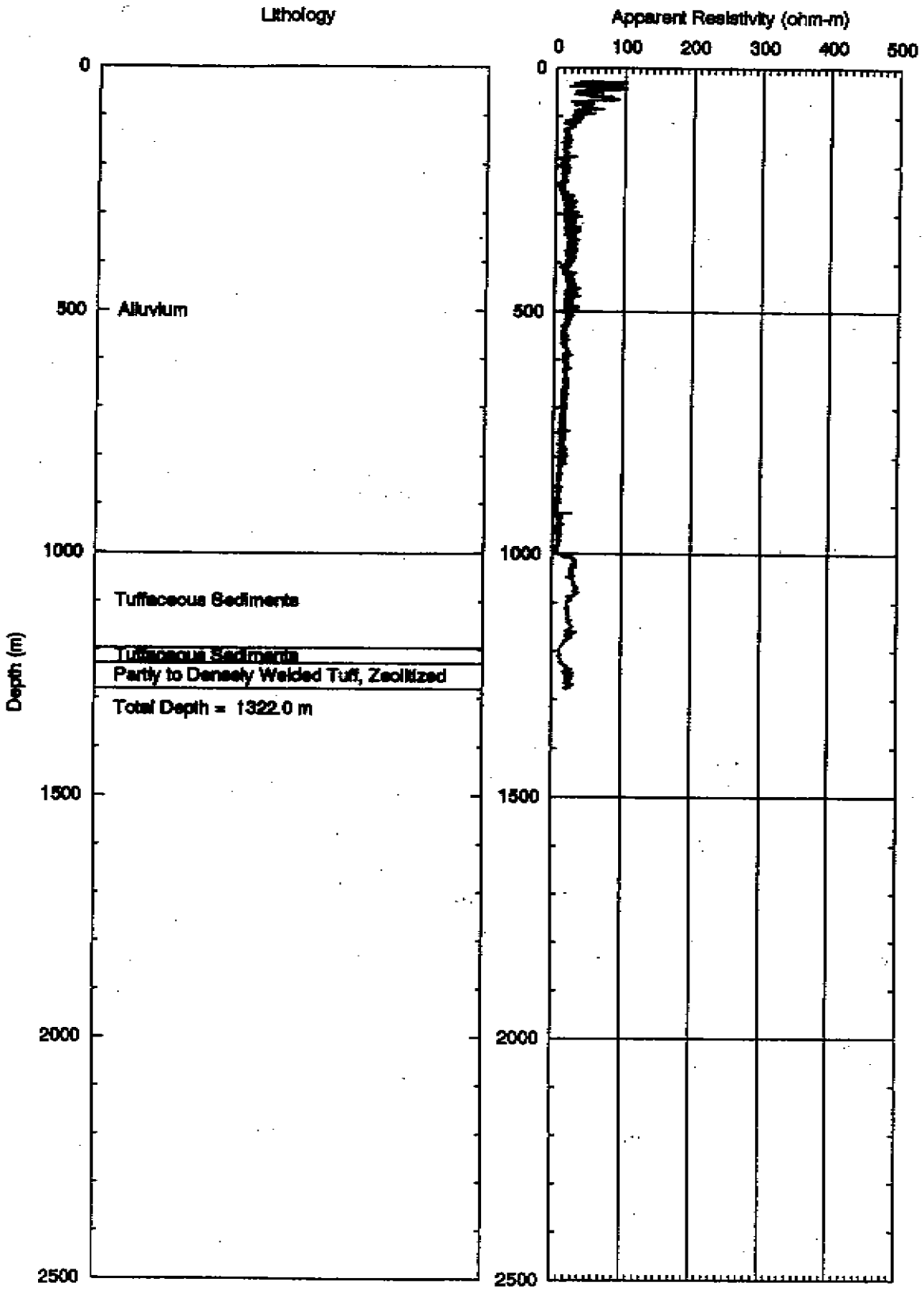

Figure 4–16. Lithologic log and lateral log for UCe-11.

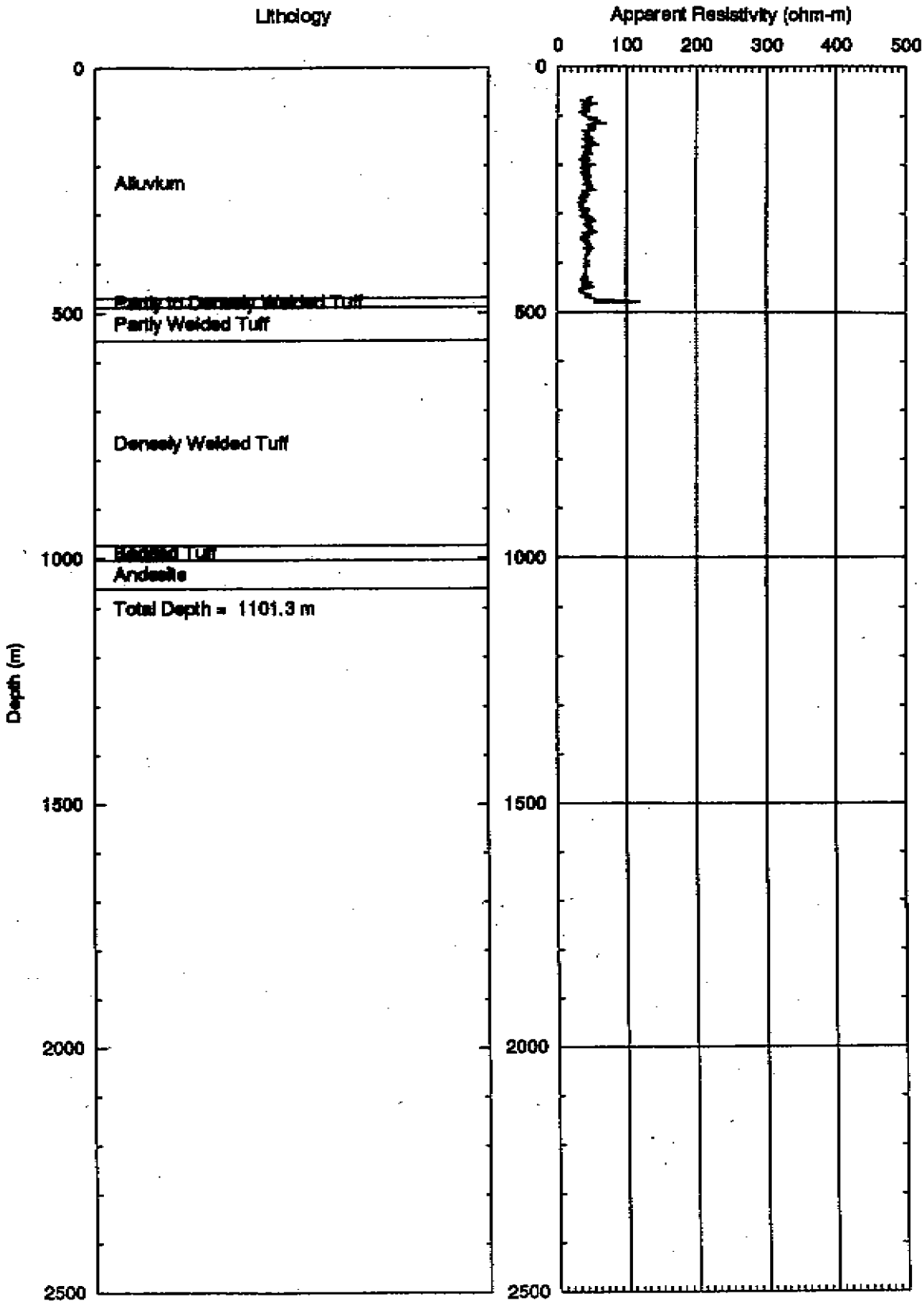

Figure 4–17. Lithologic log and lateral log for UCe-12.

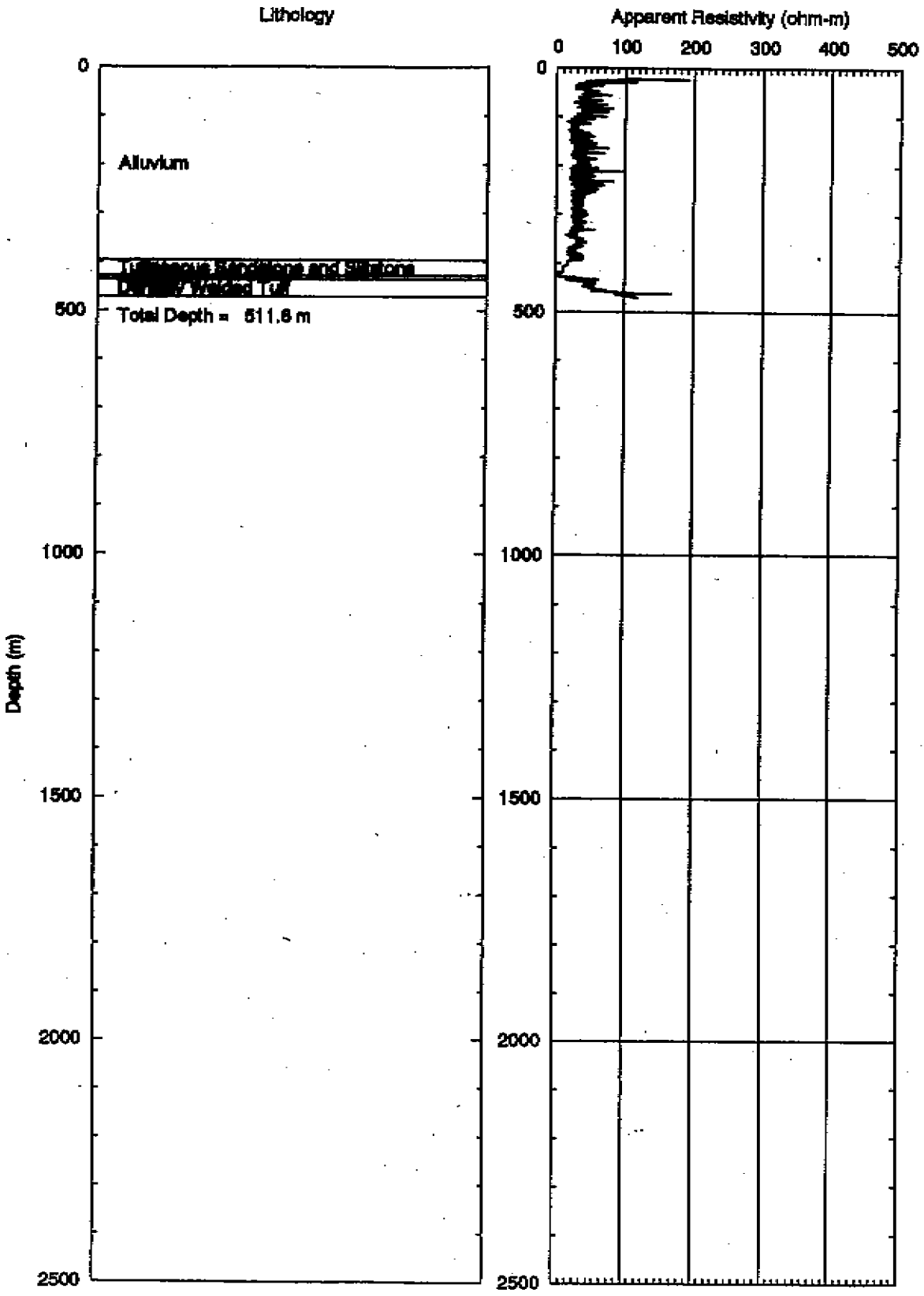

Figure 4–18. Lithologic log and lateral log for UCe-14.

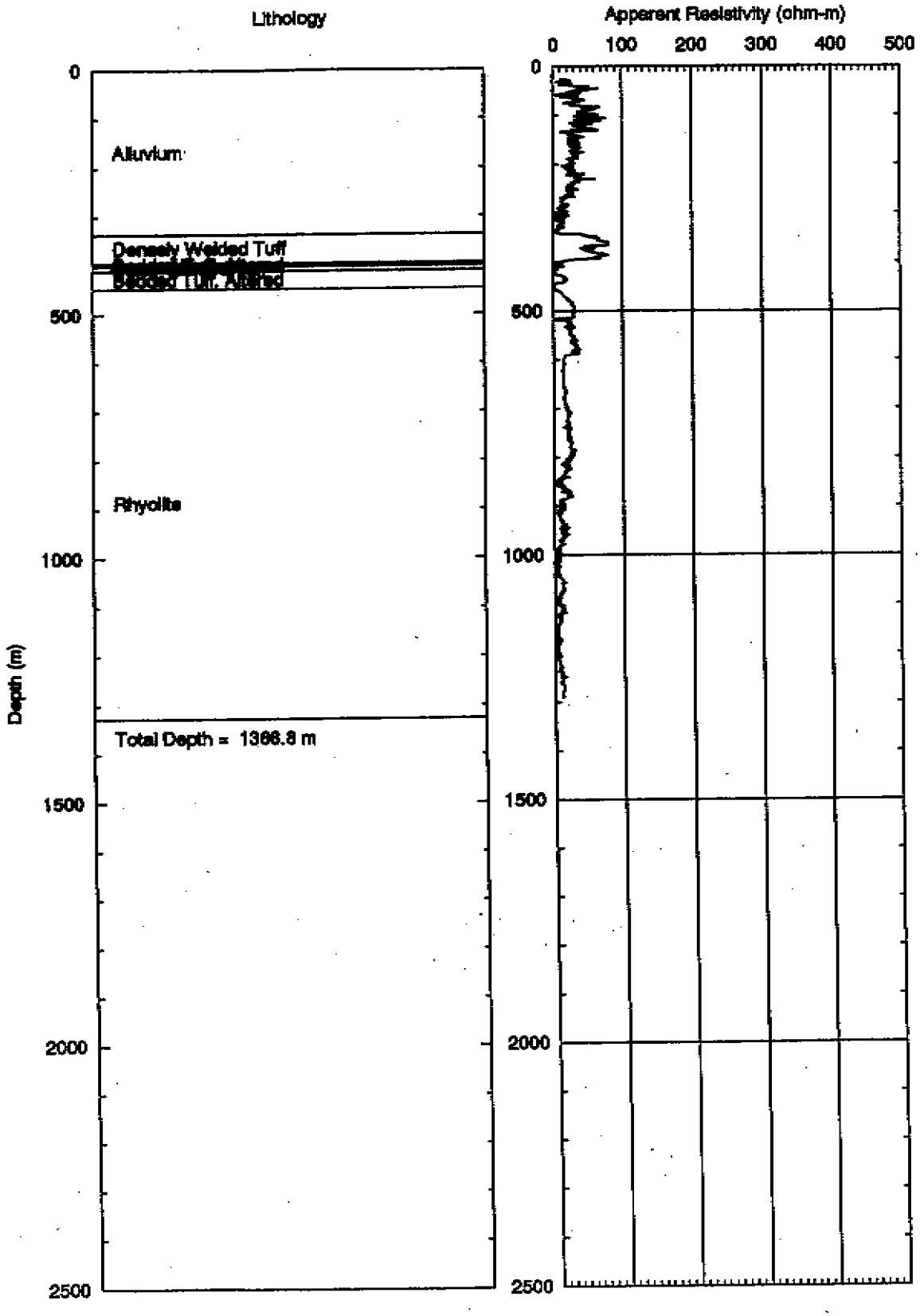

Figure 4–19. Lithologic log and lateral log for UCe-16.

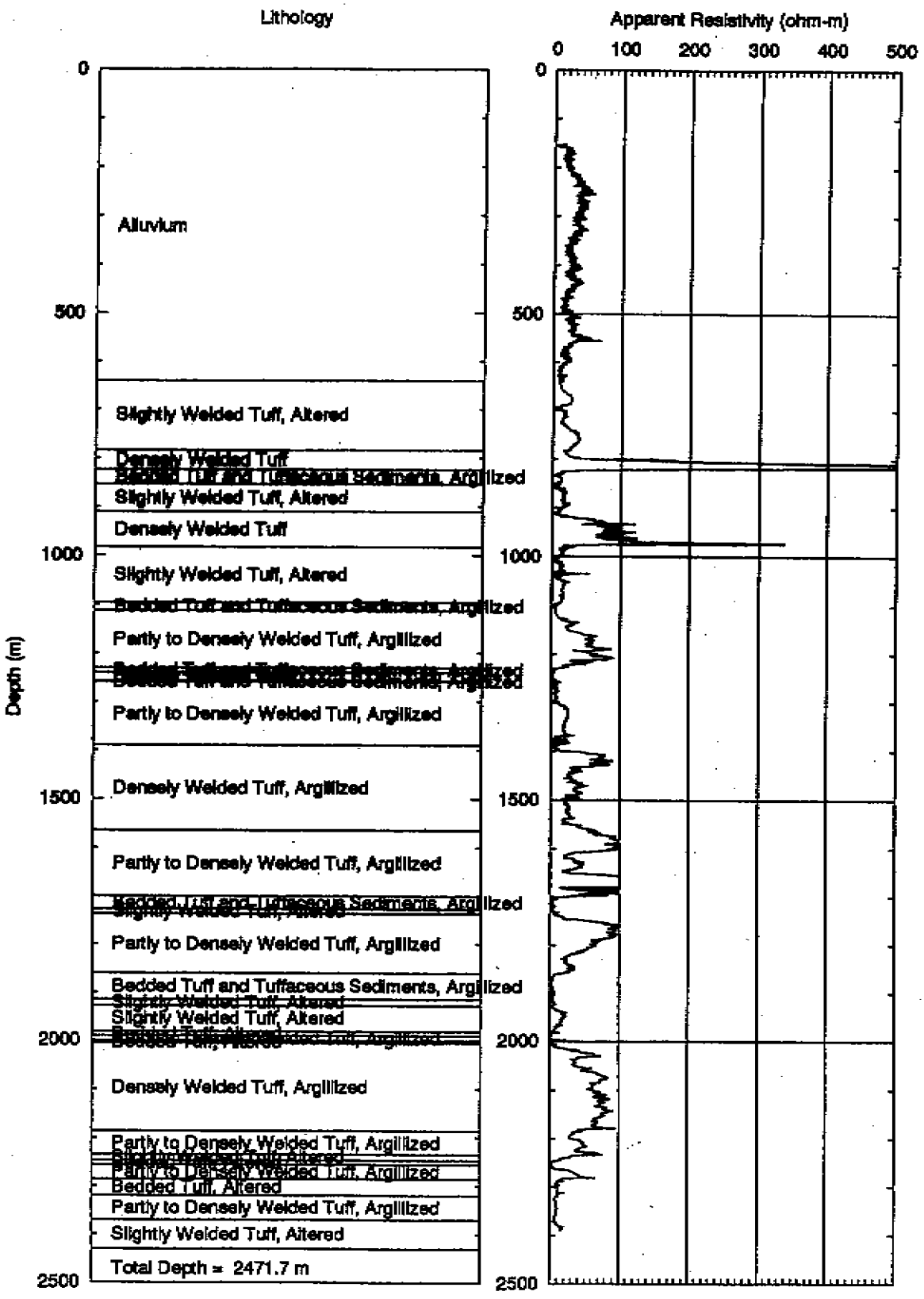

Figure 4–20. Lithologic log and lateral log for UCe-17.

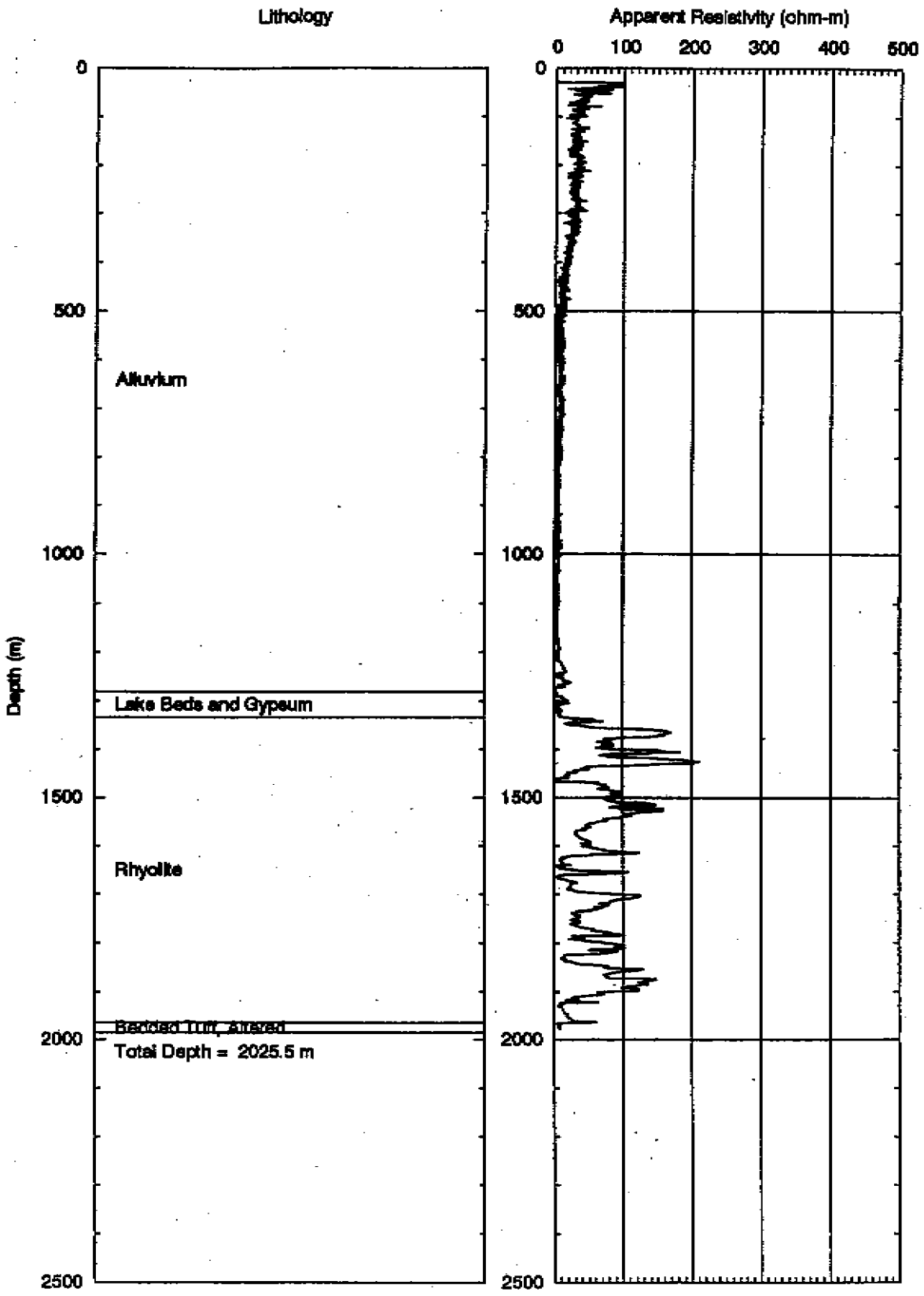

Figure 4–21. Lithologic log and lateral log for UCe-18.

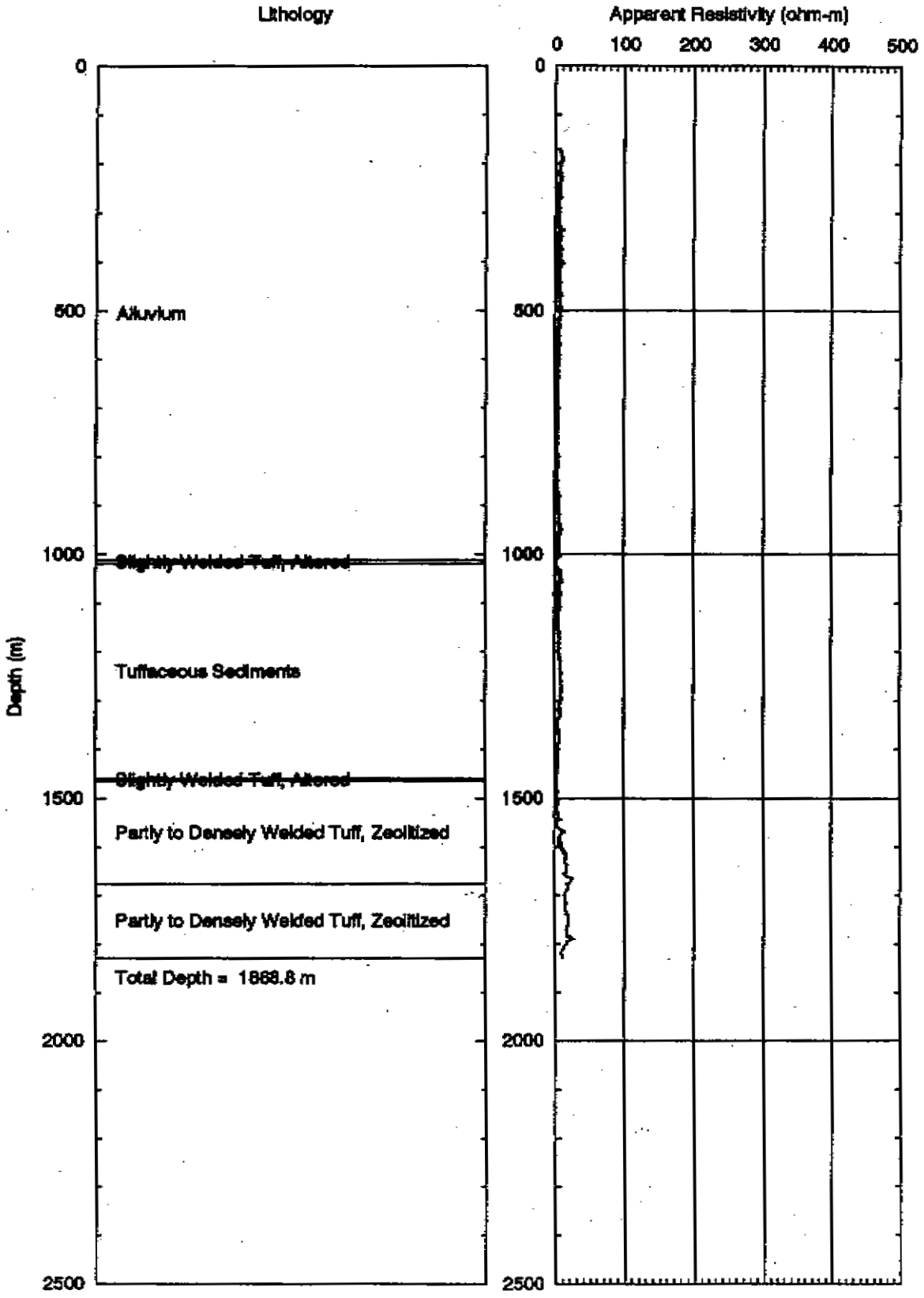

Figure 4–22. Lithologic log and lateral log for UCe-20.

APPENDIX 5

ANION AND CATION SORPTION ON AQUIFER MATERIALS FROM THE CENTRAL NEVADA TEST AREA

Prepared by Charalambos Papelis

ANION AND CATION SORPTION ON AQUIFER MATERIALS FROM THE CENTRAL NEVADA TEST AREA

Prepared by

Charalambos Papelis

Water Resources Center
Desert Research Institute
University and Community College System of Nevada

Prepared for

Nevada Operations Office
U.S. Department of Energy
Las Vegas, Nevada

September 1998

ACKNOWLEDGMENTS

It is my pleasure to acknowledge the individuals who contributed to the timely completion of this project component. Patricia Bernot, Nicole Brown, Brian Light, Steve Manning, and Derek Sloop deserve special acknowledgment for their careful experimental work and for data reduction. I also thank Jim Clark at Arizona State University for assistance with the electron microscope work of the CNTA thin sections. The continued support of Monica Sanchez is greatly appreciated.

INTRODUCTION

During the period of nuclear weapon production and testing, the U.S. conducted a series of tests at several test sites. These tests resulted in contamination from radionuclides as well as from other toxic metals and organic compounds. Common radionuclides found in contaminated areas include both uranium and heavy transuranic elements (man–made radionuclides heavier than uranium), mainly neptunium, plutonium, and americium, as well as lighter radionuclides, frequently fission products of the heavier radioisotopes.

In addition to radionuclides, some of the nuclear tests resulted in contamination by other inorganic and organic hazardous substances. These contaminants include the metals lead, copper, and cadmium, anions of arsenic and chromium, and organic contaminants such as polyvinyl chloride (PVC), polystyrene, and phenols (Bryant and Fabryka-Martin, 1991). Substantial quantities of these contaminants were incorporated in some of the nuclear devices and stemming and were released in the environment by the detonation of the device. The above contaminants are considered health hazards either because of their toxicity or because they are suspected or proven carcinogens (Francis, 1994; Sax, 1981).

The potential adverse health effects of radionuclides and other inorganic contaminants released during detonation of nuclear devices have long been recognized. The health hazard potential of these contaminants depends on the migration potential away from the source of contamination and into the accessible environment. Once in the accessible environment, contaminants can adversely affect the health of humans and animals. The fate and transport of dissolved contaminants are largely determined by the degree of contaminant interaction with the soil matrix. Radionuclides and metals with high sorption affinity for the mineral phases present, are expected to be severely retarded compared to groundwater flow. Inorganic contaminants with little affinity for the mineral phases present are expected to be retarded significantly less and, in the limiting case of truly conservative ions, solutes are expected to travel essentially with the velocity of the groundwater.

Any attempt for a realistic estimate of the time required for any contaminant to travel from the source of contamination to the accessible environment, therefore, requires experimental studies to evaluate the affinity of the contaminants of concern for the mineral phases likely to be encountered in the flowpath of the groundwater. Estimates for the movement of contaminants away from sources of contamination are obtained from hydrologic and geochemical transport codes (Anderson and Woessner, 1992; Hemond and Fechner, 1994). These codes require hydrologic

and geochemical parameters as input which must be either estimated or experimentally determined. The reliability of predictions based on these codes depends directly on the quality of the input parameters. Uncertainties in parameter estimation can lead to significant uncertainties in radionuclide transport simulations because of the frequently long time allowed for contaminant migration in model simulations (up to 10 000 years).

The scope of this project was to provide parameters used by transport codes to describe the equilibrium partitioning of contaminants between the aqueous and mineral interface. Specifically, the scope of this project component was to estimate the affinity of three cations (lead, cesium, and strontium) and two anions (chromate and selenite) for aquifer materials from the Central Nevada Test Area (CNTA), located in Hot Creek Valley, between Tonopah and Ely, Nevada. The Central Nevada Test Area is the site of the Faultless underground nuclear test conducted on January 19, 1968 at a depth of 975 m below ground surface.

The adsorbates used in this study are likely to be found in sites contaminated by nuclear testing. Lead (Pb) is very commonly found in nuclear test sites because large quantities of Pb, tens of tons typically, were used for the shielding of nuclear devices. Environmental concerns associated with Pb stem from its high toxicity (Francis, 1994; Laws, 1993). Lead is expected to be retarded strongly in many geological settings, because of its high affinity for oxides, hydroxides, clays, zeolites, and other aluminosilicate minerals and its potential for precipitation, even at relatively low concentrations.

To assess the migration potential of a cation with lower affinity for these types of mineral surfaces, experiments were conducted with strontium (Sr) and cesium (Cs) as well. Strontium is a radionuclide commonly found in nuclear test sites, known to sorb primarily by ion–exchange reactions. Health–hazard–related concerns are not based on the toxicity of Sr, but rather on the biogeochemical similarity of this element to calcium, a fact which can potentially result in accumulation of this radioisotope in bones (Laws, 1993). Cesium is also commonly found at nuclear testing areas. It tends to bind more strongly to ion-exchange sites compared to Sr, but for amphoteric, surface-hydroxyl sites (such as those found on oxides and the edge sites of clay minerals) the affinity of the two cations is similar and substantially reduced compared to Pb. The three cations, therefore, serve as models of strongly and weakly binding cations, depending on the sorbent aquifer material.

In addition to the cations, two anions, chromate and selenite, were used as models for a relatively weakly and a strongly binding anion, respectively. Chromate was selected because it is fairly toxic, it is a known carcinogen, and is commonly found among the contaminants associated

with nuclear testing. For oxides and hydroxides, chromate displays intermediate binding affinity. Selenite, however, has been shown to bind strongly on oxides and hydroxides (Hayes and Leckie, 1987; Hayes et al., 1987). Although selenium is a trace nutrient, it is fairly toxic at higher concentrations and a suspected carcinogen.

Equilibrium partitioning between the aqueous phase and a mineral phase, typically in the form of a distribution coefficient derived from experiments with crushed rock, has been used commonly in transport codes attempting to model the fate and transport of contaminants in the environment. This approach has been criticized for the following reasons. First, the distribution coefficients thus derived in the laboratory may overestimate the retardation of contaminants in the field. This is because the specific surface area of the fine particles used in laboratory studies may be orders of magnitude higher than the specific surface area in situ, leading to overestimation of the retardation coefficient by orders of magnitude.

Second, the equilibrium distribution coefficients do not provide any information on the rate of the sorption reactions. Depending on the relative time scales related to groundwater flow and the sorption processes involved, sorption may occur under either equilibrium or nonequilibrium conditions. Estimates of the groundwater velocity can be obtained from hydrogeologic parameters. Estimates of the sorption rate processes involved can be obtained from batch rate of uptake experiments and sorption experiments in laboratory soil columns.

In order to estimate these transport parameters and to gain the maximum possible insight with respect to retardation of the contaminants of concern at the field scale, based on bench scale laboratory experiments, we conducted batch equilibrium, batch rate of uptake, and column experiments. The remainder of this report is organized as follows. The adsorbent characterization and the general experimental procedures are presented next. The results and discussion are presented subsequently, organized by experiment type (batch equilibrium, batch rate of uptake, and column experiments), followed by a section summarizing the results and conclusions.

MATERIALS AND METHODS

ADSORBENT CHARACTERIZATION

The adsorbents were different CNTA aquifer materials obtained from the U.S. Geological Survey Core Library in Mercury, Nevada. Seven different core samples were collected. Because of time and budgetary limitations, however, it was not possible to conduct laboratory experiments with all seven samples. A rather extensive characterization, however, was performed on all materials, to evaluate possible differences and similarities. Based on the characterization, and in order to perform experiments with relevant aquifer material as diverse as possible, we decided to conduct experiments with one sample each of alluvium, tuffaceous sediments, and densely welded tuff. Specifically, the following three samples were used: UC-1-I-1 546-551 m (alluvium), UC-1-I-1 985-987 m (tuffaceous sediments), and HTH-3 296 m (densely welded tuff).

A fairly extensive characterization of the adsorbent was conducted which included solid structure as determined by x-ray diffraction (XRD), particle size distribution, as well as determination of specific surface area, porosity, microporosity, and bulk and true density. In addition, the morphology and composition of the adsorbents was examined by scanning electron microscopy (SEM) combined with energy dispersive x-ray spectroscopy (EDX). These parameters provided important information for the experimental design and are also required for the evaluation of geochemical transport parameters obtained from the experimental data.

The adsorbent was first reduced in size. The size reduction and subsequent sieving resulted in three different size fractions: particles smaller than 125 μm, particles between 125 and 212 μm, and particles between 212 and 595 μm. The smallest and largest size fractions were used for the equilibrium batch experiments, while the largest size fraction was used for the batch rate of uptake and column experiments.

A summary of the physicochemical characterization of the three aquifer materials is shown in Table 1. In summary, it can be said that the results were fairly similar for the three samples, although the density of the tuffaceous sediments (2.56 g/cm^3) was slightly lower than the density of the other materials (2.67 g/cm^3). In addition, the BET surface area of the densely welded tuff (6.24 m^2/g) was lower than the surface area of the alluvium (13.8 m^2/g) and tuffaceous sediments (16.7 m^2/g). These results are consistent with the lower micropore volume of the densely welded tuff compared to the alluvium and tuffaceous sediments. It should be noted, however, that the BET values may be underestimating the total available surface area for sorption, if the sample

contains swelling clays (smectites). Even if the percentage of clays by weight is low, the error in the reported total surface area may be significant because of the high specific surface area of smectites (600 - 800 m^2/g).

The morphology of the samples was examined by scanning electron microscopy (SEM). Analyses were performed both on the powders used in the experiments and small core fragments. In addition, the energy dispersive x-rays (EDX) attachment of the SEM allowed us to identify the composition of individual mineral grains. The mineralogical composition of the samples was determined based on a combination of techniques. Bulk mineralogy was determined by powder x-ray diffraction (XRD) of the crushed sample. In addition, a semi-quantitative mineralogical composition of the core was obtained from SEM/EDX analysis of microprobe-polished thin sections of the core combined with image analysis.

The bulk mineralogical composition of the three samples is shown in Table 2. Both the bulk XRD results of the crushed, homogenized cores and the results of the XRD of the clay size fraction of the alluvium and tuffaceous sediment samples are shown. The XRD analysis of the clay size particle fraction could not be performed on the densely welded tuff because of the structure of this material. As shown in Table 2, the major components of all samples were quartz and feldspars, while the clay particle size fraction of the alluvium and tuffaceous sediments consisted mostly of beidellite (a smectite clay) and illite (a mica group mineral).

The drawback of the bulk mineralogical composition based on powder XRD is that relatively minor components may be overlooked. These relatively minor components, however (for example, clays and iron oxides), may account for a substantial fraction of sorption sites. In addition, amorphous or disordered materials (for example hydrous phyllosilicates) may yield very broad peaks not easily identified as a mineral phase. The SEM/EDX analysis of the thin sections mentioned above can provide some additional information.

This process is based on the intensity of elastically backscattered electrons as a function of the atomic number of the backscattering element. Heavier elements are more efficient backscatterers, so that minerals containing heavier elements (e.g., iron oxides) appear brighter than minerals containing lighter elements (e.g., quartz). By identifying the composition of grains of a particular gray scale and determining the percentage of the thin section corresponding to this particular gray scale one can obtain at least a semiquantitative estimate of the mineralogical composition of a rock, including amorphous phases that may not be detectable by XRD. One limitation of the technique is that because of similar composition, different minerals may sometimes not be distinguishable based on backscatter image intensity. Albite and quartz, for example, are

sometimes indistinguishable. The results of the backscatter image analysis (Table 3) are in agreement with the bulk XRD analysis; additional important sorbing phases, however, such as hydrous aluminosilicates and iron oxides were also identified. Examples of backscatter images of thin sections are shown in Figure 1 (alluvium), Figure 2 (tuffaceous sediments), and Figure 3 (densely welded tuff).

The surface area of the adsorbents was determined based on nitrogen adsorption measurements, using Micromeritics ASAP 2400 or Gemini 2000 Analyzers, and the BET model (Brunauer et al., 1938). This method can be used to obtain an estimate of the total surface area of adsorbents having surface areas from a fraction of a square meter per gram to several hundred square meters per gram. Although the method has several shortcomings, it continues to be the most widely used and general method for particle surface area estimation (Gregg and Sing, 1982). The measured surface areas ranged from 16.7 (tuffaceous sediments) to 6.24 m^2/g (densely welded tuff). As noted above, however, the BET specific surface area may be underestimating the actual surface area if smectite clays are present in the sample.

Because the equilibrium partitioning of ions is a function of the specific surface area (see discussion in the Equilibrium Batch Sorption Experiments Section), the specific surface area of all three particle size fractions for all samples was measured and is reported in Table 4. As can be seen, the specific surface area was a rather weak function of particle size, suggesting that the majority of the surface area was internal. This finding is not surprising because specific surface areas associated with nonporous particles of the same dimensions are expected to be at least two orders of magnitude lower.

EXPERIMENTAL PROCEDURES

Batch Equilibrium Experiments

The batch sorption experiments were performed with two different size fractions of each type of material (material smaller than 125 μm and material between 212 and 595 μm). Sorption experiments were performed in individual 12–mL polypropylene centrifuge tubes. A specific amount of solid was added to the centrifuge tube. The amount of solid varied depending on the final solid concentration desired. Almost all experiments with the smaller size fraction (smaller than 125 μm) were conducted with 1.0 g/L adsorbent (alluvium, tuffaceous sediments, or densely welded tuff). All experiments reported here were performed with synthetic groundwater simulating the composition of groundwater from well HTH-1 of CNTA at 741 m depth. A variable amount of either 1.0 M HNO_3 (nitric acid) or 0.1 M NaOH (sodium hydroxide) was added

to adjust the pH to the approximate final pH value desired. The amounts of acid and base required for pH adjustment were determined by trial and error. After the initial acid or base addition, the solution was allowed to equilibrate without further pH adjustments.

Because of the relatively constant pH of the groundwater in both the alluvial and volcanic aquifers, most experimental data were collected at a slightly basic pH (7 - 9). Data at lower pH values were also occasionally collected to help us interpret the type of sorption process involved. In order to derive sorption isotherm parameters, experiments at different concentrations had to be performed. Again, because of work scope limitations, only a limited range of concentrations could be used. The concentrations used in these experiments ranged from 10^{-6} to 10^{-4} M. The adsorbate added was either $Pb(NO_3)_2$ (lead nitrate), $CsNO_3$ (cesium nitrate), $Sr(NO_3)_2$ (strontium nitrate), K_2CrO_4 (potassium chromate), or Na_2SeO_3 (sodium selenite) depending on the experiment being performed. The necessary quantity of high quality, NANOpure™ water was added to result in a final solution volume of 10 mL. All reagents used were of ACS reagent grade quality or better. NANOpure™ water was used exclusively for all solutions prepared.

The individual centrifuge tubes were equilibrated for at least 24 h by end–over–end rotation at 8 rpm. Given the fast intrinsic rate of sorption reactions (Hayes and Leckie, 1986) and preliminary rate of uptake experiments, 24 h equilibration time was considered adequate. Although true equilibrium, in a strict thermodynamic sense, was most likely not reached within the 24 h equilibration period, the conclusions presented here are still valid, based on the much shorter time scale for the sorption processes described here, compared to processes such as solid solution formation and phase transformations, which would tend to shift the position of equilibrium.

Following equilibration, the pH of the suspension was measured using an Orion model 720 pH meter with an Orion Ross glass combination electrode. The pH meter was calibrated daily using pH 4.00, 7.00, and 10.00 buffers. Solid–solution separation was achieved by centrifugation at 9,000 rpm for 20 min. using a Marathon K/R 21 centrifuge and a 2–mL aliquot of the supernatant was removed for metal analysis. The supernatant was acidified with 24 µL of concentrated HNO_3 (Fisher Optima™ quality) before analysis.

The samples were analyzed using a Perkin Elmer 4110 ZL atomic absorption spectrometer with graphite furnace and Zeeman background correction. Duplicates were run for each sample and the results were averaged. In all cases a peak area mode was used for analysis using appropriate metal standards. The fractional uptake (percent sorbed) for each sample was calculated as:

$$\% \text{ Sorbed} = \frac{C_o - C_s}{C_o} \times 100 \quad (1)$$

where C_o is the total metal concentration added to the sample and C_s is the metal concentration remaining in the supernatant.

Batch Rate of Uptake Experiments

All experiments were performed in 250-mL, jacketed Wheaton "cellstir" reactors. This type of reactor includes ports for sampling and a magnetic stirrer. This particular design was chosen because it incorporates several very important features. First, the reactor is jacketed, allowing water at constant temperature to flow between the double glass walls, thereby keeping the temperature in the reactor constant. It is well known that the rates of chemical reactions are strongly temperature dependent, so that precise temperature control is crucial for any kinetic experiments. A Lauda constant temperature bath was connected to the jacketed reactor to insure a constant temperature of 25 °C throughout the experiment. Second, the stirrer assembly is designed to keep particles in suspension, without touching the reactor bottom, thereby avoiding particle breakup. Size reduction of particles during the experiment (because of abrasion) would result in changing particle dimensions (and therefore diffusion path length) in the course of the experiment and preclude interpretation of the rate-of-uptake data. Finally, the adopted design incorporates ports for reagent introduction, sample collection, and pH monitoring.

The experiments were conducted as follows. An appropriate amount of solid was suspended in synthetic groundwater. The solid was then equilibrated with the synthetic groundwater for at least 24 h, at constant temperature, before addition of the adsorbate. The pH was adjusted to the desired value using either HNO_3 or NaOH. Following this pre-equilibration period, the sorbate was added, marking the onset of the experiment.

The pH was monitored throughout the experiment and adjusted, if necessary. The pH at which uptake experiments were conducted was chosen based on equilibrium experiments so that fractional uptake at equilibrium would be between 40 and 90%. pH variation during the course of the experiment did not exceed 0.02 units. Sampling was more frequent during the earlier stages of the experiment when the rate of change was expected to be greatest. Samples were withdrawn as a function of time with a 10-mL plastic syringe equipped with a three-way stopcock to which a Teflon tube (for sampling) and a 0.2-μm nylon filter (Alltech, Nylon 66, 25 mm) were attached. The slurry was immediately filtered (total sampling time was less than 1 min.) and fractional uptake was determined by comparing the concentration in the filtrate to the total concentration in the slurry.

Column Experiments

Experiments with the tuffaceous sediments and densely welded tuff were conducted in 10-cm long plastic columns with a diameter of 2.5 cm. The flowrate in the columns was kept constant using a constant head set up. The flowrate achieved in this way is a function of the total hydraulic head, which can be adjusted by raising or lowering the constant head reservoir above the column, and the losses in the column, a strong function of particle size distribution and adsorbent type. The same particle size fraction was used for both columns, i.e., the size fraction between 212 and 595 μm. Because of the different mineralogical composition of the two materials, the resulting flowrates were different, even though the particle size distributions were presumably very similar. Under these conditions, the average linear velocity in the columns was approximately 8.6 m/d in the densely welded tuff column and 8.6×10^{-2} m/d in the tuffaceous sediment column.

RESULTS AND DISCUSSION

EQUILIBRIUM BATCH SORPTION EXPERIMENTS

Cation Sorption

Cation sorption, including sorption of Pb, Cs, and Sr on CNTA aquifer materials will be discussed first, followed by estimation of the isotherm parameters describing the equilibrium partitioning of these cations at the mineral–water interface.

Lead Sorption

Sorption of 10^{-6} M Pb on 1 g/L CNTA aquifer materials is shown in Figure 4. It can be seen that sorption of Pb was pH dependent under these conditions. This behavior is not surprising because lead is known to bind strongly on pH-dependent, amphoteric oxide sites and to form inner-sphere coordination complexes (Chisholm-Brause et al., 1990; Chisholm-Brause et al., 1989; Roe et al., 1991). In addition, because the hydrolysis of Pb is extensive, even around neutral pH and at fairly low concentrations (Baes and Mesmer, 1986), formation of surface precipitates is entirely possible. Lastly, Pb has a high selectivity for pH-independent, ion-exchange sites of clay minerals and zeolites, so that the overall sorption may be a combination of sorption reactions.

The experimental results shown in Figure 4 were consistent with these expectations. Sorption of Pb on CNTA alluvium was definitely pH dependent (at pH 3 the fractional uptake was approximately 20%). The pH-dependent behavior can be explained either by surface precipitation or by sorption on amphoteric surface-hydroxyl sites of oxides. As previously mentioned, iron oxides were present in the alluvium sample (Table 3). Sorption of Pb on the densely welded tuff suggests similar trends. The rather sharp increase of Pb uptake with pH was evident and has been previously reported (Hayes, 1987). The steep fractional uptake curve may be evidence of surface precipitation, although, based on macroscopic experiments alone, this hypothesis cannot be tested.

The results of Pb sorption on tuffaceous sediments are also shown in Figure 4. Although the relative uptake is approximately the same as on the other two sorbents, the uptake curve appears to be less pH-dependent. These results are also consistent with the mineralogical composition of the sample, because the tuffaceous sediment sample contained no iron oxides and its major cation sorbing phases were smectites (beidellite) and possibly hydrous aluminosilicates

(e.g., zeolites). Under these conditions and given the low ionic strength of the synthetic groundwater, sorption by cation exchange would be expected.

Strontium Sorption

Sorption of 10^{-6} M Sr as a function of pH and aquifer material type is shown in Figure 5. No results for Sr sorption on alluvium are shown because the concentration of Sr in solution at equilibrium was higher than 10^{-6} M, which would mean negative sorption, or generation of Sr, instead of sorption. The "additional" amount of Sr was traced back to the concentration of Sr in equilibrium with the CNTA alluvium soil. It was determined that this equilibrium concentration was approximately 10^{-6} M (for 1 g/L soil suspended in 10 mL of water). Unfortunately for Sr sorption studies, Sr is a relatively common element in the Earth's crust. Its average abundance in the crust is 384 ppm (Emsley, 1989), making Sr the 15th most abundant element (more abundant than sulfur and carbon). Because approximately 10^{-6} M Sr would be present in the water at equilibrium with the soil, any additional Sr would result in negative sorption. The implication of these results is that under low concentration conditions Sr would be highly mobile.

Sorption of Sr on tuffaceous sediments and densely welded tuff, shown in Figure 5, was consistent with the expected sorption behavior of an alkaline earth metal on a combination of pH-dependent and pH-independent sorption sites. It appears that Sr sorption on tuffaceous sediments was less pH dependent compared to sorption on the densely welded tuff. This observation is consistent with the sorbing mineral phases present in the two samples. The primary sorbing minerals in the tuffaceous sediments were smectite clays and possibly zeolites, on both of which cations are expected to sorb primarily by cation exchange. The presence of iron oxides on the densely welded tuff, however, could account for the pH-dependence of Sr sorption on these minerals.

Cesium Sorption

Cesium sorption on all CNTA aquifer materials is shown in Figure 6. Because the concentration of Cs was not significant in any of the CNTA samples, experiments could be conducted with all three materials. The results were consistent with the expected behavior of an alkali metal and the mineralogical characterization of the samples. Sorption was observed on all three samples, presumably as a combination of binding on both permanent-charge and surface-hydroxyl sites. Sorption on the alluvium and the densely welded tuff appeared to be more pH dependent than sorption on the tuffaceous sediments.

Note that sorption on both alluvium and the densely welded tuff appears to be pH independent below pH approximately 7 to 8 and increasingly pH dependent above this pH value. It is in the latter pH region that contribution of iron oxides to the sorption capacity of the soil would be more pronounced, as the surface charge of the iron oxides decreases from positive to zero at the point of zero charge (PZC) and eventually becomes negative above the PZC. The PZC of iron oxides is generally assumed to be in the 7.5 to 9.0 pH range (Bohn et al., 1985; McBride, 1994; Sposito, 1984; Stumm, 1992).

As can be seen from Figure 6, sorption of Cs on the tuffaceous sediments appeared to be pH independent, consistent with the absence of iron oxides and the presence of smectite clays and possibly hydrous aluminosilicates. Under the low ionic strength conditions of the groundwater at the CNTA site, it was not expected that edge sites of smectite clay minerals would contribute significantly to cation sorption relative to sorption at permanent-charge sites. The relative importance of edge (surface-hydroxyl) and interlayer (permanent-charge) sites of smectites for cation sorption as a function of ionic strength has been previously shown (Papelis and Hayes, 1996).

Comparison of Cation Sorption on CNTA Aquifer Materials

It is instructive to compare qualitatively the sorption behavior of the three cations as a function of sorbent material. The sorption of Pb and Cs on CNTA alluvium is shown in Figure 7. Unfortunately, sorption of Sr cannot be included because of the high dissolved Sr concentration in the alluvium, especially at low pH values. A comparison of Pb and Cs sorption, however, shows that the sorption of both cations was pH dependent, for reasons explained earlier.

Although qualitatively the sorption behavior of the two cations appears to be similar, Pb fractional uptake was higher compared to Cs. This higher affinity of Pb for surface-hydroxyl sites compared to Cs, an alkali metal, is not surprising. Lead has been shown to form inner-sphere complexes and polynuclear complexes or surface precipitates on surface-hydroxyl sites of oxides (Chisholm-Brause et al., 1990; Chisholm-Brause et al., 1989; Roe et al., 1991), whereas alkali metals are typically thought as forming outer-sphere ion-pair complexes on oxide surfaces (Chen et al., 1998).

Cation sorption on CNTA tuffaceous sediments is shown in Figure 8. The data suggest a clear cation selectivity for this sorbent. Lead binding was the strongest, followed by Cs, and finally Sr. Assuming that the mineral phases controlling sorption in the tuffaceous sediments were smectites and hydrous aluminosilicates (e.g., zeolites) this trend is consistent with previously

obtained data in our laboratory (sorption of Pb, Sr, and Cs on zeolitized tuffs from the Nevada Test Site, to be reported elsewhere). Lead sorption was expected to be high because of the electronic structure of this element (which is also reflected in the much more extensive hydrolysis chemistry of Pb, compared to Sr and Cs, and the formation of Pb inner-sphere complexes, compared to outer-sphere complexes for Sr and Cs).

The higher affinity of Cs for the tuffaceous sediments compared to Sr can also probably be explained by differences in the chemical nature of the two cations. The nonhydrated radius of the Cs cation is larger than the nonhydrated radius of the Sr cation, which results in the reverse order of hydrated radii, i.e., the hydrated radius of Sr is larger than the hydrated radius of Cs. As the affinity of cations for ion exchange sites is inversely proportional to the hydrated radius of the ion, it is not surprising that Cs tends to bind more strongly than Sr. In addition, as seen in Figure 8, sorption of Sr appears to be more pH dependent than Cs. This result could be explained by differences in the relative importance of binding at permanent-charge and surface-hydroxyl sites for the two cations. As mentioned above, Cs is expected to bind more strongly at permanent-charge sites, while Sr, an alkaline earth metal, is expected to bind more strongly on surface-hydroxyl sites compared to Cs, an alkali metal.

The comparison of cation sorption on densely welded tuff is shown in Figure 9. Both differences and similarities between the three cations are worth discussing. As in the case of alluvium and tuffaceous sediments, the fractional uptake of Pb was higher than the uptake of Sr or Cs. Based on the pH-dependent sorption behavior evident for all cations, one could speculate that surface-hydroxyl sites on oxides may be responsible for the observed behavior. Indeed, the densely welded tuff had the highest concentration of iron oxides (Table 3). It is true that the densely welded tuff probably had the highest concentration of clay minerals as well, but if these clay minerals were of the mica type (illite was found in both alluvium and the tuffaceous sediments) the cation exchange capacity of the densely welded tuff would be substantially reduced.

Although, most of the data points obtained for Pb would tend to suggest a pH-independent behavior, the fractional uptake at approximately pH 5.5 we believe is not an experimental error and simply suggests a sharp fractional uptake curve. Steep fractional uptake curves have been observed frequently and may be indicating surface precipitation. Although at 10^{-6} M the solution would be undersaturated with respect to Pb under equilibrium conditions (Baes and Mesmer, 1986), the onset of surface precipitation cannot be predicted based on equilibrium thermodynamic calculations in the bulk solution (Sposito, 1986). Unlike Pb, Sr and Cs are not likely to hydrolyze significantly under these experimental conditions, so that the pH-dependent behavior must be attributed to sorption on amphoteric, surface-hydroxyl sites.

Lastly, it should be noted that, unlike sorption on tuffaceous sediments, the fractional uptake of Sr and Cs was very similar in the case of the densely welded tuff. The most likely explanation is that, as shown by the pH-dependent behavior, uptake was primarily by sorption on surface-hydroxyl sites and under these conditions Sr and Cs show similar behavior. (Compare with the previously discussed case of the tuffaceous sediments, where sorption was attributed mainly to permanent-charge sites and Cs uptake was substantially higher than Sr uptake).

Estimation of Equilibrium Partitioning of Cations at CNTA Mineral–Water Interfaces

Most transport codes which attempt to incorporate chemical reactions to model the migration of contaminants in the subsurface environment require parameters describing the partitioning of the contaminants of concern between the aqueous and mineral interfaces. Although sorption modeling based on the surface-complexation paradigm has been extensively used during the last two decades, because of computational requirements, most transport codes still use parameters derived from isotherms to incorporate surface chemical reactions into numerical models.

Several sorption isotherms have been developed and used during the years. Among the most commonly used are the linear, Langmuir, and Freundlich isotherms (Davis and Hayes, 1986b; Weber and DiGiano, 1996). Plotting of sorption data as a linear isotherm results in estimation of a conditional distribution coefficient, K_d, a ratio of the mass of sorbate sorbed per mass of sorbent, q_e (g/g), to the aqueous concentration of sorbate in equilibrium with the sorbed contaminant, C_e (g/m^3), as shown in Eq. (2).

$$K_d = \frac{q_e}{C_e} \tag{2}$$

Distribution coefficients have been used extensively to model organic contaminant sorption on aquifer materials. For inorganic contaminants, however, K_d is frequently a strong function of pH, temperature, and other geochemical conditions (e.g., speciation and redox potential) (Stumm, 1992).

Use of distribution coefficients to model contaminant partitioning at the mineral-water interface assumes that the isotherm is linear and that sorption is controlled by equilibrium, as opposed to kinetics (usually referred to as the local equilibrium approach). Sorption of inorganic contaminants on mineral surfaces is frequently non-linear. In addition, distribution coefficients can result in severe errors when used without reference to the specific experimental conditions under

which they were determined. Unfortunately, neglecting the above guidelines is still fairly common in radionuclide transport models (Nakamura et al., 1988; Ohnuki et al., 1989; Ooi et al., 1987).

Two additional important aspects related to the use of distribution coefficients to model contaminant transport should be specifically emphasized at this point. The first one is related to the use of single point K_d s. It should be obvious, that such K_d values are, strictly speaking, only valid for the particular conditions under which they were determined. Use of a single-point K_d at a substantially different concentration may result in severe errors. In addition, it should be recognized that as the fractional uptake of an ion decreases, the potential for error in calculating the retardation factor increases. This is because very little uptake, close to the detection limit of the analytical technique, resulting in a small distribution coefficient, can easily be translated into a modest retardation on the order of 5 to 10 (depending on the bulk density and porosity of the aquifer). If the true uptake were considered negligible, however, no retardation would result. This is particularly important in pH-dependent sorption, which is always the case for anion sorption, where a change of the pH by a fraction of a unit may therefore result in differences in retardation by an order of magnitude.

In this project, distribution coefficients were estimated, based on the experimental data. To test the linearity of these isotherms and therefore whether a K_d approach would be applicable, the data were linearized, a process which results in the estimation of parameters for the non-linear Freundlich isotherm, shown in Eq (3).

$$q_e = K_F C_e^{1/n} \tag{3}$$

These parameters, K_F, $(g/g)/(g/m^3)^{1/n}$, and 1/n (–), represent the equivalent of K_d and the exponent of the equilibrium concentration, respectively (1/n is assumed to be 1, by definition, for linear isotherms). The parameter 1/n is a function of both the cumulative magnitude and diversity of energies associated with a particular sorption reaction (Weber and DiGiano, 1996). It can also be shown that 1/n is related to the enthalpy of adsorption. The isotherm is concave for $1/n < 1$, convex for $1/n>1$, and a straight line for $1/n=1$.

The linear and Freundlich isotherm parameters for all cations and all CNTA aquifer materials are shown in Table 5. The table includes the K_d, K_F, and 1/n values for all isotherms at pH 8 for the finer particles (particle size smaller than 125 μm). Parameters at other pH values were calculated from the sorption experimental results discussed in the previous section, but are not reported here. All isotherms were forced through zero.

Several conclusions can be drawn by inspection of Table 5. First, the sorption parameters can vary by orders of magnitude as a function of both adsorbate and adsorbent. It should be remembered that all these values correspond to the same pH. If pH is considered an additional variable, the total variation in K_d (K_F) may be several orders of magnitude, resulting in retardation factors varying by several orders of magnitude. The distribution factors are the highest for Pb, which is not surprising, given that Pb is known to bind very strongly on permanent- and pH-dependent charge sites and to form surface precipitates, as discussed above. In addition, Pb appears to bind almost equally on all three aquifer materials.

The two other cations, Sr and Cs, have fairly similar affinities for the aquifer material, although the K_d for Sr sorption on alluvium appears to be high and almost as high as the Pb distribution coefficient. The reason for this is not clear. The fact that this value is based on a single point and the Sr dissolution problems associated with this soil may be the reason for this apparent anomaly. The values of the Freundlich parameter 1/n are also worth considering. As pointed out above, the value of this parameter is related to the enthalpy of adsorption and the site energy distribution of the adsorbent. With the exception of Pb sorption on tuffaceous sediments, it appears that the 1/n values are less than one for Pb and Cs, but more than one for Sr. These differences may point to differences in the sorption behavior of these ions, although the number of data points is not large enough to support any positive conclusions.

Strictly speaking, obviously, the Freundlich isotherm would be more appropriate to describe cation sorption on CNTA aquifer materials. Because the non-linearity of the isotherm, however, is not too severe, a linear isotherm could be used instead, if there were a significant computational advantage to using the simpler isotherm. At any rate, recognition of the limits of applicability of this approach (concentration range and other geochemical condition requirements) would be necessary before using the simpler linear isotherm. Any additional uncertainties in other geochemical parameters, such as pH and ionic strength, would probably further increase the error from predicting partitioning at these interfaces using a linear isotherm.

The dependence of K_d on specific surface area should be obvious. As K_d represents the mass of sorbate sorbed per unit mass of the sorbent for a specific equilibrium concentration, one would expect that smaller particles, with relatively higher specific surface area would have substantially higher sorption capacity per unit mass, compared to large particles with low specific surface area. The distribution coefficients obtained from crushed rock in the laboratory have therefore been criticized for not realistically representing the true retardation of contaminants in the environment, where accessible specific surface areas might be substantially lower. One can easily prove that the distribution coefficient can be scaled up from the values obtained in the laboratory,

as long as the specific surface area of the adsorbent used in the batch sorption experiments and the specific surface area *in situ* can be estimated. An estimate of the specific surface area of the adsorbent used in the laboratory can be obtained from the BET isotherm and nitrogen adsorption (krypton adsorption for low surface areas). The specific surface area *in situ* is much more difficult to estimate. In addition, the ability of the BET model to represent the true specific surface area of a mineral assembly depends on the mineral composition, as discussed above.

In an attempt to test the hypothesis of K_d dependence on specific surface area, we conducted experiments with the particle size fraction from 212 to 595 μm and compared the obtained distribution coefficients with the distribution coefficients obtained with the smaller particle size fraction (particle sizes smaller than 125 μm). Although the size difference is small, the comparison of the two data sets is important. The linear and Freundlich isotherm parameters for the larger size fraction are listed in Table 6. The results of experiments with the larger size fraction are similar to the previously discussed results. The affinity of Pb for all samples is higher compared to the affinity of the other cations. In addition, there were no dramatic differences between aquifer material for the same cation. The exponents of the Freundlich isotherm were also fairly consistent within each cation. Lead exponents appear to deviate the most from linearity and cesium the least. The fact that the exponents are larger than one for Sr and less than one for Pb and Cs could reflect different types of sorption reactions.

The ratio of K_d s corresponding to the two sets of data is included in Table 6, as $K_{d\text{-}212}/K_{d\text{-}125}$. Although either K_d or K_p could be used, the K_d was used here because it was calculated for all cations and all aquifer materials. This ratio is expected to be smaller than one, because the K_d for the finer particles is expected to be larger. In addition, in an ideal case where the K_d would be directly proportional to the specific surface area of the adsorbent, the ratio of the K_d s would exactly equal the ratio of specific surface areas. There are several reasons why one would not expect to encounter such an ideal case scenario. First, the relative mineral composition is unlikely to be independent of particle size. To the extent that different cations have different affinities for different minerals (because of different sorption sites present) the K_d is expected to be a function of the sample composition and not just the specific surface area. In addition, the specific surface area, as determined by the BET method is known to underestimate the specific surface area of expanding clays (smectites) so that the reported specific surface area may not truly represent the number of sites present in the system.

Even with these limitations, consideration of the ratio of K_d s in Table 6 provides some useful insight. In general, the estimated K_d ratio is of the right order of magnitude and follows the expected trend. With the exception of Sr sorption on alluvium, all other ratios are considered to be

in reasonable agreement with the expected specific surface area ratios, as obtained from Table 4. It can be seen from Table 4 that the BET surface area of these adsorbents was relatively independent of size, suggesting substantial internal surface area. In fact, the BET surface area of alluvium was larger for the largest particles, possibly caused by sample heterogeneity. Based on the BET results, the ratio of specific surface areas between the larger and smaller particles would be 1.15, 0.62, and 0.84 for alluvium, tuffaceous sediments, and densely welded tuff, respectively.

These numbers are at least in an order-of-magnitude agreement with the K_d ratios reported in Table 6. The ratio was the lowest for Pb (average 0.28), intermediate for Sr (average 0.47, excluding the results with alluvium) and highest for Cs (average 0.56). It is interesting to note that the K_d ratio appears to be relatively constant for each cation, possibly a function of the sorption process involved. These differences, however, between cations and between aquifer material can not be fully justified without additional research.

Anion Sorption

Anion sorption, including sorption of Cr^{VI} and Se^{IV} on CNTA aquifer materials will be discussed first, followed by estimation of the isotherm parameters describing the partitioning of these anions at the mineral–water interface at equilibrium.

Chromate Sorption

Sorption of 10^{-6} M Cr^{VI} on the three CNTA aquifer materials is shown in Figure 10. The results generally agreed well with the expected behavior for anion sorption, increasing sorption with decreasing pH. This behavior is expected only when anions sorb on amphoteric, surface-hydroxyl sites (e.g., oxides, hydroxides, etc.). Clays, zeolites, and other minerals with permanent-charge sites have very low anion exchange capacities. It has been suggested that any anion sorption capacity of smectites, for example, beyond what can be accounted for by sorption on edge sites, must be attributed to impurities in the sample.

The observed sorption on the three CNTA materials correlates well with the previously discussed composition of the three samples. Maximum sorption was observed for the alluvium and the densely welded tuff samples, while sorption on the tuffaceous sediments was markedly reduced. Although qualitatively correct, the extent of Cr^{VI} sorption on these materials was somewhat higher than expected. Chromate has typically been thought of and has been modeled as forming ion-pair, outer-sphere complexes. Sorption of Cr^{VI} on the CNTA materials, however, is considered high reaching, especially for the densely welded tuff sample, almost quantitative removal from solution around pH 6. In addition, the change in the fractional uptake from zero to

100% occurred within less than 2 pH units. Even on the tuffaceous sediments, the sample which presumably had no iron oxides, limited sorption was present (20% uptake at pH 4).

Despite the apparent high Cr^{VI} sorption, however, the observed trend was consistent with expectations, with the tuffaceous sediment sample (the sample with the lowest oxide concentration) showing the lowest sorption and the densely welded tuff (the sample with the highest oxide concentration) showing the highest sorption. It should be added, that because these results appeared somewhat unusual, several experiments were repeated and the differences in the results between different sets were statistically insignificant.

Selenite Sorption

The results of sorption experiments with 10^{-6} M Se^{IV} on all adsorbents are shown in Figure 11. It can be seen that the only sample with some appreciable Se^{IV} sorption was the alluvium. Again, the sorption of Se^{IV} on iron oxides present in the alluvium samples was expected. The sorption behavior shown in Figure 11 agrees well with numerous studies of Se^{IV} sorption on oxides and hydroxides (Balistrieri and Chao, 1990; Hayes et al., 1988; Hayes et al., 1987; Papelis et al., 1995a). Selenite is considered to form strong, inner-sphere, coordination complexes on most oxides. This hypothesis is consistent both with the observed response to ionic strength variations (Hayes et al., 1988; Papelis et al., 1995a) and with evidence from x-ray absorption spectroscopic experiments (Hayes et al., 1987).

The results from experiments with tuffaceous sediments were also consistent with essential absence of oxide surfaces from this sample. The results with the densely welded tuff, however, were puzzling because very little sorption was observed with the sample that had the highest concentration of iron oxides. It will be remembered that Cr^{VI} uptake by the densely welded tuff was the highest among all samples (Figure 10). Because these results were rather puzzling the experiments were repeated and the results shown represent three different data sets. The results for the three different data sets were statistically indistinguishable. A possible explanation could be based on sample heterogeneity which could result in having performed these experiments with the densely welded tuff with a sub-sample with considerably different composition from the thin section analyzed by electron microscopy.

Comparison of Anion Sorption on CNTA Aquifer Materials

A comparison of the results obtained with Cr^{VI} and Se^{IV} on all three different materials reveals differences and similarities. For both anions, when any sorption was observed, the observed behavior was consistent with expected anion sorption, increasing fractional uptake with

decreasing pH. In addition, the material sorbing anions the least was the tuffaceous sediment sample. For all three samples, however, sorption of Cr^{VI} exceeded sorption of Se^{IV}.

These results are inconsistent with past experimental work with these two anions on a variety of oxides. As mentioned above, previous studies suggest that Cr^{VI} forms weak or intermediately strong outer-sphere complexes on oxide surfaces, whereas Se^{IV} forms strong inner-sphere complexes on oxides. A similar trend was recently observed in experiments conducted in our laboratory using zeolitized tuffs from the Nevada Test Site (to be reported elsewhere). Sorption of Se^{IV} definitely exceeded sorption of Cr^{VI} under the same conditions.

One would be tempted to explain the observed behavior based on the redox chemistry of the two elements. It is well known that the oxidation state of both elements has a dramatic effect on their sorption behavior. Selenium in the +6 oxidation state, selenate, binds much more weakly than selenite and is thought to form outer-sphere complexes on iron oxides (Hayes et al., 1988; Hayes et al., 1987). This anion is thought to sorb no more strongly than sulfate, a major, rather inert, anion. Chromium, on the other hand, in the +3 oxidation state, is a cation (Cr^{3+}), known to form extremely strong complexes on amphoteric sites and to form insoluble precipitates. The hypothesis of the surface-catalyzed oxidation of Se^{IV} to Se^{VI} can definitely not be ruled out, although studies have shown that the oxidation rate is rather slow. It is not impossible, however, to assume that reduction of iron on the mineral surfaces might help oxidize selenium, thereby substantially reducing selenium sorption. Redox reactions controlling the fate of Se in soil have been reported (Pickering et al., 1995; Tokunaga et al., 1998).

Reduction of Cr^{VI} to Cr^{III} cannot be ruled out either, although the shape of the fractional uptake curves obtained and shown in Figure 10 are consistent with anion sorption, not cation. The question whether redox reactions were responsible for the observed sorption behavior of the two anions, however, could be answered by collecting spectroscopic data with both *in situ* and *ex situ* techniques, x-ray absorption and x-ray photoelectron spectroscopies, respectively. Such advanced research techniques, however, were far beyond the scope of this project. A final possible explanation for the observed strong sorption of Cr^{VI} on CNTA materials may be the formation of mixed precipitates with metal cations from the groundwater or cations in equilibrium with the mineral phases present.

Estimation of Equilibrium Partitioning of Anions at CNTA Mineral–Water Interfaces

As for the cations, parameters describing equilibrium partitioning of the anions, Cr^{VI} and Se^{IV}, at the mineral–water interface were determined for both the linear and Freundlich isotherms

and the results are presented in Table 7. It should be noted that the parameters reported for both isotherms were calculated in terms of the respective elements, not the corresponding anions (e.g., for Se isotherm calculations, the molecular weight of selenium was used, not the molecular weight of the selenite anion).

The results shown in Table 7 are consistent with expectations for the sorption of the two anions. The K_d s are considerably lower than the estimates for the cations, as expected because anions can only bind at amphoteric surface sites. In fact, all K_d s reported for Cr^{VI} are single point K_d s because concentrations higher than 10^{-6} M did not result in any appreciable sorption at pH 8. Se^{IV} is considered to bind more strongly and this is reflected in the generally higher K_d s for Se^{IV} compared to Cr^{VI}. The lowest K_d for Se^{IV} was obtained with the tuffaceous sediment material, which is not surprising, given that there were no oxides present in the tuffaceous sediments. The nonlinearity of the isotherms appears to be adsorbent specific and the Freundlich 1/n exponent was less than one in all cases.

As stated above, sorption of anions on the larger size fraction was even lower compared to the smaller size fraction. In fact, the fractional uptake for both Cr^{VI} and Se^{IV} was basically comparable to the experimental uncertainty under these conditions. No sorption and no sorption isotherm parameters are therefore reported. Given the already low sorption parameters estimated for anions using the smaller particle size fraction, it should not be surprising that even weaker sorption would result in retardation indistinguishable from 1 and that, therefore, estimation of K_d s and K_F s would be misleading.

RATE OF UPTAKE BATCH SORPTION EXPERIMENTS

The kinetics of inorganic ion sorption on mineral surfaces has been the topic of considerable controversy over the last few years. This is partly because of the complex processes occurring at mineral-water interfaces. These rates, however, may be crucial in determining whether a particular sorption process should be considered as either equilibrium or nonequilibrium sorption. Fast processes relative to groundwater flow are expected to be at least in pseudo-equilibrium with respect to the composition of the surrounding groundwater and could, therefore, be modeled with an equilibrium partition coefficient, such as those presented above. On the other hand, processes slow compared to groundwater flow may be substantially far from equilibrium and modeling of the process by a rate constant rather than an equilibrium constant would be more appropriate.

A number of different processes have been invoked to explain the kinetics of ion sorption at mineral-water interfaces. In many studies a two-step process was observed, including a fast initial uptake followed by much slower gradual uptake that may continue for a period of days to months (Anderson and Rubin, 1981; Davis and Hayes, 1986a). The slow uptake process was explained based on formation of binuclear complexes, particle-particle interactions, diffusion into adsorbents, surface precipitation, or slow intrinsic chemical reaction rates (Anderson and Rubin, 1981; Davis and Hayes, 1986a; Nyffeler et al., 1984; Papelis et al., 1995b; Stumm, 1992; Theis et al., 1988). Pressure jump techniques, however, have shown that ion attachment on mineral surfaces is a very fast process for a variety of anions and cations on several mineral surfaces (Hachiya et al., 1984a; Hachiya et al., 1984b; Hayes and Leckie, 1986; Zhang and Sparks, 1990a; Zhang and Sparks, 1990b).

In this study we performed a limited number of rate of uptake experiments with two cations, Pb and Sr, to estimate the potential of equilibrium vs. nonequilibrium sorption on CNTA aquifer materials. Because of time and resource limitations, these studies were necessarily limited in scope and were therefore not always conclusive. They provide, however, support for choosing an equilibrium approach to model the sorption of anions and cations on aquifer materials from CNTA. Because anions tend to sorb more weakly on most aquifer materials compared to cations, the study was limited to the rates of cation sorption. The sorption behavior of two cations, Pb and Sr, is different enough to allow assessment of the rate of different sorption processes, so the rate experiments presented here are limited to these two cations. Lead sorption will be discussed first, followed by strontium sorption.

Lead Sorption

The rate of Pb uptake by all three CNTA aquifer materials is shown in Figure 12. The solid concentration was 1.0 g/L for all three samples. All experiments were conducted with the largest size fraction, 212-595 μm. The Pb concentration was kept constant at 10^{-6} M. By keeping the concentration as low as possible the potential for surface precipitation would also be kept as low as possible. On the other hand, concentrations much lower than 10^{-6} M would result in 100% removal from solution, so that it would be impossible to study the kinetics of the reaction. The pH of the synthetic groundwater was kept constant at approximately 8 to simulate the geochemical environment at CNTA.

Inspection of Figure 12 shows that the sorption of Pb was fast on all three CNTA materials, but especially fast on the densely welded tuff and tuffaceous sediment samples. While on the alluvium sample approximately 60% uptake was achieved within the first minute, the

reaction did not reach pseudoequilibrium until approximately three hours. On the other two samples, however, the reaction was almost instantaneous resulting in final uptakes approximately 60 and 80% for the tuffaceous sediments and densely welded tuff, respectively. Although there is scatter in the data, the average final uptake in the tuffaceous sediment sample appears to be approximately 60% and slightly higher than the initial point (approximately 50%). Even if there is a slight time-dependent increase in sorption, however, the reaction appears to be complete within the first 10 minutes.

These results are somewhat puzzling, considering the nature of these samples. Although the rate data on the alluvium could be defended, the very fast uptake of Pb by tuffaceous sediments and densely welded tuff could be expected only if these materials were nonporous, with all surface sites readily accessible by dissolved ions. The characterization of these two samples, however, both in terms of specific surface area and mineralogy is consistent with substantial porosity and therefore potential for diffusion-limited sorption. One possible explanation for such behavior is the formation of surface precipitates on the external surface areas of the particles. This hypothesis, however, cannot be tested without additional, elaborate spectroscopic experiments to verify the molecular structure of the sorbed complexes. Such experiments, obviously, were beyond the scope of this work.

Strontium Sorption

The rate of Sr uptake by all three aquifer materials is shown in Figure 13. The larger particle size fraction was used for these experiments as well. The concentration of Sr was 10^{-6} M and the solid concentration was 1.0 g/L for all solids. As can be seen, the uptake of Sr was also very fast, essentially instantaneous. One can also observe that the uptake reported for the alluvium sample is negative. This is because of the dissolution of Sr from the alluvium aquifer material and was mentioned earlier. The results for the alluvium sample and the low Sr concentration are therefore not useful.

As in the case of Pb rate of uptake, the sorption of Sr on tuffaceous sediments and densely welded tuff was almost instantaneous, although a very slight and gradual increase in Sr uptake can be noticed during the first few hours of the experiment. Obviously, the argument used in the case of Pb that a rapid surface precipitation process may be responsible for the instantaneous uptake of the ion cannot be used in the case of Sr, given the very high solubility of Sr and its negligible tendency to hydrolyze. The results reported here could only be explained based on the low concentration of Sr used in these experiments. The lower the concentration of the ion, the more accessible the sorption surface sites of the mineral and the more rapid the uptake.

Estimation of Rate Constants from Batch Rate of Uptake Experiments

As mentioned above, the sorption of inorganic ions on mineral surfaces has been interpreted by a number of sorption processes. Depending on the assumed process, a different model would be appropriate. It is, therefore, not surprising that a plethora of models have been proposed to model reaction rates (Connors, 1990; Sparks, 1989; Sposito, 1994; Stumm and Morgan, 1996). Given the uncertainty of the data and considering the complexity of each model, it was decided to use a first order model to obtain reaction rate constants for the two cations. It should be remembered, however, that agreement of kinetic data with any particular model does not necessarily reveal anything about the mechanism of the reaction. These rate constants, therefore, should only be viewed as a macroscopic description of the rate of uptake of these ions from solution and not proof for any particular sorption mechanism.

A first order rate process is represented by the following equation:

$$\frac{dC}{dt} = -kC \tag{4}$$

where C is the concentration at time t and k is the first order rate constant. It is obvious from the above equation that k must have units of inverse time. By rearranging this equation one obtains:

$$\frac{dC}{C} = -k \cdot dt \tag{5}$$

which can be easily integrated to give:

$$ln\,C = -kt + Const. \tag{6}$$

so that when the logarithm of the concentration is plotted vs. time the slope of the straight line should be the first order rate constant.

The rate of Pb uptake by all three CNTA aquifer materials, modeled as a first order process is shown in Figure 14. The logarithm of the concentration of Pb is plotted as a function of time, yielding a straight line with slope equal to the first order rate constant. The numbers calculated for the tuffaceous sediments and densely welded tuff were 3.58×10^{-3} and 9.11×10^{-4} h^{-1}, respectively. Based on Figure 14, a single rate appears to be appropriate for modeling these data. The data on alluvium, however, suggest a distinct two step process with a initial fast uptake, up to approximately 3 hours, followed by a very slow desorption process. These data are just a different presentation of the rate data shown in Figure 12. The rate constants for all samples are summarized in Table 8.

The rate of Sr uptake by the CNTA adsorbents, modeled as a first order rate process is shown in Figure 15. Similar to the discussion of the results for Pb, one can see that, based on Figure 15, sorption was essentially instantaneous. Under these conditions, a single low first order rate was used to model the sorption of Sr on all three aquifer materials. The rate constants for each adsorbent are listed in Table 8.

COLUMN EXPERIMENTS

Column experiments with CNTA aquifer materials were also conducted to obtain an independent and, presumably, more realistic estimates of retardation factors for the different cations and anions in all different aquifer materials. All column experiments were conducted with the larger size fraction, between 212 and 595 μm. Because of the fine grain size of the alluvium, experiments with this type of material could not be performed, because the water velocity in the column would be prohibitively small. Experiments were performed with the tuffaceous sediments and densely welded tuff samples. Because of the different mineralogical composition of the two materials, the resulting flowrates were different, even though the particle size distributions were similar. Under these conditions, the linear velocity in the columns was approximately 8.6 m/d in the densely welded tuff column and 8.6×10^{-2} m/d in the tuffaceous sediment column. These velocities were generally higher than the groundwater velocities used in the transport model.

Because of time and work scope limitations, column studies could not be performed with all elements. Given the more critical nature of cation studies, we decided to perform experiments with one cation only. Based on the equilibrium studies and the retardation factors estimated from the distribution coefficients, it was expected that Pb would require very long times for breakthrough. We, therefore, conducted the column studies with Sr only. A continuous supply of Sr in synthetic groundwater was provided for the experiments.

A number of transport parameters can be obtained by analyzing the results from column experiments. Assuming, as a hypothetical case, that the solute of interest is not retarded at all and that hydrodynamic dispersion in the column is negligible, breakthrough of the solute should be observed as exactly one pore volume passes through the column. In a real case, however, because of hydrodynamic dispersion, some solute will arrive before water traveling with the average linear velocity, while a complete breakthrough will only be observed at times larger than corresponding to one pore volume. At exactly one pore volume, however, the relative concentration at the outflow, C/C_o, where C is the outflow concentration and C_o the inflow concentration, is expected to be 0.5, assuming a symmetrical retardation curve. A retardation factor under the specific

experimental conditions can be derived by directly considering the number of pore volumes required to observe a relative concentration of 0.5.

The above analysis assumes local equilibrium sorption. If the linear velocity is too high compared to the time required for equilibrium, nonequilibrium sorption would be occurring. Transport models can model nonequilibrium sorption by dividing the total number of reactive sorption sites into two fractions: instantaneously reacting sites in the mobile fraction of pore volume, and slowly reacting sites in the immobile zone. Testing whether nonequilibrium sorption is occurring can be performed by the so called flow interruption technique, where, after breakthrough has occurred, the flow is interrupted and the solution is allowed to equilibrate with the solid phase. After resuming the steady flow, if the relative concentration is below 1, nonequilibrium sorption must be assumed. Nonequilibrium sorption because of diffusional mass transfer effects has been reported (Bahr, 1989; Brusseau et al., 1990; Brusseau et al., 1991; Brusseau et al., 1989; Goltz and Roberts, 1988; Selim and Ma, 1995). Assuming physical nonequilibrium is detected using the flow interruption technique, solute diffusivities can be obtained from the experimental data.

In the present study both columns were operated long enough to elute more than 100 pore volumes. No Sr breakthrough, however, was observed in any of the columns. These results, although they can not be used to estimate retardation coefficients, are important because they are consistent with the large retardation factors obtained from batch sorption experiments. Even if nonequilibrium sorption were the case, absence of any Sr breakthrough after 100 pore volumes would indicate very strong retardation. It should be remembered that retardation factors obtained from column experiments are correlated with the number of pore volumes required to observe a relative outflow concentration of 0.5. Since the relative outflow concentration even after 100 pore volumes was essentially zero, one must assume that the retardation factor under these conditions is substantially higher than 100.

SUMMARY AND CONCLUSIONS

The scope of this project component was to estimate the affinity of three cations (lead, cesium, and strontium) and two anions (chromate and selenite) for aquifer materials from the Central Nevada Test Area, Hot Creek Valley, Nevada. The Central Nevada Test Area is the site of the Faultless underground nuclear test conducted on January 19, 1968 at a depth of 975 m below ground surface.

In an attempt to obtain as much information as possible with respect to cation and anion partitioning at these mineral-water interfaces and to assess whether the sorption processes would be best modeled as equilibrium or nonequilibrium processes, batch equilibrium, batch rate of uptake (kinetic), and experiments in soil columns were conducted. Parameters to be used in transport codes can be obtained independently from these experiments.

To obtain values with aquifer materials as diverse as possible and likely to be encountered in the flowpath of the contaminants of concern, experiments were conducted with alluvium, tuffaceous sediments, and densely welded tuff samples obtained from the U.S. Geological Survey Core Library in Mercury, Nevada. The aquifer materials were reduced in size and three different particle size fractions were obtained. The sorbents were characterized by x-ray diffraction (XRD), particle size distribution, surface area determination, and density determination. In addition, the morphology and composition of the sorbents were examined by scanning electron microscopy (SEM) combined with energy dispersive x-ray spectroscopy (EDX). Examination of thin sections using SEM/EDX in conjunction with image analysis was used to obtain a semiquantitative mineralogical composition of the adsorbents. Based on a combination of these techniques, it was determined that the major components of all samples were quartz and feldspars. In addition, minor components were smectite and mica type clay minerals. Iron oxides were present in the alluvium and densely welded tuff, but not in the tuffaceous sediments.

All experiments were conducted with synthetic groundwater simulating groundwater composition from well HTH-1 at 741 m depth. Anion and cation concentrations ranged from 10^{-6} to 10^{-4} M. For most experiments the solid concentration was 1.0 g/L. Reagent grade chemicals and high purity water were used for all experiments.

Sorption of cations was consistent with sorption on two different types of sites, permanent-charge sites of smectite clays and zeolites and amphoteric, pH-dependent sites of oxide minerals. The relative importance of these two types of sites was a function of the cation and the adsorbent.

Sorption on alluvium and densely welded tuff sorbents was more pH dependent compared to sorption on tuffaceous sediments. These differences could be explained by the presence of iron oxides in the alluvium and densely welded tuff samples. In all cases, Pb was the most strongly sorbing cation, followed by Sr and Cs. The affinity of these two cations for mineral surfaces was also a function of the mineralogical composition of the sample. The sorption of Pb was most likely a combination of sorption at permanent-charge and surface-hydroxyl sites, as well as surface precipitation.

Both chromate and selenite displayed a typical behavior for anions sorbed on amphoteric oxide surfaces. The sorption of both anions was higher in the alluvium and densely welded tuff samples and substantially lower in the tuffaceous sediment sample, as expected based on the mineralogical composition of the adsorbents. Chromate appeared to bind more strongly than selenite in the small size fraction particles, contrary to expectations. Possible explanations for this behavior hinge on redox reactions involving these elements and possible formation of mixed chromium phases and precipitates. The behavior of both elements with the larger particle size fraction, however, was very similar. These results demonstrate the importance of combining macroscopic experiments with a detailed characterization of the adsorbents to help explain the observed behavior. Such detailed information can only be obtained by a combination of bulk, macroscopic investigations and microscopic investigation of the sorbing mineral surfaces.

Distribution coefficients were obtained from the sorption experiments for both cations and anions. These ranged from 1.86×10^{-2} m^3/g for Pb in the alluvium to 5.18×10^{-4} m^3/g for Cs in the alluvium. The distribution coefficients were reported for pH 8 only, the approximate pH of the groundwater at CNTA. Distribution coefficients for the anions were lower than for cations and ranged from 1.02×10^{-4} m^3/g for Se^{IV} in the alluvium to essentially no sorption for Cr^{VI} in the densely welded tuff (at pH 8). In order to assess the linearity of the isotherms, Freundlich parameters were also estimated. In most cases the Freundlich exponent was less than one, with Pb showing the most nonlinear behavior. Strontium exponents, however, were larger than one. Selenite exponents were also less than one.

In order to evaluate the dependence of the distribution coefficients on specific surface area, experiments were also conducted with a larger size fraction and the ratio of distribution coefficients was correlated with the ratio of specific surface areas. The three different size fractions had similar specific surface areas, indicating that most of the surface area was internal. The distribution coefficients were lower for the larger particles, but the ratio of distribution coefficients correlated fairly well with the ratio of specific surface areas.

Batch rate of uptake experiments were conducted with the larger particle size fraction and the cations Pb and Sr. The reactions were typically very fast, essentially instantaneous, except for Pb sorption on alluvium, where equilibration required about 3 hours. The rates of uptake were modeled as first order rate processes. Except for Pb sorption on alluvium, where a two step process was necessary, all other reactions were modeled by a single first order rate. The slow rates with both elements and all aquifer materials were on the order of 10^{-4} h^{-1}, whereas the rate for the initial fast uptake of Pb by alluvium was 0.313 h^{-1}. These fast rates can only be justified by instantaneous sorption on readily accessible sites or surface precipitation processes, in the case of Pb.

Column experiments were conducted with tuffaceous sediments and densely welded tuff and with the larger particle size fraction. Experiments were conducted with Sr only. In both columns at least 100 pore volumes were eluted without any significant Sr breakthrough. These results suggest very high retardation factors, consistent with the retardation estimated from batch equilibrium experiments. Overall, the rate of uptake and column experiments were consistent with the batch equilibrium experiments and can be used to justify using batch equilibrium experiments to estimate retardation factors to be used in transport models. The limitations of the use of distribution coefficients, however, should not be ignored. Special attention is needed when distribution coefficients are used to estimate the partitioning of contaminants at concentrations outside the concentration range used to obtain these distribution coefficients, when conditions at different pH values are being modeled and sorption reactions are pH dependent, or when isotherms are strongly nonlinear.

REFERENCES

Anderson, M.A. and A.J. Rubin (1981). *Adsorption of Inorganics at Solid-Liquid Interfaces*, Ann Arbor Sci., Ann Arbor, MI, 357 pp.

Anderson, M.P. and W.W. Woessner (1992). *Applied Groundwater Modeling: Simulation of Flow and Advective Transport*. Academic Press, San Diego, 381 pp.

Baes, C.F., Jr. and R.E. Mesmer (1986). *The Hydrolysis of Cations*. Robert E. Krieger Publ. Co., Malabar, FL, 489 pp.

Bahr, J.M. (1989). "Analysis of nonequilibrium desorption of volatile organics during field test of aquifer decontamination," *J. Contam. Hydrol.* **4,** 205-222.

Balistrieri, L.S. and T.T. Chao (1990). "Adsorption of selenium by amorphous iron oxyhydroxide and manganese dioxide," *Geochim. Cosmochim. Acta.* **54,** 739-751.

Bohn, H.L., B.L. McNeal, and G.A. O'Connor (1985). *Soil Chemistry*. John Wiley & Sons, New York, 341 pp.

Brunauer, S., P.H. Emmett, and E. Teller (1938). "Adsorption of gases in multimolecular layers," *J. Am. Chem. Soc.* **60,** 309-319.

Brusseau, M.L., R.E. Jessup, and P.S.C. Rao (1990). "Sorption kinetics of organic chemicals: Evaluation of gas-purge and miscible-displacement techniques," *Environ. Sci. Technol.* **24,** 727-735.

Brusseau, M.L., R.E. Jessup, and P.S.C. Rao (1991). "Nonequilibrium sorption of organic chemicals: Elucidation of rate-limiting processes," *Environ. Sci. Technol.* **25,** 134-142.

Brusseau, M.L., P.S.C. Rao, R.E. Jessup, and J.M. Davidson (1989). "Flow interruption: A method for investigating sorption nonequilibrium," *J. Contam. Hydrol.* **4,** 223-240.

Bryant, E.A. and J. Fabryka-Martin (1991). "Survey of hazardous materials used in nuclear testing," Report No. LA-12014-MS, Los Alamos National Laboratory, Los Alamos, NM.

Chen, C.-C., C. Papelis, and K.F. Hayes (1998). "Extended x-ray absorption fine structure (EXAFS) analysis of aqueous Sr^{II} ion sorption at clay-water interfaces." In *Sorption of Metals by Geomedia: Variables, Mechanisms, and Model Applications*, (Edited by E.A. Jenne), Academic Press, San Diego, 333-348.

Chisholm-Brause, C.J., K.F. Hayes, A.L. Roe, G.E. Brown, Jr., G.A. Parks, and J.O. Leckie (1990). "Spectroscopic investigation of Pb(II) complexes at the γ-Al_2O_3/water interface," *Geochim. Cosmochim. Acta.* **54,** 1897-1909.

Chisholm-Brause, C.J., A.L. Roe, K.F. Hayes, G.E. Brown, Jr., G.A. Parks, and J.O. Leckie (1989). "XANES and EXAFS study of aqueous Pb(II) adsorbed on oxide surfaces," *Physica B.* **158,** 674-675.

Connors, K.A. (1990). *Chemical Kinetics: The Study of Reaction Rates in Solution*. VCH, New York, 480 pp.

Davis, J.A. and K.F. Hayes (1986a). *Geochemical Processes at Mineral Surfaces*, ACS Symposium Series, No.323. American Chemical Society, Washington, D.C., 683 pp.

Davis, J.A. and K.F. Hayes (1986b). "Geochemical processes at mineral surfaces: an overview." In *Geochemical Processes at Mineral Surfaces*, (Edited by J.A. Davis and K.F. Hayes), ACS Symposium Series, No. 323. American Chemical Society, Washington, D.C., 2-18.

Emsley, J. (1989). *The Elements*. Oxford University Press, Oxford, 256 pp.

Francis, B.M. (1994). *Toxic Substances in the Environment*. Environmental Science and Technology. John Wiley & Sons, New York, 360 pp.

Goltz, M.N. and P.V. Roberts (1988). "Simulations of physical nonequilibrium solute transport models: Application to a large-scale field experiment," *J. Contam. Hydrol.* **3**, 37-63.

Gregg, S.J. and K.S.W. Sing (1982). *Adsorption, Surface Area and Porosity*. Academic Press Inc., London, 303 pp.

Hachiya, K., M. Sasaki, T. Ikeda, N. Mikami, and T. Yasunaga (1984a). "Static and kinetic studies of adsorption-desorption of metal ions on a γ-Al_2O_3 surface. 2. Kinetic study by means of pressure-jump technique," *J. Phys. Chem.* **88**, 27-31.

Hachiya, K., M. Sasaki, Y. Saruta, N. Mikami, and T. Yasunaga (1984b). "Static and kinetic studies of adsorption-desorption of metal ions on a γ-Al_2O_3 surface. 1. Static study of adsorption-desorption," *J. Phys. Chem.* **88**, 23-27.

Hayes, K.F. (1987). "Equilibrium, spectroscopic, and kinetic studies of ion adsorption at the oxide/aqueous interface," Ph.D. Dissertation, Stanford University, Stanford, CA.

Hayes, K.F. and J.O. Leckie (1986). "Mechanism of lead ion adsorption at the goethite-water interface." In *Geochemical Processes at Mineral Surfaces*, (Edited by J.A. Davis and K.F. Hayes), ACS Symposium Series, No. 323. American Chemical Society, Washington, D.C., 114-141.

Hayes, K.F. and J.O. Leckie (1987). "Modeling ionic strength effects on cation adsorption at hydrous oxide/solution interfaces," *J. Colloid Interface Sci.* **115**, 564.

Hayes, K.F., C. Papelis, and J.O. Leckie (1988). "Modeling ionic strength effects on anion adsorption at hydrous oxide/solution interfaces," *J. Colloid Interface Sci.* **125**, 717-726.

Hayes, K.F., A.L. Roe, G.E. Brown, Jr., K.O. Hodgson, J.O. Leckie, and G.A. Parks (1987). "In situ X-ray absorption study of surface complexes: selenium oxyanions on α-FeOOH," *Science*. **238**, 783.

Hemond, H.F. and E.J. Fechner (1994). *Chemical Fate and Transport in the Environment*. Academic Press, San Diego, 338 pp.

Laws, E.A. (1993). *Aquatic Pollution: An Introductory Text*. Environmental Science and Technology. John Wiley & Sons, New York, 611 pp.

McBride, M.B. (1994). *Environmental Chemistry of Soils*. Oxford University Press, New York, 406 pp.

Nakamura, S., S. Mori, H. Yoshimuta, Y. Ito, and M. Kanno (1988). "Uranium adsorption properties of hydrous titanium oxide granulated with polyacrylonitrile," *Separ. Sci. Technol.* **23,** 731-743.

Nyffeler, U.P., Y.H. Li, and P.H. Santschi (1984). "A kinetic approach to describe trace-element distribution between particles and solution in natural aquatic systems," *Geochim. Cosmochim. Acta.* **48,** 1513-1522.

Ohnuki, T., S. Takebe, and T. Yamamoto (1989). "Development of a migration prediction system (MIGSTEM) for cationic species of radionuclides through soil layers," *J. Nucl. Sci. Technol.* **28,** 795-804.

Ooi, K., K. Ashida, S. Katoh, and K. Sugasaka (1987). "Rate of uranium adsorption on hydrous titanium (IV) oxide granulated with poly acrylic hydrazide," *J. Nucl. Sci. Technol.* **24,** 315-322.

Papelis, C., G.E. Brown, Jr., G.A. Parks, and J.O. Leckie (1995a). "X-ray absorption spectroscopic studies of cadmium and selenite adsorption on aluminum oxides," *Langmuir.* **11,** 2041-2048.

Papelis, C. and K.F. Hayes (1996). "Distinguishing between interlayer and external sorption sites of clay minerals using x-ray absorption spectroscopy," *Colloids & Surfaces, A.* **107,** 89-96.

Papelis, C., P.V. Roberts, and J.O. Leckie (1995b). "Modeling the rate of cadmium and selenite adsorption on micro- and mesoporous transition aluminas," *Environ. Sci. Technol.* **29,** 1099-1108.

Pickering, I.J., G.E. Brown, Jr., and T.K. Tokunaga (1995). "Quantitative speciation of selenium in soils using x-ray absorption spectroscopy," *Environ. Sci. Technol.* **29,** 2456-2459.

Roe, A.L., K.F. Hayes, C.J. Chisholm-Brause, G.E. Brown, Jr., G.A. Parks, K.O. Hodgsonet al. (1991). "In situ X-ray absorption study of lead ion surface complexes at the geothite-water interface," *Langmuir.* **7,** 367-373.

Sax, N.I. (1981). *Cancer Causing Chemicals.* Van Nostrand Reinhold, New York, 466 pp.

Selim, H.M. and L. Ma (1995). "Transport of reactive solutes in soils: a modified two-region approach," *Soil Sci. Soc. Am. J.* **59,** 75-82.

Sparks, D.L. (1989). *Kinetics of Soil Chemical Processes.* Academic Press, San Diego, 210 pp.

Sposito, G. (1984). *The Surface Chemistry of Soils.* Oxford University Press, Oxford,, 234 pp.

Sposito, G. (1986). "Distinguishing adsorption from surface precipitation." In *Geochemical Processes at Mineral Surfaces,* (Edited by J.A. Davis and K.F. Hayes), ACS Symposium Series, No. 323. American Chemical Society, Washington, D.C., 217-228.

Sposito, G. (1994). *Chemical Equilibria and Kinetics in Soils.* Oxford University Press, Oxford, 268 pp.

Stumm, W. (1992). *Chemistry of the Solid-Water Interface.* John Wiley & Sons, New York, 428 pp.

Stumm, W. and J.J. Morgan (1996). *Aquatic Chemistry: Chemical Equilibria and Rates in Natural Waters*. Environmental Science and Technology. John Wiley, New York, 1022 pp.

Theis, T.L., T.L. Iyer, and L.W. Kaul (1988). "Kinetic studies of cadmium and ferricyanide adsorption on goethite," *Environ. Sci. Technol.* **22**, 1013-1017.

Tokunaga, T.K., S.R. Sutton, S. Bajt, P. Nuessle, and G. Shea-McCarthy (1998). "Selenium diffusion and reduction at the water-sediment boundary: Micro-XANES spectroscopy of reactive transport," *Environ. Sci. Technol.* **32**, 1092-1098.

Weber, W.J., Jr. and F.A. DiGiano (1996). *Process Dynamics in Environmental Systems*. Environmental Science and Technology. John Wiley, New York, 943 pp.

Zhang, P.C. and D.L. Sparks (1990a). "Kinetics and mechanisms of sulfate adsorption/desorption on goethite using pressure-jump relaxation," *Soil Sci. Soc. Am. J.* **54**, 1266-1273.

Zhang, P.C. and D.L. Sparks (1990b). "Kinetics of selenate and selenite adsorption/desorption at the goethite/water interface," *Environ. Sci. Technol.* **24**, 1848-1856.

Table 1. Summary of the Physicochemical Characterization of the Aquifer Materials

	Alluvium	Tuffaceous Sediments	Densely Welded Tuff
Bulk Density (g/cm^3)	1.12	1.12	1.29
True Density (g/cm^3)	2.67	2.56	2.66
Porosity (–)	0.15	0.13	0.11
BET Surface Area (m^2/g)	13.8	16.7	6.24
Average Pore Diameter (Å)	140	130	160
Micropore Volume (mm^3/g)	1.5	1.8	0.25

Table 2. Mineralogical Composition of the Adsorbents Based on X-Ray Diffraction

	Alluvium	Tuffaceous Sediments	Densely Welded Tuff
Bulk XRD Analysis	quartz, albite, calcite, orthoclase	quartz, anorthite, orthoclase	quartz, albite, orthoclase, anorthite
XRD Analysis of Clay Particle Size Fraction	Beidellite (major) Illite, K-feldspar (minor)	Beidellite (major) Illite (minor) K-feldspar (trace)	Could Not Be Determined

Table 3. Adsorbent Composition Based on Electron Backscatter Image Analysis (Percent)

Mineral Phase	Alluvium	Tuffaceous Sediments	Densely Welded Tuff
Iron Oxides	0.88		2.48
Apatite	0.42	0.20	0.38
Chlorite	1.10		
Calcite	7.34	1.28	
Orthoclase	2.16	20.46	18.72
Smectites/Biotite		1.75	7.25
Mica Group Clays	5.36		
Albite/Quartz	82.73		
Plagioclase		40.70	42.87
Quartz			28.29
Hydrated Aluminosi-licates/Quartz		35.54	
Ilmenite		0.07	

Table 4. BET Specific Surface Area of the Adsorbents (All Size Fractions) (m^2/g)

Particle Size Fraction (μm)	Alluvium	Tuffaceous Sediments	Densely Welded Tuff
< 125	13.8	16.7	6.2
125 – 212	11.9	10.6	5.0
212 – 595	15.9	10.4	5.2

Table 5. Linear and Freundlich Isotherm Parameters for Cation Sorption – pH 8; Particle Size Smaller than 125 µm

	K_d (m^3/g)	K_F $(g/g)/(g/m^3)^{1/n}$	1/n (–)
Lead			
Alluvium	1.86×10^{-2}	5.32×10^{-3}	0.68
Tuffaceous Sediments	1.33×10^{-2}	2.47×10^{-2}	1.25
Densely Welded Tuff	1.39×10^{-2}	5.61×10^{-3}	0.68
Strontium			
Alluvium	1.33×10^{-2}	*	*
Tuffaceous Sediments	1.16×10^{-3}	1.54×10^{-3}	1.30
Densely Welded Tuff	6.11×10^{-4}	6.55×10^{-4}	1.11
Cesium			
Alluvium	5.18×10^{-4}	4.94×10^{-4}	0.68
Tuffaceous Sediments	1.51×10^{-3}	1.29×10^{-3}	0.77
Densely Welded Tuff	5.40×10^{-4}	5.25×10^{-4}	0.83

* Single point K_d, no K_F can be calculated.

Table 6. Linear and Freundlich Isotherm Parameters for Cation Sorption – pH 8; Particle Size Between 212 and 595 micrometers

	K_d (m^3/g)	K_F $(g/g)/(g/m^3)^{1/n}$	1/n (–)	$K_{d\,212}/K_{d\,125}$
Lead				
Alluvium	6.78×10^{-3}	2.67×10^{-3}	0.67	0.37
Tuffaceous Sediments	3.14×10^{-3}	1.56×10^{-3}	0.66	0.24
Densely Welded Tuff	3.14×10^{-3}	1.89×10^{-3}	0.76	0.23
Strontium				
Alluvium	2.22×10^{-5}	*	*	0.00167
Tuffaceous Sediments	4.19×10^{-4}	7.36×10^{-4}	1.43	0.36
Densely Welded Tuff	3.50×10^{-4}	6.69×10^{-4}	1.55	0.57
Cesium				
Alluvium	3.27×10^{-4}	2.40×10^{-4}	0.55	0.63
Tuffaceous Sediments	7.10×10^{-4}	6.67×10^{-4}	0.95	0.47
Densely Welded Tuff	3.13×10^{-4}	2.99×10^{-4}	0.93	0.58

* Single point K_d, no K_F can be calculated.

Table 7. Linear and Freundlich Isotherm Parameters for Anion Sorption – pH 8; Particle Size Smaller than 125 micrometers

	K_d (m^3/g)	K_F $(g/g)/(g/m^3)^{1/n}$	1/n (–)
Chromate			
Alluvium	2.04×10^{-5}	*	*
Tuffaceous Sediments	1.01×10^{-5}	*	*
Densely Welded Tuff	No sorption at pH 8		
Selenite			
Alluvium	1.02×10^{-4}	9.18×10^{-5}	0.71
Tuffaceous Sediments	5.59×10^{-6}	8.49×10^{-6}	0.30
Densely Welded Tuff	4.18×10^{-5}	4.05×10^{-5}	0.90

* Single point K_d, no K_F can be calculated.

Table 8. First Order Rate Constants of Pb and Sr Sorption on CNTA Aquifer Materials (h^{-1})

	Lead	Strontium
Alluvium	$k_1 = 0.313$ $k_2 = -2.40 \times 10^{-3}$	4.26×10^{-5}
Tuffaceous Sediments	3.58×10^{-3}	-1.74×10^{-4}
Densely Welded Tuff	9.11×10^{-4}	1.22×10^{-4}

FIGURE CAPTIONS

Figure 1. Electron backscatter image of alluvium thin section

Figure 2. Electron backscatter image of tuffaceous sediment thin section

Figure 3. Electron backscatter image of densely welded tuff thin section

Figure 4. Sorption of Pb by CNTA aquifer materials

Figure 5. Sorption of Sr by CNTA aquifer materials

Figure 6. Sorption of Cs by CNTA aquifer materials

Figure 7. Cation sorption on CNTA alluvium

Figure 8. Cation sorption on CNTA tuffaceous sediments

Figure 9. Cation sorption on CNTA densely welded tuff

Figure 10. Sorption of chromate by CNTA aquifer materials

Figure 11. Sorption of selenite by CNTA aquifer materials

Figure 12. Rate of Pb uptake by CNTA aquifer materials

Figure 13. Rate of Sr uptake by CNTA aquifer materials

Figure 14. Uptake of Pb by CNTA aquifer materials modeled as a first order rate process

Figure 15. Uptake of Sr by CNTA aquifer materials modeled as a first order rate process

Figure 1.

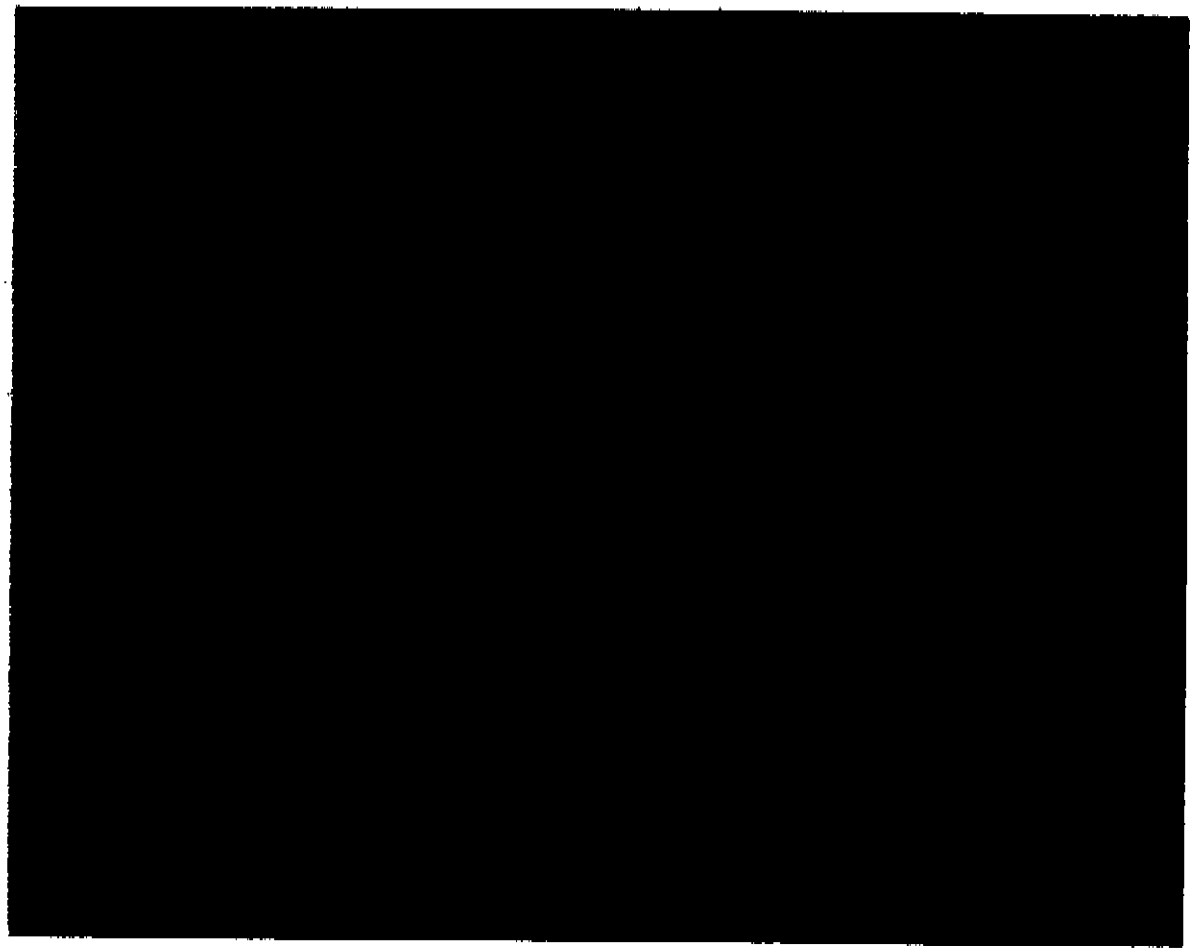

Figure 2.

Figure 3.

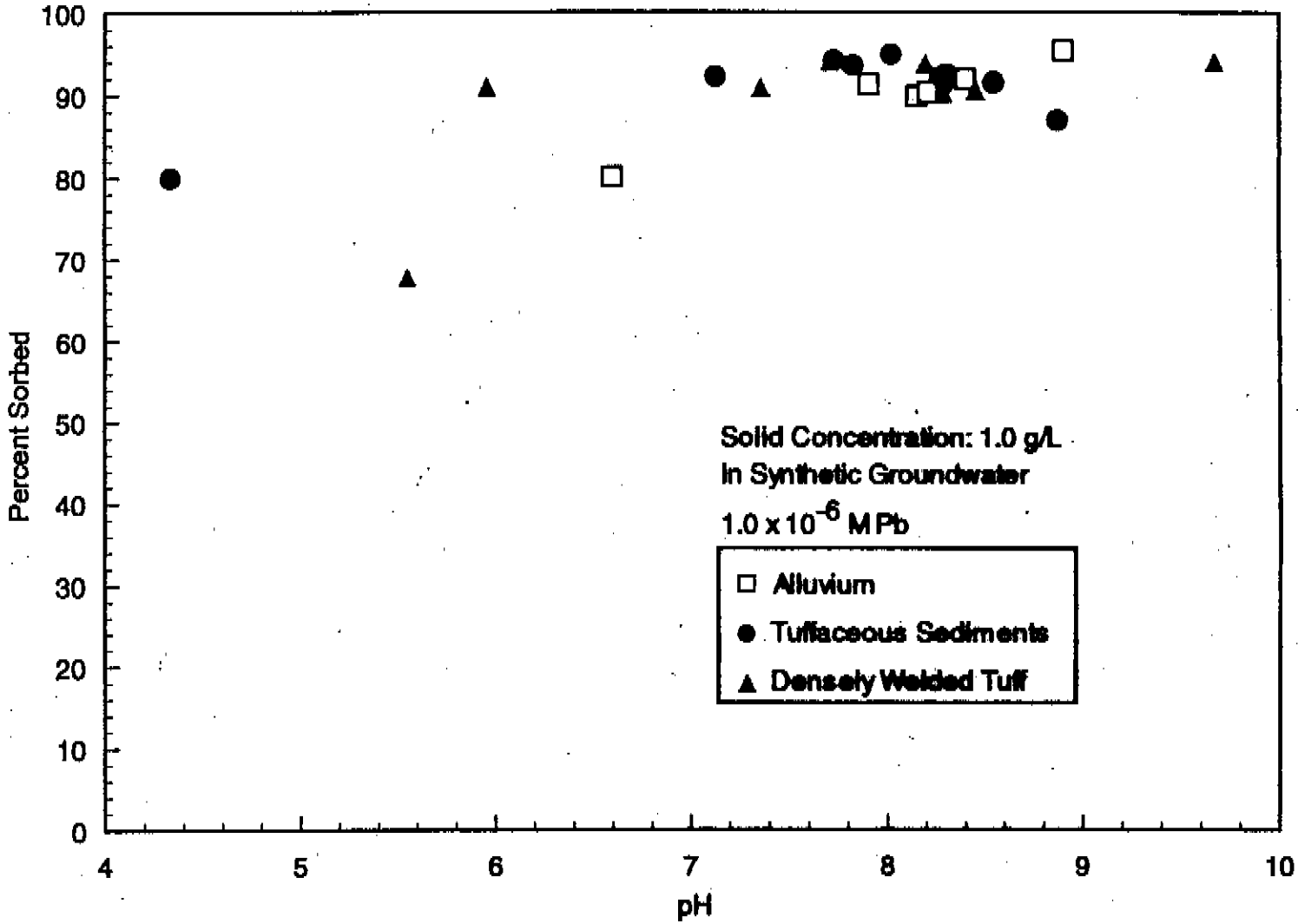
Percent Sorbed
pH
Solid Concentration: 1.0 g/L
In Synthetic Groundwater
1.0 x 10^-6 M Pb
Alluvium
Tuffaceous Sediments
Densely Welded Tuff

Figure 4.

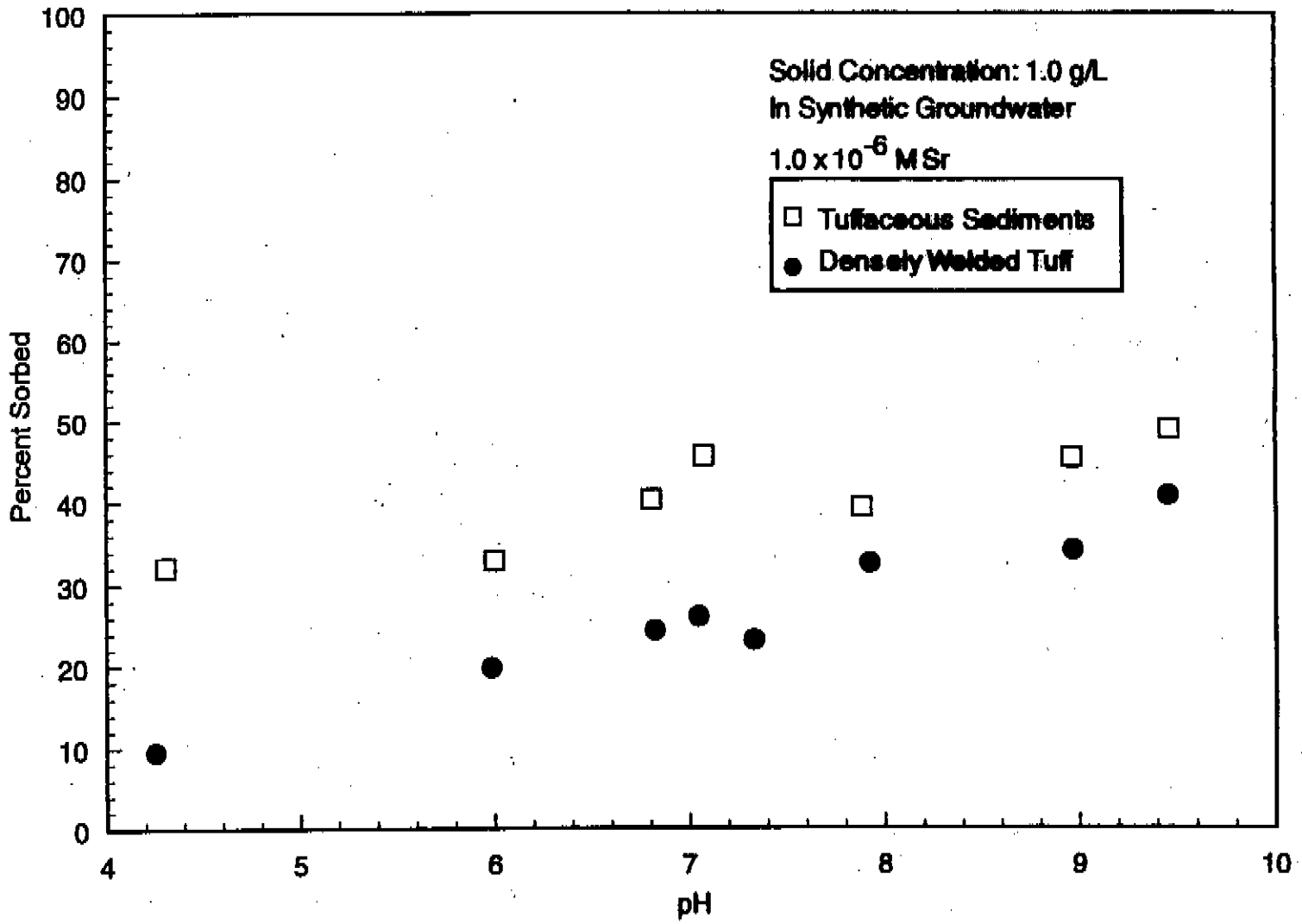
Solid Concentration: 1.0 g/L
In Synthetic Groundwater
1.0 x 10^-6 M Sr
Tuffaceous Sediments
Densely Welded Tuff
Percent Sorbed
pH
0
10
20
30
40
50
60
70
80
90
100
4
5
6
7
8
9
10

Figure 5.

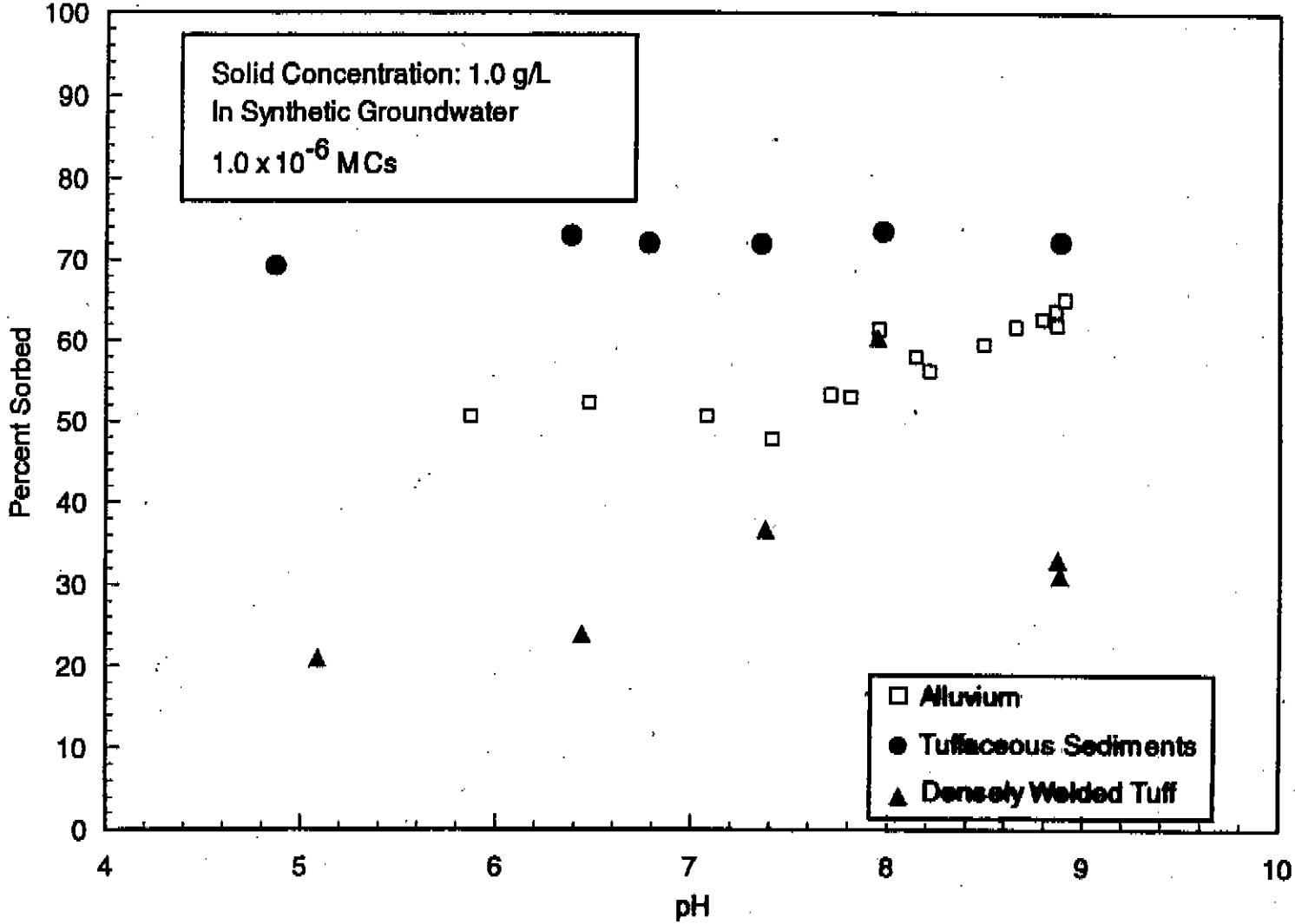
Solid Concentration: 1.0 g/L
In Synthetic Groundwater
1.0 x 10-6 M Cs
Percent Sorbed
pH
Alluvium
Tuffaceous Sediments
Densely Welded Tuff
0
10
20
30
40
50
60
70
80
90
100
4
5
6
7
8
9
10

Figure 6.

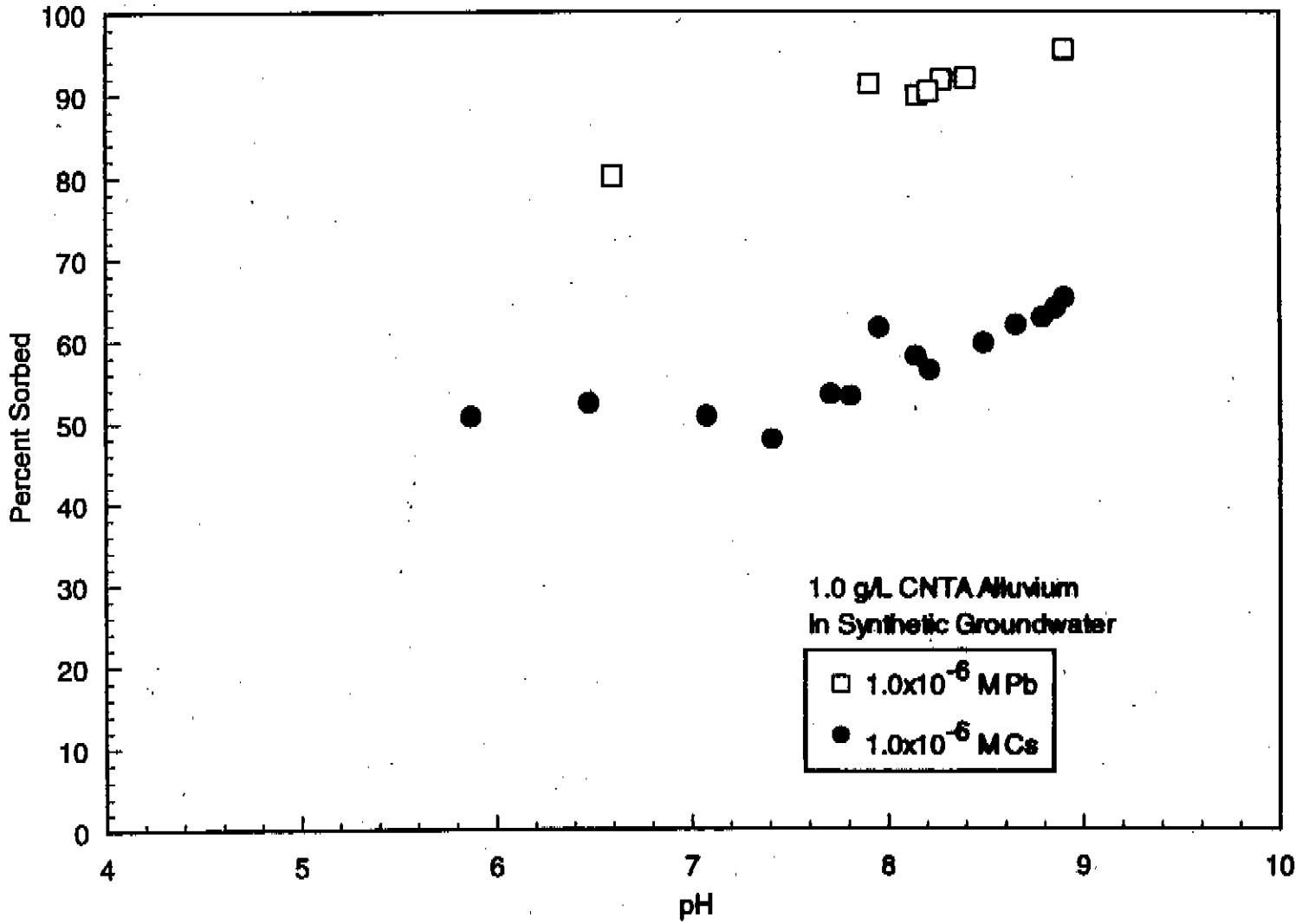
Percent Sorbed
pH
1.0 g/L CNTA Alluvium
In Synthetic Groundwater
1.0x10-6 M Pb
1.0x10-6 M Cs

Figure 7.

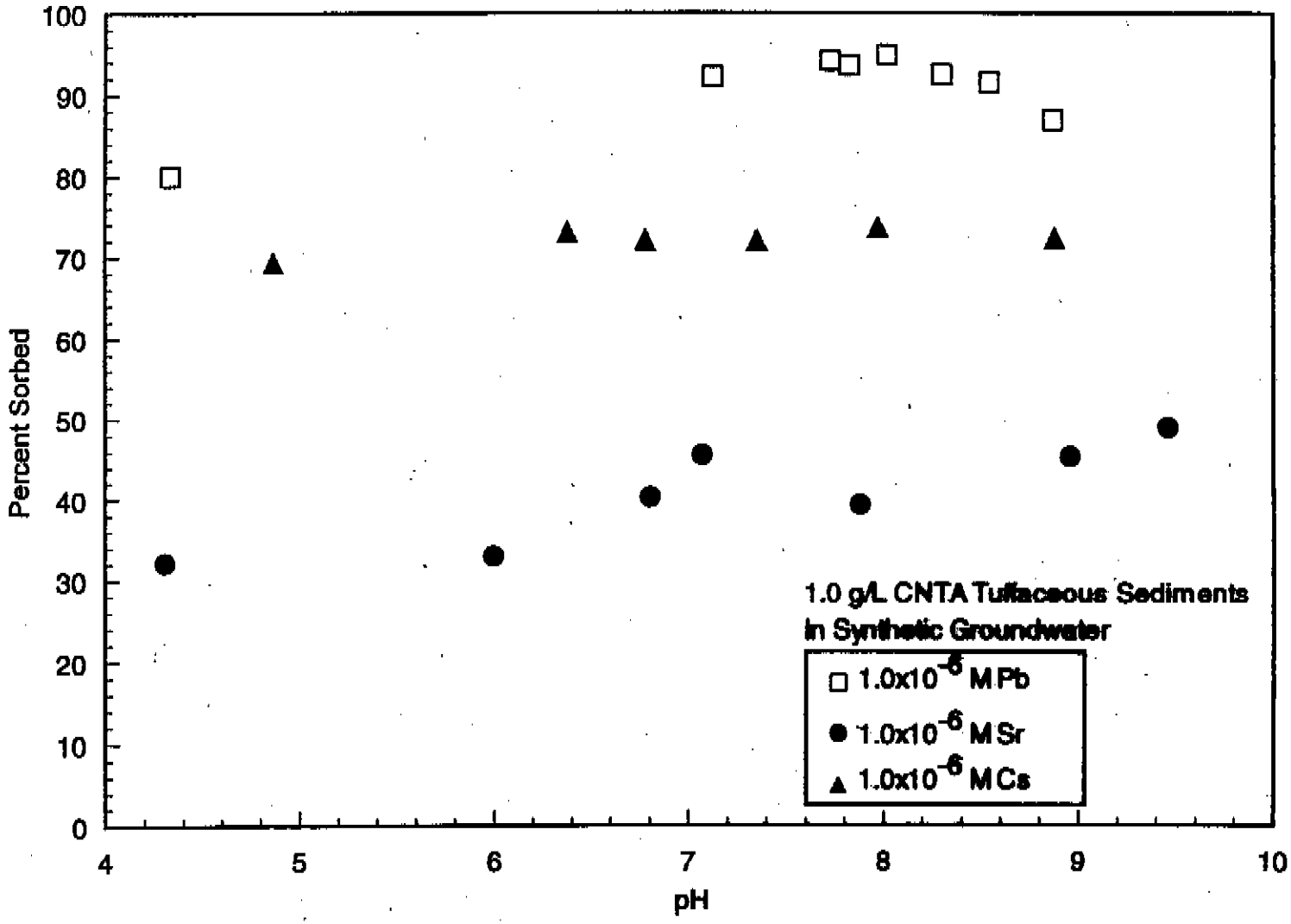
Percent Sorbed
pH
1.0 g/L CNTA Tuffaceous Sediments
In Synthetic Groundwater
1.0x10-6 M Pb
1.0x10-6 M Sr
1.0x10-6 M Cs

Figure 8.

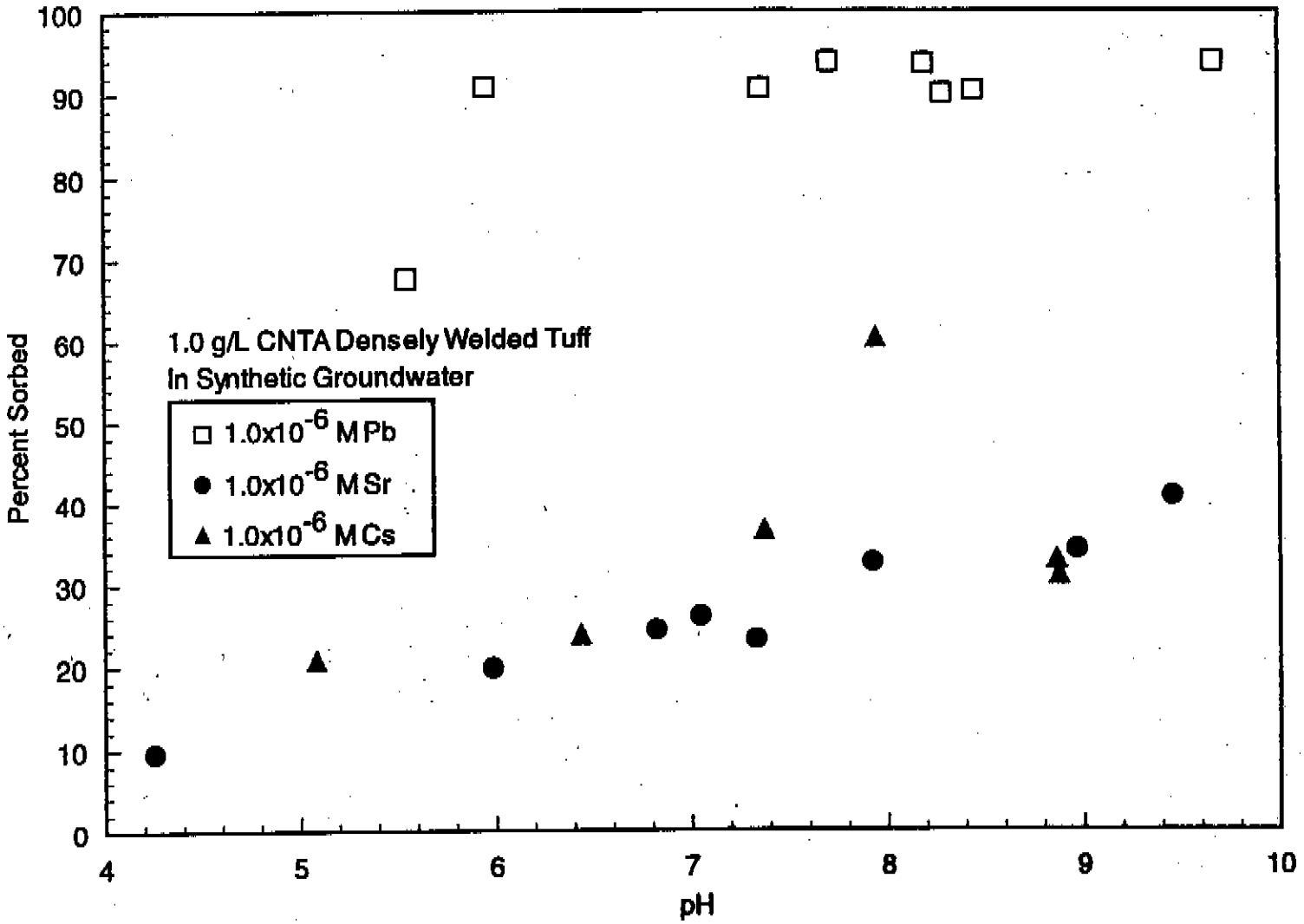
100
90
80
70
60
50
40
30
20
10
0
Percent Sorbed
4
5
6
7
8
9
10
pH
1.0 g/L CNTA Densely Welded Tuff
In Synthetic Groundwater
1.0x10-6 M Pb
1.0x10-6 M Sr
1.0x10-6 M Cs

Figure 9.

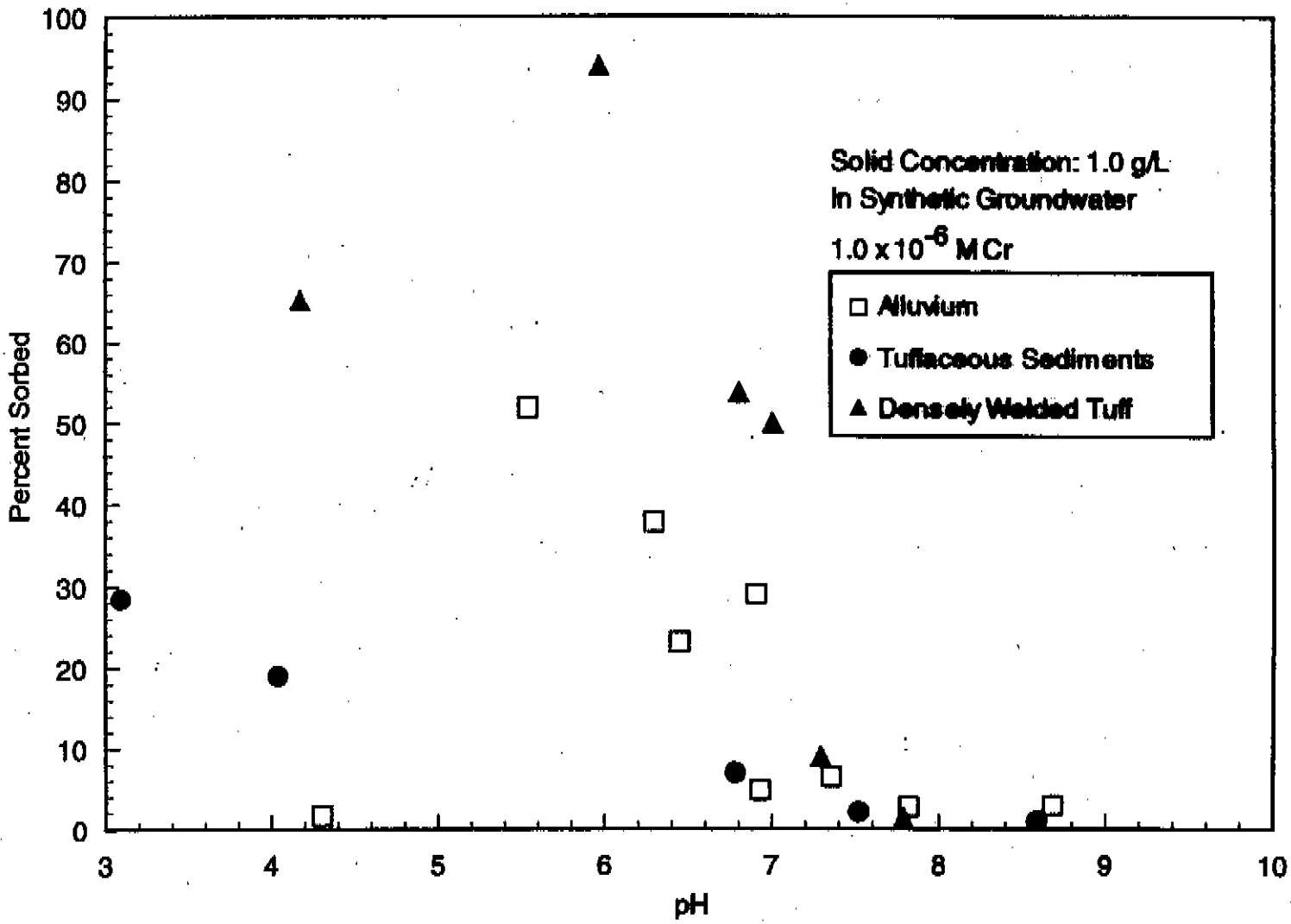
Solid Concentration: 1.0 g/L
In Synthetic Groundwater
1.0 x 10-6 M Cr
Alluvium
Tufaceous Sediments
Densely Welded Tuff
Percent Sorbed
pH
100
90
80
70
60
50
40
30
20
10
0
3
4
5
6
7
8
9
10

Figure 10.

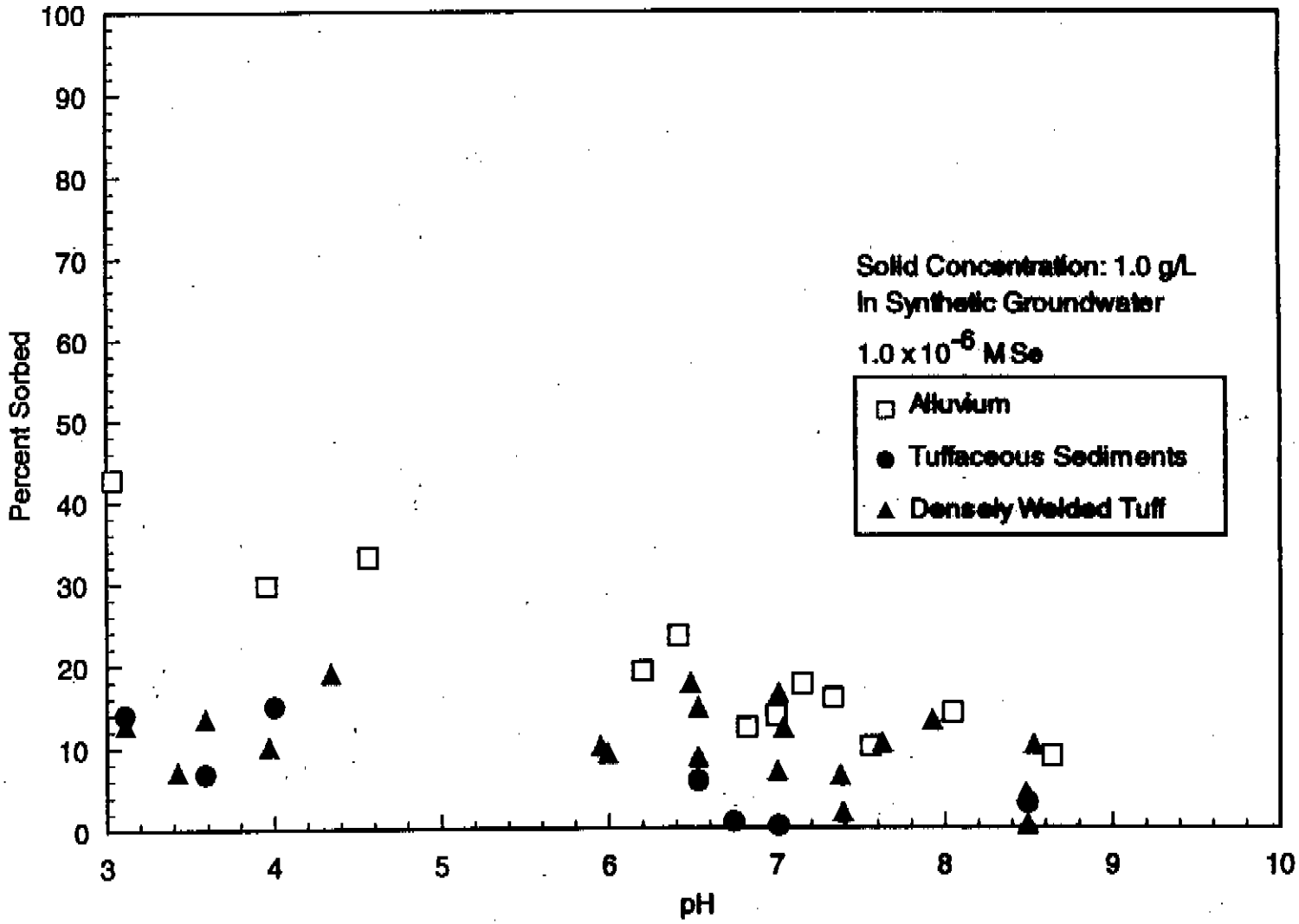
Percent Sorbed
pH
Solid Concentration: 1.0 g/L
In Synthetic Groundwater
1.0 x 10-6 M Se
Alluvium
Tuffaceous Sediments
Densely Welded Tuff

Figure 11.

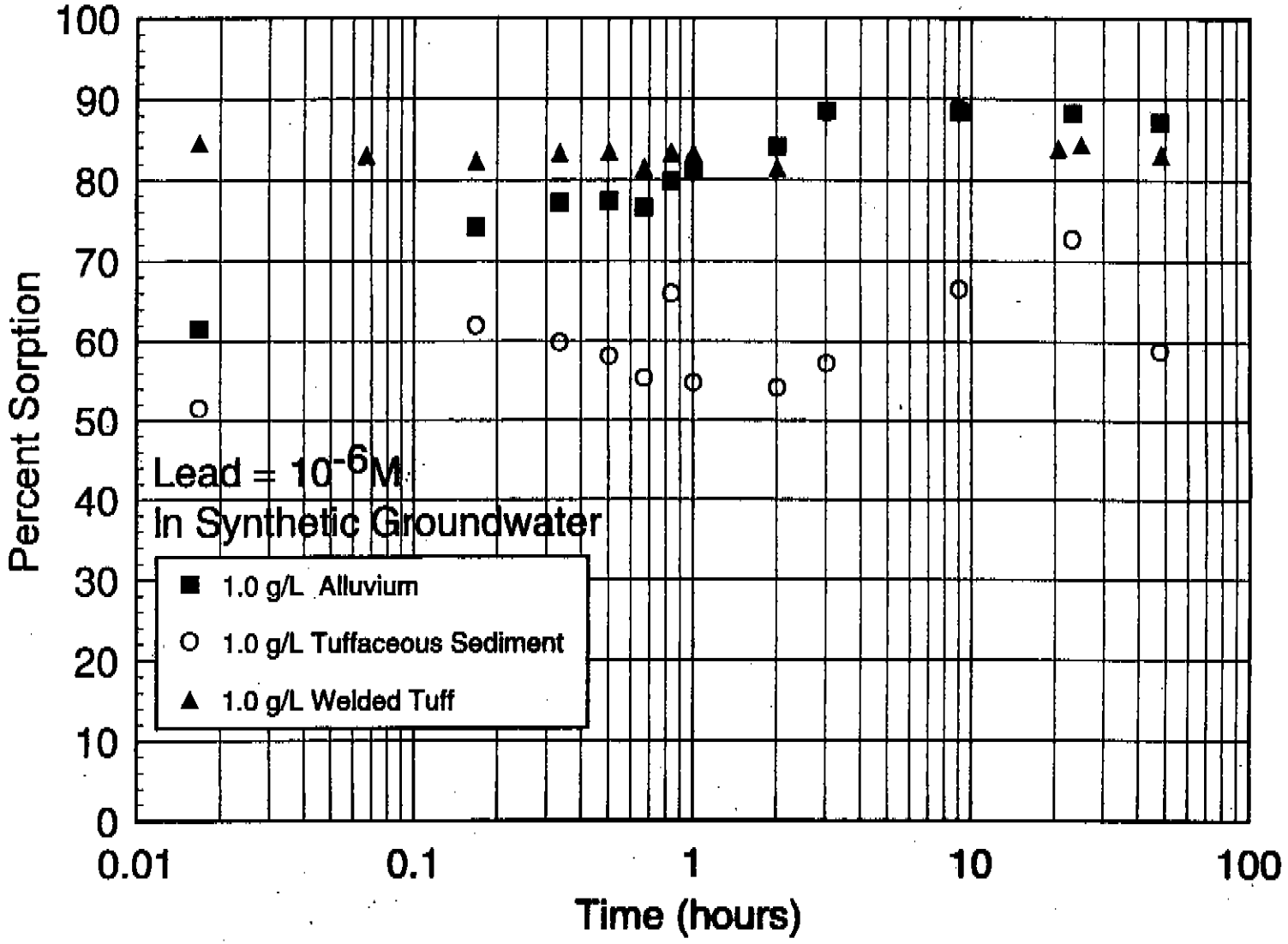
Percent Sorption
Time (hours)
Lead = 10-6M
In Synthetic Groundwater
1.0 g/L Alluvium
1.0 g/L Tuffaceous Sediment
1.0 g/L Welded Tuff
100
90
80
70
60
50
40
30
20
10
0
0.01
0.1
1
10
100

Figure 12.

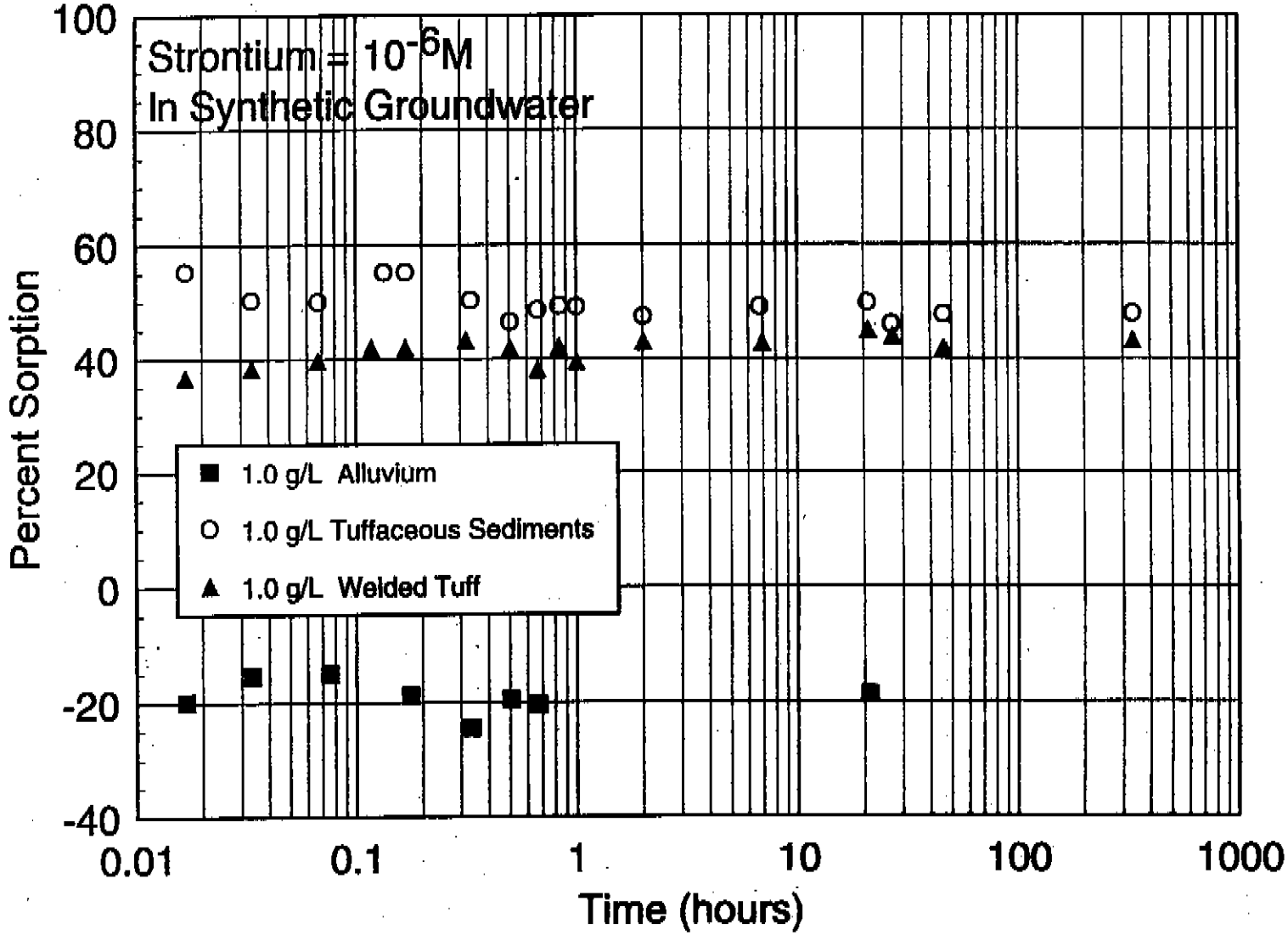
Strontium = 10^{-6}M
In Synthetic Groundwater
Percent Sorption
Time (hours)
100
80
60
40
20
0
-20
-40
0.01
0.1
1
10
100
1000
1.0 g/L Alluvium
1.0 g/L Tuffaceous Sediments
1.0 g/L Welded Tuff

Figure 13.

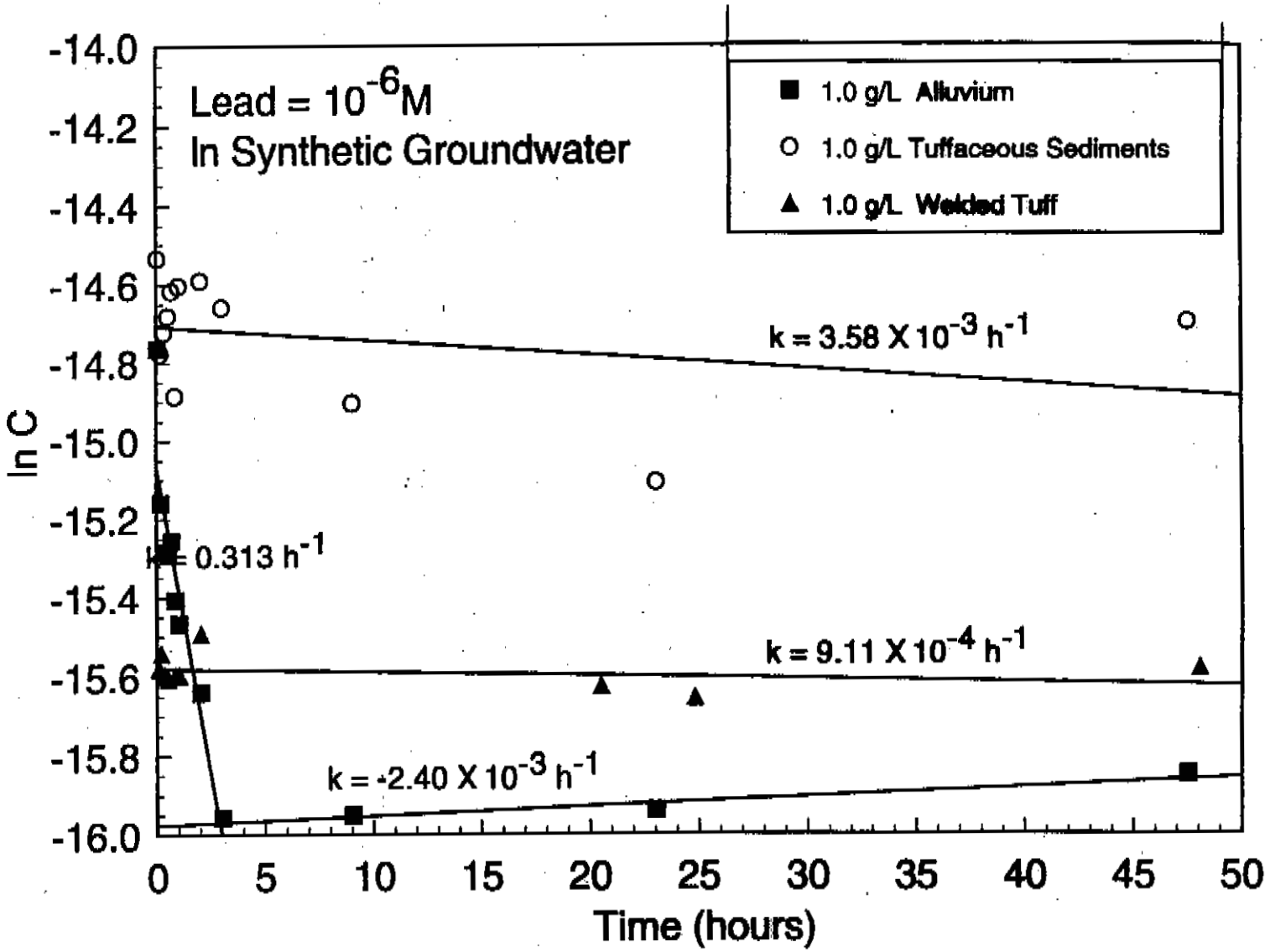
Lead = 10^{-6}M
In Synthetic Groundwater
1.0 g/L Alluvium
1.0 g/L Tuffaceous Sediments
1.0 g/L Welded Tuff
$k = 3.58 \times 10^{-3}$ h^{-1}
$k = 0.313$ h^{-1}
$k = 9.11 \times 10^{-4}$ h^{-1}
$k = -2.40 \times 10^{-3}$ h^{-1}
ln C
Time (hours)
-14.0
-14.2
-14.4
-14.6
-14.8
-15.0
-15.2
-15.4
-15.6
-15.8
-16.0
0
5
10
15
20
25
30
35
40
45
50

Figure 14.

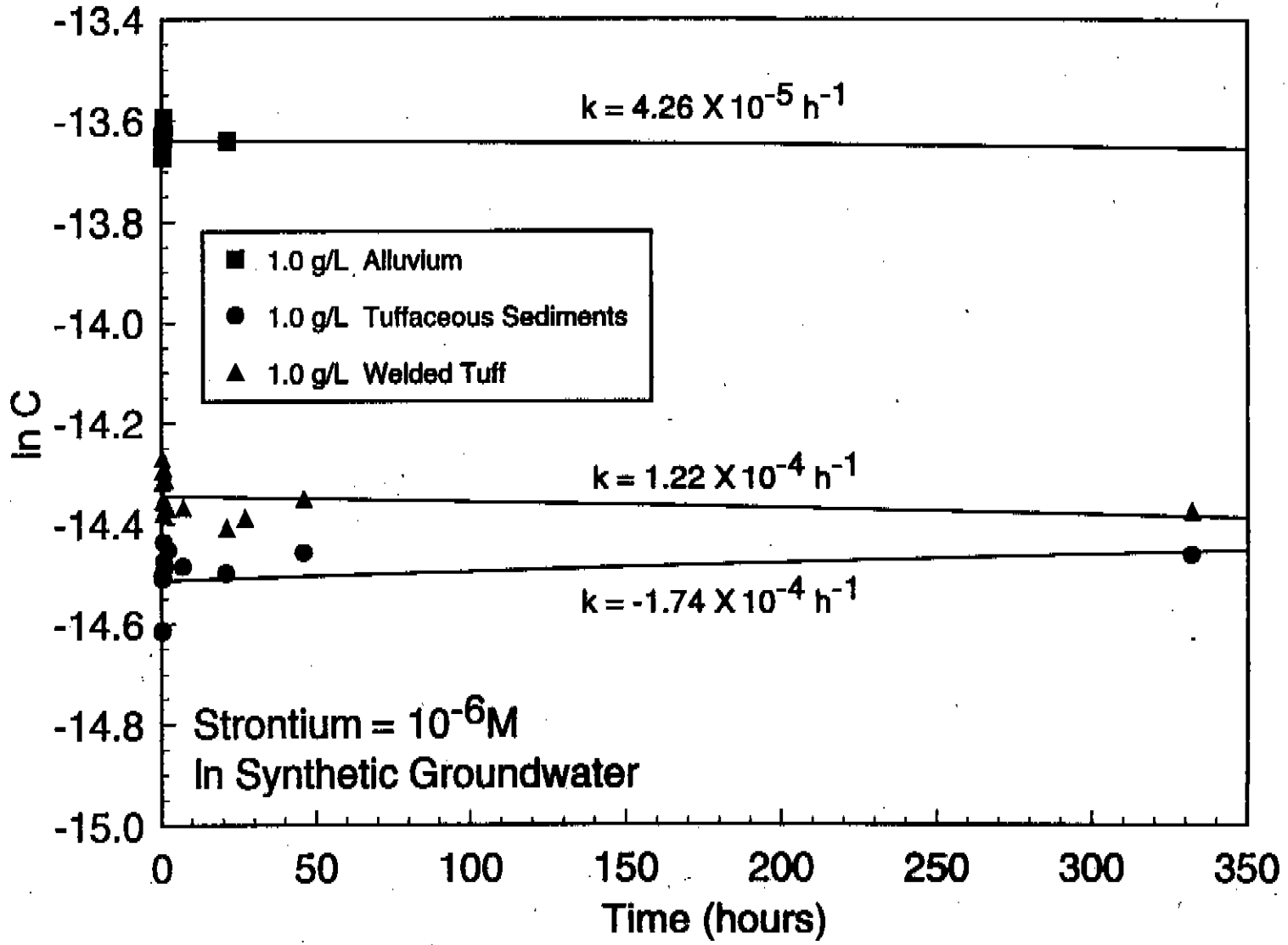
-13.4
-13.6
-13.8
-14.0
-14.2
-14.4
-14.6
-14.8
-15.0
ln C
k = 4.26 X 10-5 h-1
1.0 g/L Alluvium
1.0 g/L Tuffaceous Sediments
1.0 g/L Welded Tuff
k = 1.22 X 10-4 h-1
k = -1.74 X 10-4 h-1
Strontium = 10-6M
In Synthetic Groundwater
0
50
100
150
200
250
300
350
Time (hours)

Figure 15.

APPENDIX 6

MASS FLUX AND CONCENTRATION DATA

Tabulation of peak mass flux ($\overline{Q}_{max}$), standard deviation in mass flux ($\sigma\overline{Q}_{max}$), peak mean concentration ($\overline{C}_{max}$), and standard deviation in peak mean concentration ($\sigma\overline{C}_{max}$) with time of occurrence in years.

The numeral portion of the Case ID denotes the solute number (refer to Appendix 6). The letters in the case ID refer to the sensitivity cases: i for prompt injection; k for increased mean *K* in the alluvium; l for increased vertical correlations scale of *K*; p for reduced porosity and retardation in the welded tuffs; al for increased dispersivity values.

Solute #	Radionuclide Name	Release and Retardation Case
1	^{3}H	1
2	^{14}C	1
7	^{85}Kr	1
8	^{85}Rb	1
16	^{36}Cl	2
17	^{129}I	2
18	^{90}Sr	3
19	^{90}Y	3
20	^{90}Zr	3
27	^{99g}Tc	4
31	^{134}Cs	5
32	^{134}Ba	5
14	^{137}Cs	5
15	^{137}Ba	5
37	^{151}Sm	6
38	^{151}Eu	6
41	^{152}Eu	6
42	^{152}Gd	6
43	^{154}Eu	6
44	^{154}Gd	6
52	^{234}U	6
55	^{238}U	6
56	^{237}Np	6
59	^{239}Pu	6
60	^{240}Pu	6
61	^{236}U	6
63	^{241}Am	6
64	$^{237\#2}Np$	6

Case	Q_{max}	Time	σQ_{max}	Time	C_{max}	Time	σC_{max}	Time
1pm	0.0000e+000	NA	0.0000e+000	NA	0.0000e+000	NA	0.0000e+000	NA
1md	4.7423e-015	1.1221e+002	4.9467e-014	1.1221e+002	5.2760e-010	1.5331e+002	5.3801e-009	1.5331e+002
1ff	8.4037e-012	8.4815e+001	8.6294e-011	7.1116e+001	8.8009e-006	8.4815e+001	9.1884e-005	8.4815e+001
1l	0.0000e+000	NA	0.0000e+000	NA	0.0000e+000	NA	0.0000e+000	NA
1i	0.0000e+000	NA	0.0000e+000	NA	0.0000e+000	NA	0.0000e+000	NA
1ik	9.3128e-009	5.7418e+001	1.9111e-008	5.7418e+001	9.3797e-011	5.7418e+001	1.2900e-010	5.7418e+001
1al1	0.0000e+000	NA	0.0000e+000	NA	0.0000e+000	NA	0.0000e+000	NA
1al2	0.0000e+000	NA	0.0000e+000	NA	0.0000e+000	NA	0.0000e+000	NA
2pm	4.1772e-009	1.0441e+004	1.5539e-008	3.4273e+003	1.3577e-002	1.0331e+004	6.8308e-002	8.3588e+000
2md	7.5930e-011	1.8245e+003	3.5933e-010	6.0536e+002	1.3583e-004	2.0163e+003	5.5877e-004	1.9615e+003
2ff	1.6598e-008	3.7249e+002	8.3779e-008	3.7249e+002	5.4359e-002	3.0985e+003	2.5478e-001	9.6153e+002
2l	3.8104e-009	5.6191e+003	2.0328e-008	5.2903e+003	7.0543e-003	5.1807e+003	5.0993e-002	5.1807e+003
2i	1.1153e-009	4.1396e+003	4.4591e-009	2.8245e+003	3.3565e-009	8.3040e+003	9.4294e-009	6.2766e+003
2ik	3.9537e-007	1.1221e+002	5.3827e-007	1.1221e+002	3.0942e-008	2.4684e+003	8.1254e-008	3.7560e+003
2al1	4.2721e-009	1.0331e+004	1.4633e-008	3.3177e+003	1.0593e-002	9.5643e+003	5.0471e-002	3.2081e+003
2al2	4.4056e-009	1.0660e+004	1.3022e-008	3.0985e+003	8.2442e-003	9.5643e+003	3.7220e-002	3.2081e+003
7pm	0.0000e+000	NA	0.0000e+000	NA	0.0000e+000	NA	0.0000e+000	NA
7md	1.8564e-015	1.1221e+002	1.9363e-014	1.1221e+002	1.5584e-010	1.3961e+002	1.6198e-009	1.3961e+002
7ff	4.5616e-012	7.1116e+001	4.7624e-011	7.1116e+001	4.3316e-006	8.4815e+001	4.5223e-005	8.4815e+001
7l	0.0000e+000	NA	0.0000e+000	NA	0.0000e+000	NA	0.0000e+000	NA
7i	0.0000e+000	NA	0.0000e+000	NA	0.0000e+000	NA	0.0000e+000	NA
7ik	5.7630e-009	5.7418e+001	1.1826e-008	5.7418e+001	5.8045e-011	5.7418e+001	7.9828e-011	5.7418e+001
7al1	0.0000e+000	NA	0.0000e+000	NA	0.0000e+000	NA	0.0000e+000	NA
7al2	0.0000e+000	NA	0.0000e+000	NA	0.0000e+000	NA	0.0000e+000	NA
8pm	2.5795e-008	2.8633e+004	3.0394e-008	1.3400e+004	1.1121e-001	4.8249e+004	2.9721e-001	4.9016e+004
8md	1.0438e-010	4.4273e+003	4.2176e-010	4.4958e+003	1.8577e-004	3.7150e+003	7.4759e-004	3.1670e+003

Case	Q_{max}	Time	σQ_{max}	Time	C_{max}	Time	σC_{max}	Time
8ff	3.3455e-008	1.9263e+004	8.7643e-008	3.7249e+002	1.5369e-001	2.8359e+004	2.8922e-001	1.5044e+004
8l	2.0352e-008	2.9071e+004	3.8567e-008	5.2903e+003	1.8729e-001	1.3198e+005	1.0684e+000	1.3044e+005
8i	2.2954e-009	7.2081e+003	6.6857e-009	3.9752e+003	1.3879e-008	1.1132e+005	5.5224e-008	1.1450e+005
8ik	4.0049e-007	1.1221e+002	5.4525e-007	1.1221e+002	4.6323e-008	2.7071e+004	1.8143e-007	2.5975e+004
8al1	2.6261e-008	3.0496e+004	3.0485e-008	1.4057e+004	7.5520e-002	4.0688e+004	1.5225e-001	4.9893e+004
8al2	2.6114e-008	3.2688e+004	2.9721e-008	1.2852e+004	5.9782e-002	4.0468e+004	9.3796e-002	1.2304e+004
16pm	2.4081e-008	3.0277e+004	2.8944e-008	1.4934e+004	9.7575e-002	4.9893e+004	2.7390e-001	1.9646e+004
16md	5.6753e-011	3.9341e+003	2.2806e-010	3.9478e+003	1.2775e-004	3.4547e+003	4.9636e-004	3.4410e+003
16ff	3.3078e-008	2.0016e+004	4.7490e-008	4.3862e+003	1.4384e-001	2.8551e+004	2.8991e-001	1.7304e+004
17pm	2.5784e-008	3.0277e+004	2.9936e-008	1.4934e+004	1.0920e-001	4.9893e+004	3.0200e-001	5.0222e+004
17md	5.7271e-011	4.1259e+003	2.3015e-010	4.1396e+003	1.2877e-004	3.5506e+003	5.0029e-004	3.5643e+003
17ff	3.4606e-008	2.0016e+004	4.7962e-008	4.3862e+003	1.5341e-001	2.8551e+004	3.0145e-001	1.7304e+004
18pm	0.0000e+000	NA	0.0000e+000	NA	0.0000e+000	NA	0.0000e+000	NA
18md	0.0000e+000	NA	0.0000e+000	NA	0.0000e+000	NA	0.0000e+000	NA
18ff	2.4975e-011	1.1221e+002	2.2120e-010	1.1221e+002	4.4047e-005	1.3276e+002	4.5986e-004	1.3276e+002
19pm	0.0000e+000	NA	0.0000e+000	NA	0.0000e+000	NA	0.0000e+000	NA
19md	0.0000e+000	NA	0.0000e+000	NA	0.0000e+000	NA	0.0000e+000	NA
19ff	6.2926e-015	1.1221e+002	5.5733e-014	1.1221e+002	1.1098e-008	1.3276e+002	1.1586e-007	1.3276e+002
20pm	3.6623e-011	2.1096e+007	4.3255e-011	9.3589e+006	1.0688e-001	3.4060e+007	2.8624e-001	3.3677e+007
20md	6.2611e-015	1.6441e+005	5.7492e-014	1.6441e+005	3.2686e-009	1.6441e+005	3.4081e-008	1.6441e+005
20ff	4.4848e-009	2.4341e+003	2.3315e-008	5.6427e+002	4.8058e-002	4.1191e+003	2.1410e-001	4.1191e+003
27pm	2.3411e-008	3.2123e+004	2.7004e-008	1.4260e+004	9.1750e-002	4.9438e+004	2.6000e-001	1.9739e+004
27md	1.8729e-011	9.3285e+003	5.4909e-011	7.6846e+003	7.2722e-005	1.0972e+004	2.3447e-004	6.0408e+003
27ff	1.8256e-008	2.1164e+004	2.1475e-008	7.3559e+003	1.1532e-001	3.1794e+004	1.7572e-001	8.8342e+004
31pm	0.0000e+000	NA	0.0000e+000	NA	0.0000e+000	NA	0.0000e+000	NA
31md	0.0000e+000	NA	0.0000e+000	NA	0.0000e+000	NA	0.0000e+000	NA

Case	Q_{max}	Time	oQ_{max}	Time	C_{max}	Time	oC_{max}	Time
31ff	0.0000e+000	NA	0.0000e+000	NA	0.0000e+000	NA	0.0000e+000	NA
32pm	4.4129e-011	1.7622e+007	4.9866e-011	8.2850e+006	1.0927e-001	2.8274e+007	2.9379e-001	3.1101e+007
32md	1.1731e-014	2.7398e+006	4.4141e-014	2.7398e+006	4.2443e-008	2.7398e+006	2.2640e-007	2.7398e+006
32ff	7.6989e-009	6.8755e+002	2.3303e-008	4.6838e+002	2.9935e-002	2.7376e+006	1.2759e-001	9.0673e+002
14pm	0.0000e+000	NA	0.0000e+000	NA	0.0000e+000	NA	0.0000e+000	NA
14md	0.0000e+000	NA	0.0000e+000	NA	0.0000e+000	NA	0.0000e+000	NA
14ff	5.3421e-013	2.4920e+002	5.5773e-012	2.4920e+002	3.3953e-006	2.4920e+002	3.5448e-005	2.4920e+002
15pm	4.4129e-011	1.7622e+007	4.9866e-011	8.2850e+006	1.0927e-001	2.8274e+007	2.9379e-001	3.1101e+007
15md	1.1731e-014	2.7398e+006	4.4141e-014	2.7398e+006	4.2443e-008	2.7398e+006	2.2640e-007	2.7398e+006
15ff	7.6989e-009	6.8755e+002	2.3303e-008	4.6838e+002	2.9935e-002	2.7376e+006	1.2759e-001	9.0673e+002
37pm	0.0000e+000	NA	0.0000e+000	NA	0.0000e+000	NA	0.0000e+000	NA
37md	0.0000e+000	NA	0.0000e+000	NA	0.0000e+000	NA	0.0000e+000	NA
37ff	1.3389e-017	2.2218e+003	7.9945e-017	2.2218e+003	4.7985e-010	2.2218e+003	1.9930e-009	2.2218e+003
38pm	3.2187e-012	2.4110e+008	3.8493e-012	1.0608e+008	1.0929e-001	3.8400e+008	2.9954e-001	4.0329e+008
38md	0.0000e+000	NA	0.0000e+000	NA	0.0000e+000	NA	0.0000e+000	NA
38ff	8.0227e-010	4.4136e+003	2.8125e-009	4.4136e+003	3.5491e-002	7.8578e+005	1.4452e-001	8.7971e+003
41pm	0.0000e+000	NA	0.0000e+000	NA	0.0000e+000	NA	0.0000e+000	NA
41md	0.0000e+000	NA	0.0000e+000	NA	0.0000e+000	NA	0.0000e+000	NA
41ff	0.0000e+000	NA	0.0000e+000	NA	0.0000e+000	NA	0.0000e+000	NA
42pm	3.2187e-012	2.4110e+008	3.8493e-012	1.0608e+008	1.0929e-001	3.8400e+008	2.9954e-001	4.0329e+008
42md	0.0000e+000	NA	0.0000e+000	NA	0.0000e+000	NA	0.0000e+000	NA
42ff	8.0227e-010	4.4136e+003	2.8125e-009	4.4136e+003	3.5491e-002	7.8578e+005	1.4452e-001	8.7971e+003
43pm	0.0000e+000	NA	0.0000e+000	NA	0.0000e+000	NA	0.0000e+000	NA
43md	0.0000e+000	NA	0.0000e+000	NA	0.0000e+000	NA	0.0000e+000	NA
43ff	0.0000e+000	NA	0.0000e+000	NA	0.0000e+000	NA	0.0000e+000	NA
44pm	3.2187e-012	2.4110e+008	3.8493e-012	1.0608e+008	1.0929e-001	3.8400e+008	2.9954e-001	4.0329e+008

Case	Q_{max}	Time	σQ_{max}	Time	C_{max}	Time	σC_{max}	Time
44md	0.0000e+000	NA	0.0000e+000	NA	0.0000e+000	NA	0.0000e+000	NA
44ff	8.0227e-010	4.4136e+003	2.8125e-009	4.4136e+003	3.5491e-002	7.8578e+005	1.4452e-001	8.7971e+003
52pm	0.0000e+000	NA	0.0000e+000	NA	0.0000e+000	NA	0.0000e+000	NA
52md	0.0000e+000	NA	0.0000e+000	NA	0.0000e+000	NA	0.0000e+000	NA
52ff	7.9237e-010	4.4136e+003	2.7778e-009	4.4136e+003	3.2977e-002	8.7971e+003	1.4098e-001	8.7971e+003
55pm	3.1013e-012	2.3233e+008	3.7869e-012	1.0608e+008	1.0301e-001	3.8400e+008	2.8147e-001	4.0329e+008
55md	0.0000e+000	NA	0.0000e+000	NA	0.0000e+000	NA	0.0000e+000	NA
55ff	8.0227e-010	4.4136e+003	2.8125e-009	4.4136e+003	3.5487e-002	7.8578e+005	1.4452e-001	8.7971e+003
56pm	1.1542e-015	1.4027e+007	1.2051e-014	1.4027e+007	1.8040e-005	1.4027e+007	1.8835e-004	1.4027e+007
56md	0.0000e+000	NA	0.0000e+000	NA	0.0000e+000	NA	0.0000e+000	NA
56ff	8.0113e-010	4.4136e+003	2.8085e-009	4.4136e+003	3.3708e-002	8.7971e+003	1.4410e-001	8.7971e+003
59pm	0.0000e+000	NA	0.0000e+000	NA	0.0000e+000	NA	0.0000e+000	NA
59md	0.0000e+000	NA	0.0000e+000	NA	0.0000e+000	NA	0.0000e+000	NA
59ff	7.0636e-010	4.4136e+003	2.4762e-009	4.4136e+003	2.6227e-002	8.7971e+003	1.1212e-001	8.7971e+003
60pm	0.0000e+000	NA	0.0000e+000	NA	0.0000e+000	NA	0.0000e+000	NA
60md	0.0000e+000	NA	0.0000e+000	NA	0.0000e+000	NA	0.0000e+000	NA
60ff	5.0380e-010	4.4136e+003	1.8907e-009	3.3177e+003	1.6503e-002	5.5095e+003	5.9284e-002	5.5095e+003
61pm	2.0776e-013	5.2603e+007	1.4041e-012	2.5425e+007	5.3175e-003	2.5425e+007	4.7896e-002	2.5425e+007
61md	0.0000e+000	NA	0.0000e+000	NA	0.0000e+000	NA	0.0000e+000	NA
61ff	4.0791e-010	8.7971e+003	1.3596e-009	8.7971e+003	3.4671e-002	7.8578e+005	1.2082e-001	5.8304e+005
63pm	0.0000e+000	NA	0.0000e+000	NA	0.0000e+000	NA	0.0000e+000	NA
63md	0.0000e+000	NA	0.0000e+000	NA	0.0000e+000	NA	0.0000e+000	NA
63ff	1.0377e-011	2.2218e+003	6.1963e-011	2.2218e+003	3.7192e-004	2.2218e+003	1.5447e-003	2.2218e+003
64pm	3.2187e-012	2.4110e+008	3.8493e-012	1.0608e+008	1.0929e-001	3.8400e+008	2.9954e-001	4.0329e+008
64md	0.0000e+000	NA	0.0000e+000	NA	0.0000e+000	NA	0.0000e+000	NA
64ff	8.0157e-010	4.4136e+003	2.8100e-009	4.4136e+003	3.5491e-002	7.8578e+005	1.4452e-001	8.7971e+003

DISTRIBUTION

Raymon D. Cox, Acting, Director
Contracts Management Division
Nevada Operations Office
U.S. Department of Energy
P.O. Box 98518
Las Vegas, NV 89193-8518

Beverly Colbert
Contracts Management Division
Nevada Operations Office
U.S. Department of Energy
P.O. Box 98518
Las Vegas, NV 89193-8518

David Cowser
Bechtel Nevada
P.O. Box 98521
Las Vegas, NV 89193-8521

Doug Duncan
Hydrology Program Manager
Environment, Safety & Health Division
Nevada Operations Office
U.S. Department of Energy
P.O. Box 98518
Las Vegas, NV 89193-8518

Paul Gretskey
International Technology Corporation
P.O. Box 93838, M/S 439
Las Vegas, NV 89193-3838

Kenneth A. Hoar, Director
Environment, Safety & Health Division
Nevada Operations Office
U.S. Department of Energy
P.O. Box 98518
Las Vegas, NV 89193-8518

Marjory Jones
Desert Research Institute
Water Resources Center
2215 Raggio Parkway
Reno, NV 89512-1095

Randy Laczniak
U.S. Geological Survey
Water Resources Division
6770 S. Paradise Rd.
Las Vegas, NV 89119

Leslie A. Monroe
Environment, Safety & Health Division
Nevada Operations Office
U.S. Department of Energy
P.O. Box 98518
Las Vegas, NV 89193-8518

Monica Sanchez
Environmental Restoration Division
Nevada Operations Office
U.S. Department of Energy
P.O. Box 98518
Las Vegas, NV 89193-8518

Peter Sanders
Environmental Restoration Division
Nevada Operations Office
U.S. Department of Energy
P.O. Box 98518
Las Vegas, NV 89193-8518

David Shafer
Water Resources Center
Desert Research Institute
755 E. Flamingo Road
Las Vegas, NV 89119-7363

David K. Smith
Isotopes Sciences Division
Lawrence Livermore National Laboratory
P.O. Box 808, M/S L231
Livermore, CA 94550

Runore C. Wycoff, Director
Environmental Restoration Division
Nevada Operations Office
U.S. Department of Energy
P.O. Box 98518
Las Vegas, NV 89193-8518

Nevada State Library and Archives
State Publications
100 North Stewart Street
Carson City, NV 89710-4285

Archives
Getchell Library
University of Nevada, Reno

Beverly Carter
MacKay School of Mines Library
University of Nevada, Reno

Document Section, Library
University of Nevada, Las Vegas
4505 Maryland Parkway
Las Vegas, NV 89154

Library
Desert Research Institute
2215 Raggio Parkway
Reno, Nevada 89512-1095

Library
IT Corporation
Bldg. B-1
P.O. Box 93838, M/S 439
Las Vegas, NV 89193-3838
ATTN: Toni Miller, M/S 439

Library
Southern Nevada Science Center
Desert Research Institute
755 E. Flamingo Road
Las Vegas, NV 89119-7363

Technical Information Resource Center
Nevada Operations Office
U.S. Department of Energy
P.O. Box 98518
Las Vegas, NV 89193-8518

Public Reading Facility
Nevada Operations Office
U.S. Department of Energy
P.O. Box 98521
Las Vegas, NV 89193-8521

Office of Scientific and Technical Information
U.S. Department of Energy
P.O. Box 62
Oak Ridge, TN 37831-9939